Karlsruhe Institute of Technology

# Characterisation of energy loss processes of 18.6 keV electrons inside the windowless tritium source of KATRIN

Zur Erlangung des akademischen Grades eines

DOKTORS DER NATURWISSENSCHAFTEN

von der KIT-Fakultät für Physik des
Karlsruher Instituts für Technologie genehmigte

DISSERTATION

von

M. Sc. Lutz Schimpf

aus Reutlingen

| | |
|---|---|
| Referentin: | Prof. Dr. Kathrin Valerius<br>(KIT, Institut für Astroteilchenphysik) |
| Korreferent: | Prof. Dr. Bernhard Holzapfel<br>(KIT, Institut für Technische Physik) |

Tag der mündlichen Prüfung: 19.02.2021

# Contents

# 1. Introduction

Wolfgang Pauli's postulation of an electrically neutral, weakly interacting particle 90 years ago marks the birth of neutrino physics. Although neutrinos are the most abundant particles in the universe, the domain of neutrino physics is a very challenging field of research, since neutrinos are elusive particles due to their missing electric charge and the small interaction cross section. Consequently, it required more than 20 years of research until the first of the three neutrino flavours was detected by the Cowan-Reines neutrino experiment [RC53, RC56]. After the detection of neutrinos, it took another four decades to provide the irrefutable proof by the discovery of neutrino oscillations [FHI$^+$98] that neutrinos are massive particles, which demonstrates the incompleteness of the standard model of particle physics where neutrinos are massless. With this groundbreaking discovery, the sector of neutrino physics beyond the standard model was entered, which sets intriguing prospects for novel ideas and conceptional extensions of the standard model. In order to test or improve the theories beyond the standard model, the determination of the absolute mass scale of the neutrinos is of major interest. However, even more than 20 years after the experimental proof of a non-vanishing neutrino mass, the exact neutrino masses are yet undetermined despite numerous and long-standing experimental efforts to measure them.

The currently leading experiment in the field of direct neutrino-mass determination is the Karlsruhe Tritium Neutrino Experiment (KATRIN). The KATRIN experiment is targeted to measure the effective electron antineutrino mass with a sensitivity of $m(\nu_e) = 0.2\,\mathrm{eV}\,c^{-2}$ (90% confidence level) by investigating the energy spectrum of the tritium β-decay. For the precision measurement of the β-spectrum, a MAC-E-type electrostatic filter is used, which operates as a high-pass filter in order to discriminate the kinetic energy of the β-electrons provided by the high-luminosity windowless gaseous tritium source.

The KATRIN experiment started data taking in spring 2019 and requires three full years worth of data to reach the final sensitivity. Already from the first month of inaugurational data taking at a reduced source activity, an improved upper limit of

$$m(\nu_e) < 1.1\,\mathrm{eV}\,c^{-2} \quad (90\%\text{ confidence level})$$

on the effective electron antineutrino mass could be achieved [AAA$^+$19b]. This limit tightens the previous one of $m(\nu_e) < 2\,\mathrm{eV}\,c^{-2}$ (95% confidence level) of the preceding experiments at Mainz and Troitsk [KBB$^+$05, ABB$^+$11] by about a factor of two.

In order to reach the final sensitivity, not only the statistical uncertainty on the measured β-spectrum must be further reduced, but also a very precise characterisation and most careful suppression of the systematics of the experiment is required. As conceived in the design of the experiment, the total systematic uncertainty on the observable, $m_\nu^2$, of $\sigma_{\mathrm{sys}}^{\mathrm{tot}}(m_\nu^2) < 17 \times 10^{-3}\,\mathrm{eV}^2\,c^{-4}$ must not be exceeded [KAT05]. This goal is in accordance with a statistical uncertainty achievable with three years of data. One of the five major systematics contributing to this systematic uncertainty budget is the energy loss from

inelastic scattering of the signal electrons with the source gas inside the gaseous tritium source. At the nominal source density of $5 \times 10^{21}$ molecules/m$^2$ nearly 60% of the signal electrons scatter inelastically inside the source at least once. The energy loss from the scattering processes causes a systematic distortion of the measured β-spectrum. In order to take this distortion into account in the neutrino-mass analysis, a precise description of the probability distribution of these energy losses, the so-called energy-loss function, is required. An empirical model for the energy-loss function of 18.6 keV electrons scattering off molecular tritium exists, which was determined at the Troitsk ν-mass experiment [ABB$^+$00]. However, this model does not meet the high requirements of KATRIN, since the parameter uncertainties would lead to an uncertainty on $m_\nu^2$ which exceeds the total systematic uncertainty budget by more than a factor of two. It is thus absolutely essential for the success of KATRIN to measure the shape of the energy-loss function of tritium with unprecedented precision in-situ with the experimental setup of KATRIN.

For the measurement of the energy-loss function, a precision electron source is required, which generates an angular selected beam of electrons at a well defined kinetic energy. For this purpose, a custom photoelectron source concept was developed over many years at KATRIN. Due to the high demands on the energy stability, the energy spread, and the angular selectivity, the development required the expertise of many dissertations [Val09, Bok13, Bab14, Zac15, Sch16, Beh17, Sac20]. The developed photoelectron source was finally integrated into the beamline of KATRIN in 2018 and was commissioned in fall 2018 as part of the experimental work of this thesis. During the technical commissioning, numerous subcomponents had to be installed and implemented in the control and monitoring system and their functionality had to be verified. After the photoelectron source was successfully commissioned, the in-situ performance in the experimental setup of KATRIN had to be characterised. As these tasks require various expertises, the commissioning and the characterisation was carried out in complementing work together with R. Sack (University of Münster) [Sac20].

The commissioning and characterisation of the photoelectron source as well as the precision measurement of the energy-loss function of both molecular deuterium and tritium with the KATRIN experiment is the scope of this thesis.

The thesis is structured as it follows:

An introduction to the field of neutrino physics is provided in chapter 2, where the postulation of neutrinos and the discovery of the thee neutrino flavours are discussed. The theory of neutrino oscillations is introduced and their experimental proof is discussed, which shows that neutrinos are massive particles. Furthermore, the different measurement approaches of the determination of the neutrino mass are outlined, including an introduction to the direct measurement approach of KATRIN, which is based on the investigation of the energy spectrum of the tritium β-decay.

The measurement principle of the KATRIN experiment as well as the experimental setup is described in detail in chapter 3.

In chapter 4, an introduction to the domain of electron-impact scattering is given, including a discussion of the elastic and inelastic scattering processes at the respective electron energies and their contribution to the shape of the energy-loss function. Furthermore, the existing empirical and literature-based energy-loss models are introduced to provide an overview of the current state of research. The chapter is concluded by a discussion of the impact on the measurement result of KATRIN due to the inelastic scattering inside the gaseous tritium source.

The photoelectron source, which constitutes an essential part of the energy loss measurements, is the subject of chapter 5. The description comprises an introduction to the

working principle and the setup of the photoelectron source, which is important for the understanding of the properties of the energy-loss function measurements. Furthermore, the performance of the photoelectron source during the first commissioning and the energy-loss function measurements is presented. The focus of the experimental work of this thesis was on the performance of the optical setup, which consists of a Laser-Driven Light Source and a pulsed UV laser. The latter can be used to generate a pulsed electron beam, which allows one to measure the time-of-flight of the electrons between the photoelectron source and the focal plane detector.

For the measurements using the pulsed photoelectron beam, a dedicated pile-up reconstruction is required, which is introduced in chapter 6. The occurrence of non-Poissonian pile-up events at the focal plane detector is one of the major systematics of the measurements using the pulsed photoelectron beam. The pile-up, which is a result of the strongly time-focused electron pulses, causes deviations of the measured photoelectron rate in the order of several percent even at moderate electron rates of $<10^4$ electrons per second. Consequently, a robust correction technique is essential not only for the measurement of the energy-loss function but for any other measurement using the pulsed photoelectron beam. In order to correct the systematic rate loss, a novel pile-up reconstruction is introduced in this work, which is based on detailed flight time and detector simulations.

Before the measurement of the energy-loss function of tritium was performed in spring 2019, a test of the complex measurement and analysis strategy was carried out during the commissioning of the full beamline of KATRIN in fall 2018, when deuterium was circulated in the source. The measurements using deuterium allowed to prepare for the first measurement of the energy-loss function of tritium, the precise and reliable results of which where required for the first neutrino-mass analysis of KATRIN. In chapter 7, the data taking as well as the analysis of the measurement data are presented. The analysis of the measurement data is carried out using two different analysis techniques, which are a singular value decomposition (SVD) deconvolution and an analytical fit using a novel semi-empirical model of the energy-loss function. Besides the analysis considering only integral measurement data, the analytical fit approach is also applied to an extended data set including differential measurement data obtained from time-of-flight measurements carried out by R. Sack (University of Münster). The chapter is concluded with a critical discussion and evaluation of the quality of the different analysis approaches with respect to the KATRIN requirements. It is shown that the analysis technique of the analytical fit performs significantly better than the deconvolution and that the former method meets the requirements of KATRIN. Based on these results, the analytical fit was established as the standard analysis techniques for the following measurements of the energy-loss function of tritium.

The first precision measurements of the energy-loss function of molecular tritium is reported in chapter 8. The parametrisation of the energy-loss function is obtained from a combined fit of three integral and four differential data sets. The latter were provided by C. Rodenbeck (University of Münster). In order to determine both the statistical and systematic uncertainties of the energy-loss function, several individual sources of systematic uncertainties are characterised. The major systematics are found to be due to the uncertainty of the transmission function model, the pile-up correction, and the applied analysis cuts. The impact of the systematics on the measurement result is determined with dedicated Monte Carlo simulations, which show that the systematic uncertainties are subdominant compared to the statistical uncertainty. With a propagation of the model uncertainties it is demonstrated that the result of the first measurement of the energy-loss function of tritium meets the KATRIN requirements in order to reach the final sensitivity of $m(\nu_e) = 0.2\,\mathrm{eV}\,c^{-2}$ (90% confidence level). This new precision parametrisation of the energy-loss function was already used in the analysis of the first neutrino-mass measurement

campaign, which led to the improved upper limit of $m(\nu_e) < 1.1\,\mathrm{eV}\,c^{-2}$ (90% confidence level) [AAA$^+$19b].

This thesis concludes with a summary and evaluation of the results in chapter 9 leading to an outlook on the future measurement results of KATRIN.

# 2. Neutrino physics

Within the last eight decades, neutrino physics has become an important field of research in the domain of (astro)particle physics and cosmology. Joint efforts of physicists contributing to international research projects have lead to groundbreaking new discoveries, e.g. by using neutrinos in multi-messenger astronomy [AAA+18a]. Especially since neutrinos have a vanishing charge and are only weakly interacting they are a handy tool to investigate far distant galaxies.

Although it was proven in 1998 that neutrinos must have a non-vanishing rest mass by the discovery of neutrino oscillations [FHI+98], the actual value of their mass is still unknown. Many experiments have tried to measure the exact mass but none of them succeeded so far [RK88, KBB+05, ABB+11].

The following sections give an introduction to the domain of neutrino physics, covering the discovery of the neutrinos in Sec. 2.1, the important neutrino oscillation experiments in Sec. 2.2, and the different measurement approaches of state-of-the-art neutrino-mass experiments in Sec. 2.4.

The sections are mainly based on Ref. [Zub12], which provides an excellent overview on this topic.

## 2.1 Discovery and integration in the standard model

The origin of neutrino physics leads back to the time after the discovery of radioactive decays by H. Bequerell and M. Curie in 1896 (see e.g. Ref. [RV17]). After the classification of radioactive decays into $\alpha$ and $\beta$-radiation by E. Rutherford in 1899 [Rut99], many experiments with radioactive elements were performed. While investigating the energy spectrum of electrons emitted by the decay of Radium B and C (nowadays known as $^{214}$Pb and $^{214}$Bi), J. Chadwick found out in 1914 that the energy spectrum did not match his expectations of a discrete energy spectrum but was continuous as shown in Fig. 2.1 (see e.g. Ref. [JAK+00]).

The unexpected continuous shape of the $\beta$-spectrum could not be explained by a radioactive two-body decay

$$ {}^{\mathrm{A}}_{\mathrm{Z}}\mathrm{X} \rightarrow {}^{\mathrm{A}}_{\mathrm{Z}-1}\mathrm{Y} + e^{-} , \tag{2.1} $$

since the continuous spectrum would violate the conservation of energy and momentum. In order to solve the problem, a new particle was postulated by W. Pauli in 1930 [PKW64]. The neutron, as the neutrino was initially called, was postulated to be a neutral and very light spin-$\frac{1}{2}$ particle, which is created during the $\beta$-decay in addition to the electron. The resulting three-body decay solves the violation of energy and momentum, as the additional particle can carry away momentum.

The theoretical formulation of the process, including the creation of the neutron (which was now called neutrino after the discovery of what is today known as neutrons in 1932

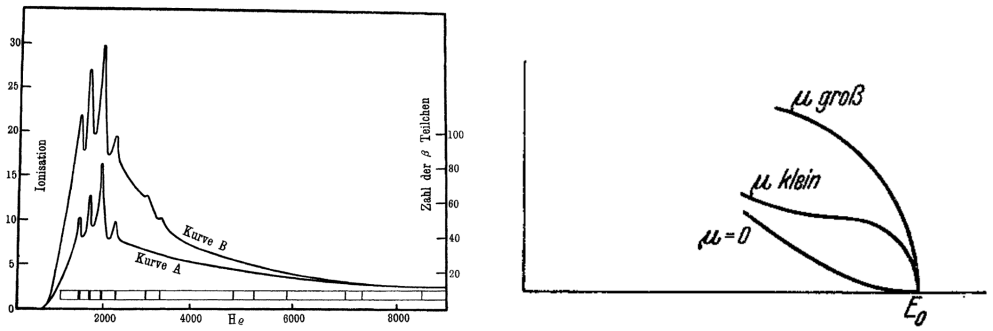


Figure 2.1: **Left:** β-spectra of Radium B and C as measured by J. Chadwick in 1914 using the novel point counter of Geiger (labelled with *Kurve A*) as well as an ionisation counter (labelled with *Kurve B*). The two y-axes label are *ionisation* and *number of β-particles*. A continuous spectrum was measured, superimposed with four discrete lines belonging to the Radium B decay. The shapes of the spectra did not match the expectations of a discrete energy spectrum and thus required an improved theory of β-decays. Figure reprinted from Ref. [Cha14]. **Right:** Theoretical shapes of the endpoint of the β-spectrum for different neutrino masses $\mu$ as derived by E. Fermi in 1934. According to the agreement with experimental data, the neutrino mass was expected to be close to zero. The original paper was published in German, with the labels $\mu$ *klein* and $\mu$ *groß* translating to *small* $\mu$ and *large* $\mu$, respectively. Figure reprinted from Ref. [Fer34], with permission of Springer.

[Cha32]), was first published by E. Fermi in 1934 [Fer34]. Already in this very early publication, E. Fermi pointed out that the most significant signature of the mass of the neutrinos is found close to the endpoint, as shown on the right side of Fig. 2.1. As the available measurement data and the theoretical spectrum for $m_\nu \approx 0$ were in agreement, E. Fermi assumed that the neutrino mass has to be close to zero or even vanishes completely.

A postulation of a new particle is always followed by the question of the possibility to proof its existence. First cross section calculations for the inverse β-decay were performed by H. Bethe already in the same year of Fermi's postulation. The small number of $\sigma < 10^{-44}\,\mathrm{cm}^2$ lead him to the conclusion that it will be "absolutely impossible to observe processes of this kind with the neutrinos created in nuclear transformations" [BP34].

### Discovery of the neutrino

With the development of nuclear reactors, artificial and powerful neutrino sources were available. The experimental proof of the existence of neutrinos was finally provided in 1953 by the so-called poltergeist project. The Cowan-Reines neutrino experiment [RC53, RC56] consist of two tanks filled with a total of $300\,\ell$ of liquid scintillator, each surrounded by 110 photomultiplier tubes. The detectors were placed next to the Hanford Plant reactor, with the aim to detect the inverse β-decay

$$\bar{\nu}_e + p \rightarrow n + e^+ \,. \tag{2.2}$$

The detection method used a coincidence of two $\gamma$-rays from the annihilation of the positron with an electron followed by a detection of a pair of $\gamma$-rays from the neutron capture by the cadmium solved in the scintillator. The very clear signature inside the detector allowed to measure the electron antineutrino flux with a signal to background ratio of 17/1.

At the time of the discovery, an upper limit of the neutrino mass $m_\nu < 250\,\mathrm{eV}$ was determined by investigations of the endpoint energy of the tritium β-decay [LM52]. Since

the mass was too small to be measured, the result still agreed with the common expectation that neutrinos are massless particles.

As two other generations (flavours) of leptons, namely the muon $\mu^{\pm}$ and the tauon $\tau^{\pm}$ were discovered in 1936 [NA37] and 1975 [PAB$^+$75], respectively, different experiments were build to proof the existence of the corresponding muon (anti)neutrino $\nu_\mu$ ($\bar{\nu}_\mu$) as well as the tauon (anti)neutrino $\nu_\tau$ ($\bar{\nu}_\tau$).

The first detection of muon neutrinos was achieved at the Brookhaven AGS in 1962 [DGG$^+$62]. The muon neutrinos were created mainly from the decays of charged pions generated by dumping a proton beam

$$\pi^- \to \mu^- + \bar{\nu}_\mu \quad \text{and} \quad \pi^+ \to \mu^+ + \nu_\mu \,. \tag{2.3}$$

At sufficient high beam energies it is possible to detect the neutrinos by the matter interaction

$$\bar{\nu}_\mu + p \to \mu^+ + n \quad \text{and} \quad \nu_\mu + n \to \mu^- + p \,. \tag{2.4}$$

By using a spark chamber as detector the discrimination between muons and electrons was possible. If the generated neutrinos had the same properties as the electron neutrino, the same amount of electrons and muons would be detected. However, with a 29 to 6 muon-to-electron ratio, it was clearly shown that generated muon neutrinos are different to electron neutrinos.

The last neutrino flavour was discovered by the DONUT experiment at Fermilab in 2001 [KUA$^+$01], where a beam of tauon neutrinos was generated by the decay of $D_s$ mesons into a $\tau^-$ and $\bar{\nu}_\tau$ and the subsequent decay of the $\tau^-$ into another $\nu_\tau$.

The discovery was achieved by observing the interaction of the $\nu_\tau$ with matter in a charged current reaction

$$\nu_\tau + {}^{\mathrm{A}}_{\mathrm{Z}}\mathrm{X} \to \tau^- + {}^{\mathrm{A}}_{\mathrm{Z+1}}\mathrm{Y} \,. \tag{2.5}$$

As the created $\tau$ has only a very short life time of $2.9 \times 10^{-13}$ s, the tauon typically decays within 2 mm (for a beam energy of 800 GeV) [Pat01] generating a second kink due to the decay

$$\tau^- \to e^- + \bar{\nu}_e + \nu_\tau \,. \tag{2.6}$$

The single particle tracks from neutrino interactions were recorded with high-resolution emulsion plates allowing a spacial resolution for particle tracks of 1 µm precision. The existence of the so-called tauon-kink was confirmed at a total of four interactions [KUA$^+$01].

With the discovery of the $\nu_\tau$, the particle content in the leptonic sector of the standard model of particle physics (see Fig. 2.2) was completed, containing the three charged leptons $e^{\pm}$, $\mu^{\pm}$, $\tau^{\pm}$ as well as the corresponding (anti)neutrinos $\nu_{e,\mu,\tau}$ ($\bar{\nu}_{e,\mu,\tau}$).

At the time of the discovery of the $\nu_\mu$, neutrinos were still assumed to be massless, as theoretical calculations including a vanishing neutrino mass agreed well with experimental data. The agreement of the theory and the experimental data changed with the appearance of the so-called solar neutrino problem.

### 2.1.1 Solar neutrino problem

Neutrinos are a perfect tool to investigate astronomical objects, since they cannot be electromagnetically deflected and thus point back to their origin. Furthermore, neutrinos are only weakly interacting, which allows them to travel long distances without being absorbed or deflected by matter.

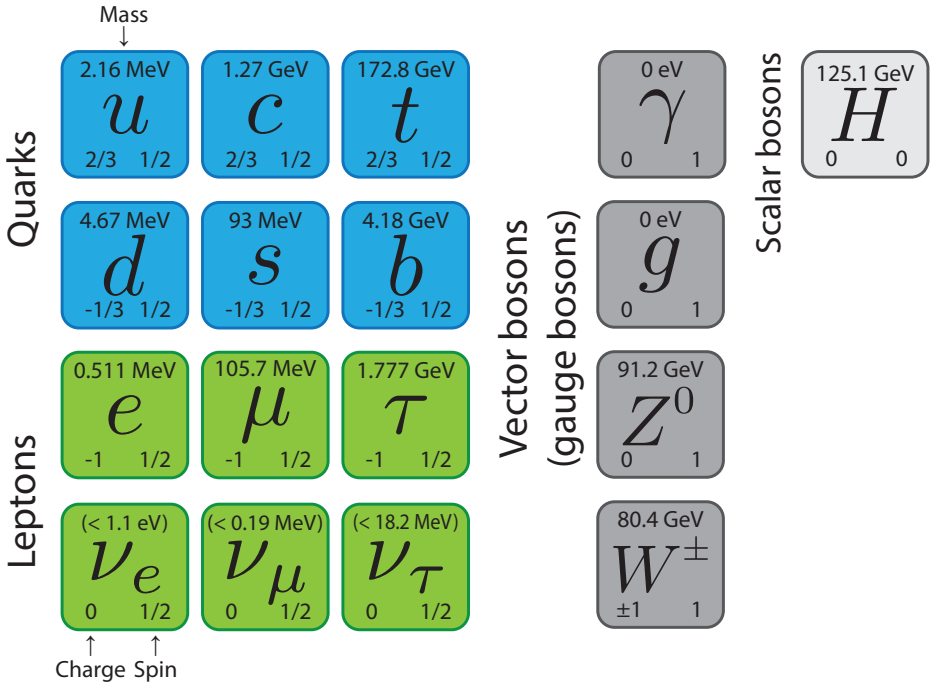


Figure 2.2: Particles in the standard model of particle physics. The particles are arranged into four groups according to their spin and interactions. The four groups are quarks, leptons, gauge bosons, and scalar bosons. The exact masses of the three neutrino generations are still unknown. The values in the figure are according to Ref. [ZB+20].

The first experiment using neutrinos as messenger particles was Homestake, which was built to measure the absolute solar neutrino flux and to confirm the calculations of J. Bahcall [BFIS63, Bah64, BPB01].

The dominant fusion processes in the solar core, which are associated with the emission of neutrinos, are (see e.g. Ref. [Zub12])

$$\begin{aligned} p + p &\rightarrow \mathrm{D} + e^+ + \nu_e && \text{(pp)} \\ p + e^- + p &\rightarrow \mathrm{D} + \nu_e && \text{(pep)} \\ {}^7\mathrm{Be} &\rightarrow {}^7\mathrm{Li} + \nu_e \\ {}^8\mathrm{B} &\rightarrow {}^8\mathrm{Be}^* + e^+ + \nu_e \\ {}^3\mathrm{He} + p &\rightarrow {}^4\mathrm{He} + e^+ + \nu_e && \text{(hep)}\,, \end{aligned} \tag{2.7}$$

which lead to the energy spectrum displayed in Fig. 2.3.

In order to determine the flux of neutrinos reaching the earth, R. Davis used a large tank filled with 615 t of perchloro-ethylene ($C_2Cl_4$), where the solar neutrinos interact with the chlorine by inverse β-decay (with a threshold energy of 0.814 MeV)[CDRD+98]

$${}^{37}\mathrm{Cl} + \nu_e \rightarrow {}^{37}\mathrm{Ar}^+ + e^-\,. \tag{2.8}$$

${}^{37}$Ar decays with a half-life of $T_{1/2} = 35\,\mathrm{d}$ [CDRD+98] by electron capture

$${}^{37}\mathrm{Ar} \rightarrow {}^{37}\mathrm{Cl} + \nu_e\,, \tag{2.9}$$

which allowed to determine the neutrino interactions by measuring the activity of the ${}^{37}$Ar inside the detector volume.

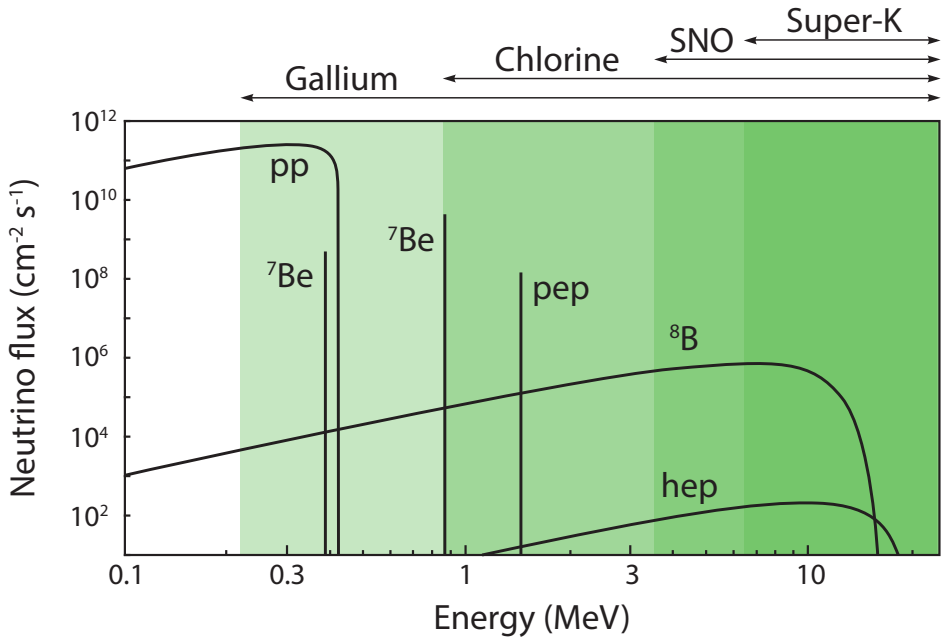


Figure 2.3: Energy spectrum of solar neutrinos and the sensitivity range of the different detection methods. Graphic according to Refs. [Bah, A$^+$20]

With this method the absolute neutrino flux above the detection threshold was determined to be [CDRD$^+$98]

$$R = 2.56 \pm 0.16(\text{stat.}) \pm 0.15(\text{syst.})\,\text{SNU}\,, \tag{2.10}$$

which is not in agreement with the theoretical predictions of [BPB01]

$$R_{\text{theo}} = 7.6^{+1.3}_{-1.1}\,\text{SNU}\,. \tag{2.11}$$

Thus, either the experiment was wrong, or the theoretical calculations assuming a vanishing neutrinos mass. The so-called solar neutrino problem, was an early hint on physics beyond the standard model and opened the field to new theories.

As the discrepancy was confirmed later on by other experiments, such as Super-K [HIK$^+$06], GALLEX [Kir98], and SAGE [AGG$^+$09], the theory had to be wrong.

An important contribution to the solution of the solar neutrino problem was provided by the SNO experiment.

### The SNO experiment

First experimental results, which did not suffer from a lack of neutrinos compared to the theoretical calculations, were obtained by the Sundbury Neutrino Obeservatory (SNO). The SNO experiment used a 1000 t heavy water ($D_2O$) detector, surrounded by 9700 photomultipliers to detect the Cherenkov light from electrons being created inside the volume [AAA$^+$02]. Benefit of using heavy water as detector volume is that not only charged current reactions

$$\nu_e + \text{D} \rightarrow e^- + p + p - 1.44\,\text{MeV} \quad \text{(CC)} \tag{2.12}$$

can be detected but also neutral current reactions

$$\nu + \text{D} \rightarrow \nu + p + n - 2.225\,\text{MeV} \quad \text{(NC)} \tag{2.13}$$

as well as elastic scatterings

$$\nu + e^- \rightarrow \nu + e^- \quad \text{(ES)} \tag{2.14}$$

(see e.g. Ref. [Zub12]).

The charged current reaction is flavour dependent as the solar neutrinos have less energy than the rest mass of the muon (comp. Figs. 2.3 and 2.2) and thus can only create electrons. However, the neutral current reactions as well as the elastic scattering are flavour independent.

In the first experimental phase, the generated neutrons from the NC interactions were detected by the emission of 6.3 MeV $\gamma$-rays from the neutron capture process [AAA+02]

$$n + \mathrm{D} \rightarrow {}^3\mathrm{H} + \gamma\,. \tag{2.15}$$

The $\gamma$-rays Compton scatter with electrons, which generate Cherenkov light.

The huge benefit of being sensitive to neutral currents and thus not being flavour sensitive is that interactions of all three neutrino flavours can be considered. Therefore, the total neutrino flux from the sun can be measured. Already the results from the phase I measurements [AAA+02]

$$\phi_{\mathrm{NC}} = 5.09^{+0.44}_{-0.43}(\text{stat.})\ ^{+0.46}_{-0.43}(\text{syst.}) \cdot 10^6\,\mathrm{cm}^{-2}\,\mathrm{s}^{-1} \tag{2.16}$$

were in agreement with the prediction of

$$\phi_{\mathrm{NC}}^{\mathrm{theo}} = 5.05^{+1.01}_{-0.81} \cdot 10^6\,\mathrm{cm}^{-2}\,\mathrm{s}^{-1}\,. \tag{2.17}$$

This was the proof that neutrinos from the sun, although being generated as electron neutrinos, partly arrive at the earth as muon neutrinos and thus perform a flavour transformation. The effect can be explained with the theory of neutrino oscillations, which was first confirmed for atmospheric neutrinos in 1998 by the Super-Kamiokande detector [FHI+98].

The solar neutrino problem, which can be considered as the first evidence for neutrino oscillations, existed for about four decades from the time it was raised by R. Davis to the time it was finally solved.

## 2.2 Neutrino oscillations

The theory of neutrino oscillations was first proposed by B. Pontecorvo in 1957 [Pon58], inspired by the new theories on flavour oscillations in the kaon system [PP55, GMP55]. Although this first publication only proposed oscillations between neutrino and antineutrinos, and not between different neutrino flavours, the idea was adapted by Z. Maki, M. Nakagawa, and S. Sakata in 1962 to describe oscillations between the two known $\nu_e$ and $\nu_\mu$ neutrinos flavours [MNS62].

As the formalism requires neutrinos to be massive particles but neutrinos are incorporated in the standard model as massless particles, an extension of the standard model is needed. However, the exact nature of this extension is still one of the important questions in neutrino physics (see Sec. 2.3).

### 2.2.1 Formalism of neutrino oscillations

The theory of neutrino oscillations is based on the assumption that the three physical flavour eigenstates $|\nu_\alpha\rangle$ with $\alpha = e, \mu, \tau$ are connected to three mass eigenstates $|\nu_i\rangle$ for $i = 1, 2, 3$ with an unitary $3 \times 3$ mixing matrix $U$ according to

$$|\nu_\alpha\rangle = \sum_i U_{\alpha i}\,|\nu_i\rangle \quad \text{and} \quad |\nu_i\rangle = \sum_\alpha U^*_{\alpha i}\,|\nu_\alpha\rangle\ . \tag{2.18}$$

The mixing matrix $U$ is known as the PMNS-matrix, named after Pontecorvo, Maki, Nakagawa, and Sakata and consists of three mixing angles $\theta_{ij}$ as well as a CP violating phase $\delta$. The PMNS matrix can be written as the concatenation of three rotational matrices (one containing the CP phase)

$$\begin{aligned} U &= \begin{pmatrix} U_{e1} & U_{e2} & U_{e3} \\ U_{\mu 1} & U_{\mu 2} & U_{\mu 3} \\ U_{\tau 1} & U_{\tau 2} & U_{\tau 3} \end{pmatrix} \\ &= \begin{pmatrix} 1 & 0 & 0 \\ 0 & c_{23} & s_{23} \\ 0 & -s_{23} & c_{23} \end{pmatrix} \begin{pmatrix} c_{13} & 0 & s_{13}\mathrm{e}^{-\mathrm{i}\delta} \\ 0 & 1 & 0 \\ -s_{13}\mathrm{e}^{-\mathrm{i}\delta} & 0 & c_{13} \end{pmatrix} \begin{pmatrix} c_{12} & s_{12} & 0 \\ -s_{12} & c_{12} & 0 \\ 0 & 0 & 1 \end{pmatrix} \\ &= \begin{pmatrix} c_{12}c_{13} & s_{12}c_{13} & s_{13}\mathrm{e}^{-\mathrm{i}\delta} \\ -s_{12}c_{23} - c_{12}s_{23}s_{13}e^{-\mathrm{i}\delta} & c_{12}c_{23} - s_{12}s_{23}s_{13}e^{-\mathrm{i}\delta} & s_{23}c_{13} \\ s_{12}s_{23} - c_{12}c_{23}s_{13}e^{-\mathrm{i}\delta} & -s_{23}c_{12} - s_{12}c_{23}s_{13}e^{-\mathrm{i}\delta} & c_{23}c_{13} \end{pmatrix}, \end{aligned} \tag{2.19}$$

with $c_{ij} = \cos(\theta_{ij})$ and $s_{ij} = \sin(\theta_{ij})$, respectively. For the case of neutrinos being Majorana particles, two additional Majorana phases have to be added to the matrix

$$U_{\mathrm{M}} = U \cdot \begin{pmatrix} 1 & 0 & 0 \\ 0 & e^{\mathrm{i}\alpha_1} & 0 \\ 0 & 0 & e^{\mathrm{i}\alpha_2} \end{pmatrix}. \tag{2.20}$$

The following derivation of the neutrino oscillation probabilities is based on Ref. [Zub12] and uses the notation $h = \hbar = c = 1$ for simplicity.

As the mass eigenstates $|\nu_i\rangle$ are stationary, the time evolution is given as

$$|\nu_i(x,t)\rangle = e^{-\mathrm{i}(E_i t - p_i x)} |\nu_i\rangle . \tag{2.21}$$

The transition probability from the initial flavour eigenstate $|\nu_\alpha\rangle$ to another flavour eigenstate $|\nu_\beta\rangle$ at position $x$ and time $t$ is given by

$$P(\nu_\alpha \to \nu_\beta)(t) = |\langle \nu_\beta | \nu_\alpha(x,t)\rangle|^2 . \tag{2.22}$$

In order to calculate the transition probability, state $|\nu_\alpha(x,t)\rangle$ has to be expressed in terms of $|\nu_\beta\rangle$. Using the relations in Eqs. (2.18) and (2.21), Eq. (2.22) can be rewritten as

$$\begin{aligned} P(\nu_\alpha \to \nu_\beta)(x,t) &= |\langle \nu_\beta | \nu_\alpha(x,t)\rangle|^2 \\ &= \left| \left\langle \nu_\beta \middle| \sum_i U_{\alpha i} e^{-\mathrm{i}(E_i t - p_i x)} \middle| \nu_i \right\rangle \right|^2 \\ &= \left| \left\langle \nu_\beta \middle| \sum_{i,\beta} U_{\alpha i} e^{-\mathrm{i}(E_i t - p_i x)} U^*_{\beta i} \middle| \nu_\beta \right\rangle \right|^2 \\ &= \sum_{i,j} U_{\alpha i} U^*_{\alpha j} U^*_{\beta i} U_{\beta j} e^{-\mathrm{i}(E_i t - p_i x)} e^{\mathrm{i}(E_j t - p_j x)} . \end{aligned} \tag{2.23}$$

Due to their small mass, neutrinos are relativistic particles with the energy-momentum relation

$$E_i = \sqrt{m_i^2 + p_i^2} \simeq p_i + \frac{m_i^2}{2p_i} \simeq E + \frac{m_i^2}{2E} \tag{2.24}$$

for the case of $p \gg m_i$ (which allows one to expand the square root as a Taylor series) and

$E \approx p$. Furthermore, it can be assumed that

$$x = L = v \cdot t \simeq c \cdot t \quad \rightarrow L \overset{c=1}{\simeq} t\,, \tag{2.25}$$

which allows one to simplify the exponent in Eq. (2.23) to

$$(E_i - E_j) \cdot t - (p_i - p_j) \cdot x = \frac{m_i^2 - m_j^2}{2E} \cdot L = \frac{\Delta m_{ij}^2}{2} \frac{L}{E}\,. \tag{2.26}$$

The final transition probability is then obtained from Eqs. (2.23) and (2.26)

$$P(\nu_\alpha \rightarrow \nu_\beta)(L,E) = \sum_i \left| U_{\alpha i} U_{\beta i}^* \right|^2 + 2\mathrm{Re} \sum_{j>i} U_{\alpha i} U_{\alpha j}^* U_{\beta j}^* U_{\beta j} \exp\left( -\mathrm{i} \frac{\Delta m_{ij}^2}{2} \frac{L}{E} \right)\,. \tag{2.27}$$

The first term describes the average transition probability $\langle P_{\alpha\rightarrow\beta} \rangle = \langle P_{\beta\rightarrow\alpha} \rangle$, which is a constant, and the latter describes the oscillation part, depending on the oscillation parameters $E$, $L$, and $\Delta m_{ij}^2$. In this representation it is clearly visible that oscillations only occur if neutrinos consist of mass eigenstates with a non-vanishing mass difference. Thus, the existence of neutrino oscillations implies that neutrinos are massive particles.

**Example of two particle oscillations**

For the case of two particle oscillations, the mixing matrix becomes a $2 \times 2$ matrix

$$U = \begin{pmatrix} \cos\theta & \sin\theta \\ -\sin\theta & \cos\theta \end{pmatrix}\,, \tag{2.28}$$

which is a valid approximation if one of the three mixing angles of a three particle system is small compared to the others. In this case, the transition probability between the two flavours becomes

$$P(\nu_\alpha \rightarrow \nu_\beta)(L,E) = \sin^2(2\theta) \sin^2\left( \frac{\Delta m_{ij}^2}{4} \frac{L}{E} \right)\,, \tag{2.29}$$

which is called the appearance channel. The disappearance channel, i.e. the probability of a neutrino to be measured in its initial flavour, is given as

$$P(\nu_\alpha \rightarrow \nu_\alpha)(L,E) = 1 - P(\nu_\alpha \rightarrow \nu_\beta)(L,E)\,. \tag{2.30}$$

In order to measure the appearance or the disappearance of a flavour, the optimal distance between the source and the detector, called the baseline, is at $\frac{L}{E} \approx \frac{1}{\Delta m_{ij}^2}$, as the oscillations have fully evolved at this distance (see Fig. 2.4). When placing a detector far away from the source, i.e. $\frac{L}{E} \gg \frac{1}{\Delta m_{ij}^2}$, the finite resolution of $\frac{L}{E}$ makes the neutrinos loose coherence and thus only the average transition probability can be measured. Neutrino oscillation experiments are therefore commonly categorised into long and short baseline experiments, where the detector is only a few kilometres or several hundreds of kilometres distant to the neutrino source.

### 2.2.2 Neutrino oscillation experiments

Different neutrino sources are available, which are both of natural and artificial origin. Artificial neutrino sources are accelerators (see Eq. (2.3)) and nuclear reactors, whereas common natural sources are the sun (see Eq. (2.7)) and the atmosphere, where cosmic rays generate neutrinos in extensive air showers. In order to discover neutrino oscillations

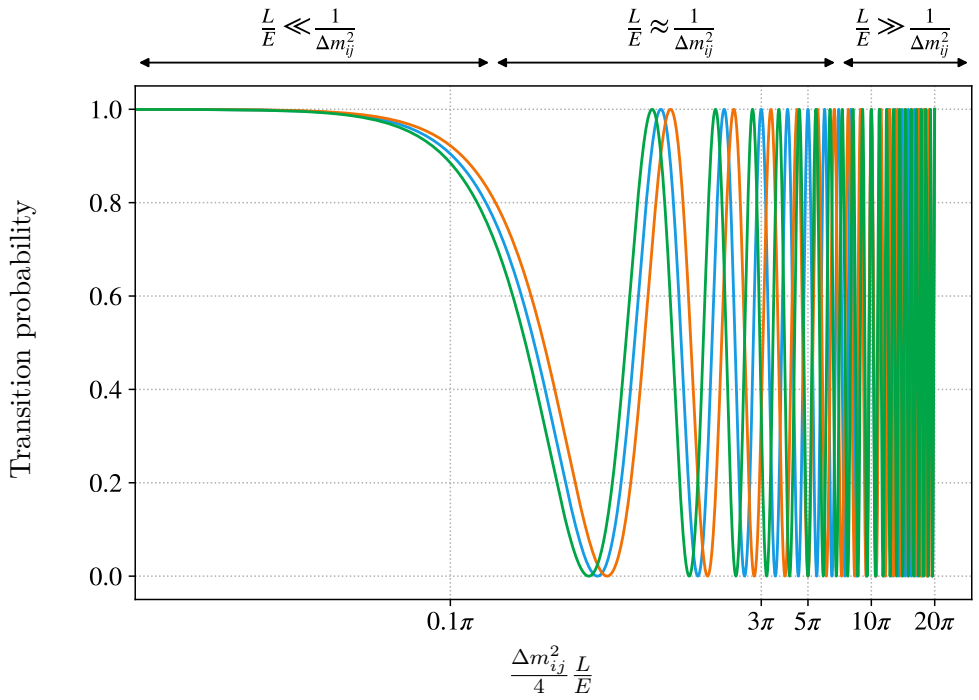


Figure 2.4: Transition probability of the disappearance channel for the two flavour case. Three curves are plotted with slightly different values of $E$ to visualize how the neutrinos loose coherence for larger distances. The maximum sensitivity to oscillations is in the range, where $\frac{L}{E} \approx \frac{1}{\Delta m^2_{ij}}$.

and to determine the oscillation parameters, each of the sources are used allowing the investigation of different $\frac{L}{E}$ ratios.

The experimental proof of neutrino oscillations was first achieved by the Super-Kamiokande experiment [FHI+98] in 1998 by measuring the $\nu_e$-to-$\nu_\mu$ ratio of atmospheric neutrinos. Many other neutrino experiments were built to determine the oscillation parameters $\theta_{ij}$ and $\Delta m^2_{ij}$ by investigating the appearance and disappearance probabilities of neutrinos stemming from accelerators, the sun, and nuclear reactors. Both the discovery and the state of the art experiments to measure the mixing angle and the mass differences are discussed in the following.

### Discovery of neutrino oscillations

The existence of neutrino oscillations was first confirmed with the Super-Kamiokande detector in 1998, which is a 50 kt water Cherenkov detector equipped with 11 146 photo multiplier tubes (50 inch) [FHI+98]. Neutrinos that pass the detector can interact with the nucleons in the water generating either $e^\pm$ or $\mu^\pm$ depending on their flavour. The created charged particles generate Cherenkov rings while passing the water, which are detected with the photomultipliers. The shape of the rings does not only allow the direction of an incident neutrino to be determined but also its flavour. As electrons generate electromagnetic showers, the rings are washed out compared to the ones generated from muons.

Due to the ability of discriminating the neutrino flavour and its direction, the $\nu_e$ and $\nu_\mu$ flux of atmospheric neutrinos was investigated as a function of the zenith angle.

Depending on the zenith angle, the neutrinos arriving at the detector have different propagation lengths $L$, as the up-going muons first have to pass the earth in order to reach the detector. Thus, the up- and down-going neutrinos have a different (dis)appearance proba-

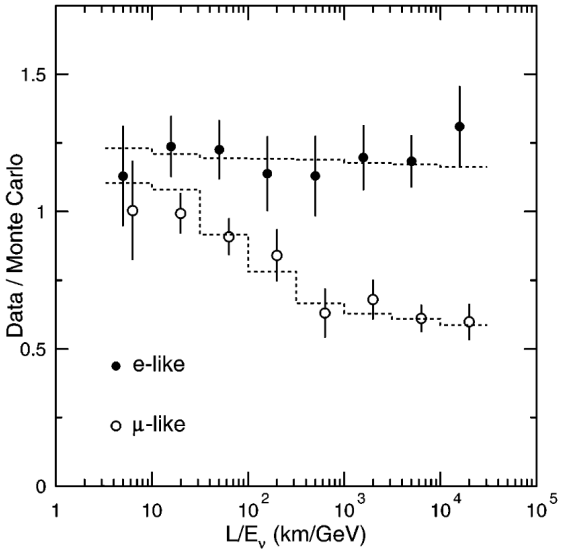


Figure 2.5: First results of the Super-Kamiokande detector showing the ratio of the measured (flavour dependent) neutrino rates compared to the expected rate with no oscillations assumed. A significant disappearance of the muon neutrino flux is visible with increasing $\frac{L}{E}$ as the muon neutrinos oscillate into tauon neutrinos. The measurement data is in good agreement with MC data including $\nu_\mu \leftrightarrow \nu_\tau$ oscillations (dashed line). Figure reprinted from Ref. [FHI$^+$98] with permission of American Physical Society.

bility. The measurement result, as displayed in Fig. 2.5, shows a significant disappearance of the muon neutrino flux by nearly a factor of two, as they oscillate into tauon neutrinos.

**Determination of the oscillation parameters**

From the investigation of the disappearance channels (compare Eqs. (2.29) and (2.30)), it is not only possible to provide the experimental proof of neutrino oscillations but also the oscillation parameters, i.e the mixing angle $\theta_{ij}$ and the mass differences $\Delta m^2_{ij}$, can be determined. Many neutrino oscillation experiments existed, are currently taking data, or are under construction in order to precisely measure the oscillation parameters by investigating accelerator, reactor, and atmospheric neutrinos [Dre03, AAB$^+$18, SA$^+$20, AAA$^+$16a, AAA$^+$14, AAA$^+$18b, AAA$^+$19a, CAA$^+$20, AAA$^+$16c].

The most precise analysis of the $\theta_{12}$ oscillation parameters is provided by the Super-Kamiokande collaboration by investigating the disappearance probability of $^8$B neutrinos (compare Fig. 2.3) including measurement results of the KamLAND and SNO experiment. The obtained oscillation parameters are [AHH$^+$16]

$$\begin{aligned} \sin^2(\theta_{12}) &= 0.307^{+0.013}_{-0.012} \\ \Delta m^2_{12} &= 7.49^{+0.19}_{-0.18} \times 10^{-5}\,\mathrm{eV}^2\,. \end{aligned} \tag{2.31}$$

Although the measurement of the disappearance probability only allows the absolute value $|\Delta m^2_{12}|$ to be determined, the positive sign is defined by existence of the Mikheyew-Smirnov-Wolfenstein (MSW) effect [Wol78, MS86]. The effect describes a resonant conversion of electron neutrinos to muon neutrinos inside the solar core, based on the density-dependent coherent forward scattering of the neutrinos at electrons (see e.g. Ref. [ZB$^+$20]).

In order to measure the $\theta_{23}$ oscillation parameters, neutrinos from both accelerators as well as cosmic showers can be investigated. The best results is obtained from a combined

analysis of the measurement data of T2K [AAA+18b] and NOvA [AAA+19a], both using accelerator neutrinos. The former uses a 30 GeV proton beam from the J-PARC accelerator with a near detector being located 280 m far from the origin of the beam, measuring the initial $\nu_\mu$ flux. As far detector, the Super-Kamiokande detector is used, which is located at a distance of 295 km to the accelerator. The NOvA experiment uses a muon (anti)neutrino beam at an energy of 2 GeV provided by the Fermilab NuMI, with a near detector and a far detector located 1 km and 860 km from the beam origin.

From the combined analysis of the measurement data, a result of

$$\begin{aligned} \sin^2(\theta_{23}) &= 0.547 \pm 0.021 && \text{inverted hierarchy} \\ \sin^2(\theta_{23}) &= 0.545 \pm 0.021 && \text{normal hierarchy} \\ \Delta m^2_{23} &= -2.546^{+0.034}_{-0.040} \times 10^{-3}\,\text{eV}^2 && \text{inverted hierarchy} \\ \Delta m^2_{23} &= 2.453(34) \times 10^{-3}\,\text{eV}^2 && \text{normal hierarchy} \end{aligned} \tag{2.32}$$

is obtained [ZB+20].

The $\theta_{13}$ oscillation parameters are obtained by investigating the disappearence channel of reactor electron antineutrinos on a short baseline of $\mathcal{O}(1\,\text{km})$. Leading experiments are the Daya-Bay [AAB+18], RENO [SA+20], and Double CHOOZ [AAA+16a] experiment. All of them use two Gd-loaded scintillation detectors, with the near detector being placed at a distance of approximately 300 m and the far detectors located at around 0.5 km to 1.3 km from the reactors.

A combined analysis of the most recent measurement results of the three experiments yields [ZB+20]

$$\sin^2(\theta_{13}) = 2.18(7) \times 10^{-2}\,. \tag{2.33}$$

**Mass hierarchy**

The available data from the neutrino oscillation experiments only allows the absolute value of $|\Delta m^2_{12}|$ and $|\Delta m^2_{23}|$ (comp. Eqs. 2.31 and 2.32) to be determined. Although the sign of $\Delta m^2_{12}$ is known due to the existence of the MSW effect, the sign of $\Delta m^2_{23}$ as well as the absolute mass scale of the mass eigenstates $\nu_i$ are still unknown. Thus, the ordering of the mass eigenstates $\nu_i$ it not yet defined, which allows for different scenarios.

If $\Delta m^2_{23}$ is positive, the masses of the three mass eigenstate would be arranged in ascending order and the lightest mass eigenstate would be $\nu_1$. However, if the sign of $\Delta m^2_{23}$ is negative, the hierarchy would be inverted, since $|\Delta m^2_{23}| > \Delta m^2_{12}$. Hence, the lightest mass eigenstate would be $\nu_3$, as illustrated in Fig. 2.6. If the mass scale turns out to be significantly larger than $\Delta m^2_{23}$, the mass difference becomes negligible and the mass eigenstates would have approximately the same mass.

This leads to the three possible mass hierarchies:

- **Normal hierarchy:** $m_1 < m_2 \ll m_3$
- **Inverted hierarchy:** $m_3 \ll m_1 < m_2$
- **Quasi-degenerate masses:** $m_1 \simeq m_2 \simeq m_3$

In order to solve the open question of the mass ordering, the future experiments JUNO [AAA+16c] and DUNE [CAA+20] are targeted to measure the exact mass hierarchy. The absolute mass scale can however only be determined from dedicated neutrino-mass experiments, which will be discussed in Sec. 2.4.

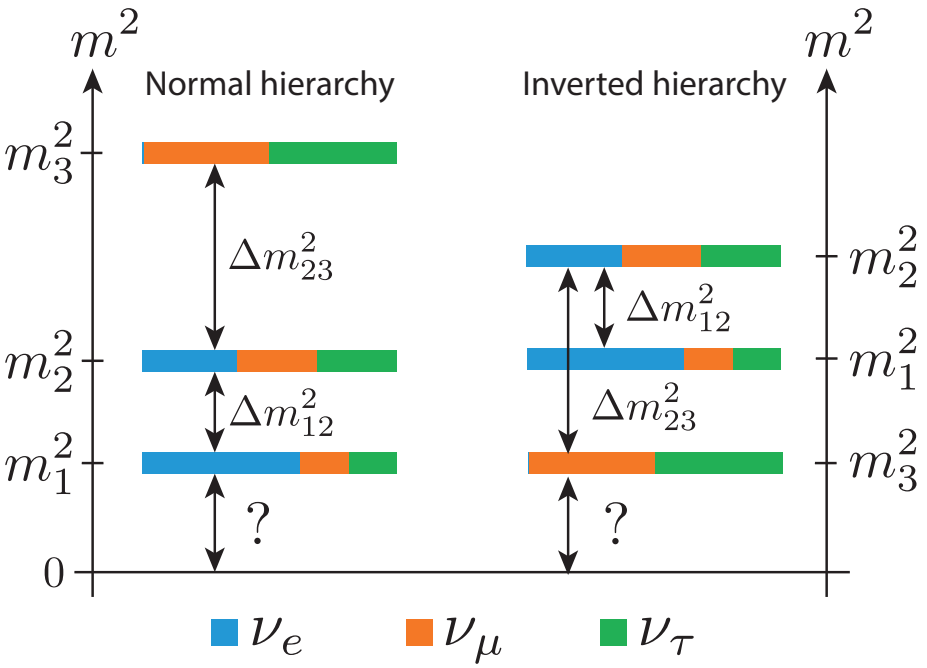


Figure 2.6: Mass ordering for the case of a normal hierarchy and inverted hierarchy. In the case of the normal hierarchy, the lightest mass eigenstate is $\nu_1$, whereas for the case of the inverted hierarchy $\nu_3$ would be the lightest mass eigenstate. Although the mass differences are known, the absolute scale of the masses is yet unknown. The flavour content of the mass eigenstates is indicated with the three colours.

## 2.3 Theory of neutrino-mass generation

The following section gives an overview of mass generation in the standard model and introduces the three most popular beyond standard model approaches of neutrino-mass generation, based on the textbook Ref. [Zub12].

In the standard model, all Dirac particles obtain their masses through the mass term of the Lagrangian

$$\mathcal{L}_{\mathrm{m}} = m_{\mathrm{D}} \bar{\psi} \psi \,, \tag{2.34}$$

where $m_{\mathrm{D}}$ is the Dirac mass of a particle and $\psi$ is a four-component Dirac spinor. The equation can be rewritten using the two-component Weyl spinors $\psi_{\mathrm{L}}$ and $\psi_{\mathrm{R}}$

$$\mathcal{L}_{\mathrm{m}} = m_{\mathrm{D}} \left( \bar{\psi}_{\mathrm{L}} \psi_{\mathrm{R}} + \bar{\psi}_{\mathrm{R}} \psi_{\mathrm{L}} \right) , \tag{2.35}$$

with the indices $L$ and $R$ indicating the chirality.

The existence of the masses can be explained by the coupling of the particles to the Higgs field

$$\phi = \begin{pmatrix} \phi^+ \\ \phi^0 \end{pmatrix} , \tag{2.36}$$

where the (electrically neutral) vacuum state of the field is

$$\phi_0 = \frac{1}{\sqrt{2}} \begin{pmatrix} 0 \\ v \end{pmatrix} , \tag{2.37}$$

with the vacuum expectation value (vev) $v$.

The contribution to the Lagrange density of the standard model from leptons coupling to the Higgs field is described by the Yukawa coupling

$$\mathcal{L}_{\text{Yuk}} = -c_\ell \bar{\ell}_{\text{R}} \phi^\dagger \begin{pmatrix} \nu_{\ell,\text{L}} \\ \ell_{\text{L}} \end{pmatrix} + \text{h.c.}\,, \tag{2.38}$$

where $\ell = e, \mu, \tau$. By using the vacuum state of the Higgs field as defined in Eq. (2.37), the the Yukawa term becomes

$$\mathcal{L}_{\text{Yuk}} = -c_\ell \frac{v}{\sqrt{2}} \left[ \bar{\ell}_{\text{R}} \ell_{\text{L}} + \bar{\ell}_{\text{L}} \ell_{\text{R}} \right] , \tag{2.39}$$

where $c_\ell \frac{v}{\sqrt{2}}$ can be identified as the Dirac mass term $m_{\text{D}}$. Since the mass term is depending on a free coupling constant $c_\ell$, it cannot be predicted but needs to be determined by measurements. As no right handed neutrino singlets $\nu_{\text{R}}$ exist in the standard model, neutrinos appear to be massless.

In order to include massive neutrinos to the Lagrange density, a first approach is to assume the existence of a $\nu_{\text{R}}$ singlet as for the other fermions. The Yukawa term becomes

$$\mathcal{L}_{\text{Yuk}} = -c_\ell \bar{\ell}_{\text{R}} \phi_0^\dagger \begin{pmatrix} \nu_{\ell,\text{L}} \\ \ell_{\text{L}} \end{pmatrix} - c_{\nu_\ell} \bar{\nu}_{\ell,\text{R}} \tilde{\phi}_0^\dagger \begin{pmatrix} \nu_{\ell,\text{L}} \\ \ell_{\text{L}} \end{pmatrix} + \text{h.c.}\,, \tag{2.40}$$

with the transformed vacuum state (see e.g. Ref. [GK07])

$$\tilde{\phi}_0 = \frac{1}{\sqrt{2}} \begin{pmatrix} v \\ 0 \end{pmatrix} . \tag{2.41}$$

As this extension yields a neutrino-mass term similar to the one for the charged leptons, the mass is proportional to the Higgs vev. Since it is known that the neutrino masses are many orders of magnitude smaller compared to the other lepton masses, the coupling constant $\tilde{c}_{\nu_\ell}$ has to deviate from the ones of the leptons accordingly. However, there is no explanation for this large differences in the coupling constants.

Another approach of neutrino-mass generation is to consider neutrinos being Majorana particles, i.e. the neutrino and the antineutrino would be the same fundamental particle. By introducing the charge-conjugated spinor $\psi^c$, the Lagrangian becomes

$$\mathcal{L}_{\text{m}} = \frac{1}{2} m_{\text{M}} \bar{\psi} \psi^c + \text{h.c.}\,. \tag{2.42}$$

The spinors can be again split into its chiral projections, which allows one to identify a right- and left-handed mass term

$$\begin{aligned} \mathcal{L}_{\text{m}}^{\text{L}} &= \frac{1}{2} m_{\text{L}} \left( \bar{\psi}_{\text{L}} \psi_{\text{R}}^c + \bar{\psi}_{\text{R}}^c \psi_{\text{L}} \right) \\ \mathcal{L}_{\text{m}}^{\text{R}} &= \frac{1}{2} m_{\text{R}} \left( \bar{\psi}_{\text{L}}^c \psi_{\text{R}} + \bar{\psi}_{\text{R}} \psi_{\text{L}}^c \right) , \end{aligned} \tag{2.43}$$

using the identity $\psi_{\text{L,R}}^c = (\psi^c)_{\text{L,R}} = (\psi_{\text{R,L}})^c$. Thus, the theory of neutrinos being Majorana particles could both satisfy the restriction of the standard model that only left-handed neutrinos exist and the need for neutrinos being massive particles by obtaining the Majorana mass $m_{\text{L}}$ from Eq. (2.43).

In a last more general approach, the theory of Dirac masses and Majorana mass terms can

be combined into one mass term

$$\mathcal{L}_{\mathrm{m}} = \frac{1}{2} m_{\mathrm{D}} \left( \bar{\psi}_{\mathrm{L}} \psi_{\mathrm{R}} + \bar{\psi}^{c}_{\mathrm{L}} \psi^{c}_{\mathrm{R}} \right) + \frac{1}{2} \left( m_{\mathrm{L}} \bar{\psi}_{\mathrm{L}} \psi^{c}_{\mathrm{R}} + m_{\mathrm{R}} \bar{\psi}^{c}_{\mathrm{L}} \psi_{\mathrm{R}} \right) + \mathrm{h.c.}\,, \tag{2.44}$$

which can be written as matrix equation

$$\mathcal{L}_{\mathrm{m}} = \frac{1}{2} \left( \bar{\psi}_{\mathrm{L}}, \bar{\psi}^{c}_{\mathrm{L}} \right) \begin{pmatrix} m_{\mathrm{L}} & m_{\mathrm{D}} \\ m_{\mathrm{D}} & m_{\mathrm{R}} \end{pmatrix} \begin{pmatrix} \psi^{c}_{\mathrm{R}} \\ \psi_{\mathrm{R}} \end{pmatrix} . \tag{2.45}$$

The Dirac-Majorana mass therm thus results in a Dirac mass and two Majorana masses, and allows for different scenarios regarding their mass scales. A popular model is to assume that the left-handed Majorana mass $m_{\mathrm{L}}$ vanishes and that $m_{\mathrm{D}}$ is much smaller than $m_{\mathrm{R}}$, which results in a mass matrix

$$M = \begin{pmatrix} 0 & m_{\mathrm{D}} \\ m_{\mathrm{D}} & m_{\mathrm{R}} \end{pmatrix} . \tag{2.46}$$

The mass eigenvalues of the matrix are

$$m_1 = \frac{m_{\mathrm{D}}^2}{m_{\mathrm{R}}} \quad \text{and} \quad m_2 = m_{\mathrm{R}} \left( 1 + \frac{m_{\mathrm{D}}^2}{m_{\mathrm{R}}^2} \right) \approx m_{\mathrm{R}}\,, \tag{2.47}$$

where $m_1$ is identified as the mass of the light (active) neutrinos with masses in the sub-eV region and $m_2$ is identified as the mass of a heavy right-handed (sterile) neutrino with possibles masses above the GeV region. This scenario is basis for the so-called see-saw mechanism (see e.g. Ref. [ZB$^+$20]).

## 2.4 Neutrino-mass experiments

The discovery of neutrino oscillations in 1998 [FHI$^+$98] and the resulting prove that neutrinos must have a non-vanishing rest mass highlight the importance of determining the absolute scale of the neutrino masses. Even before this discovery, different experiments aimed to measure the absolute value of the neutrino mass (see e.g. Ref. [RK88]). Very first experiments were carried out already in 1947 [Kon47].

The approaches of measuring the neutrino mass are diverse and cover cosmological investigations, flight time measurements of supernova neutrinos, or the investigation of the shape of the β-spectrum. However, no experiment succeeded so far in determining the exact mass of the neutrinos and thus only upper limits exist. The currently best upper limit on the effective mass of the electron (anti)neutrino was determined by the KATRIN experiment [AAA$^+$19b, ZB$^+$20] in 2019 and is

$$m(\nu_e) < 1.1\,\mathrm{eV} \quad (90\,\%\ \mathrm{C.L.})\,. \tag{2.48}$$

In the following, the different measurement approaches are grouped into model-dependent approaches, and experiments, which are model independent and only based on the kinematics of the β-decay.

### 2.4.1 Model-dependent approaches

Different measurement approaches for the determination of the neutrino mass exist, where the inference of the neutrino mass is model-dependent. This means that either the analysis of the measurement data is based on a complex model or the model requires further beyond-standard-model extensions, e.g. that neutrinos must be Majorana particles. Strong constraints on the neutrino mass have been observed in recent years from diverse experiments, which are introduced in the following.

#### 2.4.1.1 Cosmological observations

The current concordance model to describe the evolution of our universe is the ΛCDM model containing dark energy, cold dark matter, and (baryonic) matter. Since neutrinos have a non-vanishing mass, they contribute to the model as hot dark matter and play a visible role in the structure formation on small scales in the early universe.

Massive but weakly interacting neutrinos stream out of gravitational potential wells damping matter fluctuations on small scales $\lambda < \lambda_{FS}$, with $\lambda_{FS}$ being the free-streaming length (see e.g. Ref. [LP12]).

In order to investigate this effect, the Baryon Oscillation Spectroscopic Survey (BOSS) [BSS+14] recorded the position of 1.5 million galaxies within a volume of $V = 2.31 \times 10^9\,(\mathrm{Mpc/h})^3$ to obtain a matter power spectrum[1]. Depending on the sum of the neutrino masses $\Sigma m_\nu$, the power on small scales is reduced.

Similar observations can be made when measuring the Cosmic Microwave background (CMB) anisotropy, which was done by the satellite missions COBE [Smo99], WMAP [BLW+13], and Planck [AAA+16b].

A combined analysis of both the BOSS data and the Planck data (in addition including SN Ia data) [Upa19], yields

$$\Sigma m_\nu < 183\,\mathrm{meV} \text{ to } 540\,\mathrm{meV} \quad (95\,\%\ \mathrm{C.L.})\,, \tag{2.49}$$

depending on whether the dark energy equations of state parameter $w$ is fixed to -1 or is a free parameter in the analysis.

#### 2.4.1.2 Supernova observations

Core collapse supernovae produce large amounts of neutrinos, carrying away 99 % of the energy released in a supernova (see e.g. Ref. [Zub12]).

Two processes exist, which contribute to the huge amount of neutrinos. At first, the shockwave of the deleptonisation burst

$$e^- + p \rightarrow n + \nu_e \tag{2.50}$$

emits the trapped neutrinos around the core.

The burst takes only a few milliseconds and is followed by the generation of electrons from the approximately 10 s long Kelvin-Helmholtz cooling phase, where neutrinos are also generated from the annihilation process (see e.g. Ref. [Jan17])

$$e^+ + e^- \rightarrow \nu_i + \bar{\nu}_i\,. \tag{2.51}$$

If the neutrino bursts from a core collapse supernova are observed on earth, information on their mass can be obtained from the spread of their arrival time. The flight time $t_F$ depends on the mass $m_\nu$ and the energy $E$ according to

$$t_F = t - t_0 \approx L\left(1 + \frac{m_\nu^2}{2E^2}\right) \tag{2.52}$$

with $L$ being the distance between the source and the detector (see e.g. Ref. [Zub12]).

[1] In cosmology, the constant $h$ is defined as $h = H_0/(100 \cdot \mathrm{km\,s^{-1}Mpc^{-1}})$ with $H_0$ being the Hubble constant. In Ref. [BSS+14] a value of $h = 0.7$ is used.

As the emission time $t_0$ is unknown, only the arrival time difference $\Delta t$ of two neutrinos

$$\Delta t = \Delta t_0 + \frac{L m_\nu^2}{2}\left(\frac{1}{E_2^2} - \frac{1}{E_1^2}\right) \tag{2.53}$$

can be determined, with $\Delta t_0 = t_{02} - t_{01}$ being the start time difference of the two neutrinos. Although the equation can be solved for $m_\nu^2$, a large uncertainty remains as $\Delta t_0$ is based on the model describing the super nova process.

By the occurrence of the supernova SN1987A, a total of approximately $10^{28}$ [LL02] supernova neutrinos traversed the earth, leading to the detection of 24 supernova neutrinos by the Kamiokande II [HKK$^+$87], Irvine-Michigan-Brookhaven (IMB) [BBB$^+$87], and Baksan [AA08] detectors.

Improved combined analyses of the data were performed both in a Bayesian [LL02] and a frequentist [PVCI09] approach, which provide the upper limits of

$$\begin{aligned} m_\nu &< 5.7\,\text{eV} \quad (95\,\%\ \text{C.L., Bayesian}) \\ m_\nu &< 5.8\,\text{eV} \quad (95\,\%\ \text{C.L., Frequentist})\,. \end{aligned} \tag{2.54}$$

#### 2.4.1.3 Neutrinoless double beta decay

Double β-decay was first discovered in 1987 for the isotope $^{82}$Se [EHM87] and describes the simultaneous β-decay of two nucleons

$$\begin{aligned} 2\nu\beta^+\beta^+ &: \quad {}^{\mathrm{A}}_{\mathrm{Z}}\mathrm{X} \rightarrow {}^{\mathrm{A}}_{\mathrm{Z-2}}\mathrm{Y} + 2e^+ + 2\nu_e \\ 2\nu\beta^-\beta^- &: \quad {}^{\mathrm{A}}_{\mathrm{Z}}\mathrm{X} \rightarrow {}^{\mathrm{A}}_{\mathrm{Z+2}}\mathrm{Y} + 2e^- + 2\bar{\nu}_e\,. \end{aligned} \tag{2.55}$$

As this decay is a process of second order, it is suppressed compared to single β-decays. In order to avoid a background signal from single β-decays, only the elements are used, which have an energetically forbidden transition for single β-decays. A total of 35 natural $2\nu\beta^-\beta^-$ isotopes are known in theory, of which seven have been observed in experiments [GK07].

If neutrinos are Majorana particles, the process of double β-decay can be modified to a process, where neutrinos are exchanged within the two nucleons instead of being emitted (see Fig. 2.7). This process is called neutrinoless double β-decay ($0\nu\beta\beta$). Besides the requirement that the neutrinos must be Majorana particles, this process also demands a change of the sign of the helicity, as the emitted (anti)neutrino is right-handed but can only be absorbed as a left-handed neutrino. However, this flip in helicity is only possible for massive neutrinos [Zub12].

In the case of a $0\nu\beta\beta$ decay, the exchanged neutrino does not carry away energy. Thus, the entire decay energy is translated into the kinetic energy of the electrons/positrons (and the nucleus). The measurement of the sum of their kinetic energies would thus result in a monoenergetic line located at the endpoint $Q$ of the continuous spectrum of the $2\nu\beta\beta$ decay.

The measurement of the $0\nu\beta\beta$ decay allows the determination of the effective Majorana neutrino mass $\langle m_{\beta\beta}\rangle$ by proxy of the half-life $T_{1/2}^{0\nu\beta\beta}$

$$\langle m_{\beta\beta}\rangle^2 = \frac{m_e^2}{G^{0\nu\beta\beta}\left|\mathcal{M}^{0\nu\beta\beta}\right|^2 T_{1/2}^{0\nu\beta\beta}}\,, \tag{2.56}$$

with $G^{0\nu\beta\beta}$ being the phase space factor (usually scaling with $Q^5$) and $\mathcal{M}^{0\nu\beta\beta}$ the nuclear transition matrix element.

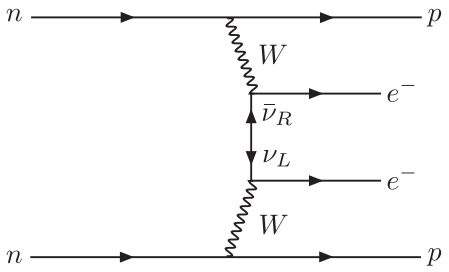


Figure 2.7: Feynman diagram of the $0\nu\beta^-\beta^-$ decay. A neutrino is exchanged during the simultaneous decay of two nucleons. This is only possible if neutrinos are Majorana particles and if a change of helicity is possible. The latter requires neutrinos to be massive particles.

The obtained observable is the coherent sum over the mass eigenstates

$$\langle m_{\beta\beta} \rangle = \left| \sum_{i=1}^{3} U_{ei}^2 \, m_i \right| . \tag{2.57}$$

Many experiments exist with the aim to detect $0\nu\beta\beta$ decays in different elements, such as $^{76}$Ge (GERDA [Maj15], MAJORANA [AAA+19c]), $^{136}$Xe (EXO [ABB+19b], KamLAND-Zen [S+17]), and $^{100}$Mo/$^{82}$Se (SuperNEMO [Piq06]).

Up to now, no signals from $0\nu\beta\beta$ decays have been detected, which allows only lower limits on $T_{1/2}^{0\nu\beta\beta}$ and upper limits on $\langle m_{\beta\beta} \rangle$ to be derived.

The best limit of a combined analysis of GERDA data yields [ABB+19a]

$$\langle m_{\beta\beta} \rangle < 70\,\text{meV to } 160\,\text{meV} \quad (90\,\%\ \text{C.L.}) . \tag{2.58}$$

Due to the CP-violating and Majorana phases (comp. Eq. (2.20)) the contributions from the mass eigenstates can cancel out, which might effectively reduce $\langle m_{\beta\beta} \rangle$ or makes it vanish completely. Thus, this observable is not directly comparable to the neutrino mass obtained from direct measurements.

### 2.4.2 Model-independent approaches

Model-independent approaches focus on the measurement of the β-decay spectrum, the shape of which is dependent on the mass of the neutrinos (comp. Fig. 2.1).

The analysis is only based on kinematic calculations and the modelling of the spectral shape, which are well understood physical problems. Based on Fermi's golden rule, the shape of the differential β-spectrum

$$\frac{\mathrm{d}\Gamma}{\mathrm{d}E} = \frac{G_F^2 \cos^2(\theta_C)}{2\pi^3} \, |\mathcal{M}|^2 \, F(Z,E) \, p(E+m_e) \cdot \sum_{i=1}^{3} |U_{ei}|^2 \, \epsilon \sqrt{\epsilon^2 - m_i^2} \; \Theta(\epsilon - m_i) \tag{2.59}$$

can be derived, with $G_F$ being the Fermi coupling constant, $\theta_C$ the Cabbibo angle, $\mathcal{M}$ the nuclear transition matrix element, and $\epsilon = E_0 - E$ the energy difference with respect to the endpoint energy $E_0$ [KBD+19]. The Fermi function $F(Z,E)$ considers the Coulomb interaction between the daughter nuclei and the electron, and the Heaviside step function $\Theta$ ensures energy conservation, so that only energetically allowed states contribute to the spectrum.

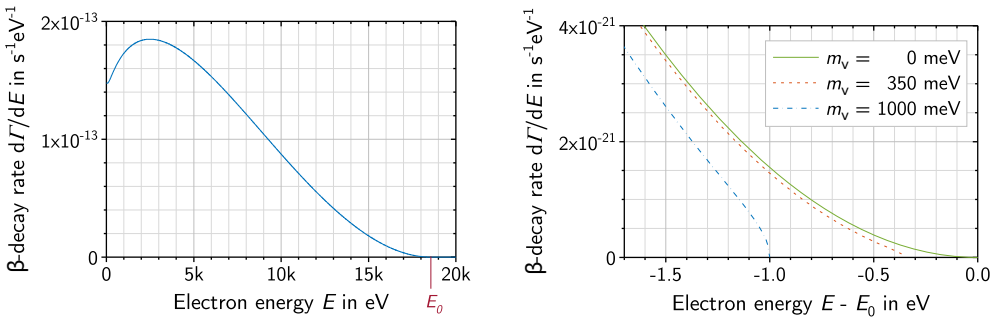


Figure 2.8: Differential β-spectrum of tritium with a detail view of the endpoint region, where the impact of non-vanishing neutrino masses are most prominent. A non-vanishing neutrino mass shifts the effective endpoint of the spectrum towards lower energies. Figure reprinted from Ref. [KBD+19].

The existence of non-vanishing neutrino masses causes a distortion of the β-spectrum, which is most prominent close to the endpoint. As it is displayed in Fig. 2.8, massive neutrinos shift the effective endpoint of the spectrum towards lower energies and thus cause a shape distortion of the spectrum below the endpoint.

The observable from β-decay experiments is the incoherent sum over the mass eigenstates

$$m_\nu^2 = \sum_{i=1}^{3} \left|U_{ei}^2\right| m_i^2 \,, \tag{2.60}$$

in the case of quasi-degenerate neutrino masses.

Only a small list of β-emitters are suitable for this purpose as the sources need to have rather low endpoint energies in order to have sufficiently high rates close to the endpoint. The most suitable elements are tritium, holmium, and rhenium. The experiments using these elements are discussed in the following.

#### 2.4.2.1 Holmium and rhenium experiments

The isotopes $^{163}$Ho and $^{187}$Re are used in recently developed experiments such as the ECHo [GBC+17], HOLMES [NAB+18], and MARE [DMv+11] experiments.

The experiments make use of the extremely low endpoint energy of the electron capture of holmium [EBB+15]

$$^{163}\mathrm{Ho} \rightarrow {}^{163}\mathrm{Dy} + \nu_e \,, \quad Q = 2.83\,\mathrm{keV} \tag{2.61}$$

and the β-decay of rhenium [DMv+11]

$$^{187}\mathrm{Re} \rightarrow {}^{187}\mathrm{Os}^+ + e^- + \bar{\nu}_e \,, \quad Q = 2.47\,\mathrm{keV} \,, \tag{2.62}$$

which increases the decay probability in the region of interest close to the endpoint of the spectrum. In order to measure the released energy from the electron capture and the decay, respectively, the source substrate is directly used as cryogenic calorimeter, where the decay energy is measured as a rise in the temperature. This measurement principle has the benefit that the total decay energy is measured, which thus includes final state excitations of the daughter molecule.

However, using the $^{163}$Ho or $^{187}$Re as β-source has the disadvantage that the half-life $T_{1/2}(^{163}\mathrm{Ho}) = 4570(50)\,\mathrm{yr}$ [GBC+17] and $T_{1/2}(^{187}\mathrm{Re}) = 4.12(11) \times 10^{10}\,\mathrm{yr}$ [GFGV00] are very long. Thus, large amounts of source substrate are required.

A first upper limit

$$m(\nu_e) < 15\,\text{eV} \quad (90\,\%\ \text{C.L.}) \tag{2.63}$$

from measurements of the β-spectrum of $^{187}$Re with cryogenic microcalorimeters is provided by the MIBETA experiment [SAB$^+$04]. The recently developed microcalorimeter experiments aim for final sensitivities in the lower sub-eV range.

#### 2.4.2.2 Tritium experiments

The radioactive hydrogen isotope $^3$H was already used by numerous experiments [FHK$^+$86, RBS$^+$91, SD95, KBB$^+$05, ABB$^+$11] and is currently used as source at the KATRIN experiment.

Tritium decays by $\beta^-$-decay to its mirror nuclei $^3$He$^+$

$$^3\text{H} \rightarrow {}^3\text{He}^+ + e^- + \bar{\nu}_e \tag{2.64}$$

with a half-life of $T_{1/2} = 12.33(2)\,\text{yr}$ [UL00].

The usage of tritium has the following benefits:

- **Short half-life**
  With increasing half-life less amounts of tritium are required.
- **Low endpoint energy**
  The low endpoint energy of $E_0 = 18.57\,\text{keV}$ in the case of molecular tritium ($T_2$) results in a higher decay probability in the region of interest close to the endpoint.
- **Existence as gas**
  The use of gaseous tritium inside windowless eliminate energy losses due to solid-states effects that occur in solid sources.
- **Super-allowed decay**
  In the case of the super-allowed transition ($J = 1/2 \rightarrow J = 1/2$) of Eq. (2.64), the nuclear transition-matrix element in Eq. (2.59) is energy independent.
- **Atomic structure (Z=1)**
  Coulomb interactions with other electrons in the atomic hull do not occur. Furthermore, the inelastic scattering cross section depends on Z, which reduces the influence of energy losses due to scattering with the source gas.

The current best upper limit [ZB$^+$20] on the effective neutrino mass

$$m(\nu_e) < 1.1\,\text{eV} \quad (90\,\%\ \text{C.L.}) \tag{2.65}$$

is provided by the KATRIN experiment, which was obtained from the analysis of the measurement data obtained from the first month of data taking in 2019 [AAA$^+$19b]. With the sensitivity goal of $m(\nu_e) = 0.2\,\text{eV}$ (90 % C.L.) after three net years of measurement time, KATRIN will be the first direct neutrino-mass experiment entering the sub-eV regime.

Since gaseous tritium is commonly used in its molecular form, the decay is accompanied by final-states excitations of the $^3$H$^3$He$^+$ molecule. Although the final states can be calculated with high precision due to the simple molecular structure, it is still one of the major systematics of molecular tritium sources [KAT05].

Future tritium experiments, such as Project 8, therefore plan to use an atomic tritium source to reach a final sensitivity of $m(\nu_e) < 40\,\text{meV}$ (90 % C.L.) [EAB$^+$17].

# 3. The KATRIN experiment

The **Ka**rlsruhe **Tri**tium **N**eutrino Experiment (KATRIN) is targeted to measure the absolute mass scale of the electron (anti)neutrino from a direct measurement by investigating the endpoint of the tritium β-spectrum. KATRIN is designed to lower the sensitivity limit of the preceding experiments in Mainz [KBB$^+$05] and Troitsk [ABB$^+$11] from 2 eV by one order of magnitude to 0.2 eV at a confidence level of 90 % (0.35 eV at 5$\sigma$) after three years of net measurement time.

After the commissioning was completed and tritium was finally injected into the source in 2018 the first neutrino-mass measurements were performed. As part of the step-wise unblinding of the measurement data, an improved upper limit on the neutrino mass

$$m(\nu_e) < 1.1\,\text{eV} \quad (90\,\%\ \text{C.L.}) \tag{3.1}$$

was published [AAA$^+$19b, ZB$^+$20].

This first result was obtained after a short measurement time of only 521.7 h at a reduced source activity of 22 % of the nominal activity. KATRIN is now performing three neutrino-mass measurement campaigns per year until 2025 to achieve its sensitivity goal.

This chapter gives an overview of the KATRIN experiment including a description of the measurement principle in Sec. 3.1 followed by a description of the experimental setup of KATRIN in Sec. 3.2.

## 3.1 Measurement principle

As introduced in Sec. 2.4.2.2, the KATRIN experiment is designed to measure the effective electron (anti)neutrino mass with sub-eV sensitivity from direct kinematic measurements of the tritium β-spectrum.

In order to measure the shape of the β-spectrum, the decay rate as a function of the kinetic energy of the electrons is measured in a narrow energy range around the endpoint of the spectrum. For the discrimination of the kinetic energy of the electrons a so-called MAC-E-type spectrometer is used. The measured data is then evaluated by performing a four parameter fit to the integral spectrum comprising $m_\nu^2$ as one of the free fit parameters.

Since the spectrometer is the keystone of measuring the shape of the β-spectrum, the working principle of the MAC-E filter is explained in detail in Sec. 3.1.1. The construction of the fit model, taking into account the characteristic properties of the spectrometer and the entire experimental setup, is described in Sec. 3.1.2.

### 3.1.1 The MAC-E filter principle

The MAC-E filter principle was first published by Beamson et al. in 1980 [BPT80] and was also used by the preceding neutrino-mass experiments in Mainz and Troitsk.

A MAC-E filter combines a magnetic adiabatic collimation mechanism with an electrostatic filter potential, which allows the total kinetic energy of magnetically guided electrons to be discriminated with a high energy resolution.

In case of isotropically emitted electrons from radioactive decays, the electrons perform a cyclotron motion along the field lines of the magnetic guiding field with field strength $B$. The cyclotron motion is defined by the pitch angle $\theta$ between the momentum vector and the field line. Therefore, the total momentum $\vec{p}$ of the electrons it split into a momentum component $\vec{p}_{\parallel}$ being parallel and a component $\vec{p}_{\perp}$ being perpendicular to the field line. The length of these components are $\left|\vec{p}_{\parallel}\right| = |\vec{p}| \cdot \cos(\theta)$ and $|\vec{p}_{\perp}| = |\vec{p}| \cdot \sin(\theta)$, respectively. Thus, the total kinetic energy of the electrons is given as

$$E_{\mathrm{kin,tot}} = \frac{\vec{p}^2}{2m_e} = \frac{\vec{p}_{\perp}^2 + \vec{p}_{\parallel}^2}{2m_e} = E_{\perp} + E_{\parallel}\,, \tag{3.2}$$

with $m_e$ being the electron's rest mass.

If the electrons pass an electrostatic field while being magnetically guided, the electrons are decelerated as kinetic energy is being translated into potential energy. In order to pass the electrostatic potential, the component of the kinetic energy parallel to the electric field must be larger than the latter, i.e.

$$E_{\mathrm{kin},\parallel} > qU_{\mathrm{ret}}\,, \tag{3.3}$$

where $qU_{\mathrm{ret}}$ is the product of the filter potential $U_{\mathrm{ret}}$ and the electron charge $q$. As the filter is only sensitive to $E_{\mathrm{kin},\parallel}$, a collimation of the electron impulse is required to enable a precise discrimination of the total kinetic energy. This collimation can be achieved by the so-called magnetic adiabatic collimation of momentum. The collimation process is based on the important property that the magnetic moment $\mu_{\mathrm{m}}$ of the cyclotron motion

$$\mu_{\mathrm{m}} = \frac{E_{\mathrm{kin},\perp}}{B} = \text{const.}\,, \tag{3.4}$$

is constant under the condition of radial symmetric magnetic fields, where the gradient $\mathrm{d}B/\mathrm{d}t$ is close to zero [BPT80]. As a consequence of Eq. (3.4), the perpendicular component of the kinetic energy decreases linearly with the magnetic field strength and is transformed into the parallel component due to energy conservation. The decrease of the magnetic field strength along the centre of mass trajectory of an electron therefore causes a collimation of the electrons impulse to be parallel to the field lines.

A MAC-E filter setup, as illustrated in Fig. 3.1, contains a vacuum vessel with solenoids located on both sides of the vessel. In the case of KATRIN, the solenoids are superconducting to provide sufficient strong fields of up to 6 T. Since the magnetic flux $\Phi = B \cdot A$ of the area $A$ is conserved, the field lines expand as the magnetic field decreases towards the centre of the spectrometer. Thus, the diameter of the vessel has to be large enough to cover the expanded flux tube. The level of the expansion is determined by the required energy resolution of the spectrometer.

However, the magnetic field strength at the centre of the spectrometer will never vanish entirely and momenta of non-zero pitch angles cannot be entirely collimated according to Eq. (3.4). This results in a finite energy resolution of the MAC-E filter. The energy resolution $\Delta E_{\mathrm{MAC-E}}$ of an isotropic source is therefore given as the ratio of the magnetic field strength at the analysing plane $B_{\mathrm{A}}$ and at the source $B_{\mathrm{src}}$

$$\frac{\Delta E_{\mathrm{MAC-E}}}{E} = \frac{B_{\mathrm{A}}}{B_{\mathrm{src}}}\,. \tag{3.5}$$

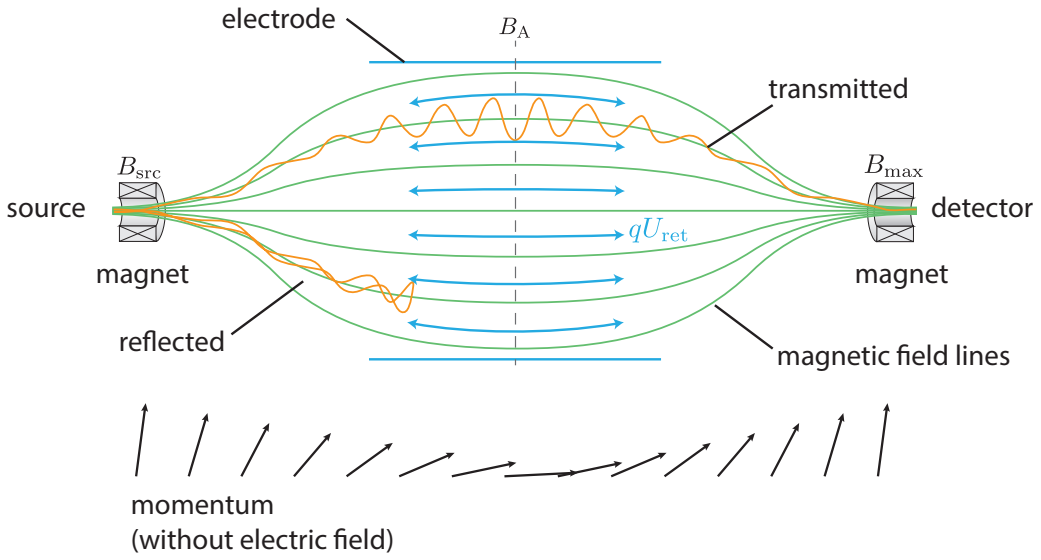


Figure 3.1: Schematic drawing of a MAC-E filter to illustrate its working principle. The magnetic field lines (green) guide electrons along cyclotron trajectories (orange) through the electrostatic filter potential (blue). The decrease of the magnetic field causes a collimation of the electrons momentum to be parallel to the magnetic field lines. An electron is transmitted if $E_{\mathrm{kin},\parallel} > qU_{\mathrm{ret}}$ at the analysing plane (i.e. at $B_{\mathrm{A}}$). Otherwise it is back-reflected towards the source.

Using Eq. (3.4) it is possible to calculate the remaining perpendicular component of the kinetic energy in the analysing plane

$$E_{\perp,\mathrm{A}} = E_{\mathrm{src}} \cdot \sin^2(\theta) \frac{B_{\mathrm{A}}}{B_{\mathrm{src}}} \tag{3.6}$$

for an electron being emitted with the pitch angle $\theta$ and the kinetic energy $E_{\mathrm{src}}$ at the magnetic field $B_{\mathrm{src}}$. Thus, the transmission condition of Eq. (3.3) is fulfilled if

$$E_{\parallel,\mathrm{A}} = E_{\mathrm{src}} - E_{\perp,\mathrm{A}} = E_{\mathrm{src}} - E_{\mathrm{src}} \cdot \sin^2(\theta) \frac{B_{\mathrm{A}}}{B_{\mathrm{src}}} > qU_{\mathrm{ret}} \tag{3.7}$$

and the transmission probability can be written as

$$\mathcal{T}(E_{\mathrm{src}}, \theta, U_{\mathrm{ret}}) = \begin{cases} 1 & E_{\mathrm{src}} \cdot \left(1 - \sin^2(\theta) \frac{B_{\mathrm{A}}}{B_{\mathrm{src}}}\right) > qU_{\mathrm{ret}} \\ 0 & \text{else} \end{cases} . \tag{3.8}$$

For an isotropic source of electrons with angular distribution $\omega(\theta) = \sin(\theta)$, Eq. (3.8) has to be integrated over the pitch angle, which gives the transmission function

$$T(E_{\mathrm{src}}, \theta, U_{\mathrm{ret}}) = \int_0^{\theta_{\max}} \mathcal{T}(E_{\mathrm{src}}, \theta, U_{\mathrm{ret}}) \sin(\theta) \, \mathrm{d}\theta \, . \tag{3.9}$$

Although the integration limit $\theta_{\max}$ would be 90° for an isotropic source, the maximum transmission angle in the KATRIN experiment is limited due to magnetic reflection at the so-called pinch magnet, which is located at the detector side of the MAC-E filter. By integrating this magnetic reflection into the setup it is possible to improve the energy resolution of the spectrometer, as electrons with pitch angles larger than the reflection angle are removed from the measurement signal (see Fig. 3.2). Furthermore, systematic effects

can be reduced since electrons with high pitch angles are more likely affected by systematic effects, such as the the energy loss due to scattering inside the source (see Sec. 4.3). Thus, limiting the acceptance window for the pitch angle is desired by design.

Magnetic reflection of an electron occurs due to the decollimation of the electron momentum with rising magnetic field strengths. Depending on the initial pitch angle in the source, $\theta$ can reach 90° when traversing a stronger magnetic field, which causes a sign flip of the parallel component of the momentum vector. The minimum pitch angle in the source $\theta_{\text{refl.}}$, which results in a magnetic reflection, is

$$\theta_{\text{refl.}} = \arcsin\left(\sqrt{\frac{B_{\text{src}}}{B_{\text{max}}}}\right) . \tag{3.10}$$

With this condition, the transmission function of the KATRIN experiment becomes [KBD+19]

$$T(E_{\text{src}}, qU_{\text{ret}}) = \begin{cases} 0 & E_{\text{s}} < 0 \\ 1 - \sqrt{1 - \frac{E_{\text{s}}}{E_{\text{src}}} \cdot \frac{B_{\text{src}}}{B_A}} & 0 \leq E_{\text{s}} \leq \Delta E_{\text{MAC-E}} \\ 1 - \sqrt{1 - \frac{B_{\text{src}}}{B_{\text{max}}}} & E_{\text{s}} > \Delta E_{\text{MAC-E}} \end{cases} , \tag{3.11}$$

with $E_{\text{s}} = E_{\text{src}} - qU_{\text{ret}}$ being the remaining surplus energy of the electron at the analysing plane relative to the retarding potential.

The shape of the transmission function is shown in Fig. 3.2 for the nominal magnetic field setting of KATRIN as described in Sec. 3.2.

### 3.1.2 Measurement and analysis strategy

In order to investigate the spectral shape of the tritium β-spectrum close to the endpoint, a scan with the retarding potential $U_{\text{ret}}$ of the MAC-E filter is performed and the rate of the β-electrons passing the filter potential is measured at the detector. The list of measurement points is distributed in a way, so that the endpoint of the β-spectrum is densely covered. Furthermore, a certain amount of data points is located above the endpoint, which allows one to determine the amplitude $A_{\text{bg}}$ of the background component contributing to the measurement. The measurement time, which is spend at each retarding potential value $U_{\text{ret}}$ is not only depending on the decay rate, but also on the sensitivity to the distortions of the spectrum from a non-vanishing neutrino mass, which is illustrated in Fig. 3.3. One scan takes about 3.5 h and is repeated continuously but with alternating directions. An exemplary β-spectrum scan in the region of 30 eV below and 5 eV above the endpoint energy $E_0$ with the corresponding measurement time distribution is shown in Fig. 3.3.

In order to obtain the neutrino-mass signal from the shape distortion of the β-spectrum, either a negative Poisson-likelihood fit or a $\chi^2$ fit to the data is performed, as shown in Fig. 3.3. For the construction of the fit model, a detailed description of the β-spectrum as measured with the experimental setup is required including all major systematic effects, which cause a distortion of the ideal integral β-spectrum. The systematic effects, such as the energy resolution of the MAC-E filter, energy losses due to scattering with the source gas, or the excitation of the final states of the daughter molecular system, are combined into the so-called response function $R(E, U_{\text{ret}})$.

The shape of the integral spectrum $\dot{N}(U_{\text{ret}})$ can thus be described as the convolution of the response function with the differential β-spectrum of Eq. (2.59)

$$\dot{N}(U_{\text{ret}}; E_0, m_\nu^2) \sim \int_{qU_{\text{ret}}}^{E_0} \frac{\mathrm{d}\Gamma}{\mathrm{d}E}(E_0, m_\nu^2) \cdot R(E, U_{\text{ret}})\, \mathrm{d}E . \tag{3.12}$$

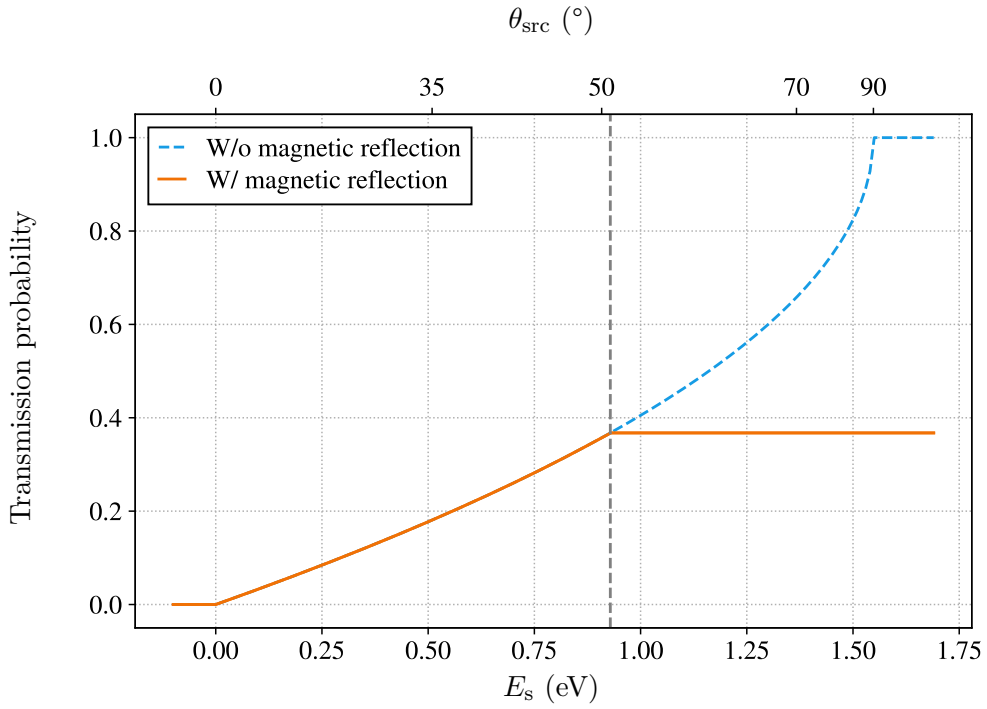


Figure 3.2: Transmission function of a MAC-E filter for the design settings of the KATRIN beam line, i.e. $B_{\mathrm{A}} = 3\,\mathrm{G}$, $B_{\mathrm{src}} = 3.6\,\mathrm{T}$, $B_{\mathrm{max}} = 6\,\mathrm{T}$, and for an electron energy of $E_{\mathrm{kin}} = 18.575\,\mathrm{eV}$. As it is visible, the orange transmission function is cut off at a maximal angle of 50.8° due to the magnetic reflection. The result is an improved energy resolution of 0.93 eV. If there was no magnetic reflection, the transmission function would follow the blue dashed line.

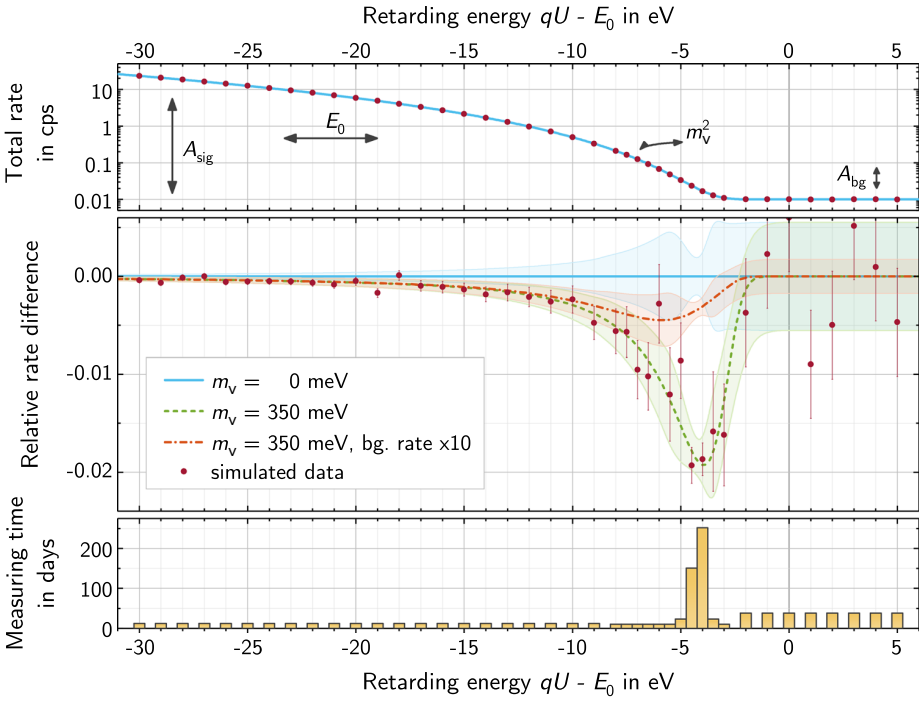


Figure 3.3: Monte Carlo simulation of a possible KATRIN result after three years of data taking for a neutrino mass of 350 meV. A four parameter fit including three nuisance parameters $A_{\mathrm{sig}}$, $E_0$, and $A_{\mathrm{bg}}$ is performed to obtain the observable $m_\nu^2$. The most sensitive region to spectral distortions is located around 4 eV below the endpoint, where the signal-to-background ratio is approximately 1. The most sensitive region shifts to lower energies if the background is increased. Depending on the decay rate and the sensitivity to the spectral distortions, the scanning strategy is based on an optimized and non-flat measurement time distribution. Figure reprinted from Ref. [KBD+19].

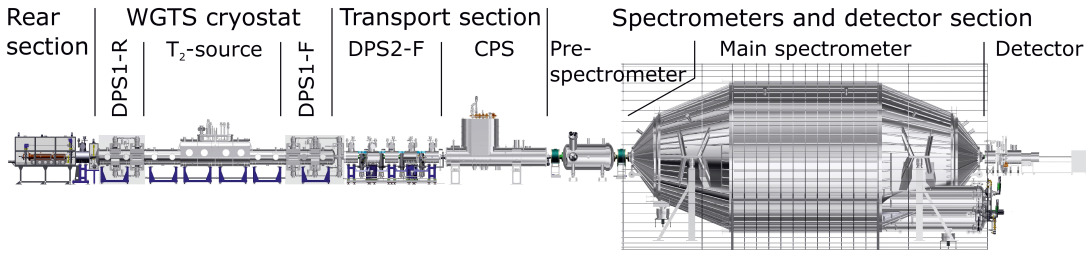


Figure 3.4: Overview of the KATRIN experiment. The main components are: The rear section containing important calibration and monitoring systems; The windowless gaseous tritium source (WGTS) with differential pumps on both sides (DPS1-R/F); The transport section consisting of a differential (DPS2-F) and cryogenic pumping section (CPS); The spectrometer and detector section comprising the pre- and main spectrometer, and the detector. The overall length of the experimental setup is more than 70 m. Figure reprinted from Ref. [FRS+19].

Besides the two parameters $E_0$ and $m_\nu^2$ defining the shape of the β-spectrum, two additional parameters are required in the fit function, which are the amplitude $A_{\mathrm{sig}}$ of the measured β-spectrum as well as the amplitude of the background signal $A_{\mathrm{bg}}$. The two additional free parameters are included in the fit in order to absorb minor differences between the predicted value and the actual measurement condition.

The full fit model, including the three nuisance parameters $A_{\mathrm{sig}}$, $E_0$, and $A_{\mathrm{bg}}$ as well as the observable $m_\nu^2$ is

$$\dot{N}(U_{\mathrm{ret}}; A_{\mathrm{sig}}, E_0, m_\nu^2, A_{\mathrm{bg}}) = A_{\mathrm{sig}} \cdot \int_{qU_{\mathrm{ret}}}^{E_0} \frac{\mathrm{d}\Gamma}{\mathrm{d}E}(E_0, m_\nu^2) \cdot R(E, U_{\mathrm{ret}})\,\mathrm{d}E + A_{\mathrm{bg}}\,. \tag{3.13}$$

A complete discussion of the fit model covering all major corrections is provided in Ref. [KBD+19].

## 3.2 Experimental setup

The experimental setup of KATRIN, as displayed in Fig. 3.4, extends over a more than 70 m long beam line, which consists of several essential subsystems.

The source of the β-electrons is the so-called windowless gaseous tritium source (WGTS) where molecular tritium gas is circulated inside a closed loop system. The β-electrons from the tritium decays inside the WGTS are magnetically guided by superconducting magnets towards the spectrometers by passing the pumping section, which is located at the front side of the WGTS. The pumping section consists of a differential pumping section (DPS) and a cryogenic pumping section (CPS), which suppress the tritium migration from the windowless source towards the spectrometer. The spectrometer section is required to perform a precise discrimination of the kinetic energy of the β-electrons arriving from the WGTS. Electrons that are neither reflected by the filter potential nor magnetically reflected at the pinch magnet pass the main spectrometer and are counted with the Si-detector of the focal plane detector (FPD) system.

A full description of the experimental setup is provided in the design report Ref. [KAT05].

### 3.2.1 Windowless gaseous tritium source

The windowless gaseous tritium source (WGTS) is a 16 m long and 27 t heavy cryostat, which is the origin of the signal electrons from the tritium β-decay.

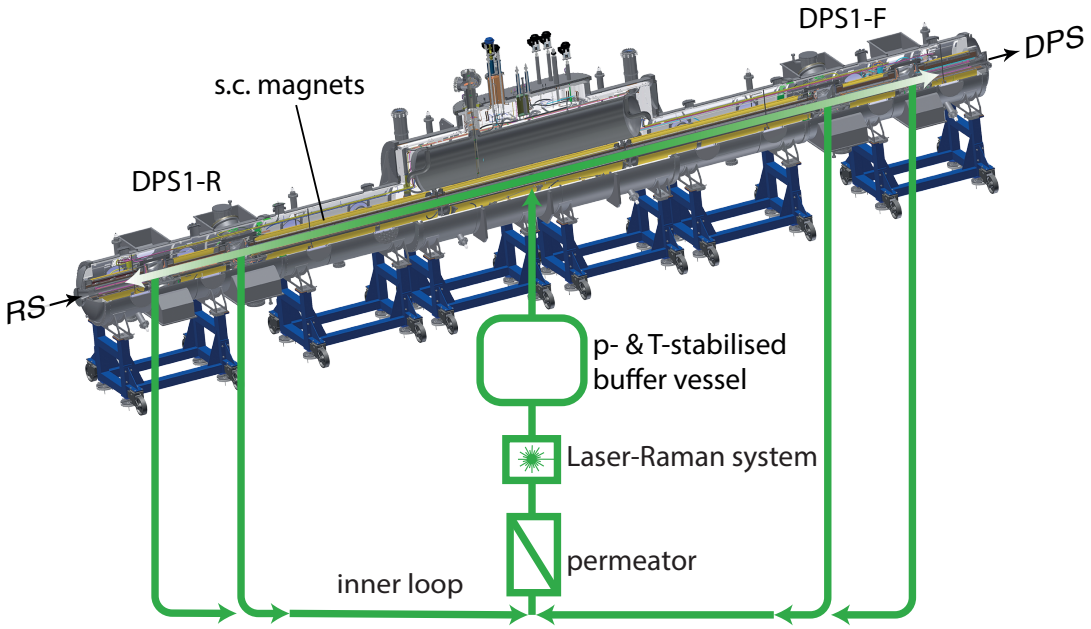


Figure 3.5: CAD drawing of the WGTS in three-quarter section including a strongly simplified scheme of the loops system. Tritium is injected at the centre of the source from a pressure and temperature stabilised buffer vessel and migrates to both sides, where it is pumped out by the differential pumps at the DPS1-R/F. The pumped tritium is cleaned by passing a permeator and the gas composition is constantly monitored with a Laser-Raman system before it is returned into the buffer vessel. The signal electrons are magnetically guided by a total of seven superconducting magnets.

It consists of a 10 m long pipe with a diameter of 90 mm, where the tritium is injected through fine capillaries from a pressure and temperature stabilised buffer vessel. The injected tritium migrates to both ends of the chamber, where 6 turbo molecular pumps are installed each. These first differential pumping stages (DPS1-R/F) pump out 99 % of the injected tritium and return it to the pressure- and temperature-stabilised buffer vessel via the inner loop system. This closed tritium circuit contains a palladium membrane filter (permeator) to remove all non-hydrogen isotopologues and an in-line Laser-Raman spectroscopy system, which allows the tritium purity to be monitored. With this inner loop system, as illustrated in Fig. 3.5, it is possible to inject a constant flow rate of $1.8\,\mathrm{mbar}\,\ell\,\mathrm{s}^{-1}$[KAT05] of gas with a tritium purity higher than 95 % into the WGTS. This corresponds to a total throughput of approximately 40 g tritium per day. This high throughput is required to provide the strong source activity of about 100 GBq, which results in an integrated particle density of $\rho_0 d = 5.0 \times 10^{17}\,\mathrm{cm}^{-2}$. On average, more than 15 tritium ions are generated from one β-decay resulting mainly in positively charged ions, such as $(^3\mathrm{HeT})^+$ and $\mathrm{T}_2^+$ [Kle18, KAT05]. Together with the signal electrons they form a cold plasma inside the WGTS. Due to recombination processes and a flux of $2 \times 10^{11}\,\mathrm{s}^{-1}$ of positive ions leaving the WGTS towards the pumping section, the plasma is quasi-neutral [Kle18, Kuc16].

A high stability of the source activity is crucial for the sensitivity goal of KATRIN, since temporal fluctuations of this value would distort the measured β-spectrum. Therefore, a source stability of $0.1\,\%\,\mathrm{h}^{-1}$ is required by design. Since the conductance of the injection capillaries and the source beam tube is dependant on the temperature, fluctuations of the latter translate directly into instabilities of the source activity. Therefore, a temperature stabilisation of the $0.1\,\%\,\mathrm{h}^{-1}$ level is required. Since the temperature of the injected gas has impact on the generated signal electrons in means of Doppler broadening by the initial

thermal motion of the tritium molecules, the source is operated at the low temperature of 30 K. In order to stabilise the temperature with the required precision, a two-phase neon cooling system is used.

The source chamber is surrounded by a set of seven superconducting solenoids, which generate a magnetic guiding field for the signal electrons of up to 3.6 T and 5.6 T at the DPS1-F [A$^+$18]. As the magnetic field along the experimental setup is not constant, the magnetic field lines expand or contract. In order to make sure that there is no geometric obstruction of the signal electrons by any parts along the beamline, the so-called magnetic flux tube $\Phi(z) = A(z) \cdot B(z) = \text{const.}$ must pass the entire beamline up to the detector. Defined by the diameter of the source tube and the magnetic field, the flux tube is $\Phi = 191\,\text{T}\,\text{cm}^2$ [A$^+$18].

The rear side of the WGTS is connected to the rear section, which contains important calibration and monitoring devices (see Sec. 3.2.5) and the so-called rear wall, which closes the WGTS at the rear end.

### 3.2.2 Pumping section

The first stage of differential pumps (DPS1-F) of the WGTS reduces the tritium flux only by 99%. Thus, a further reduction of the tritium flux is required in order to avoid a contamination of the spectrometer section with tritium, which would cause background events from decays inside the spectrometer potentials. If such a decay takes place in the spectrometer volume, the energy discrimination is not correct, as the electron is generated within the retarding potential. As a result, the events from inside the spectrometer would smear out the shape of the β-spectrum. Therefore, a strict limit of a tritium-induced background rate of not more than 1 mcps is allowed [KAT05]. In order to meet this limit, a reduction of the initial tritium inlet flow by at least 14 orders of magnitudes is required. This huge tritium suppression factor can only be achieved by combining a differential pumping section and a cryogenic pumping section.

#### 3.2.2.1 Differential pumping section

The main purpose of the differential pumping section is to reduce the tritium flux in the direction of the main spectrometer. However, two other important purposes must be fulfilled, which are the adiabatic transport of the signal electrons and the simultaneous blocking of positive charged ions, as the latter follow the same magnetic guiding field.

The beamline of the DPS2-F (see Fig. 3.6) is made of five beam tube elements connected by six pumps ports (PP0-5) where a cascade of six turbo molecular pumps (Leybold MAG-W 2800) are installed. By tilting the beam tubes by 20° a chicane is formed to prevent a direct line of sight, which increases the number of collisions of the neutral molecules with the walls of the beam tube and thus increases the pumping efficiency. A total reduction of the flux by more than seven orders of magnitude relative to the WGTS injection flow rate is achieved at the end of the DPS2-F [MBB$^+$21].

In order to guide the electrons towards the spectrometer section, each of the beam tube elements is surrounded by a superconducting solenoid, which generate a magnetic field of up to 5 T [A$^+$18]. This magnetic guiding field also guides tritium ions, which thus cannot be pumped by the turbo molecular pumps. Therefore, the DPS2-F includes an ion retention system, which consists of a positive charged ring electrode in PP5 that reflect positive ions back into the direction of the WGTS. As these electrodes could create penning traps, additional dipole electrodes are installed in the beam tube elements 1 to 4. These electrodes cause an $\vec{E} \times \vec{B}$ drift, which slowly drifts ions towards the walls where they neutralise.

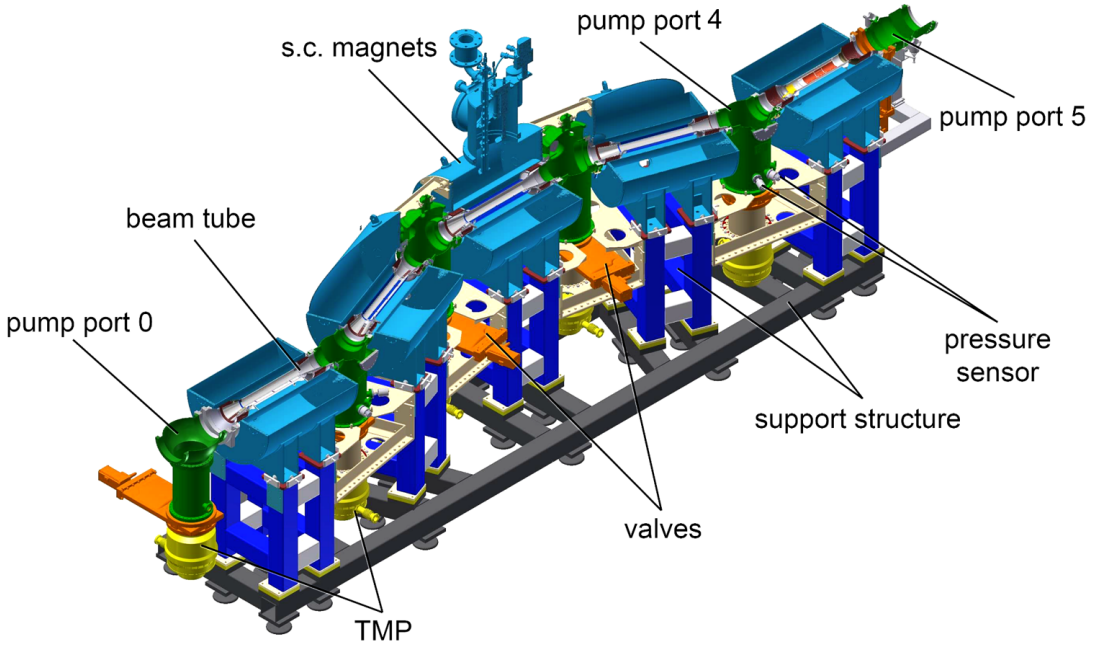


Figure 3.6: CAD drawing of the DPS2-F in three-quarter section. The pumping ports are coloured in green. Two turbo molecular pumps (yellow) are installed at PP0 (the top one is not visible) and one pump at each of the pump ports 1 to 4. The five beam tube segments are surrounded by the superconducting solenoids (light blue). The entire section is 7.3 m long and has a weight of 10 t. Figure reprinted from Ref. [FRS+19].

Towards the pumping port 4, the pressure inside the beam line decreases to about $1 \times 10^{-8}$ mbar [FRS+19]. Continuing with differential pumping in this pressure regime is not very efficient since the back-diffusion through the pumps gets as large as the pumping speed. Thus, changing from differential to cryogenic pumping is necessary to achieve the last seven orders of magnitude of tritium reduction.

#### 3.2.2.2 Cryogenic pumping section

The differential pumping sections DPS1-F and DPS2-F in combination achieve a tritium reduction of seven orders of magnitude. In order to meet the requirements of an overall retention factor of at least $10^{14}$ before entering the spectrometer section, a cryogenic pumping section is installed.

Cryogenic pumps allow to efficiently pump gases even at low pressures, by making use of cryosorption, i.e. the adsorption due to Van-der-Waals binding between the cold surface and the adsorbate. The mean sojourn time $\tau$ for an adsorption is a function of the surface temperature $T$ and is defined as

$$\tau = \tau_0 \exp\left(\frac{E_{\mathrm{des}}}{RT}\right) , \tag{3.14}$$

where $\tau_0$ is a material and gas-specific time constant in the order of $10^{-13}$ s [Boe56] , $E_{\mathrm{des}}$ the molar binding energy between the adsorbate and the adsorbens, and $R = 8.314\,\mathrm{J\,mol\,K^{-1}}$ the molar gas constant [Jou16]. For an effective pumping of tritium, desorption energies larger than $1200\,\mathrm{J\,mol^{-1}}$ and surface temperatures around 3 K are required. These requirements are the basis for the design of the cryogenic pumping section of KATRIN.

The cryogenic pumping section (CPS), as displayed in Fig. 3.7, is a 7 m long and 12 t heavy cryostat. It consists of seven beam tube segments, which form a 15° chicane to

avoid a direct line of sight in the direction of the spectrometer section. This chicane forces molecules to hit the walls several times, where they can be adsorbed. Each of the beam tube segments is surrounded by a superconducting solenoid, which provides a magnetics guiding field for the electrons with a field strength of up to 5.6 T [A$^+$18].

The beam tube segments 2-5 form the cold trap, which is operated at a temperature of 3 K. In order to increase the surface of the cold trap to approximately 2 m$^2$, the beam tube segments 2-5 are equipped with radial fins on the inside. This surface is further increased by covering the gold-plated surface of the beam tubes with an approximately 2 µm thick layer of argon frost. For this purpose, an argon injection system is installed (see Ref. [Röt19]), which consists three injection capillaries in each of the beam tube sections 2-4.

Since the total radioactive inventory, which is adsorbed of the cold trap during the tritium operation, must not exceed 1 Ci, a regeneration of the cryogenic pump is required every 60 days. To do so, the cold trap can be separated by closing the cold gate valve after beam tube section 5. The cold trap can then be heated up to 80 K to evaporate the argon frost layer together with the adsorbed tritium while purging the beam line with helium. The gas mixture is pumped out through pump port 1. Afterwards the cold trap is prepared with a new layer of argon frost [Röt19].

For the purpose of the monitoring of the source activity, the so-called forward beam monitor (FBM) is installed in pumping port 2 of the CPS. The FBM consists of a seven pixel SDD (each pixel has a diameter of 0.25 mm), which was developed for the TRISTAN update of the KATRIN detector [HAA$^+$20, Kor20]. With an energy resolution of 140 eV (FWHM at 5.9 keV), the rate of β-electrons can be constantly monitored. The FBM is installed at the front of a vacuum manipulator, which allows one to scan the entire flux tube. During the neutrino-mass measurements, the FBM is located at the outer rim of the $\Phi = 191\,\mathrm{T\,cm^2}$ flux tube.

### 3.2.3 The spectrometer section

The spectrometer section is required for a precise discrimination of the kinetic energy of the signal electrons. It consists of three MAC-E type spectrometers (see Sec. 3.1.1), which are the pre-spectrometer, the main spectrometer, and the monitor spectrometer. The very prominent component of the experimental setup shown in Fig. 3.4 is the 22 m long and approximately 10 m broad main spectrometer, which consists of a very well engineered electromagnetic setup. Furthermore, the spectrometer requires a very powerful vacuum system, in order to operate the large spectrometer at the required vacuum conditions on the $10^{-11}$ mbar level. The main spectrometer is used for the final discrimination of the kinetic energy of the signal electrons with an energy resolution of 0.93 eV. The pre-spectrometer is not used for the high precision discrimination of the electron energy, but its purpose is to reject the large amount of low energetic electrons and to prevent them from entering the main spectrometer. The third spectrometer (not included in Fig. 3.4) is the monitor spectrometer, which is used to monitor the high-voltage stability of the main spectrometer filter potential by using a krypton source.

The purpose of the individual spectrometers as well as their design is explained in detail in the following sections.

#### 3.2.3.1 Pre-spectrometer

The pre-spectrometer (PS) is a 3.4 m long MAC-E filter with an inner diameter of 1.7 m and a volume of 7.6 m$^3$. Its main purpose is to prevent the low energetic electrons from entering the main spectrometer. This is required, since the large amount of approximately $10^{11}$ electrons per second arriving at the main spectrometer would cause an increased

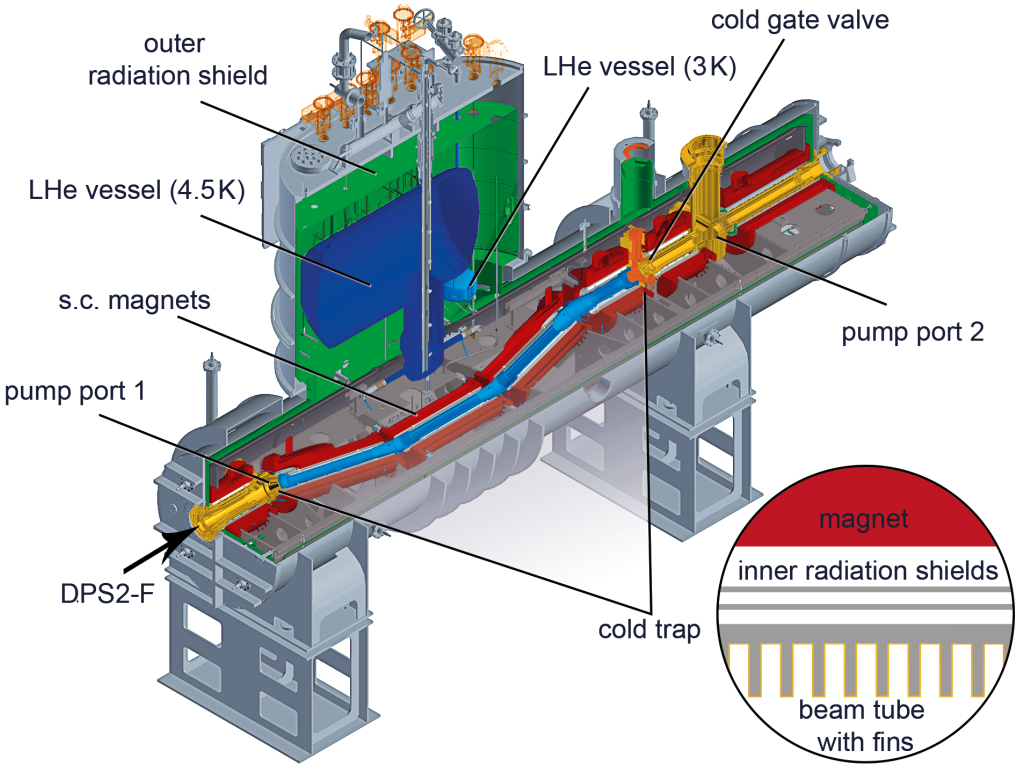


Figure 3.7: CAD drawing of the cryogenic pumping section in three-quarter section. The beam tube segments 2-5 form the cold trap (light blue), which is cooled down to 3 K using subcooled LHe from the 4.5 K circuit. The beam tube is shielded with two inner radiation shields to prevent radiative heat exchange between the cold trap and the superconducting magnets. Figure reprinted from Ref. [FRS+19].

measurement background by ionizing the residual gas inside the main spectrometer. In order to avoid this, a filter voltage is applied to its inner electrode, which is chosen to be a few kilovolts more positive than the filter voltage of the main spectrometer. The reflected electrons are guided back into the WGTS, where they neutralise at the rear wall.

The vacuum system of the pre-spectrometer is equipped with two pumping ports. At one of the pumping ports, a tandem of two turbo molecular pumps (Leybold TMP MAG W 1300) is installed. The other pumping port contains 100 m of non-evaporable getter (NEG) strips, which are required to generate an ultra high vacuum (UHV) in the order of $10^{-11}$ mbar [ABB+16].

On both sides of the vessel, superconducting magnets (PS1/PS2) with a magnetic field strength of up to 4.5 T are located to form the magnetic field lines as required by the MAC-E filter.

#### 3.2.3.2 Main spectrometer

The discrimination of the kinetic energy of the β-electrons arriving at the spectrometer section is performed with the main spectrometer. The main spectrometer is a MAC-E filter with a diameter of 9.8 m and a length of 23.2 m, resulting in a weight of approximately 200 t. Based on the working principle of a MAC-E filter, the main spectrometer combines an electrostatic filter with the adiabatic collimation of the electron momentum by a well defined decrease of the magnetic field strength along the axis of the spectrometer vessel. Besides the precision electromagnetic concept, a well engineered vacuum system is required to maintain the ultra high vacuum conditions in the 1240 $m^3$ large spectrometer volume. Both the electromagnetic concept as well as the vacuum system are summarised in the following, illustrated by the schematic drawing in Fig. 3.8.

**Electrostatic Filter**
In order to generate the electrostatic retarding potential, the entire spectrometer can be set on high voltages up to $U_{\mathrm{MS,max}} = 35\,\mathrm{kV}$. An inner wire electrode system is installed inside the vessel, which allows one to add an additional negative offset voltage in order to fine-tune the potential. For this reason, the wire electrode system contains of 248 segments, which are arranged in 15 rings along the spectrometer. Each ring can be set individually to voltages up to $U_{\mathrm{ie,max}} = -2\,\mathrm{kV}$. The negative voltage difference between the vessel walls and the wire electrodes prevents secondary electrons from entering the spectrometer volume. These secondary electrons can be either generated by cosmic rays interactions with the walls or by radioactive decays of $^{210}$Pb on the inner surface of the vessel [AAB+19, Fra17].

The actual retardation voltage $U_{\mathrm{ret}} = U_{\mathrm{MS}} + U_{\mathrm{ie}}$ can be set and monitored on the ppm-level [TMW09, RWB+19], which is required to perform precise measurements of the β-decay rate as a function of the energy.

**Magnet system**
A super conducting magnet is each placed at the front of the main spectrometer as well as at the downstream end of the spectrometer. The magnet at the entrance of the spectrometer (PS2 magnet) provides a magnetic field of up to 4.5 T [A+18]. The magnetic field decreases towards the analysing plane at the centre of the spectrometer, where the minimum magnetic field strength ($\mathcal{O}(10^{-4}\,\mathrm{T})$) is reached. In order to compress the flux tube back to the regular beam line diameter at the end of the spectrometer, the superconducting magnet at the downstream end provides a magnetic field of up to 6 T [A+18]. The so-called pinch magnet provides the strongest magnetic field along the beam line of KATRIN and thus is the point, where the magnetic reflection of the signal electrons occurs (comp. Eq. (3.10)).

A low field correction system (LFCS) and an earth magnetic field compensation system (EMCS) are installed around the main spectrometer vessel, which enables the adjustment

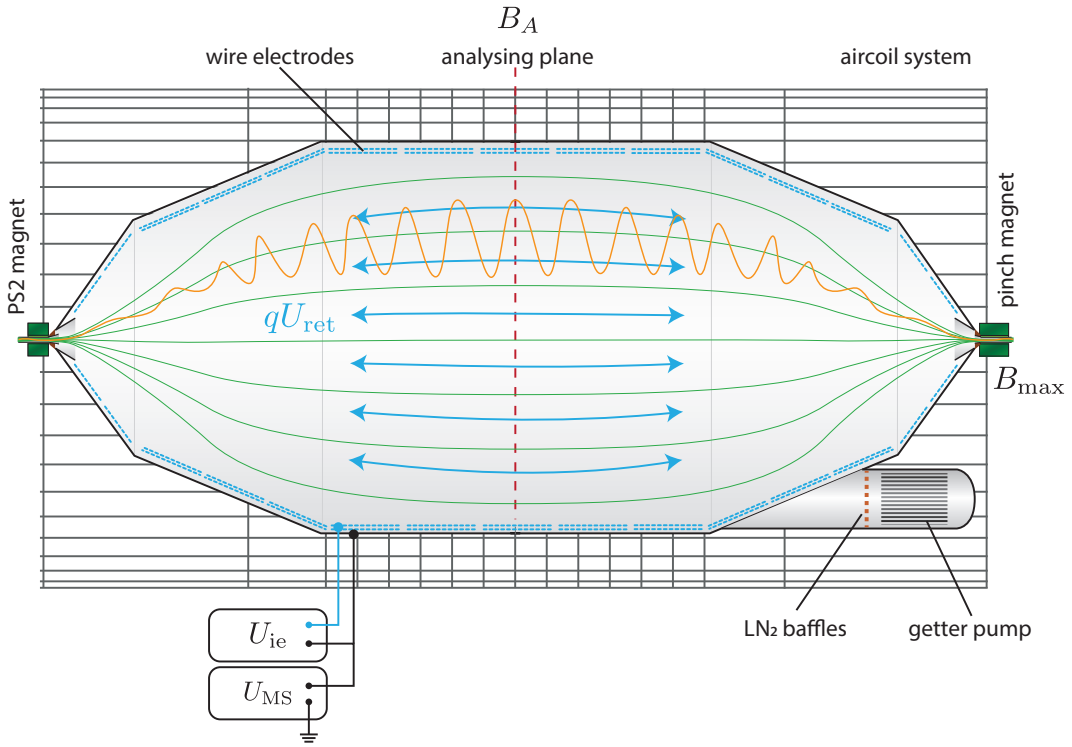


Figure 3.8: Schematic drawing of the main spectrometer. The inside of the main spectrometer vessel is equipped with wire electrode to form the retarding potential $qU_{\mathrm{ret}}$. Superconducting magnets are placed on both sides of the vessel and an air coils system is installed all along the vessel, which allow to compensate the earth magnetic field and to form the magnetic field inside at the analysing plane. In order to maintain the ultra high vacuum, three large pump ports are equipped with getter pumps. Cryogenic baffles are installed in front of the pump ports to reduce the amount of radon emanating from the getter material.

of the magnetic field inside the spectrometer. The LFCS initially consisted of 14 large air coils with a diameter of 12.6 m, but it was extended in 2019 by another six coils, which allows one to shift the analysing plane closer to the detector. By modifying the shape of the magnetic field the flux tube volume between the analysing plane and the detector can be reduced, which thus reduces the background rate.

**Vacuum system**
The β-electrons can ionise the residual gas inside the spectrometer, which causes a background signal by the secondary electrons. In order to reduce this background component, an ultra high vacuum (UHV) on the lower $10^{-11}$ mbar level is necessary inside the 1240 $m^3$ large main spectrometer volume [ABB+16]. For this purpose, the vessel is equipped with three large pumping ports with a diameter of 1.7 m. At pumping port 1 and 3, a total of six turbo molecular pumps (Leybold MAG-W-2800 R) are installed to create high vacuum conditions during the first commission or after venting the system with noble gases. However, the final UHV conditions can only be achieved by using getter pumps. Therefore, each of the pump ports 1 to 3 is equipped with one thousand 1 m long and 27 mm broad zirconium-vanadium-iron-alloy getter strips. After the getter material is activated at a temperature of 300 °C, the pumps have a pumping speed of 1000 $m^3\,s^{-1}$ for hydrogen [ABB+16]. Unfortunately, the getter material emanates radioactive $^{219/220}$Rn [FBD+11], which can enter the main spectrometer volume, where it eventually decays. The α-decay can generate secondary electrons from inner conversion and shake-off processes with energies up to several hundred keV, which contribute to the background component [WDF+13]. In order to reduce the background from radon decays, cryogenic baffles are installed in front of the getter pumps. The emanated radon is adsorbed on the surface of the LN-cooled copper baffles and prevents it from entering the spectrometer, which reduces the radon-induced background by a factor of 5.4 [GBB+18].

**Energy resolution**
With the design values for the magnetic field at the analysing plane $B_A = 3\,G$ and $B_{max} = 6\,T$ at the pinch magnet, the energy resolution close to the endpoint of the β-spectrum $E_0 = 18.6\,keV$ is

$$\Delta E_{MAC-E} = \frac{B_A}{B_{max}} \cdot E_0 = 0.93\,eV\,. \tag{3.15}$$

Since the magnetic field at the pinch magnet is larger than the source magnetic field of 3.6 T, electrons with pitch angles larger than $\theta_{refl.} = 50.8°$ in the WGTS are magnetically reflected at the pinch magnet (comp. Eq. (3.10)). As it is visible in Fig. 3.2, only 37% of the forward-emitted signal electrons are below the reflection angle $\theta_{refl.}$.

#### 3.2.3.3 Monitor spectrometer

A third MAC-E type spectrometer is used to monitor the stability of the main spectrometer filter potential $U_{ret}$ by measuring the line position and width of the (quasi-)monoenergetic conversion electrons of the $^{83m}$Kr decay [EBB+14].

For this purpose, the spectrometer of the Mainz experiment [PBB+92, KBB+05] was refurbished and installed in a building next to the spectrometer hall. The old Mainz spectrometer is 1 m in diameter and has a length of 4 m. A total of 23 ring electrodes are installed inside the vessel to form the electrostatic retarding potential. The electrodes can be galvanically coupled to the main spectrometer voltage, i.e. $U_{MonSpec} = U_{MS}$.

Super conducting magnets are installed on both sides, which initially provided a maximum magnetic field of 8.6 T, but are now limited to 6 T [EBB+14]. The magnetic field in the spectrometer is formed with two air coils to generate a field of 3 G at the analysing plane. With this setting, the same energy resolution as at the main spectrometer is achieved.

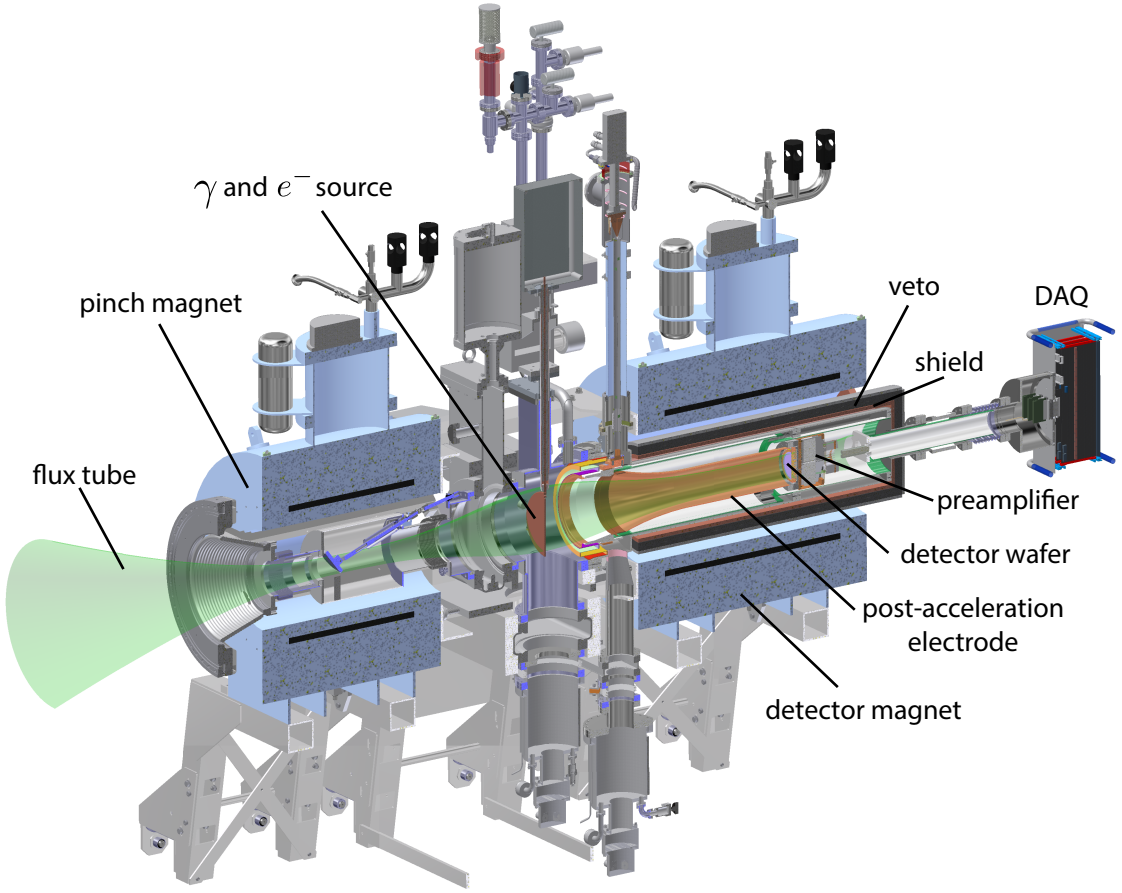


Figure 3.9: CAD drawing of the focal plane detector system in half section. The electrons are counted with the Si-detector wafer, which is located in the post-acceleration electrode. For the purpose of background reduction, an active veto system and a copper shielding are installed around the wafer. The entire detector is placed inside the bore of the superconducting detector magnet. A $\gamma$ and $e^-$ source can be placed in front of the detector to perform energy calibrations.

An implanted Kr-source is installed at the front of the monitor spectrometer. The Kr-source is made from a $^{83}$Rb ion implanted substrate, which serves as a generator (via electron capture) of the short-lived $^{83m}$Kr ($T_{1/2} = 1.83\,\mathrm{h}$) [ZBB+13]. The source can be biased with an external voltage supply to compensate the gap between the energy of the K-32 line at 17 830 eV and the main spectrometer filter voltage.

A detector, made out of 5 silicon PIN-diodes with an energy resolution of 7 keV (FWHM), is located at the rear side of the monitor spectrometer to count the signal electrons, which pass the filter.

The line scans are performed in parallel to the neutrino-mass scans, to make sure that there is no drift of the retardation voltage of the main spectrometer $U_{\mathrm{ret}}$ over several weeks.

### 3.2.4 Focal plane detector

The focal plane detector system (FPD), as shown in Fig. 3.9, is designed to count the signal electrons arriving from the main spectrometer. For this purpose, it contains a monolithic PIN-silicon wafer with a thickness of 503 µm and a diameter of 125 mm. The wafer is segmented into 148 pixels of the same area, which are radially arranged into 13 rings. In order to cover the entire 191 T cm$^2$ flux tube, the sensitive area is 90 mm in diameter.

The wafer and the attached DAQ have an average energy resolution of $\Delta E_{\mathrm{FPD}} < 2\,\mathrm{keV}$ (FWHM) [1] [ABB+15].

The detector wafer is placed inside a passive shielding consisting of a 3 cm thick layer of lead and 1.27 cm layer of high purity copper to shield external $\gamma$-radiation and X-rays from the lead, respectively. In addition to this passive shielding the detector is surrounded by an active muon veto system. The muon veto is a scintillator barrel, which is 38 cm in diameter. It is made of four panels of St. Gobain Bicron-408 plastic scintillator, which are 20 cm thick and 106 cm long.

For a further suppression of the intrinsic detector background, the wafer is installed inside a post-acceleration electrode. The electrode is set to 10 kV to accelerate the incoming signal electrons to kinetic energies, where the intrinsic noise of the detector is minimal.

The wafer with the post-acceleration electrode and the veto system is placed inside the bore of the detector magnet, which provides a magnetic field of up to 3.6 T [A+18].

Important calibration and monitoring devices are installed between the pinch and the detector magnet. This includes an $^{241}$Am source to perform energy calibrations of the detector and the PULCINELLA system, which is a photoelectron source allowing to investigate the absolute detector efficiency. The disc can also be operated as a Faraday cup to detect incoming ion or electron currents.

A complete description of the detector setup can be found in Ref. [ABB+15].

### 3.2.5 Rear section

The rear section (RS), as displayed in Fig. 3.10, is located at the upstream end of the KATRIN beam line. It has the purpose of providing important calibration and monitoring devices with the two main components being the rear wall and a photoelectron source. The rear wall is very important for the monitoring and the manipulation of source properties, whereas the photoelectron source provides a beam of quasi-monoenergetic and angular selected electrons, which can be used for multiple calibration purposes along the entire beam line of KATRIN. The photoelectron source is of special importance for the measurements presented in Sec. 7.2 and 7.2. In the following, only a brief summary of the properties of the photoelectron source is provided. A detailed discussion of the working principle, the electromagnetic design, and the optical setup is provided in Chap. 5.

#### 3.2.5.1 Rear wall

The upstream end of the WGTS is closed by the rear wall (RW). Thus, the trajectories of the electrons (and ions), which are magnetically guided in upstream direction, terminate on the rear wall surface.

This rear wall is a stainless steel disc with a diameter of 14.6 cm and has a 5 mm wide hole at the centre, which allows the beam from the photoelectron source (see Sec. 3.2.5.2 and Chap. 5) to enter the WGTS. It is located just in front of the rear section superconducting magnet (RSCM), which provides a maximum magnetic field of 4.7 T [A+18].

The rear wall is plated with gold, to ensure a temporal stable work function $\Phi_{\mathrm{RW}}$, which is inert to the tritium inside the source [Sch16]. The temporal stability and spacial homogeneity of $\Phi_{\mathrm{RW}}$ is very important, since the trajectories of the electrons and ions following the magnetic field lines end on the rear wall surface. Hence, the rear wall surface potential defines the ground potential of the cold plasma inside of the WGTS and thus defines the initial energy of the source electrons. In order to reduce the impact of the

[1] The energy resolution differs slightly between the available wafers.

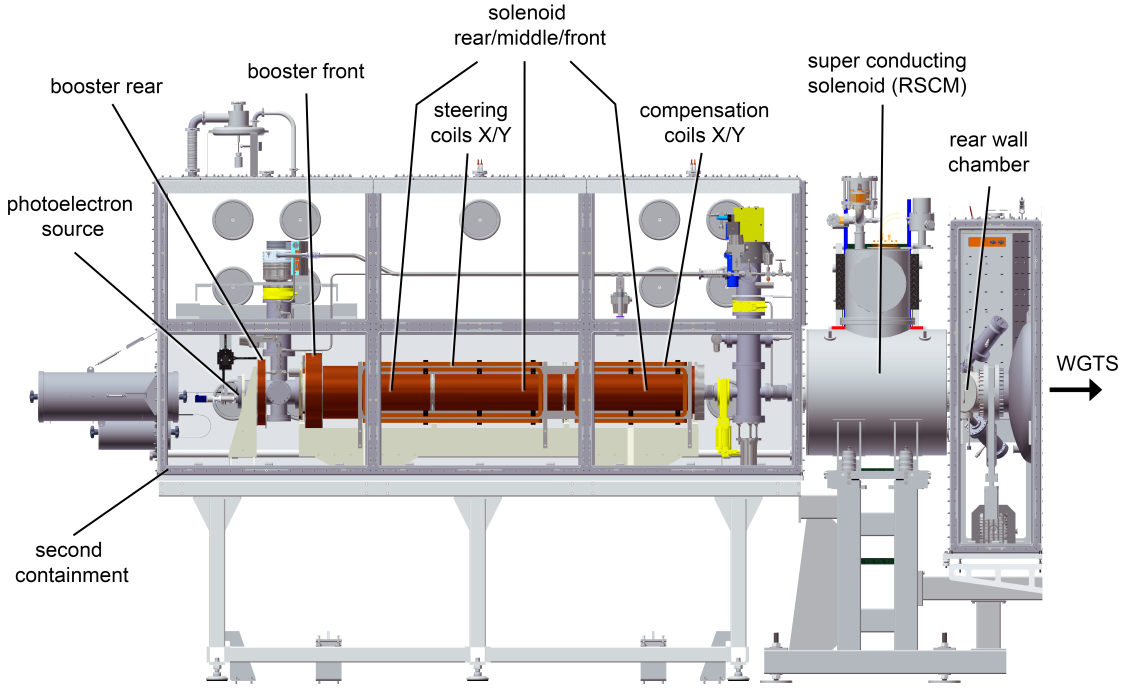


Figure 3.10: CAD drawing of the rear section. The photoelectron source is installed at the end of the beamline and is surrounded by a magnet system, which is required to generate a magnetic guiding field to steer the electrons towards the WGTS. A superconducting magnet is placed just after the rear wall to map the 191 T cm$^2$ flux tube to the rear wall. The entire setup is enclosed by a second containment to prevent even trace of tritium from the primary system from entering the ambient air.

surface potential of the stainless steel beam tube, the rear wall can be biased with an external voltage supply. Adjusting the rear wall potential to non-zero values allows one to improve both the radial as well as the longitudinal homogeneity of the plasma to less than 10 mV [Kuc16].

The rear wall is additionally used for a real-time monitoring of the source activity. This is done by measuring the intensity of the characteristic X-rays generated by the electrons penetrating the gold layer. The measurement is performed with the so-called BIXS system [Röl15], which consists of two X-ray sensors (KETEK AXAS-M SDD) placed in two of the ports of the rear wall chamber. In order to prevent the sensors from tritium contamination, a gold coated beryllium window is installed in front of the sensors.

By measuring the intensity of the characteristic gold peaks of the recorded X-ray spectrum, the relative source stability can be monitored on the 0.1 % level for time scales larger 1 min [Röl15].

#### 3.2.5.2 Photoelectron source

The so-called rear section electron gun (e-gun) is an angular selective and monoenergetic photoelectron source, which generates a pencil beam of electrons ($d < 60\,\mu m$ at the FPD [Sac20]). The beam can be guided through the entire beamline up to the FPD to investigate various systematics and to perform important calibration measurement. The over 3 m long setup combines a high precision photoelectron source (see e.g. Ref. [Beh17]) with an electrostatic acceleration electrode system and a magnet system to guide the beam towards the WGTS.

The electrons are generated by the photoelectric effect by coupling UV light into a 200 µm thick optical fibre, the end of which is coated with approximately 30 nm of gold. This photocathode is mounted inside two capacitor plates with a diameter of 10 cm, which are arranged at a distance of 10 mm. The photoelectrons are accelerated towards the front plate of the capacitor, where they exit the latter through a 6 mm wide hole. After the first non-adiabatic acceleration between the capacitor plates, the electrons are further accelerated by a cascade of three drift tubes to the final kinetic energy. The current version of the electron gun can generate electrons with energies up to 21 keV, but an upgrade to 35 keV is planned.

The capacitor plates can be tilted around a pivot point on the front plate to change the pitch angle $\theta$ of the beam (with respect to the magnetic field lines).

The electron rate and the energy spread of the beam depends on the intensity and the wavelength of the installed light source. At a wavelength of 266 nm an energy spread of 82 meV is achieved at a electron rate of $>10^4$ cps (see Chap. 5).

A detailed description of the setup of the electron gun and its working principle as well as a characterisation of its performance is available in Chap. 5 and in Ref. [Sac20].

# 4. Electron-impact scattering

One of the corner stones in achieving a neutrino mass sensitivity of 0.2 eV is the very powerful windowless gaseous tritium source with a source activity of approximately 100 GBq. Given the dimensions of the source ($d = 9\,\mathrm{cm}$ and $l = 10\,\mathrm{m}$), the required source activity leads to the integrated molecule density of $\rho_0 d = 5 \times 10^{21}\,\mathrm{m}^{-2}$. At this high gas density, the inelastic scattering of the β-electrons with the source gas becomes a dominant systematic effect, which influences the shape of the measured β-spectrum. Depending on the energy loss $\Delta E$ from the scattering process with the source gas, the surplus energy of the signal electrons and thus the transmission condition is modified. The probability distribution for the energy losses is described by the so-called energy-loss function $f(\Delta E)$. If the energy-loss function is known, it is possible to consider the change of the transmission condition in the analysis of the measurement data. The energy-loss function can be measured in-situ at KATRIN, which will be discussed in detail in Chaps. 7 and 8.

The following chapter provides an introduction to the domain of electron-impact scattering on diatomic molecules. This covers a discussion of the different processes of elastic and inelastic scattering in Sec. 4.1 and their contribution to the shape of the energy-loss function. Based on this introduction it will be possible to understand the shape of the energy-loss function and to discuss the measurement results. Furthermore, the already existing energy-loss function models for hydrogen isotopes will be discussed in Sec. 4.2. Different models exist, which are either compiled from literature data or obtained from measurements. The models will be partly used as input for simulations and for a comparison of the obtained measurement results of Chaps. 7 and 8.

After the theoretical principles have been introduced, the inelastic scattering of the signal electrons inside the gaseous tritium source of KATRIN and the resulting impact on the shape of the measured β-spectrum will be discussed in Sec. 4.3.

## 4.1 Processes of electron-impact scattering

The case of electrons scattering off diatomic molecules is more complex than the simple case of electrons scattering off a single atom, since molecules allow for additional rotational and vibrational excitations, or dissociation.

In general, the scattering processes can be grouped into two categories with the first category being elastic scattering processes and the second category being inelastic scatterings. The former includes processes, where the molecule is not excited in any form during the scattering process, whereas the latter describes processes, where the scattering causes an excitation of the molecule.

The processes of elastic and inelastic scattering are discussed in the following Secs. 4.1.1 and 4.1.2. If available, the values were calculated using tritium specific parameters. However, if these parameters were not available, the specific values for deuterium or hydrogen were used as an approximation.

### 4.1.1 Elastic scattering

Elastic scattering describes a scattering process, where there is no energy transfer caused by excitations of the molecule and only the angle of the incident electron is changed due to the coulomb interaction with the molecule's potential (so-called Rutherford scattering).

Although there is no energy transfer due to excitation, the angular change however causes a momentum transfer, which reduces the initial kinetic energy of the incident electron. The energy transfer between the deflected electron and the molecule can be calculated as a function of the deflection angle $\Delta\theta$

$$\Delta E(\Delta\theta) = 2\frac{m_\mathrm{e}}{M_{\mathrm{T}_2}} E_\mathrm{kin} \cdot (1 - \cos(\Delta\theta)) \,, \tag{4.1}$$

with $M_{\mathrm{T}_2}$ being the molecular mass of tritium [KBD+19].

At an energy of $E_\mathrm{kin} = 18.6\,\mathrm{keV}$, the elastic scattering is strongly forward-peaked resulting in a median scattering angle $\overline{\Delta\theta} = 2.1°$ [KBD+19].

For electrons with kinetic energies similar to the tritium endpoint energy, the median energy loss of

$$\overline{\Delta E} = 2.3\,\mathrm{meV} \tag{4.2}$$

is obtained [KBD+19].

Many publications exist on the calculation on elastic cross sections (see e.g. Ref. [Lan80]), but these are mainly focussed on low kinetic energies (below the ionization threshold) of the incident electrons. However, Liu [Liu87] provides an parametrization for elastic cross sections for high energetic electrons in the first Born approximation. The provided formula for the elastic cross section for the scattering at molecular hydrogen is

$$\sigma_\mathrm{el}(E_\mathrm{kin}^\mathrm{nr}) = \frac{\pi a_0^2 R}{E_\mathrm{kin}^\mathrm{nr}} \left(4.2106 - \frac{2R}{E_\mathrm{kin}^\mathrm{nr}}\right) \,, \tag{4.3}$$

where $E_\mathrm{kin}^\mathrm{nr} = \frac{1}{2} m_\mathrm{e} v^2$ is the non-relativistic kinetic energy of the electron, $R = 13.6057\,\mathrm{eV}$ the Rydberg energy, and $a_0 = 5.29 \times 10^{-11}\,\mathrm{m}$ the Bohr radius.

For electrons being emitted with the (relativistic) kinetic energy $E_\mathrm{kin}$ close to the tritium endpoint energy, the value of $E_\mathrm{kin}$ must first be converted to $E_\mathrm{kin}^\mathrm{nr}$.

From the relativistic kinetic energy $E_\mathrm{kin} = m_\mathrm{e}(\gamma - 1)$ with $\gamma^{-1} = \sqrt{1 - v^2}$ (using $c = 1$) the formula

$$E_\mathrm{kin}^\mathrm{nr}(E_\mathrm{kin}) = \frac{1}{2} m_\mathrm{e} \left(1 - \frac{m_\mathrm{e}^2}{(E_\mathrm{kin} + m_\mathrm{e})^2}\right) \tag{4.4}$$

is obtained. For electrons with $E_\mathrm{kin} = 18\,575\,\mathrm{eV}$, the formula evaluates to

$$E_\mathrm{kin}^\mathrm{nr}(18\,575\,\mathrm{eV}) = 17\,609\,\mathrm{eV}\,. \tag{4.5}$$

Using this non-relativistic kinetic energy, the total elastic scattering cross section

$$\sigma_\mathrm{el}\left(E_\mathrm{kin}^\mathrm{nr}, \mathrm{H}_2\right) = 2.86 \times 10^{-23}\,\mathrm{m}^2 \tag{4.6}$$

is obtained.

### 4.1.2 Inelastic scattering

Inelastic scattering describes scattering processes, where the molecule is excited during the scattering process. The inelastic scattering processes of electrons scattering off diatomic

molecules can be formulated as

$$e^-(E_{\mathrm{kin,i}}) + Q_2(\epsilon_\mathrm{i}) \rightarrow Q_2^*(\epsilon_\mathrm{f}) + e^-(E_{\mathrm{kin,f}})\,, \tag{4.7}$$

where $E_{\mathrm{kin,i/f}}$ is the initial/final kinetic energy of the electron and $\epsilon_{\mathrm{i/f}}$ the energy of the initial and final state of the molecule. The final state of the molecule $Q_2^*(\epsilon_\mathrm{f})$ represents many possible excitation states (indicated with the asterisk), e.g. being rotationally, vibrationally, or electronically excited, left ionized or dissociated. The energy loss of the electron is therefore

$$\Delta E = E_{\mathrm{kin,i}} - E_{\mathrm{kin,f}} = \epsilon_\mathrm{f} - \epsilon_\mathrm{i}\,. \tag{4.8}$$

A formula for the calculation of the total inelastic cross section for fast electrons scattering off tritium was derived by F. Glück (Karlsruhe Institute of Technology) based on Refs. [Ino71, Liu73, Liu87]. The total inelastic cross section can be calculated as

$$\sigma_{\mathrm{inel}}(E_{\mathrm{kin}}^{\mathrm{nr}}) = \frac{4\pi a_0^2 R}{E_{\mathrm{kin}}^{\mathrm{nr}}}\left[M_{\mathrm{tot}}^2 \cdot \ln\left(4c_{\mathrm{tot}} \cdot \frac{E_{\mathrm{kin}}^{\mathrm{nr}}}{R}\right) - 0.01\right]\,, \tag{4.9}$$

with $M_{\mathrm{tot}}^2 = 1.5363$ and $c_{\mathrm{tot}} = 1.18$.

For a non-relativistic kinetic energy of $E_{\mathrm{kin}}^{\mathrm{nr}} = 17\,609\,\mathrm{keV}$, the total inelastic cross section is

$$\sigma_{\mathrm{inel}}\left(E_{\mathrm{kin}}^{\mathrm{nr}}, \mathrm{H_2}\right) = 3.64 \times 10^{-22}\,\mathrm{m}^2\,. \tag{4.10}$$

Measurements of the total inelastic scattering cross section for electrons scattering off molecular tritium with a kinetic energy of 18.6 keV were carried out at the Troitsk $\nu$-mass experiment [ABB+00]. The obtained value

$$\sigma_{\mathrm{inel}}(18.6\,\mathrm{keV}, \mathrm{T_2}) = 3.40(7) \times 10^{-22}\,\mathrm{m}^2\,. \tag{4.11}$$

is about 7 % smaller than the calculated value in Eq. (4.10). However, both values show that the inelastic scattering cross section is more than one order of magnitude larger than the elastic scattering cross section (comp. Eq. (4.6)), which makes it the dominant process of the energy-loss spectrum.

The processes contributing to inelastic scattering are explained in the following.

#### 4.1.2.1 Vibrational and rotational excitation

In contrast to electron-impact scattering on atoms, molecules can be additionally excited rotationally and vibrationally in the scattering process. The processes can take place individually but also a simultaneous rotational and vibrational excitation is possible, which is called rovibrational excitation.

Although the pure rotational and vibrational excitation of molecules by fast electrons is very unlikely [YMYH+08], rovibrational excitations contribute significantly to the shape of the energy-loss spectrum by accompanying electronic excitations, which will be discussed in Sec. 4.1.2.2. It is therefore important to introduce the principle of vibrational and rotational excitations to understand the shape of the energy-loss spectrum.

The following paragraphs are mainly based on the text book Ref. [Dem18], if not marked otherwise.

**Vibrational excitation**

Stable molecular bindings exist, because there is an equilibrium of the repulsive force between the positive nuclei and an attractive force from sharing electrons. The exchange

of electrons between the two atoms causes a change in the electrons probability density, which influences the potential in two ways: First, their probability density is altered in a way that their maximum is between the nuclei and thus counteract the repulsive force. Second, the exchange of electrons leads to a larger spatial uncertainty, which decreases the average momentum and thus the kinetic energy of the electron according to Heisenberg's uncertainty relation [Hei27]. The result is a minimum in the shape of the interatomic potential, which causes molecular bonds at the equilibrium distance $r_{\mathrm{eq}}$. Even for the simplest of the molecules, the $H_2$ molecule, no exact analytical description of the potential exists and thus analytical models are only approximated by empirical models such as the Lennard-Jones potential (see e.g. Ref. [Ada01]) or the Morse potential [Mor29].

Approximating the potential close to the equilibrium position as a parabola allows small vibrational excitations to be described as a quantum harmonic oscillator. For a quantum harmonic oscillator, the excitation energies are a function of the angular frequency $\omega_{\mathrm{vib}}$ and the quantum number $n$ (see e.g. Ref. [CT91])

$$E_{\mathrm{HO}}(n) = \hbar\omega_{\mathrm{vib}}\left(n + \frac{1}{2}\right) \quad \text{with } n = 0,\, 1,\, 2,\, \ldots\,. \tag{4.12}$$

For higher energy excitations, this approximation is not valid as it does not take the dissociation of the molecule into account. Therefore, the potential of the molecules is commonly described by the Morse potential

$$E(r) = E_{\mathrm{D}} \cdot \left[1 - \exp\left(-a(r - r_{\mathrm{eq}})\right)\right]^2 \tag{4.13}$$

with $E_{\mathrm{D}}$ being the dissociation energy, $r_{\mathrm{eq}}$ the equilibrium position, and $a$ a molecule specific constant. Benefit of this function is that it allows an exact solution of the Schrödinger equation. The possible excitation energies are

$$E_{\mathrm{vib}}(n) = \underbrace{\hbar\omega_{\mathrm{vib}}}_{=:\Omega}\left(n + \frac{1}{2}\right) - \underbrace{\frac{\hbar^2\omega_{\mathrm{vib}}^2}{4E_{\mathrm{D}}}}_{=:\Omega_{\mathrm{D}}}\left(n + \frac{1}{2}\right)^2 \quad \text{with } n = 0,\, 1,\, 2,\, \ldots\,. \tag{4.14}$$

Although the energy difference between the excitation levels shrinks with higher $n$, the energy steps are non-zero and thus only a finite number of excitations exist below the dissociation energy. The constants $\Omega$, $E_{\mathrm{D}}$ [HW04], and $\Omega_{\mathrm{D}}$ for hydrogen and deuterium are

$$\begin{aligned} \Omega(\mathrm{H_2}) &= 0.52\,\mathrm{eV} & \Omega(\mathrm{D_2}) &= 0.37\,\mathrm{eV} \\ E_{\mathrm{D}}(\mathrm{H_2}) &= 4.51\,\mathrm{eV} & E_{\mathrm{D}}(\mathrm{D_2}) &= 4.51\,\mathrm{eV} \\ \Omega_{\mathrm{D}}(\mathrm{H_2}) &= 0.015\,\mathrm{eV} & \Omega_{\mathrm{D}}(\mathrm{D_2}) &= 0.008\,\mathrm{eV}\,. \end{aligned} \tag{4.15}$$

The energy difference between the different vibrational excitation levels are therefore smaller than 0.52 eV for hydrogen and 0.37 eV for deuterium. The splitting is expected to be even smaller for tritium compared to the values of hydrogen and deuterium. The vibrational states for the ground state of hydrogen are included in Fig. 4.1.

### Rotational excitation

Rotational excitations can be classically described as the the rotation of two masses around the common centre of mass with the angular frequency $\omega_{\mathrm{rot}}$. The kinetic energy of the rotation is $E_{\mathrm{rot}} = \frac{L^2}{2\Theta}$, with $L$ being the angular momentum and $\Theta$ the molecules' momentum of inertia. In the classical case, the energy can take any positive value as $L$ and $\Theta$ are positive real numbers.

In quantum theory, $L$ becomes an operator with the eigenvalues

$$\mathbf{L}^2 = \hbar^2 l(l+1) \quad \text{with } l = 0,\ 1,\ 2,\ ... \tag{4.16}$$

being quantised (see e.g. Ref. [CT91]), which thus results in a quantisation of the excitation energy

$$E_{\text{rot}} = \frac{\hbar^2 l(l+1)}{2\Theta} \quad \text{with } l = 0,\ 1,\ 2,\ ....\ . \tag{4.17}$$

In the case of homoatomic molecules, which applies to $T_2$, the momentum of inertia is $\Theta = M_r r_{\text{eq}}^2$ with $M_r$ being the reduced mass

$$M_r = \frac{M_1 \cdot M_2}{M_1 + M_2} \tag{4.18}$$

of the two atoms with masses $M_i$.

The rotation of the molecule causes an additional broadening of the interatomic distance due to centrifugal forces. The increase in the radius causes an increase of the momentum of inertia and thus reduces the kinetic energy for a given angular momentum.

A new equilibrium distance is set, where the centrifugal force is equal to the retracting force from the interatomic potential of the Lennard-Jones or Morse potential. An approximation can be obtained when using the Lennard-Jones potential and by performing an expansion into a series for small radius changes

$$E_{\text{rot}}(l) = \underbrace{\frac{\hbar^2}{2\Theta}}_{=:B_{\text{e}}} l(l+1) - \underbrace{\frac{\hbar^4}{2\Theta^2 r_{\text{eq}}^2 k}}_{=:D_{\text{e}}} l^2(l+1)^2 \pm \mathcal{O}(\frac{l^3}{\Theta^3}) \quad \text{with } l = 0,\ 1,\ 2,\ ... \tag{4.19}$$

with $k$ being a molecule-specific retraction constant obtained from the derivation of the Lennard-Jones potential. With $k = \omega_{\text{vib}}^2 \cdot M$, $r_{\text{eq}} = 74.16\,\text{pm}$, $B_{\text{e}} = 7.538\,\text{meV}$, $M = 8.35 \times 10^{-28}\,\text{kg}$, and $\omega \approx 1.3 \times 10^{14}\,\text{s}^{-1}$ [Dem18] a value of $D_{\text{e}} = 2.45 \times 10^{-6}\,\text{eV}$ is obtained for hydrogen. Hence, the rotational excitations ($l = 0 \rightarrow l = 1$) in the case of hydrogen are in the order of 7.5 meV. As $\Theta$ scales with $M$, the value of $B_{\text{e}}$ and $D_{\text{e}}$ are expected to be a factor of three and nine times smaller for tritium.

**Rovibrational excitation**

Although both rotational and vibrational excitations have been introduced independently of each other, scattering usually causes excitations which are a combination of both motions.

In the case of hydrogen isotopologues, the rotation frequency $\omega_{\text{rot}}$ is more than one order of magnitude lower than the vibrational frequency $\omega_{\text{vib}}$. Therefore the atomic spacing continuously changes while the molecules performs a full rotation. From both the conservation of angular momentum and the continuous change of the momentum of inertia follows that there is a constant change of the angular frequency $\omega_{\text{rot}}$ and the rotational energy $E_{\text{rot}}$. As the total energy $E = E_{\text{pot}} + E_{\text{vib}} + E_{\text{rot}}$ is conserved, too, there needs to be a continuous energy transfer between rotational, vibrational, and potential energy.

In order to approximate this interaction, the average quantum mechanic expectation value of the rotational constants $B_{\text{e}}$ and $D_{\text{e}}$ of Eq. (4.19)

$$\begin{aligned} B_n &= \langle \psi(n,r) | B_{\text{e}} | \psi(n,r) \rangle \\ D_n &= \langle \psi(n,r) | D_{\text{e}} | \psi(n,r) \rangle \end{aligned} \tag{4.20}$$

for the vibrational wave function $\psi(n, R)$ is used. In the case of the Morse potential, the

constants $B_\mathrm{e}$ and $D_\mathrm{e}$ become dependent of the vibrational excitation number $n$

$$\begin{aligned} B_n &= B_\mathrm{e} - \alpha_\mathrm{e}\left(n+\frac{1}{2}\right) \\ D_n &= D_\mathrm{e} - \beta_\mathrm{e}\left(n+\frac{1}{2}\right) . \end{aligned} \tag{4.21}$$

with the molecular-specific constants $\alpha_\mathrm{e} \ll B_\mathrm{e}$ and $\beta_\mathrm{e} \ll D_\mathrm{e}$. The energetic excitation levels for rovibrational excitation $E_\mathrm{rovib}(n,l)$ thus are the sum of the vibrational excitation energy of Eq. (4.14) and the modified rotational excitation energy of Eq. (4.19)

$$\begin{aligned} E_\mathrm{rovib}(n,l) = \Omega\left(n+\frac{1}{2}\right) - \Omega_\mathrm{D}\left(n+\frac{1}{2}\right)^2 \\ + B_n\, l(l+1) - D_n\, l^2(l+1)^2 \quad \text{with } n,l = 0,\, 1,\, 2,\, \ldots . \end{aligned} \tag{4.22}$$

Since the correction factors $\alpha_\mathrm{e}$ and $\beta_\mathrm{e}$ are much smaller than the corresponding rotational constants, the corrections are only relevant for high resolution spectroscopy. Thus, the approximation is allowed, that both rotational and vibrational excitation levels add linearly.

As the energy levels of the vibrational excitation is more than one order of magnitude larger than for the rotational excitation, the rovibrational excitations cause discrete lines in the spectrum, which appear to be broadened due to the narrow rotational excitation levels. The influence of the rovibrational excitations bands accompanying electronic excitations is visible in Fig. 4.2.

#### 4.1.2.2 Electronic excitation

An important process of inelastic scatterings are excitations of the electronic configuration of the molecule.

In this process the incident electron excites a bound electron to a higher energetic but still bound state while transferring a fraction of its initial kinetic energy. As the energy levels of the molecules are discrete, also the transferred energy has to be discrete. But in contrast to atoms, the electronic excitations can be accompanied by simultaneous rovibrational (de)excitations of the molecule, which causes a complex line spectrum.

The theory of electronic excitation as well as the influence by the rovibrational excitations is discussed in the following paragraphs.

**Pure electronic excitation**

Electronic excitations describe the excitation of the electronic configuration of the molecule.

Only in the simplest case of an hydrogen molecule, the angular momentum of the electron is constant and thus $l$ is a good quantum number. However, if the coulomb potential is not rotational symmetric or if there is an interaction with other electrons, this does not apply anymore. In the case of diatomic molecules, the resulting coulomb field of the two nuclei is axial symmetric due to the dumbbell shape of the molecule. Hence, the angular momentum $L$ performs a precession around the symmetry axis of the molecule. As a result, only the z component of the angular momentum $\mathbf{l}_z$ is constant and thus the magnetic quantum number $m_l$ becomes a good quantum number. Since the direction of motion (clockwise or counter-clockwise) around the symmetry axis does not change the energy, a new quantum number $\lambda = |m_l| = 0,\, 1,\, \ldots l$ is defined, which corresponds to the common nomenclature of atomic orbitals $\sigma$, $\pi$, $\delta$ (...) for the electronic configurations with $\lambda = 0,\, 1,\, 2,\, \ldots$ . [HW04]

In the case of two (or more) outer electrons, the angular momenta of the electrons couple, i.e. $\mathbf{L} = \sum_i \mathbf{l}_i$. As the coupling of the angular momenta of the electrons to $\mathbf{L}$ is usually

weaker than the coupling to the axial field, the $\mathbf{l}_i$ still perform a precession around the symmetry axis with $\pm\lambda_i$.

The eigenvalues for $\mathbf{L}_z$ therefore are

$$\mathbf{L}_z = \pm \left| \sum_i \lambda_i \right| \hbar = \pm\Lambda\hbar \quad \text{with } \Lambda = 0,\, 1,\, \ldots,\, \sum_i l_i \,. \tag{4.23}$$

In analogy to the nomenclature without interaction of the electrons, the electronic configurations are named $\Sigma$, $\Pi$, $\Delta$ (...) for $\Lambda = 0,\, 1,\, 2\ldots$ (see e.g. Ref. [HW04]). In addition to the coupling of the angular momentum, the spins of the electrons $\mathbf{s}_i$ also couple and form the total spin $\mathbf{S}$ with $S = \sum_i m_{s,i}$ while performing a precession motion around the generated magnetic field by the electron motion.

The $\mathbf{S}_z$ eigenvalues are

$$\mathbf{S}_z = \hbar\tilde{\Sigma} \quad \text{with } \tilde{\Sigma} = -S,\, -S+1,\, \ldots,\, S \,, \tag{4.24}$$

which causes a splitting of each of the energy levels into a multiplet of 2S+1 sub levels[1]. For $H_2$ it is a singlet and triplet state, since $S$ can only be 0 and 1. The multiplicity is written in front of the symbols, i.e. ${}^{1,3}\Sigma$. For the differentiation of the states with the same $\Lambda$, the quantum numbers $n$ and $l$ (using the letters s, p, d, f) of the individual atoms and $\lambda$ are used. This results in the nomenclature such as $2p\pi\Pi$ for one electron being excited to $n = 2$, $l = 1$, $\lambda = 1$, and $\Lambda = 1$.

Additional information is provided by adding a + or − in case the molecular function is symmetric or antisymmetric under a reflection at the molecule's symmetry axis. The indices $g$ and $u$ are used to indicate if the wave function is even or odd under a parity transformation (e.g. $\Sigma^{\pm}_{g,u}$). The Jablonski diagram as an example for $H_2$ is shown in Fig. 4.1.

**Rovibronic excitation**

If electrons scatter off diatomic molecules, the resulting excitation will usually not be a pure electronic excitation but simultaneously causes rotational and vibrational (de)excitations of the molecule. This process is called rovibronic excitation. The influence of vibrational excitations is dominant and significantly splits the electronic transitions (comp.Fig. 4.1) into a large set of lines, as it is displayed in Fig. 4.2. Each of the lines is additionally split up into a set of rotational excitations. As the energy spread due to rotational excitations is much smaller than for vibrations (seeSec. 4.1.2.1), the single rotational states usually cannot be resolved with electron spectroscopy and thus appear as a broadening of the lines.

#### 4.1.2.3 Ionisation

Similar to atoms, there exists also an ionization threshold energy $E_{\text{ion}}$ for molecules, above which the excited electrons are no longer bound to the molecule but are considered free. For a free electron, the restriction to discrete energy levels due to the interaction with the nuclei and the other electrons does not apply anymore and thus an arbitrary energy transfer to the electron is possible.

The ionisation threshold energies $E_{\text{ion}}$ for the different hydrogen isotopes are

$$E_{\text{ion}}(H_2) = 15.433\,\text{eV} \quad E_{\text{ion}}(D_2) = 15.470\,\text{eV} \quad E_{\text{ion}}(T_2) = 15.486\,\text{eV}\,, \tag{4.25}$$

[1] Commonly, $\Sigma$ is used for both the state $\Lambda = 0$ and the corresponding quantum number of $\mathbf{S}_z$. For better comprehensibility $\tilde{\Sigma}$ is used for the latter instead.

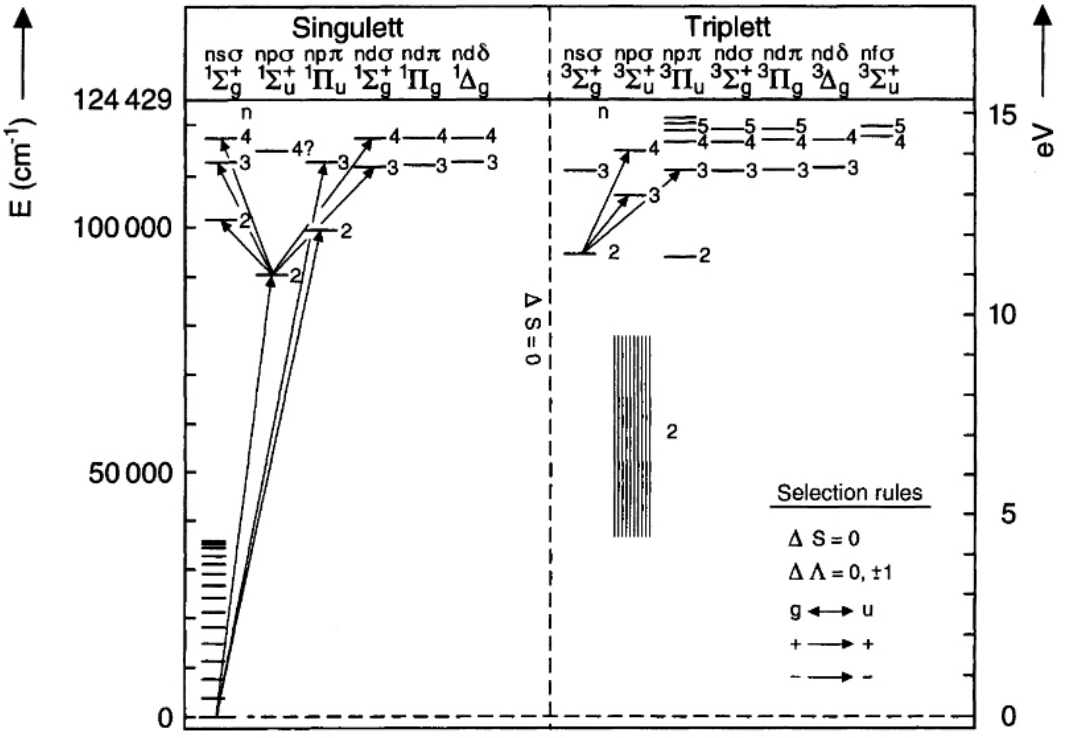


Figure 4.1: Jablonski diagram of the $H_2$ molecule. A pure electronic excitation would result in a spectrum with the lowest excitation energy of the $2p\sigma\,^1\Sigma_u^+$ at approximately 11 eV. Due to vibrational excitations, each of the states splits up (as indicated for the ground state), which results in a large set of transitions. The $2p\sigma\,^3\Sigma_u^+$ state is repulsive and causes a dissociation of the molecule, which is indicated with a continuous band. Figure reprinted from Ref. [HW04], with permission of Springer.

as provided by Ref. [WJH99].

A formula for the calculation of the ionisation cross section is provided by Ref. [Liu73]

$$\sigma_{\mathrm{ion}}(E_{\mathrm{kin}}^{\mathrm{nr}}) = 4\pi a_0^2 \frac{R}{E_{\mathrm{kin}}^{\mathrm{nr}}} \left[ (0.71 \pm 0.02) \ln\left(\frac{E_{\mathrm{kin}}^{\mathrm{nr}}}{R}\right) + (1.30 \pm 0.40) \right] , \tag{4.26}$$

which evaluates to

$$\sigma_{\mathrm{ion}}(E_{\mathrm{kin}}^{\mathrm{nr}}) = 1.73(4) \times 10^{-22}\,\mathrm{m}^2 \tag{4.27}$$

for a non-relativistic kinetic energy of $E_{\mathrm{kin}}^{\mathrm{nr}} = 17\,609\,\mathrm{keV}$. Hence, ionisation and rovibronic excitations contribute nearly equally to the total inelastic cross section in Eq. (4.10).

A formula for the calculation of the differential cross section as a function of the energy transfer $\Delta E$ of the incident electron during the ionisation process is provided by Kim et al. in Ref. [KSP00] for relativistic electrons. The so-called binary-encounter-dipole (BED) model provides an analytical description of the spectral shape of the ionisation continuum

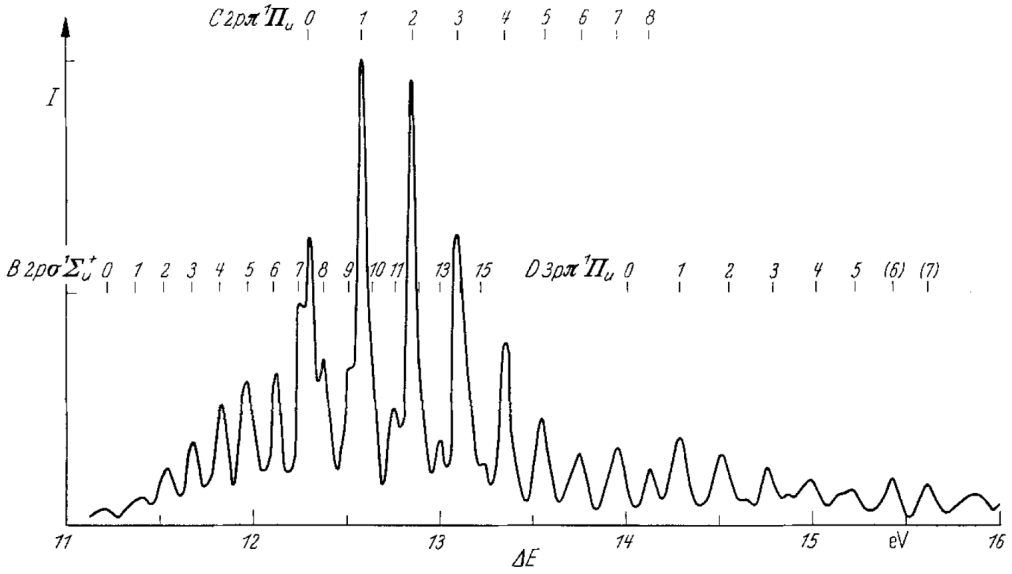


Figure 4.2: Rovibronic excitation spectrum for electrons with kinetic energies of 25 keV scattering off $H_2$ as measured by J. Geiger [Gei64]. For the three electronic states $2p\sigma\,^1\Sigma_u^+$, $2p\pi\,^1\Pi_u$, and $3p\pi\,^1\Pi_u$ the splitting into several rovibrational bands are visible. These excitation states can in fact cause discrete lines even above the ionisation threshold $E_{\mathrm{ion}}(H_2) = 15.433\,\mathrm{eV}$. Figure reprinted from Ref. [Gei64], with permission of Springer.

(omitting an overall amplitude)

$$\begin{aligned} f_{\mathrm{BED}}(\Delta E, E_{\mathrm{kin}}) =& \frac{(N_i/N)-2}{t+1}\left(\frac{1}{w+1}+\frac{1}{t-w}\frac{1+2t'}{(1+t'/2)^2}\right) \\ &+ [2-(N_i/N)]\left[\frac{1}{(w+1)^2}+\frac{1}{(t-w)^2}+\frac{b'^2}{(1+t'/2)^2}\right] \\ &+ \frac{1}{N\cdot(w+1)}\frac{\mathrm{d}f(w)}{\mathrm{d}w}\left[\ln\left(\frac{\beta_t^2}{1-\beta_t^2}\right)-\beta_t^2-\ln\left(2b'\right)\right]. \end{aligned} \tag{4.28}$$

The variables are

$$\begin{aligned} t &= \frac{E_{\mathrm{kin}}}{E_{\mathrm{ion}}} \\ t' &= \frac{E_{\mathrm{kin}}}{m_e c^2} \\ \beta_t^2 &= 1-\frac{1}{(1+t')^2} \\ b' &= \frac{E_{\mathrm{ion}}}{m_e c^2} \\ w &= \frac{\Delta E - E_{\mathrm{ion}}}{E_{\mathrm{ion}}} \\ N_i &= \int_0^\infty \frac{\mathrm{d}f(w)}{\mathrm{d}w}\mathrm{d}w = 1.173\,, \end{aligned} \tag{4.29}$$

where $N = 2$ is the number of bound electrons in the subshell and $\frac{\mathrm{d}f(w)}{\mathrm{d}w}$ the differential oscillator strength. A parametrisation for the differential oscillator strength is provided in

Ref. [KR94] in form of a polynomial

$$\frac{\mathrm{d}f(w)}{\mathrm{d}w} = a \cdot \left(\frac{E_{\mathrm{ion}}}{\Delta E}\right)^3 + b \cdot \left(\frac{E_{\mathrm{ion}}}{\Delta E}\right)^4 + c \cdot \left(\frac{E_{\mathrm{ion}}}{\Delta E}\right)^5 + d \cdot \left(\frac{E_{\mathrm{ion}}}{\Delta E}\right)^6 , \tag{4.30}$$

with the constants (for $H_2$) being $a = 1.1262$, $b = 6.3982$, $c = -7.8055$, and $d = 2.1440$.

The ionisation tail extends to up to the maximal kinetic energy of $\Delta E_{\mathrm{max}} = 0.5 \cdot (E_{\mathrm{kin}} - E_{\mathrm{ion}})$ due to the indistinguishability of the electrons in the experiment. As always the higher-energetic electron of the incident and the ejected electron is considered the signal electron, the ejected electron becomes the signal electron for energy transfers larger than $\Delta E_{\mathrm{max}}$.

#### 4.1.2.4 Dissociation

Electron-impact dissociation of diatomic molecules is caused by the following three processes

$$\begin{aligned} &e^- + Q_2 \rightarrow e^- + Q(n_1, l_1) + Q(n_2, l_2) && \text{(Pure dissociation)} \\ &e^- + Q_2 \rightarrow 2e^- + Q_2^+ \rightarrow 2e^- + Q(n, l) + Q^+ && \text{(Dissociative ionization)} . \\ &e^- + Q_2 \rightarrow Q(n, l) + Q^- && \text{(Dissociative attachment)} \end{aligned} \tag{4.31}$$

Only the pure dissociation processes contribute to the energy-loss spectrum of electrons, since the dissociative ionization is in fact an ionization process, where the ionized molecule is left in an unstable states, which is followed by dissociation. Dissociative attachment happens only for low energy electrons and thus doesn't contribute to the energy-loss spectrum for electrons with kinetic energies close to the tritium endpoint energy [MHFT12].

Pure dissociations are mainly caused either via the electronic excitation into a vibrational continuum state of an electronic state or the excitation into a repulsive electronic configuration, such as the $2p\sigma 3\Sigma_u^+$ state. While the dissociation due to vibrational excitation causes a continuous spectrum, the dissociation due to an repulsive electronic state appears as a broad peak in the energy-loss spectrum as indicated in Fig. 4.1 [YMYH$^+$08]. However, the total dissociation cross section close to the tritium endpoint energy is at least one order of magnitude smaller than the total inelastic cross section [KAT05] and thus does not contribute significantly to the energy-loss spectrum.

## 4.2 Literature-based and empirical models

For the neutrino mass analysis of the KATRIN data an energy-loss spectrum of 18.6 keV electrons scattering off molecular tritium (at 30 K) is required in order to construct the response function taking into account the shape distortions due to scattering (see Sec. 4.3). Such an energy-loss spectrum can be either constructed from literature data or it can be obtained by measurements with a suitable experimental setup.

As the endpoint region of the tritium β-spectrum is of less interest for other experiments, literature data for cross sections of the individual rovibronic excitation states (see Sec. 4.1.2) for tritium with kinetic energies close to the tritium endpoint are not available. Thus, a compilation of the energy-loss function using literature data is not possible. However, two literature-based energy-loss modes exist for hydrogen and deuterium, which were compiled at KATRIN. Besides these two literature-based models, empirical parametrisations of the energy-loss function exist, which were measured at the Troitsk ν-mass experiment. These empirical models provide a parametrisation of the energy-loss function for all three hydrogen isotopes, which are valid for kinetic energies close to the tritium endpoint energy.

Both the literature based energy-loss function models as well as the empirical models will be introduced in the following paragraphs.

### Literature-based models

Two literature-based energy-loss function models were compiled at KATRIN using literature data for hydrogen and deuterium. The first model by F. Glück (Karlsruhe Institute of Technology) (unpublished, but used in Ref. [HHW$^+$17]), is based on values from Refs. [ABG80, CM95] for the cross sections of the different vibronic excitation states of $H_2$ and the H-atom ionization tail derived from the Bethe theory [Ino71]. The vibronic excitation states of the resulting energy-loss function, as shown in Fig. 4.3, are a set of monoenergetic lines, neglecting the rotational broadening. The Glück model is included in the KEloss software package, which is used for the deconvolution of the energy-loss function from response function measurements using the electron gun (see Sec. 7.3.1). The model is used for simulations of the deconvolution process in Sec. 7.3.1 and Ref. [HHW$^+$17].

Another literature model was developed by N. Trost [Tro19], who used available cross sections for deuterium from the LXCat database[2] to compile the vibronic excitation states and a semi-empirical model for the ionization tail of electron-$H_2$ scattering from Ref. [Rud91]. In order to obtain the individual cross sections at the tritium endpoint energy, the available cross sections from the LXCat database were extrapolated by more than one order of magnitude. Similar as with the Glück model, the rotational broadening of the line spectrum was neglected, which results in a set of monoenergetic lines.

Both models are displayed in Fig. 4.3, where the lines were broadened with a Gaussian of 20 meV width for better representation.

Comparing the two literature-based models, differences in both the intensity of the electronic excitation states as well as the ionization tail are visible. These differences can either be caused by incorrect or incomplete models or by significant differences in the energy-loss functions due to isotopic effects. In both cases, the two models cannot be used as an energy-loss function model for the analysis of the measurement data of KATRIN without further improvements and verification of the models. In the case of the Trost model, it would be possible to fit the model to measurement data in order to adjust the extrapolated cross sections of the individual excitation states.

### Empirical models

As the preceding Troitsk ν-mass experiment made use of an windowless gaseous tritium source, similar systematic effects as for the KATRIN experiment had to be investigated including the measurement of the energy-loss function.

A first energy-loss function for tritium was published by Aseev et al. [ABB$^+$00], where the energy-loss function was investigated by using a monoenergetic beam of electrons, which was guided through the tritium source of the Troitsk experiment. The rate, as a function of the surplus energy of the electron beam, was investigates with a MAC-E-type spectrometer. The measurement approach was very similar to the measurement approach explained in Chaps. 7 and 8. The obtained response function was then fit with an empirical model consisting of a Gaussian kernel to describe the rovibronic excitation states below a threshold energy $\epsilon_c$ and a Lorentzian to describe the higher rovibronic excitation states and the ionization continuum above $\epsilon_c$

$$f(\Delta E)_{\text{Aseev}} = \begin{cases} A_{\text{G}} \cdot \exp\left(-\frac{2(\Delta E-\epsilon_{\text{G}})^2}{\omega_{\text{G}}^2}\right) & \text{for } \Delta E < \epsilon_c \\ A_{\text{L}} \cdot \frac{\omega_{\text{L}}^2}{\omega_{\text{L}}^2+4(\Delta E-\epsilon_{\text{L}})^2} & \text{for } \Delta E \geq \epsilon_c\,, \end{cases} \tag{4.32}$$

with the parameter values as provided in Tab. 4.1. The parameter $\epsilon_c$ is defined as the energy value where both functions intersect so that the piecewise model is continuous.

[2] `https://us.lxcat.net`

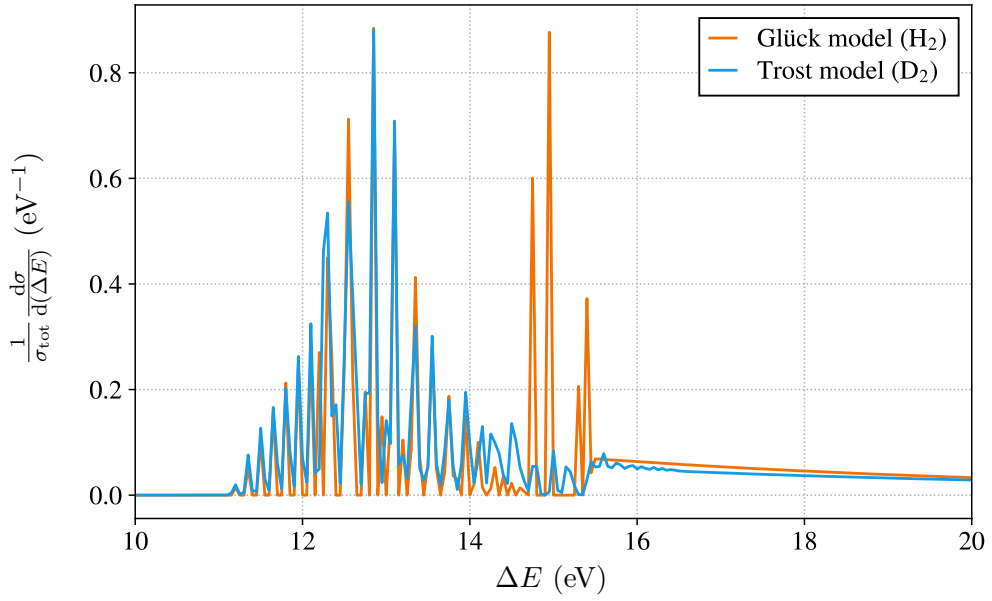


Figure 4.3: Literature-based energy-loss modes for hydrogen (Glück model) and deuterium (Trost model [Tro19]). A significant difference in the range E=[14,16] eV and the ionisation tail is visible. The monoenergetic lines were broadened with a 20 meV broad Gaussian for better visualisation.

No parameter uncertainty is provided for the position of the Gaussian kernel, since this position was determined manually and kept fixed during the fit. This influences both the uncertainty estimation of the free fit parameters as well as the correlation between them. Thus, the parameter uncertainties appear to be very small and no uncertainty band is visible in Fig. 4.4.

Similar measurements were performed by Abdurashitov et al. [A$^+$17] using hydrogen and deuterium as source gas. Although the shape of the fit function was the same as for the previously described measurements, a change in the parametrisation was made by using a common amplitude parameter and only one scaling parameter for the Gaussian part, i.e.

$$f(\Delta E)_{\mathrm{Abdu.}} = N \begin{cases} A \cdot \exp\left(-\frac{2(\Delta E-\epsilon_{\mathrm{G}})^2}{\omega_{\mathrm{G}}^2}\right) & \text{for } \Delta E < \epsilon_c \\ \frac{\omega_{\mathrm{L}}^2}{\omega_{\mathrm{L}}^2+4(\Delta E-\epsilon_{\mathrm{L}})^2} & \text{for } \Delta E \geq \epsilon_c\,. \end{cases} \tag{4.33}$$

Table 4.1: Parameters for the energy-loss function of Eq. (4.32) and 4.33 as measured at the Troitsk ν-mass experiment [ABB$^+$00, A$^+$17].

| | $A_{\mathrm{G}}$ (eV$^{-1}$) | $\omega_{\mathrm{G}}$ (eV) | $\epsilon_{\mathrm{G}}$ (eV) | $A_{\mathrm{L}}$ (eV$^{-1}$) | $\omega_{\mathrm{L}}$ (eV) | $\epsilon_{\mathrm{L}}$ (eV) | $\epsilon_c$ (eV) |
|---|---|---|---|---|---|---|---|
| $T_2$ | 0.204(1) | 1.85(2) | 12.6 | 0.0556(3) | 12.5(1) | 14.30(2) | 14.09 |

| | $A$ | $\omega_{\mathrm{G}}$ (eV) | $\epsilon_{\mathrm{G}}$ (eV) | $N$ (eV$^{-1}$) | $\omega_{\mathrm{L}}$ (eV) | $\epsilon_{\mathrm{L}}$ (eV) | $\epsilon_c$ (eV) |
|---|---|---|---|---|---|---|---|
| $D_2$ | 3.66(33) | 1.31(11) | 12.80(4) | 0.068 | 11.62(25) | 13.7(5) | 13.86 |
| $H_2$ | 3.59(17) | 1.21(5) | 12.67(2) | 0.070 | 12.13(16) | 13.2(2) | 13.64 |
| avg. | 3.60(15) | 1.22(5) | 12.695(17) | 0.070 | 11.99(13) | 13.29(18) | 13.67 |

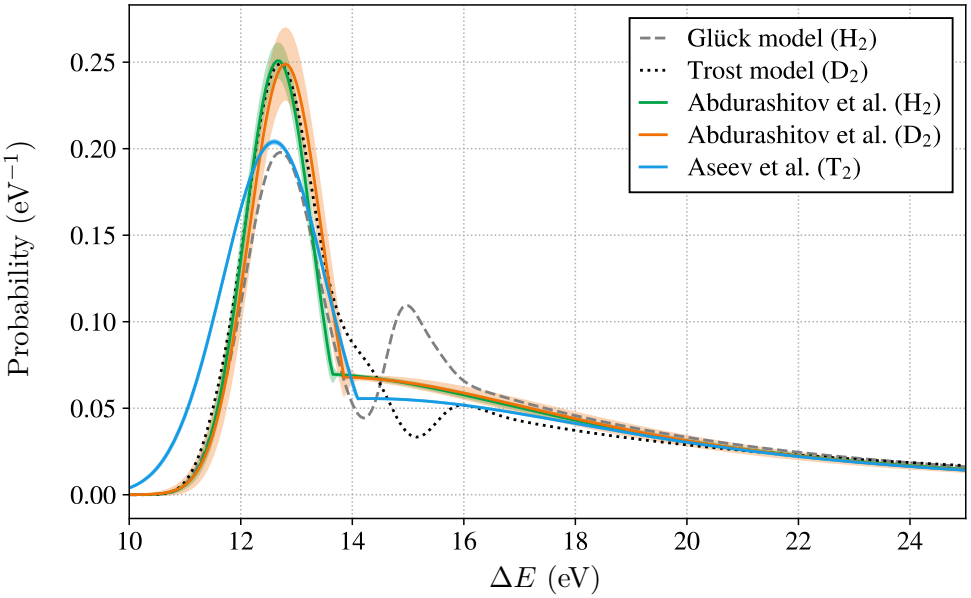


Figure 4.4: Empirical energy-loss models for all hydrogen isotopes as available in Refs. [ABB+00, A+17]. A significant difference of the model for tritium and deuterium/hydrogen is visible. Although shape differences are expected for different isotopes, the shape of the Aseev et al. model may be falsified due to the fixed position parameter $\epsilon_G$. For comparison, the literature-based models of Glück and Trost [Tro19] are included (broadened by a Gaussian kernel with $\sigma = 0.31\,\text{eV}$).

The equation can be rewritten so that $A_G = N \cdot A$ and $A_L = N$ which gives the same parametrisation as in Eq. (4.32). However, the parameter uncertainties must be propagated accordingly.

The reason for the change of the parametrisation was to include the overall scaling parameter $N$, which is calculated during the minimisation to ensure a normalisation of the energy-loss function to 1. Thus, $N$ is not a free fit parameter and no parameter uncertainty is provided. The best fit values for both isotopes and the average of both models are provided in Tab. 4.1. This time, the position parameter $\epsilon_G$ was not fixed during the fit and parameter uncertainties are available for all free parameters resulting in the significantly increased $1\sigma$ uncertainty interval, as shown in Fig. 4.4.

Besides the increased uncertainty interval, the comparison of the results of Aseev et al. and Abdurashitov et al. shows a significant difference of the shape of the energy-loss function for tritium and deuterium/hydrogen. Since the results of Abdurashitov et al. for deuterium and hydrogen differ only slightly in their shape it would be expected that the energy-loss function of tritium has a very similar shape. However, a significant difference of 200 meV between the positions of the Gaussian kernels as well as a difference of 540 meV between the widths are visible. As $\epsilon_G$ was fixed in the analysis of Aseev et al., the position of the Gaussian kernel has an unknown uncertainty. Thus, the available parametrisation of the energy-loss mode for tritium has to be called into question.

**Comparison**

In order to compare the empirical models to the two literature-based models, the spectra in Fig. 4.3 are convolved with a Gaussian distribution with a width of $\sigma = 0.31\,\text{eV}$ in

order to mimic the energy resolution of the experimental data. The value $\sigma = 0.31\,\mathrm{eV}$ is determined as the value where the Trost model agrees best with the Abdurashitov et al. $D_2$ model. It can be seen in Fig. 4.4 that the Trost model agrees well with the Abdurashitov et al. models in the region of the main peak of the rovibronic excitation states. The maximum value of the peak at $m_{\mathrm{Trost}} = 12.71\,\mathrm{eV}$ is located in between the two values of $\epsilon_{\mathrm{G}}(\mathrm{H_2}) = 12.67\,\mathrm{eV}$ and $\epsilon_{\mathrm{G}}(\mathrm{D_2}) = 12.80\,\mathrm{eV}$ of the Abdurashitov et al. models. Furthermore, the height $A_{\mathrm{Trost}} = 0.249\,\mathrm{eV}^{-1}$ of the peak is in very good agreement with the values of $A \cdot N = 0.251\,\mathrm{eV}^{-1}$ ($\mathrm{H_2}$) and $A \cdot N = 0.249\,\mathrm{eV}^{-1}$ ($\mathrm{D_2}$). However, the models differ significantly in the energy range of 14 eV to 16 eV. In this region the approximation using a Lorentz curve appears to be a too basic approximation. Similar deviations in this energy range are visible for the Glück model, however, due to the differences in the two literature-based models, the deviations are the opposite. In contrast to the good agreement of the Trost model with the measurement data of Abdurashitov et al. in the energy range below 14 eV, the Glück model does not agree with the Abdurashitov et al. model as the height of the peak $A_{\mathrm{Glück}} = 0.198\,\mathrm{eV}^{-1}$ is about 26 % smaller. In fact, the height of the peak agrees better with the Aseev et al. model ($A_{\mathrm{G}} = 0.204\,\mathrm{eV}^{-1}$), although a significant difference of the width is visible.

From the comparison it is obvious that the available models do not provide a consistent description of the energy-loss function neither for $\mathrm{H_2}$, $\mathrm{D_2}$, nor $\mathrm{T_2}$. As it will be discussed in the next section, it is essential for KATRIN have a precise description of the energy-loss function for molecular tritium in order to describe the energy losses from the scattering of the signal electrons with the source gas. It is therefore required to perform a precision measurement of the energy-loss function directly with the experimental setup of KATRIN.

## 4.3 Electron scattering inside the tritium source of KATRIN

The signal electrons from the tritium β-decay can both scatter elastically and inelastically with the source gas while being magnetically guided through the WGTS towards the spectrometer. Elastic scatterings have only a minor impact on KATRIN, as its cross section is nearly one order of magnitude smaller compared to the inelastic scattering cross section (see Eqs. (4.6) and (4.11)). Furthermore, the small median energy loss of $\overline{\Delta E} = 2.3\,\mathrm{meV}$ can be neglected in the neutrino mass analysis, since its systematic uncertainty on $m_\nu^2$ is only $5.1 \times 10^{-5}\,\mathrm{eV}^2$ [KBD+19]. Thus, the dominant process contributing to energy losses are inelastic scatterings.

The energy loss due to inelastic scattering affects the measurement of the tritium β-spectrum in two manners. The first effect is that the signal electrons can lose large amounts of energy and are therefore not transmitted within the measurement range of KATRIN. At the nominal column density setting of $\rho_0 d = 5 \times 10^{21}\,\mathrm{m}^{-2}$, the actual signal rate at the tritium endpoint is therefore reduced by nearly 60% compared to the actual source activity, as it can be seen in Fig. 4.5. The second effect is that the scattered electrons, which lose an energy portion smaller than the measurement range, still contribute to the β-spectrum, but are transmitted at less negative filter potentials. This causes a distortion of the measured β-spectrum, which has to be considered in the analysis of the measurement data. To do so, the response function of the experimental setup (see Sec. 3.1.2) needs to be modified, as described in the following (based on Refs. [KBD+19, Gro15]).

The probability for $n$-fold scattering $P_n\left(\mu(\theta)\right)$ inside the tritium source follows a Poisson distribution

$$P_n\left(\mu(\theta)\right) = \frac{\mu(\theta)^n}{n!} \exp\left(-\mu(\theta)\right) , \tag{4.34}$$

with the expectation value for the number of scatterings being $\mu(\theta)$. The latter is the

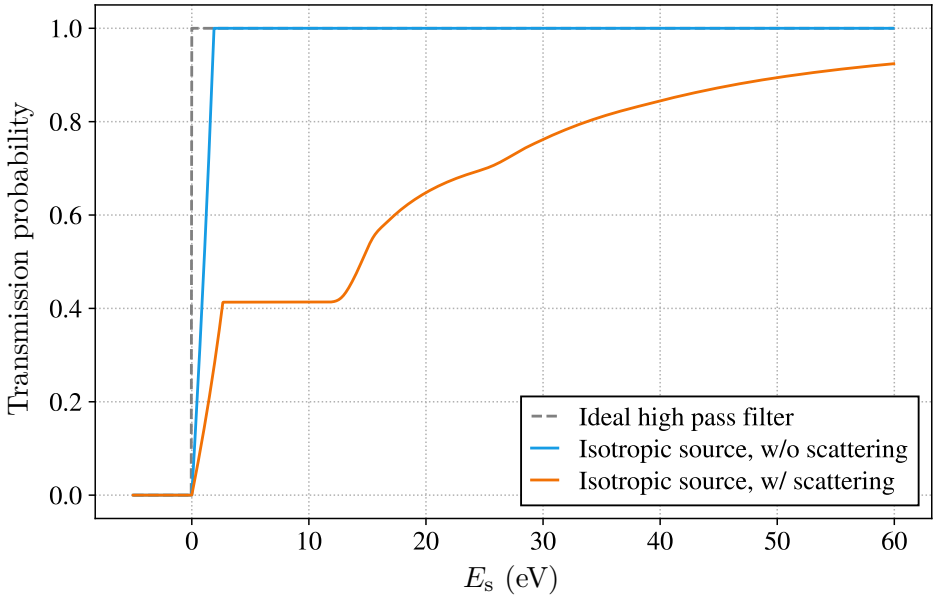


Figure 4.5: Response function of the KATRIN experiment taking into account the energy loss due to scattering. The orange curve displays the response function at nominal column density of $\rho_0 d = 5 \times 10^{21}\,\mathrm{m}^{-2}$ and an energy resolution of $\Delta E_{\mathrm{MAC-E}} = 2.7\,\mathrm{eV}$, which corresponds to the current magnetic field configuration ($B_\mathrm{A} = 6.3\,\mathrm{G}$) of KATRIN. For comparison, the undistorted transmission function $T(E_\mathrm{kin}, U_\mathrm{ret})$ as well as the transmission function for an ideal high-pass filter are included.

product of the inelastic cross section $\sigma_\mathrm{inel}$ and the effective column density $\mathcal{N}_\mathrm{eff}$

$$\mu(\theta) = \sigma_\mathrm{inel} \cdot \mathcal{N}_\mathrm{eff}\,. \tag{4.35}$$

The effective column density $\mathcal{N}_\mathrm{eff}$ is the integral of the gas-density profile between the emission point $z$ of the electron and the front end of the WGTS at $z = L/2$, with $L$ being the length of the injection chamber located symmetrically around zero, i.e.

$$\mathcal{N}_\mathrm{eff} = \frac{1}{\cos(\theta)} \int_z^{L/2} \rho(z')\mathrm{d}z'\,. \tag{4.36}$$

The weighting factor $1/\cos(\theta)$ takes account of the increased path length for non-zero pitch angles.

At the nominal column density of $\rho_0 d = 5 \times 10^{21}\,\mathrm{m}^{-2}$, which was determined to be the ideal point in terms of signal rate considering the source diameter, energy resolution, and the influence of inelastic scattering [KAT05], only about 40 % of the signal electrons leave the source unscattered. The other 60 % scatter at least once and thus lose a certain amount of energy, which causes a distortion of the experiment's response function, as it is displayed in Fig. 4.5.

If an electron scatters with the source gas, its kinetic energy is reduced by the energy fraction $\Delta E$, which changes the transmission condition of Eq. (3.8). The probability distribution of the energy loss $\Delta E$ from one scattering process is described by the energy-loss function $f(\Delta E)$. However, the electrons can scatter multiple times in the source. In order to obtain the resulting probability distribution $f_n(\Delta E)$ describing the energy-loss

distribution from the $n$ scatterings, the energy-loss function has to be convolved $n$ times with itself. The probability distribution $\mathcal{F}(\Delta E, \mu)$ taking into account the contribution from all scatterings is a superposition of the individual distributions $f_n(\Delta E)$ each weighted with the corresponding probability $P_n(\mu)$ for $n$-fold scattering [KBD+19], i.e.

$$\begin{aligned}\mathcal{F}(\Delta E, \mu) =& P_0(\mu) \cdot \delta(\Delta E) \\ &+ P_1(\mu) \cdot f(\Delta E) \\ &+ P_2(\mu) \cdot f(\Delta E) \otimes f(\Delta E) \\ &+ P_3(\mu) \cdot f(\Delta E) \otimes f(\Delta E) \otimes f(\Delta E) \\ &+ ... \\ &= \sum_{n=0} P_n(\mu) \cdot f_n(\Delta E)\,.\end{aligned} \tag{4.37}$$

In the case of the unscattered electrons, the probability distribution $f_0$ is a delta function $\delta(\Delta E)$, as unscattered electrons do not lose any energy.

By considering the energy-loss distribution $\mathcal{F}(\Delta E, \mu)$ in the transmission condition of the signal electrons, the transmission function in Eq. (3.11) becomes

$$\begin{aligned}R(E_{\mathrm{src}}, U_{\mathrm{ret}}, \mu) = \int_{\Delta E=0}^{E_{\mathrm{s}}} \int_{\theta=0}^{\theta_{\max}(z)} \Big[ &\mathcal{T}\left(E_{\mathrm{src}} - \Delta E, \theta, U_{\mathrm{ret}}\right) \sin\left(\theta\right) \\ &\cdot \mathcal{F}(\Delta E, \mu) \Big] \mathrm{d}\theta \mathrm{d}\Delta E\,,\end{aligned} \tag{4.38}$$

taking into account the energy losses from the scatterings [KBD+19]. The shape of the resulting response function is shown in Fig. 4.5.

In order to calculate the response function, a precise description of the energy-loss function for electrons scattering off molecular tritium with kinetic energies close to the tritium endpoint energy is required. The required precision of the energy-loss mode is defined by the maximal allowed contribution to the overall systematic uncertainty budged of the observable $m_\nu^2$. For the sensitivity goal $m(\nu_e) = 200\,\mathrm{meV}$ of KATRIN, a total uncertainty budget of $\sigma_{\mathrm{sys}}^{\mathrm{tot}}(m_\nu^2) \leq 17 \times 10^{-3}\,\mathrm{eV}^2$ must not be exceeded. As defined in the design report [KAT05], the contribution to $\sigma_{\mathrm{sys}}^{\mathrm{tot}}(m_\nu^2)$ due to the uncertainties of the energy-loss function has to be below the limit of $\sigma_{\mathrm{sys}}^{\mathrm{eloss}}(m_\nu^2) < 7.5 \times 10^{-3}\,\mathrm{eV}^2$.

Since no reliable models of the energy-loss function for tritium exist, it is absolutely essential to measure the energy-loss function at KATRIN with unprecedented precision. Therefore, measurements were carried out as part of this work for both deuterium and tritium, the results of which will be discussed in Chaps. 7 and 8.

# 5. Rear section photoelectron source

The rear section electron gun (e-gun), is a photoelectron source, which provides a quasi-monoenergetic and angular-selective beam of electrons. With an acceleration energy of up to 21 keV and a pitch angle reaching 90° in the pinch magnet, the electron gun covers the entire parameter space of β-electrons from tritium decay and can be used to mimic the properties of the latter. The electron gun is extensively used for calibration measurements and the determination of systematic uncertainties all along the entire experimental setup of KATRIN. It is the key component for the measurement of the energy-loss function of the signal electrons scattering off the source gas in the WGTS and is required for the periodic determination of the column density during the neutrino-mass measurements (see Ref. [Mar20]) as well as for the precise determination of the electric and magnetic fields at the analysing plane (see Ref. [Blo]).

The 3 m long setup of the electron gun combines an optical setup, a high-voltage system, and a magnet setup, for the purpose of generating the electrons and accelerating them to the desired kinetic energy while magnetically guiding the electrons towards the beamline of KATRIN. In order to make sure, the electrons do not scatter with residual gas in the beam line and to enable operation at hight voltage, the system is operated at a pressure of $<1 \times 10^{-8}$ mbar.

The rear section electron gun was commissioned in fall 2018 together with R. Sack (University of Münster) [Sac20]. The focus of this work is on the performance of the optical setup and the light source related properties, such as the energy distribution and the rate stability of the beam passing the entire beam line. The determination of the other characteristic properties, such as the work function of the photocathode as well as the energy and HV stability, are discussed in Ref. [Sac20]. The working principle as well as the performance during the commissioning are discussed in the following sections. Both the discussion of the experimental setup of the electron gun as well as its performance are important for the energy-loss function measurements, which are discussed in Chaps. 7 and 8.

## 5.1 Electromagnetic setup

The electron gun is designed to provide a beam of quasi-monoenergetic electrons with kinetic energies up to 21 keV at a rate of approximately $10^3$ cps to $10^4$ cps. For this purpose, electrons are generated from photoelectric effect by shining ultraviolet light through an 30 nm thick golden cathode. These photoelectrons are then accelerated by an electrostatic field to the desired kinetic energy and are guided towards the beamline of the KATRIN experiment by a magnetic guiding field.

The complex electromagnetic concept (see Ref. [Bab14]), which is required to obtain the angular-selective and monoenergetic beam of electrons, is illustrated in Fig. 5.1, with the components being explained in the following.

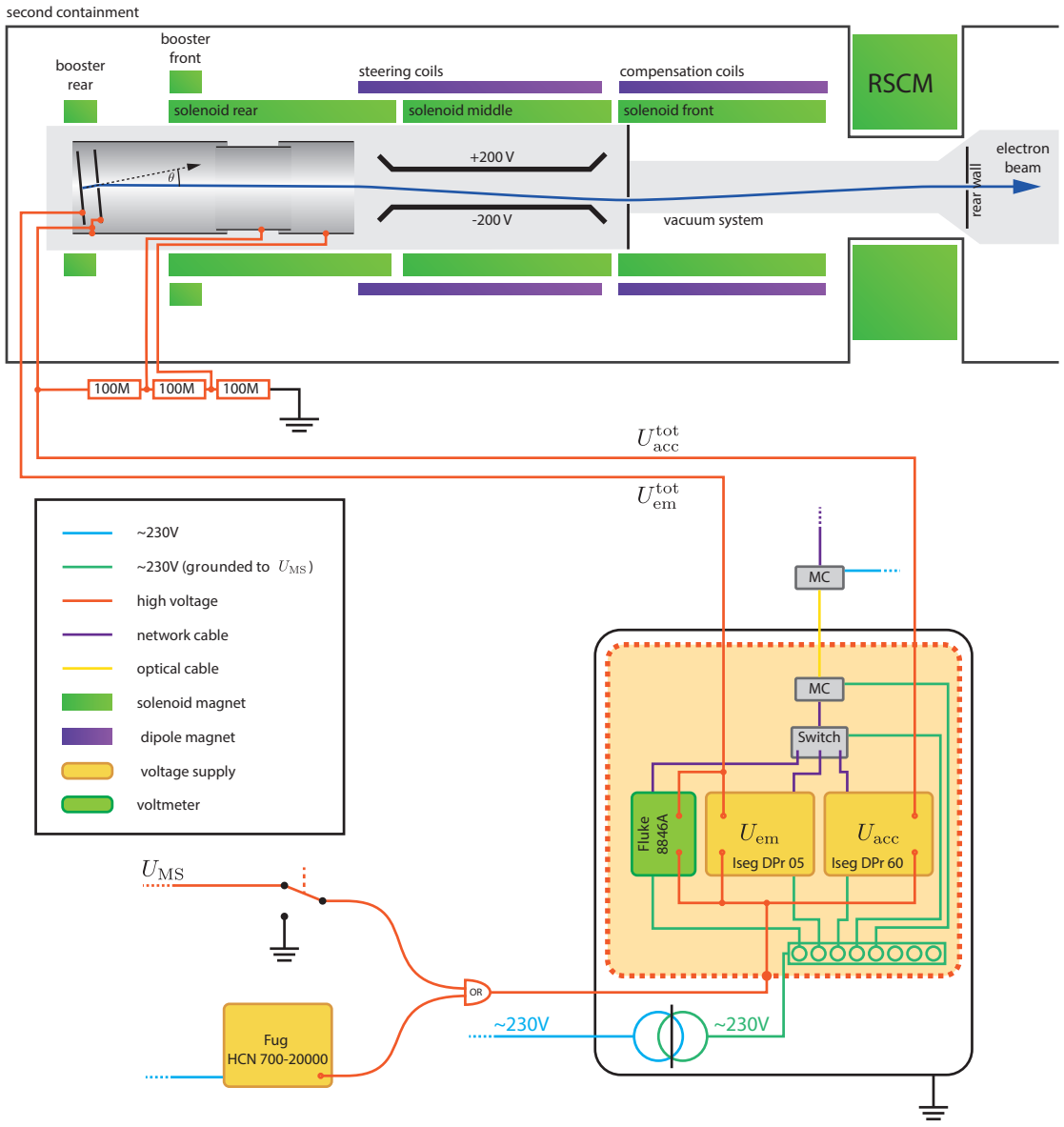


Figure 5.1: Schematic drawing of the magnet and high-voltage setup of the rear section electron gun. The voltage supplies for the emission and acceleration electrodes are placed in a high voltage cage, which is grounded to the main spectrometer voltage $U_{\mathrm{MS}}$. A voltage divider is used to scale down the voltage for the post-acceleration electrodes in front of the photoelectron source. Two electric dipole electrodes are installed in front of the cylinder electrodes to drift out ions from the WGTS. In order to reduce the flux of neutral tritium entering the e-gun chamber from the WGTS, an off-axis orifice is placed in between the rear wall and the dipole electrodes. This removes a direct line of sight between the WGTS and the photoelectron source. Five normal-conducting magnets and the rear section superconducting magnet (RSCM) generate a magnetic guiding field, which can be modified in x and y direction by four pairs of dipole coils.

### 5.1.1 Photoelectron source

The photoelectron source, as shown in Fig. 5.2, is assembled on a CF160 flange and consists of a plate capacitor made of two stainless steel discs with a diameter of 10 cm, which are arranged at a distance of 10 mm. The gold-coated ends of seven optical fibres are attached to a spacing in the back plate of the capacitor. The other ends of the fibres are installed behind a CF16 fused silica window, where the UV light is coupled into one of the fibres from outside the vacuum system with a pair of lenses (see Ref. [Sch16]). The lenses are mounted on a motorised three-axis stage, which allows one to individually select one of the fibres, as the position of the fibres inside the acceleration capacitor is optimised for different pitch angles of the electron beam (see Ref. [Bab14]).

The back plate of the capacitor (the so-called emission electrode) is set to a negative potential $U_{\mathrm{em}}^{\mathrm{tot}}$, which defines the potential energy of the photoelectrons. As the photoelectrons are emitted from the surface following a cosine distribution [PB02], they first need to be collimated to obtain a monoangular beam. For this purpose, the front plate of the capacitor (the so-called acceleration electrode) is set to a potential $U_{\mathrm{acc}}^{\mathrm{tot}}$, which is chosen to be about 4 kV more positive than $U_{\mathrm{em}}^{\mathrm{tot}}$. The strong electric field (approximately 400 kV m$^{-1}$) inside the capacitor causes a first non-adiabatic acceleration of the photoelectrons, which leads to a collimation of the angles to be parallel to the electric field. The collimated electrons leave the capacitor through a 6 mm wide hole in the front plate with a kinetic energy of $q(U_{\mathrm{em}}^{\mathrm{tot}} - U_{\mathrm{acc}}^{\mathrm{tot}})$ and enter the post-acceleration system (see Sec. 5.1.2). In order to change the pitch angle of the beam $\theta$, the capacitor can be tilted up to $\alpha_{\mathrm{max}} = \pm 15°$ around a pivot axis at the front plate with a motorised linear vacuum feedthrough. The tilt angle of $\pm 15°$ is sufficient for the electron beam to reach $\theta = 90°$ in the pinch magnet due to the adiabatic transformation of $\theta$ with increasing magnetic fields (see Ref. [Bab14]). The capacitor assembly is mounted on ceramic rods, which allow high-voltage operation of up to 21 kV. The supply voltage of the emission electrode and the acceleration electrode is each fed through the CF160 flange with HV vacuum feedthroughs.

### 5.1.2 Post-acceleration system

After the photoelectrons left the capacitor of the photoelectron source, the beam is adiabatically accelerated to its final kinetic energy by a post-acceleration system containing a cascade of three cylinder electrodes. The first of the three cylinder electrodes is directly connected to the acceleration electrode and thus has the same potential $U_{\mathrm{acc}}^{\mathrm{tot}}$. The other two electrodes are supplied with a voltage divider made of a series of three 100 MΩ resistors connected to ground potential. The electrodes thus are supplied with 2/3 and 1/3 of $U_{\mathrm{acc}}^{\mathrm{tot}}$, as it is illustrated in Fig. 5.1. This stepwise post-acceleration prevents the beam from being decollimated due to inhomogeneous fields (see Ref. [Bab14]).

### 5.1.3 Dipole electrodes

As positive charged ions from the WGTS are magnetically guided through the hole of the rear wall towards the electron gun they would be accelerated in the electrostatic field of the electrode system to kinetic energies of $-qU_{\mathrm{em}}^{\mathrm{tot}}$. If these high energetic ions impinge on the golden photocathode they could reduce the thickness of the gold layer due to sputtering. In order to avoid this degradation of the gold layer, a pair of dipole electrodes is placed inside the e-gun chamber. The dipole electrodes generate an electric field perpendicular to the magnetic field lines and thus drift out the ions by $\vec{E} \times \vec{B}$ drift (see e.g. Ref. [BMW85]). The two dipoles, which are located along the east and west side of the beam line, are set to 200 V and −200 V, respectively. The distance of the electrodes is 4 cm, which results in an electric field of 10 kV m$^{-1}$. As the electric field does not only influence the trajectory of the ions but also of the electron beam, the drift of the beam must be compensated by magnetic steering coils.

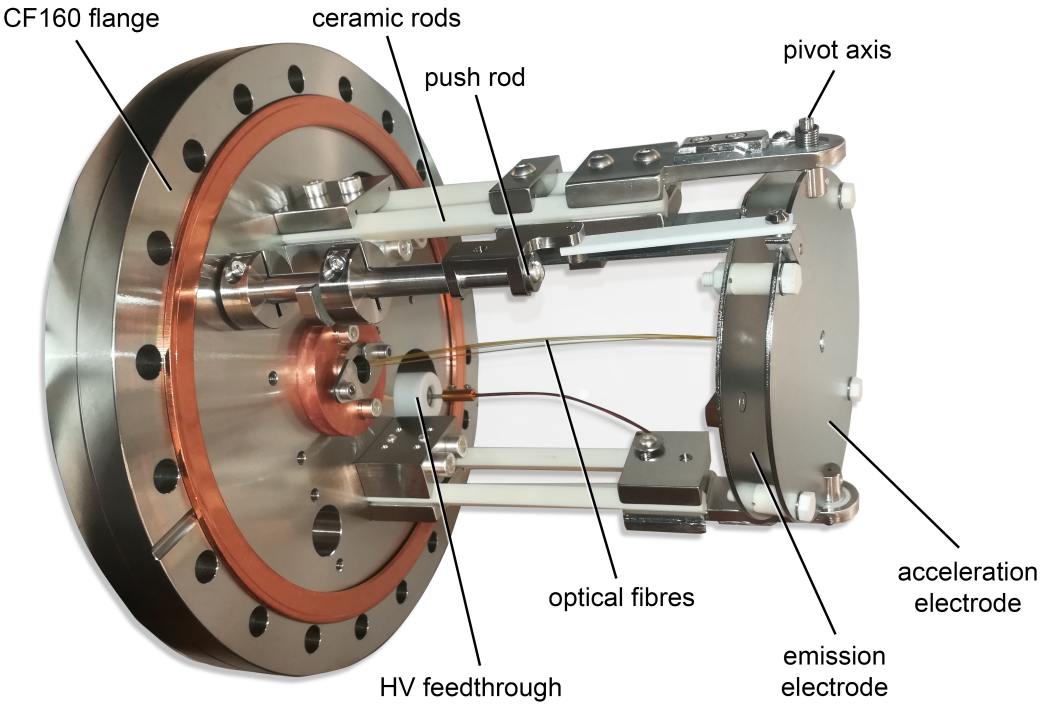


Figure 5.2: Assembly of the photoelectron source on a CF160 flange. By using a pair of lenses (not included in the picture), UV light is coupled into one of the seven fibres installed behind a CF16 window located at the centre of the CF160 flange. The gold-coated ends of the fibres is installed at the back plate (emission electrode) of the plate capacitor, where the photoelectrons are being generated. For a collimation of the beam, the front plate (acceleration electrode) is at an approximately 4 kV more positive potential. The collimated beam of photoelectrons leaves the acceleration electrode through a 6 mm wide hole. The entire plate capacitor can be tilted with a push rod along a pivot axis located at the acceleration electrode. The plate capacitor assembly is hold by ceramic rods on both sides, which allow the system to be operate at a maximum voltage of 21 kV, which is supplied from the outside with HV vacuum feedthroughs (the second feedthrough is hidden by the upper two ceramic rods).

### 5.1.4 High-voltage supply

The high-voltage system of the electron gun uses the high-voltage supply of the main spectrometer vessel as its primary voltage source. The benefit of connecting the high-voltage system directly to the main spectrometer vessel potential $U_{\mathrm{MS}}$ is that no significant high-voltage fluctuations or drifts in between the acceleration potential and the vessel potential can occur. Thus, the energy stability is only influenced by the stability of the inner electrode offset voltage $U_{\mathrm{ie}}$ and the emission electrode voltage $U_{\mathrm{em}}$, which are monitored with a 6 1/2-digit volt meter.

In order to perform measurements with the electron beam, it is essential to adjust both $U_{\mathrm{em}}^{\mathrm{tot}}$ and $U_{\mathrm{acc}}^{\mathrm{tot}}$. Therefore, two additional voltage supplies (ISEG DPr 05[1] and ISEG DPr 60) are required. The two voltage supplies are installed inside a high-voltage cage, with the inside being grounded to the main spectrometer vessel potential. The electronic devices inside the HV cage are supplied with a galvanically isolated transformer from outside (see Fig. 5.1).

The offset voltage $U_{\mathrm{em}}$ from the ISEG DPr 05 is connected to the emission electrode, and the offset voltage $U_{\mathrm{acc}}$ from the ISEG DPr 60 is connected to the acceleration electrode as well as the post-acceleration system. As the output voltages of the supplies add to the main spectrometer potential $U_{\mathrm{MS}}$, the total voltages are

$$\begin{aligned} U_{\mathrm{em}}^{\mathrm{tot}} &= U_{\mathrm{MS}} + U_{\mathrm{em}} \\ U_{\mathrm{acc}}^{\mathrm{tot}} &= U_{\mathrm{MS}} + U_{\mathrm{acc}} \,. \end{aligned} \tag{5.1}$$

The offset voltage $U_{\mathrm{em}}$ is constantly monitored with a 6 1/2-digit digital voltmeter[2], which allows one to measure the applied offset voltage with an accuracy of 1 mV in the 1000 V measurement range.

Since the vessel voltage $U_{\mathrm{MS}}$ is not the final retarding potential of the spectrometer, but an additional offset of $U_{\mathrm{ie}} = -200\,\mathrm{V}$ is applied to the inner electrode system, the resulting retarding potential is $U_{\mathrm{ret}} = U_{\mathrm{MS}} + U_{\mathrm{ie}}$. An offset potential $\Delta U_{\mathrm{r}} > 0\,\mathrm{V}$ due to the influence of the ground potential of the beam tubes connected to the main spectrometer has to be considered, which increases with the distance to the inner electrode system (see Ref. [Gro15]). A further offset $\Delta\Phi = \Phi_{\mathrm{em}} - \Phi_{\mathrm{MS}}$ exists due to the work function differences of the golden photocathode $\Phi_{\mathrm{em}} = 4.44\,\mathrm{eV}$ [Sac20] and the work function of the stainless steel surface of the main spectrometer[3] $\Phi_{\mathrm{MS}} = 3.56(4)\,\mathrm{eV}$ [Beh17].

The surplus energy of the electrons with respect to the filter potential is thus

$$E_{\mathrm{s}} = q \cdot (U_{\mathrm{em}} - U_{\mathrm{ie}} - \Delta U_{\mathrm{r}}) + \Delta\Phi \,. \tag{5.2}$$

The stability of the surplus energy is thus limited by the stability of the emission electrode voltage and the inner electrode voltage. Even though the inner electrode voltage is drifting by a factor of about $10^{-4}$, the absolute uncertainty on $E_{\mathrm{s}}$ is defined only by the monitoring precision of $U_{\mathrm{em}}$ and $U_{\mathrm{ie}}$. Thus a stability of $<10\,\mathrm{meV}$ is achieved, as further discussed in Sec. 7.2. With the ISEG DPr 05 voltage supply, the surplus energy is currently limited to $E_{\mathrm{s}}^{\mathrm{max}} < 300\,\mathrm{V}$. If larger surplus voltages are required, a manually-controlled standalone HV supply[4] can be used instead of connecting the HV cage to the main-spectrometer

[1] Upgrade to ISEG DPr 10 is planned
[2] Fluke 8846A
[3] The value of $\Phi_{\mathrm{MS}} = 3.56(4)\,\mathrm{eV}$ was determined in 2016. Since the main spectrometer has been baked out several times, the work function might have changed slightly.
[4] FuG HCN 700-20000

voltage. However, the usage of the external voltage supply reduces the energy stability, as the supply voltage is not monitored and the device has a resolution of only 10 V.

The overall high-voltage concept is visualised as a schematic drawing in Fig. 5.1.

### 5.1.5 Magnet setup

Besides the 4.7 T strong superconduction rear section magnet, the electron gun consists of a total of 13 normal-conducting magnet coils. Five of them are solenoid coils, which are required to generate a magnetic field along the 3 m setup in order to guide the electron beam towards the WGTS. The coils generate a nominal magnetic field of $B_{\mathrm{egun}} = 25\,\mathrm{mT}$ at the position of the emission electrode. Each coil is supplied with a power supply of type TDK Lambda Genesys 40-85 providing currents up to 85 A at 40 V.

The other eight coils are dipole coils (called steering coils x/y and compensation coils x/y), which are used to manipulate the axial magnetic field of the solenoids. This allows one to simultaneously move the electron beam in x and y direction, which is required to steer the beam through the off-axis orifice at the end of the e-gun chamber and to guide the beam back to the beam axis in order to pass the hole in the rear wall. The ability to adjust the beam position is essential, as the $\vec{E} \times \vec{B}$ drift inside the electric dipole electrodes is dependent on the kinetic energy of the electrons and thus needs to be compensated with the dipole coils to ensure no geometric obstruction of the beam. The coils are supplied with bipolar power supplies of type CAENels FAST-PS 1040-400 providing currents up to $\pm 10\,\mathrm{A}$ at $\pm 40\,\mathrm{V}$, which allow the beam to be steered in both positive as well as negative x and y direction.

## 5.2 Optical setup

In order to emit photoelectrons from the golden cathode, ultraviolet light with photon energies above the work function of the golden cathode ($\Phi_{\mathrm{em}} = 4.44\,\mathrm{eV}$ [Sac20]) is required. For this purpose, an optical setup is used, which consists of two different light sources as well as an intensity monitoring system. A schematic drawing of the optical setup is provided in Fig. 5.3. The primary light source of the setup is a Laser-Driven Light Source[5] (LDLS), the secondary light source is a pulsed UV laser[6] with a wavelength of 266 nm. The light sources are installed in a mobile optical enclosure outside the second containment of the rear section. In order to guide the light output to the photoelectron source, the light sources are coupled to optical fibres with a 400 µm core diameter[7]. A fibre splitter[8] with a similar core diameter and a splitting ratio of 90/10 is installed inside the second containment. This splitter is used for a real-time monitoring of the light intensity by a Si-photodiode[9] at the side of the 10 % channel. The photodiode is temperature stabilised with a thermoelectric cooler[10], which is integrated in the diode and controlled from the outside of the second containment. The diode is directly coupled to a transimpedance amplifier[11] with variable gain reaching from $1 \times 10^3\,\mathrm{V\,A^{-1}}$ to $1 \times 10^9\,\mathrm{V\,A^{-1}}$. This voltage signal is recorded with an ADC every second and is then written to the KATRIN database. The 90 % channel of the fibre splitter is connected to a pair of lenses, in order to couple the light into the fibres of the electron gun inside the vacuum system, which are accessible through a fused silica window (see Ref. [Sch16]).

The performance of the two available light sources is characterised in the following.

[5] Energetiq EQ-99XFC LDLS
[6] InnoLas Mosquitoo
[7] Gulf Photonics UV/SR (190 nm to 1100 nm NA=0.22)
[8] FONT Canada FMMC-400-FC-AL (200 nm to 300 nm)
[9] Hamamatsu S2592
[10] Hamamatsu C1103-04
[11] FEMTO DLPCA-200

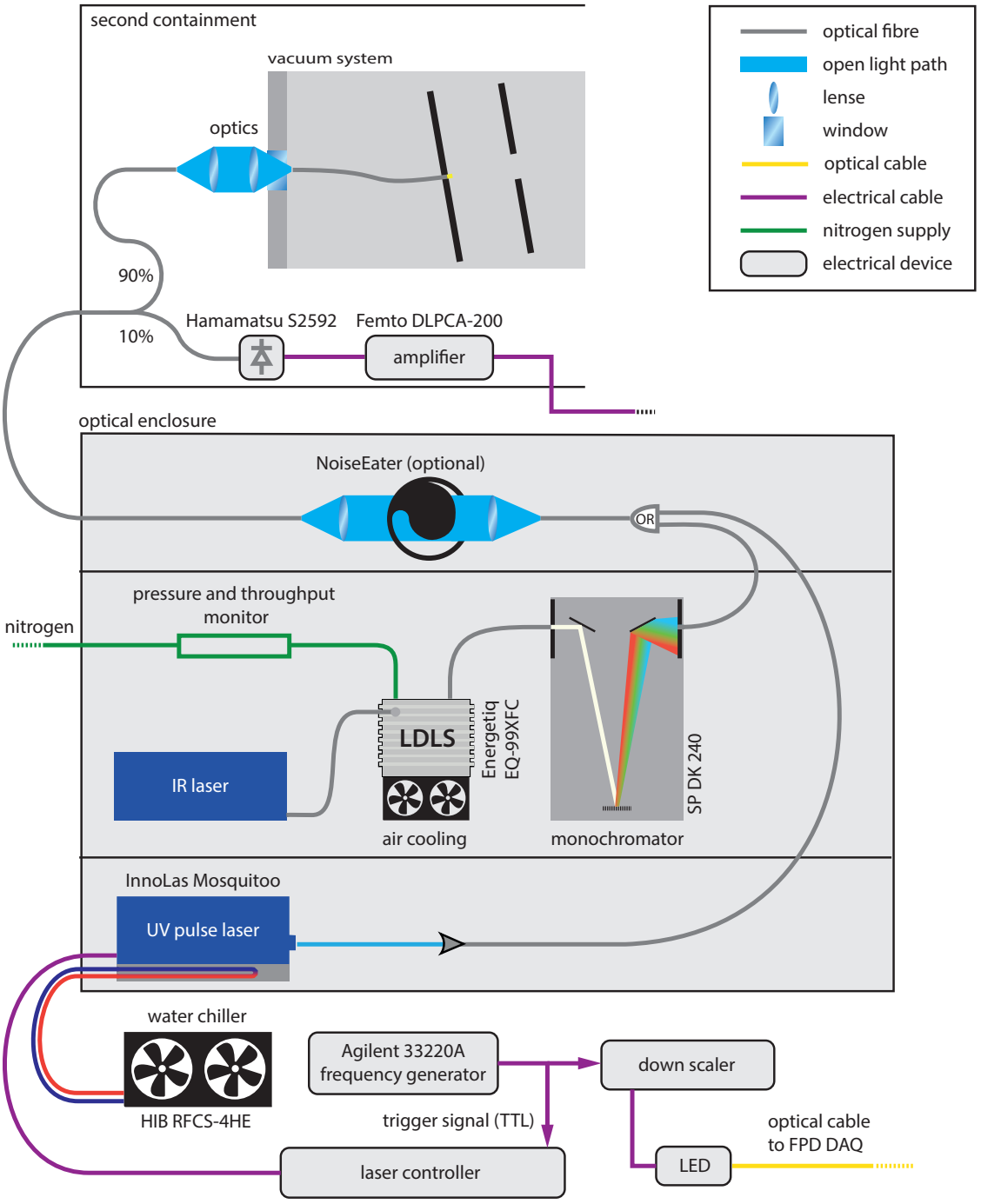


Figure 5.3: Schematic drawing of the optical setup of the rear section electron gun. The primary light source is a Laser-Driven Light Source (LDLS), which generates light with a spectral range of 170 nm to 2100 nm. Therefore, a monochromator is required to select the desired wavelength in the UV region. The secondary light source is a pulsed UV laser with a fixed wavelength of 266 nm. The laser can be triggered externally, which allows one to synchronise the pulses with the FPD. An optional stabilisation of the light intensity is possible with the so-called NoiseEater, which is a PI-controlled circular aperture. The light is coupled into the photoelectron source from the outside of the vacuum system with lenses. The intensity of the light is continuously monitored with a photodiode mounted to the 10 % channel of a fibre splitter, which is installed just in front of the photoelectron source.

### 5.2.1 Laser-Driven Light Source

The key component of the Laser-Driven Light Source is a xenon bulb, where a plasma is electrically ignited between two electrodes. After the ignition, the plasma is constantly heated by an infrared continuous wave laser. According to the data sheet[12], the plasma bulb emits light of a continuous spectrum in the range of 190 nm to 2100 nm, with a rather flat spectral power curve reaching from $10\,\mu W\,nm^{-1}$ in the UV region to $110\,\mu W\,nm^{-1}$ in the IR region. As only ultraviolet light with a narrow bandwidth is required to generate the photoelectrons, the light is coupled into an Czerny-Turner monochromator[13] with optical fibres, before guiding the light towards the photoelectron source. The monochromator enables to select the light with a variable bandwidth up to 10 nm. For the measurements, a wavelength of 250 nm at a band width of 10 nm is chosen, since this setting has the highest electron yield (see Ref. [Sac20]). At this setting, the optical power arriving at the electron gun is approximately 50 nW. Due to the emission of (far) ultraviolet light (<240 nm), ozone can be generated from the oxygen in the ambient air inside the bulb housing. The generation of ozone must be avoided, since it is a flammable gas and harmful to health. Besides these safety risks, ozone absorbs ultraviolet light and thus reduces the light yield of the lamp. Hence, the bulb is constantly purged with nitrogen at a pressure of 20 psig, which results in a throughput of 1 slm. The light yield of the lamp is not only dependent on the ozone concentration inside the housing but also on the bulb temperature. The lamp-housing temperature-coefficient[14] is $0.3\,\%\,K^{-1}$, which can strongly influence the light intensity stability. In order to avoid instabilities of the light intensity due to the temperature dependence, the light source is temperature stabilised with a thermoelectric cooler[15] to a temperature setpoint of 25 °C.

#### Performance

As one of the main purposes of the electron gun is the periodic determination of the column density with a precision of 0.1 %, the rate of the electron gun and thus the intensity of the light source has to be stable on the same level over several hours [Bab14].

After the experimental setup was assembled, dedicated stability measurements were performed to determine both the short-term stability as well as the long-term stability of the system. The stability measurements in Fig. 5.4 show that light-intensity drifts occur, which exceed the requirements by more than one order of magnitude. In order to derive the achievable stability as a function of the time gap $\Delta t$ between measurements, the average intensity $\bar{I}$ within a time frame of 0.5 h is calculated and compared to the mean of an 0.5 h sample at a distance of $\Delta t$. The time scale is chosen to be 0.5 h, as this is a common time scale for measurements being performed with the electron gun. The maximum values of the distributions of the obtained differences $\bar{I}(t_i) - \bar{I}(t_i + \Delta t)$ is displayed in Fig. 5.4. It shows that even for a short time span of 1 h between two samples, the stability is 0.8 % and thus a factor of eight above the requirements of 0.1 %. The stability reaches a rather constant level of 2.5 % to 3 % for samples with more than 10 h in between. Thus, the reproducibility of measurements with a stability of 0.1 % cannot be guaranteed with the optical setup without further optimisations.

[12] `https://www.energetiq.com/hubfs/Data%20Sheets_May%201_205%20Lowell%20Street/EQ99XFC-Data-Sheet_April%202019.pdf` accessed 2021/3/2 4:20 pm
[13] Spectral Products DK240
[14] `https://www.energetiq.com/hubfs/Energetiq_March2019/PDF/Energetiq-LDLS-FAQs.pdf?hsLang=en` accessed 2021/3/2 4:27 pm
[15] Arroyo 5300 TECSource

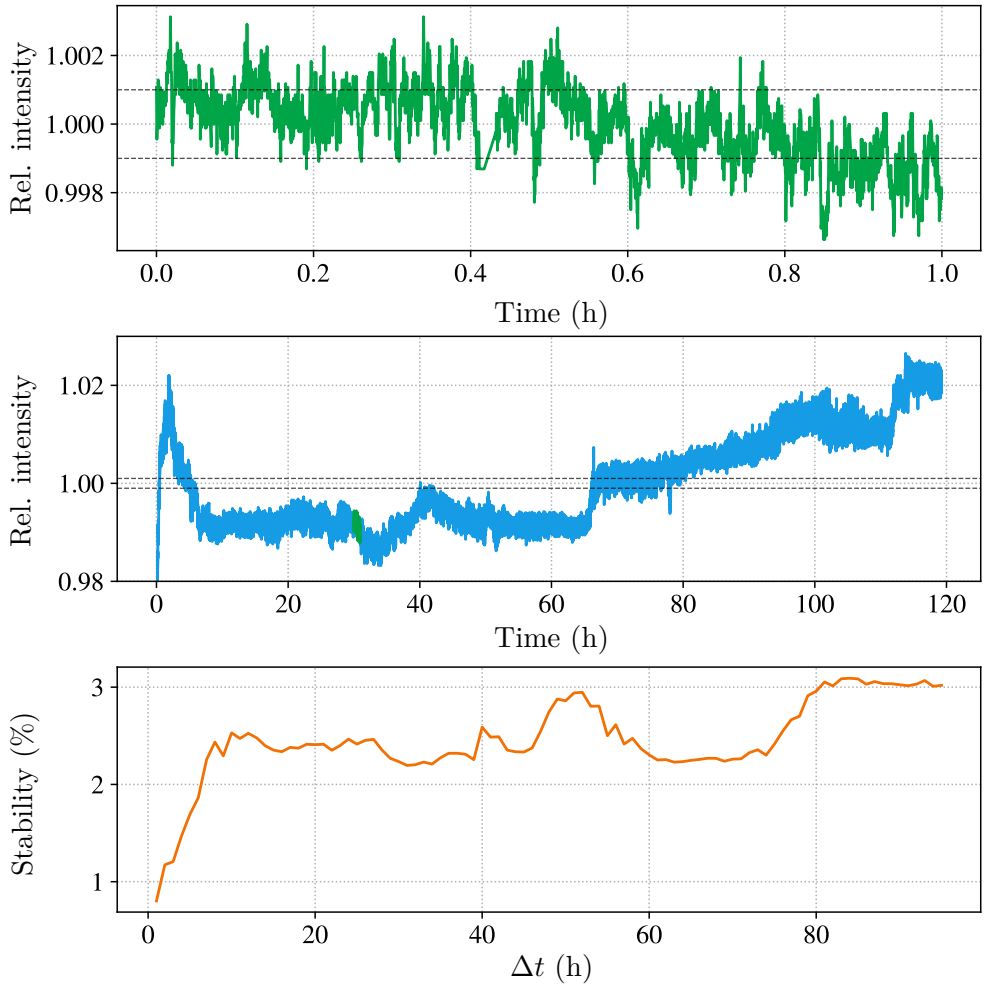


Figure 5.4: **Top/Middle:** Intensity stability of the LDLS (selecting light of 250 nm with 10 nm bandwidth) as monitored with the setup at the rear section for 1 h and 120 h measurement time. The curves show the relative deviation to the average diode signal of 0.92 V and 0.93 V (with an amplification of $10^9$ V $A^{-1}$), respectively. Even on short time scales below 1 h, intensity fluctuations in the order of 0.3 % are visible. Random drifts with a peak-to-peak value of approximately 4 % exist on the time scale of days. The dashed lines indicate the required 0.1 % stability level.
**Bottom:** Intensity difference for the averaged intensity value of two 0.5 h samples as a function of the time difference $\Delta t$ between the samples. The best stability of 0.8 % is achieved for $\Delta t \leq 1$ h. For the time span of several days, a stability of only 3 % can be achieved. The warm-up time of 1 h was excluded from this analysis.

**Active intensity stabilisation**

In order to reach a higher long-term stability of the light intensity, a custom active regulation system was added to the setup. The so-called NoiseEater[16] consists of a motorised circular aperture (comp. Fig. 5.3), which is regulated by a proportional integral (PI) controller using the intensity information from a photodiode. In order to guide the light through the circular aperture, two lenses[17] are required to collimate the light from the end of the incident fibres and to focus it back into the fibre, which guides the light towards the electron gun. The entire setup of the NoiseEater has a coupling efficiency of approximately 55 %.

In order to determine the optimal parameter settings of the regulator and the resulting light stability, test measurements were carried out.

For the test setup, a fibre splitter[18] was installed between the monochromator and the NoiseEater, which allowed both the unstabilised light output of the LDLS and the stabilised light output of the NoiseEater to be monitored. A Hamamatsu S1226-5BQ photodiode with a Keithley 6487 picoamperemeter was connected to the 20 % channel and the NoiseEater was connected to the 80 % channel. The stabilised light output of the NoiseEater was monitored with a Hamamatsu S2592 photodiode and the Femto DLPCA-200 amplifier.

From the measurements, the optimal regulator settings $P_{\mathrm{reg}} = 7416$, $I_{\mathrm{reg}} = 45\,478$, and the regulation frequency of 33.3 Hz were determined. With these settings, the NoiseEater stabilises the light output with a Gaussian uncertainty of 0.03 %, as it is shown in Fig. 5.5. Integrating the NoiseEater into the optical setup thus allows one to perform measurements with the electron gun generating a stable beam of electrons with reproducible rates.

### 5.2.2 UV pulse laser

In addition ot the LDLS, a pulsed UV laser is permanently included in the optical setup of the rear section. The laser is a frequency quadrupled $\mathrm{Nd:YVO_4}$ (1064 nm) DPSS laser of 266 nm wavelength. The pulse frequency of the laser $f_{\mathrm{P}}$ can be set to variable values in the range of 20 kHz to 100 kHz which produces light pulses with <18 ns (FWHM) pulse length. The current $I_{\mathrm{D}}$ of the pumping diode can be set in the range of 6 A to 8 A, which allows one to adjust the intensity of the laser. The intensity commonly increases with the diode current, except for the 20 kHz setting, where an intensity maximum is reached at 7 A. The laser diode is water cooled with an external cooler[19] and stabilised to a temperature of 25.00(1) °C.

The laser pulses can be either triggered internally or externally by providing a 5 V trigger signal from a function generator. When triggering the laser externally, it is possible to synchronise the light pulses with the DAQ of the FPD. For this purpose, a plastic optical fibre is installed between the rear section and the detector DAQ (card 12, channel 4) and a LED is connected in parallel to the trigger signal from the function generator. A downscaler is used in order to reduce the trigger rate, which is sent to the detector. The downscaler provides scaling ratios of 16, 128, and 1024, with the latter being the default setting during the measurements. Thus, the trigger rate sent to the detector is commonly below 100 Hz. As the timing jitter of the trigger signal from the external frequency generator is only 300 ps, an interpolation between the trigger signal of reduced frequency can be performed.

By coupling the pulsed UV laser to the photoelectron source, the electron gun can be operated in pulsed mode. Due to the time synchronisation of the trigger signal with the

[16] Developed by TEM Messtechnik

[17] Edmund optics #46-255 $d = 6$ mm $f = 9$ mm FL UV-AR Coated, UV Plano-Convex Lens

[18] In this measurement, a 80/20 splitter of FONT Canada was used. Apart from the different splitting ratio, the the splitter is identical to the 90/10 fibre splitter, which is installed in the second containment.

[19] H.I.B. Systemtechnik RFCS-4HE

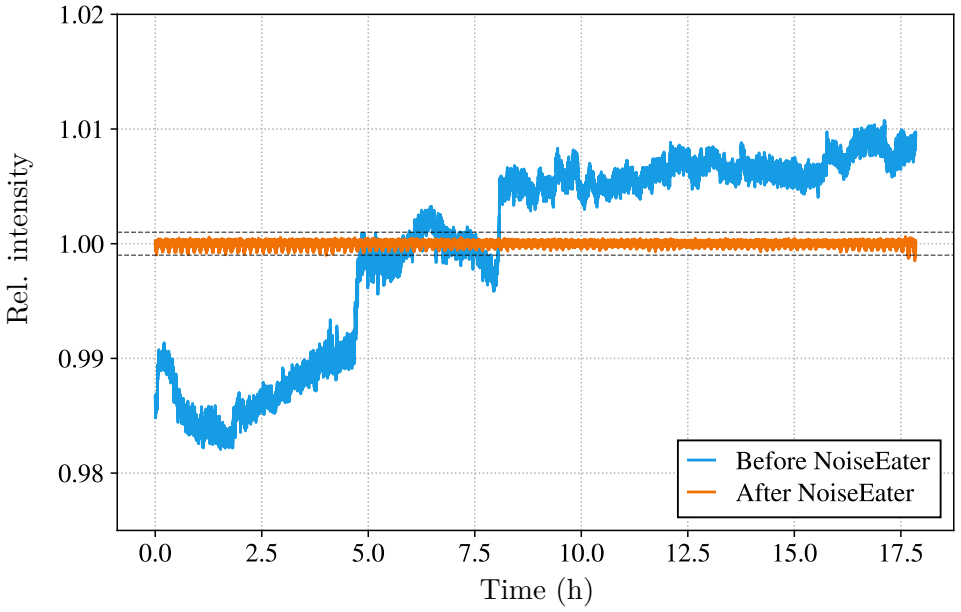


Figure 5.5: Simultaneous measurement of the unstabilised light intensity of the LDLS and the stabilised light intensity by using the NoiseEater. In contrast to the unstabilised light output of the LDLS, the intensity-stabilised light output shows no long-term drift and has a Gaussian uncertainty of only 0.03 %.

detector, the measurement of the time-of-flight of the electrons is possible. The time-of-flight mode is essential for the measurement of the energy-loss function in differential mode (see Sec. 7.3.3.1), which is described in detail in Refs. [Sac20, Rod].

#### Performance

Similar to the stability investigations for the LDLS, the performance of the UV laser was investigated.

The intensity monitoring of the UV laser (internally triggered, $f_{\mathrm{P}} = 100\,\mathrm{kHz}$, $I_{\mathrm{D}} = 8\,\mathrm{A}$) shows a periodical modulation of the light intensity with a period time of approximately 73 s, as it is visible in the Fourier spectrum in Fig. A.5. A reason for this could be the temperature stabilisation, although the laser diode temperature is stable within 10 mK. In addition to the periodic short-term fluctuations, random drifts on the timescales of several hours are visible in Fig. 5.6. Again, the stability as a function of the time is investigated, by comparing the average intensity of a 0.5 h sample to the average intensity of another sample at a variable time difference between the samples. For a time span of 1 h between the samples, a maximum uncertainty of 4.3 % is obtained, which rises up to 8 % to 12 % for time differences of several days (see bottom panel of Fig. 5.6). In order to use the laser for precision measurements, either an active stabilisation similar to the stabilisation of the LDLS or a correction of the light intensity during the analysis of the measurement data is required. The method of light intensity correction of the measurement data is explained in Sec. 5.3.2.

## 5.3 Properties of the electron beam

The four characteristic properties of the electron beam provided by the rear section electron gun are the width of the energy distribution $\sigma_{\mathrm{E}}$, the angular spread $\sigma_{\mathrm{A}}$ as well as the rate $R_{\mathrm{e-gun}}$ and the corresponding rate stability $\sigma_R$.

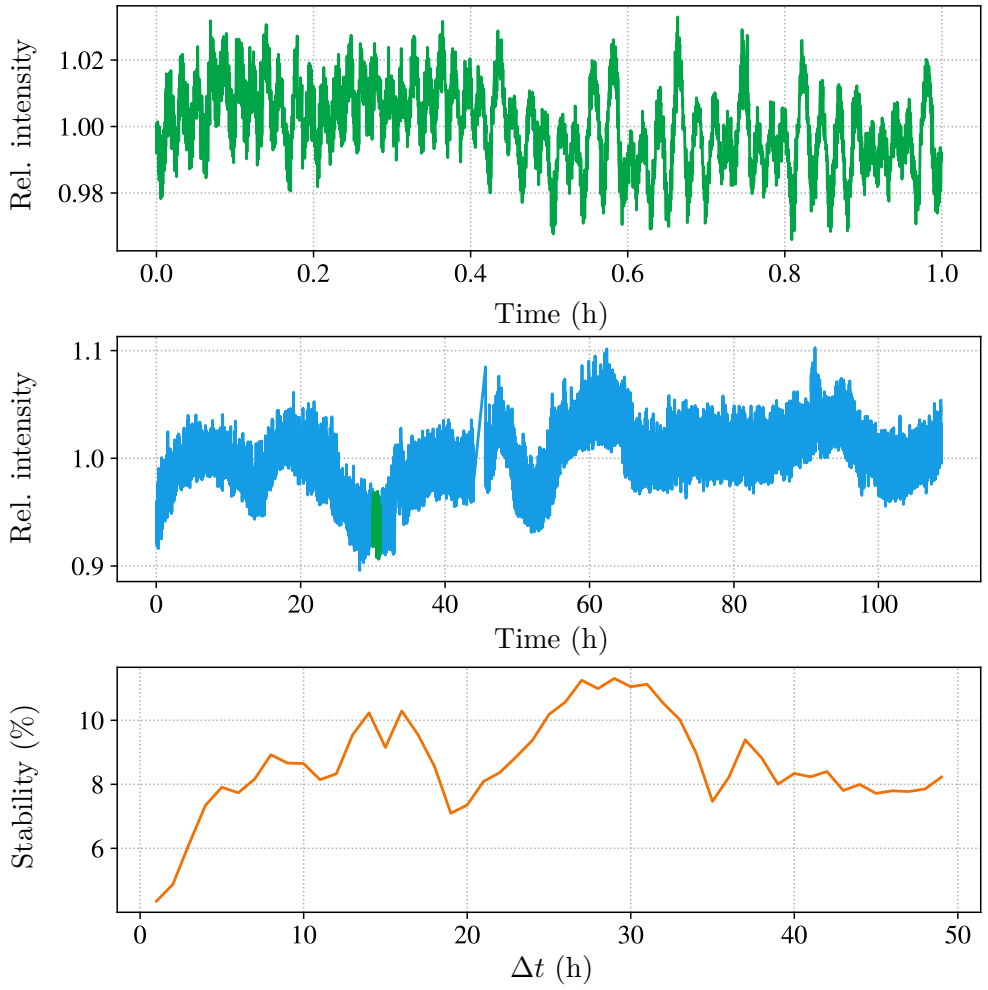


Figure 5.6: **Top/Middle:** Intensity stability of the UV laser as monitored with the setup at the rear section for a time of 1 h and 110 h. The curves show the relative deviation to the average diode signal of 0.53 V and 0.56 V (with an amplification of $10^8\,\mathrm{V\,A^{-1}}$), respectively. Long-term drifts as well as periodic short-term fluctuations are visible.
**Bottom:** Intensity difference for the averaged intensity value of two 0.5 h samples as a function of the time difference $\Delta t$ between the samples. The best stability of 4.3 % is achieved for $\Delta t \leq 1$ h. For the time span of several days, a stability of only 8 % to 12 % can be achieved. The warm-up time of 1 h was excluded from this analysis.

The design goal is to generate an electron beam with an energy distribution $\sigma_{\mathrm{E}} < 200\,\mathrm{meV}$ and an angular spread of $\sigma_{\mathrm{A}} \approx 0.7°$ (at $\theta = 0°$), defined at $B = 3.6\,\mathrm{T}$ [Bab14].

However, these design values are based on calculations and simulations (see Refs. [Bab14, Sch16]) as well as test measurements with a prototype system described in Refs. [BRB+17, Beh17]. For a full characterisation of the rear section electron gun, it is thus important to determine the energy resolution, the angular spread, and the electron rate from measurements with the final setup. The determination of these properties is discussed in the following.

### 5.3.1 Transmission function of the electron gun

The transmission function of the electron gun, as measured with the MAC-E filter, deviates from a perfect step function, as both the energy distribution and the angular spread are non-vanishing. Due to the strong collimation of the beam at the analysing plane of the main spectrometer, the energy distribution of the electron beam dominates the shape of the transmission function. For the angular spread as discussed later in this section, the angular distribution contributes with less than 20 meV to the energy resolution, which is about 10% of the nominal energy distribution. The initial energy distribution is a property of the photoelectric effect and is based on the energy distribution of the electrons in the conduction band of the metallic cathode. This shape of the energy distribution can be derived in the model of the free electron gas in three dimensions (see e.g. Ref. [Kit05]). In this theory, the density of states is given by

$$D(E) = \frac{L^3}{4\pi^2} \left( \frac{2m}{\hbar^2} \right)^{\frac{3}{2}} \cdot E^{\frac{1}{2}} \tag{5.3}$$

where $L$ is the length of the simplified potential cube, which confines the electrons in the lattice [Kit05].

The probability that the states are occupied by an electron is described by the Fermi-Dirac distribution

$$F(E,T) = \frac{1}{\exp\left(\frac{E-E_{\mathrm{F}}}{k_B T}\right) + 1} \tag{5.4}$$

where $E_{\mathrm{F}}$ is the Fermi energy, $k_B$ the Boltzmann constant, and $T$ the temperature of the metal. The actual electron population density $n(E)$ in the conduction band is thus given as the product

$$n(E,T) = D(E) \cdot F(E,T) \tag{5.5}$$

and follows the form as illustrated in Fig. 5.7 [Kit05].

Neglecting the smearing of the Fermi-Dirac distribution at non-zero temperatures, a minimum photon energy of $h\nu > E_{\mathrm{vac}} - E_{\mathrm{F}} = \Phi$ is required to emit an electron from the conduction band. The vacuum level $E_{\mathrm{vac}}$ is defined as the energy of an electron at rest outside the surface of the solid (see e.g. Ref. [CK03]). Thus, $\Phi$ is the work function of the material.

With photon energies $h\nu > \Phi$, it is possible to emit even electrons from states below the Fermi energy. The resulting energy distribution of the emitted electrons thus follows the shape of

$$\eta(E,T) = n(E + (E_{\mathrm{vac}} - h\nu), T)\Theta(E)\,. \tag{5.6}$$

The shape of the initial energy distribution is not affected by the acceleration of the electrons inside the electrostatic fields of the electron gun, which results in an electron beam following the shape of the initial energy distribution.

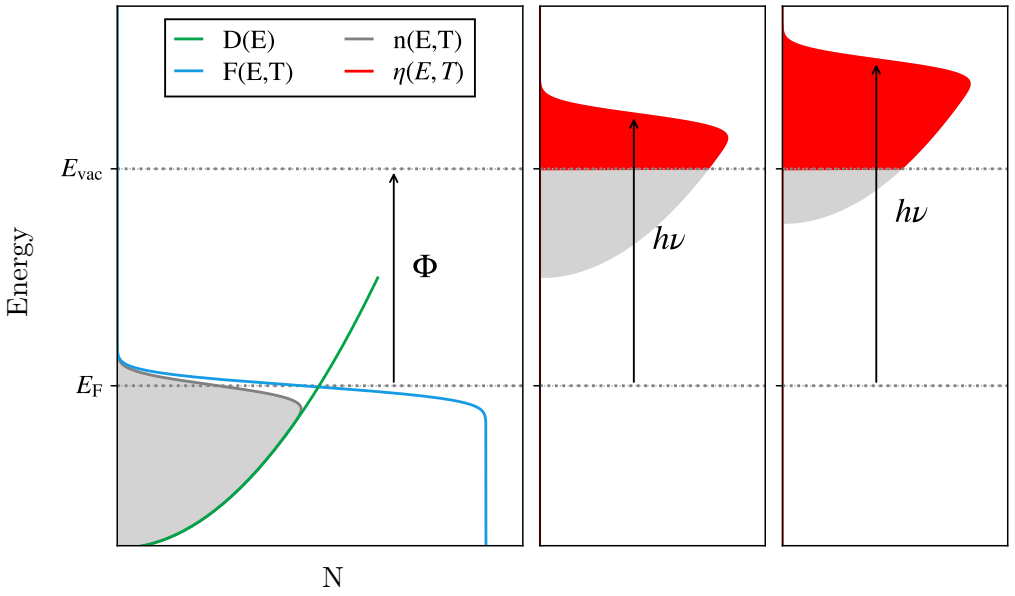


Figure 5.7: **Left:** Electron population distribution $n(E)$ of a free electron gas. The distribution is the product of the density of states $D(E)$ and the Fermi-Dirac distribution $F(E,T)$. The difference between the Fermi level $E_F$ and the vacuum energy $E_{vac}$ is the work function $\Phi$.
**Right:** Depending on the photon energy $h\nu$, electrons from the conduction band can be excited above $E_{vac}$ and are thus considered free with an initial kinetic energy distribution $\eta(E)$.

As this derivation of the energy distribution neglects all other effects, such as the scattering of the electrons in the bulk material, it is less suitable for the actual description of the energy distribution as obtained in the experiment. As discussed in Ref. [Beh17], the resulting energy distribution $\eta(E)$ can be empirically described by a generalised Gaussian with additional shape parameter $\zeta$.

The angular distribution of the emitted electrons follows a cosine distribution [PB02], which results in a non vanishing angular distribution $a(\theta)$ even after the non-adiabatic acceleration inside the plate capacitor of the photoelectron source.

For the case of an angular-selective source, the transmission function of the MAC-E filter, as derived in Eq. (3.11), has to be modified, as one has to integrate over the actual angular distribution of the beam and not an isotropic distribution. Furthermore, an integration over $\eta(E', T)$ is required, in order to take the energy distribution from Eq. (5.6) into account. The shape of the transmission function becomes

$$T_\mathrm{e}(U_\mathrm{ret}, E_\mathrm{s}) = \int_{-E_\mathrm{s}}^{\infty} \eta(E') \int_0^{\theta_\mathrm{max}(|E'|+qU_\mathrm{ret})} a(\theta)\mathrm{d}\theta\mathrm{d}E' \,. \tag{5.7}$$

**Measurement of the transmission function**

Measurements of the transmission functions were also carried out by R. Sack in Ref. [Sac20]. However, in the analysis of R. Sack, the width of the transmission function and the resulting energy distribution was determined while neglecting the contribution of the angular distribution. In the following, the shape of the transmission function will be analysed by considering the contribution of the angular distribution of the electron beam, which allows for a more precise determination of the energy distribution of the photoelectrons. In order to investigate the shape properties of the transmission function, a rate measurement at different surplus energies around $E_\mathrm{s} = 0\,\mathrm{eV}$ were performed. Two examples of transmission function scans for both light sources, are provided in Fig. 5.8. The scans were performed at an electron energy of 18.6 keV with a magnetic field setting of $B_\mathrm{A} = 2.7\,\mathrm{G}$ in the analysing plane and an initial pitch angle of approximately 0°. A fit to the transmission function is performed using the detailed transmission function model of Eq. (5.7) as well as a simple error function fit for comparison. For the construction of the former, the Peaberry python module (see Ref. [Beh17]) is used, which is included in the Kasper analysis framework. The Peaberry transmission function model consists of nine free parameters including the nuisance parameter for the background amplitude, the edge position, and the magnetic field in the analysing plane. The observables are the position $\mu_\mathrm{LDLS/laser}$, the width $\tilde{\sigma}_\mathrm{LDLS/laser}$, and the shape parameter $\zeta_\mathrm{LDLS/laser}$ of the energy distribution as well as the position $\mu_\mathrm{A}$ and width $\sigma_\mathrm{A}$ of the angular distribution. However, the simultaneous determination of the angular distribution and the energy distribution from only one transmission function can be ambiguous. Thus, a pull term is included into the fit constraining the width of the angular distribution to a value of 0.635(15)° (at 42 mT)[20]. This value was provided by F. Block (Karlsruhe Institute of Technology) [Blo] and was determined from field mapping measurements, where a large number of transmission functions were measured at different pitch angles in order to determine the magnetic fields in the analysing plane. The large number of transmission functions at different angles allows one to determine the angular distribution with higher precision than from one single fit.

In the case of the transmission function measured with the LDLS (250 nm with 10 nm bandwidth), the Peaberry model fit gives a fit result with $\chi^2/N_\mathrm{dof} = 1.23(20)$. From the

[20] In order to compare the obtained angular spreads to the simulation results of Ref. [Bab14], the result needs to be converted to a magnetic field of 3.6 T, taking into account the adiabatic transformation of the momentum (comp. Sec. 3.1.1). The obtained value of 5.9° is about a factor of eight larger than the expected value of 0.7°.

best fit result, the values of the five shape parameters of the energy distribution and the angular distribution

$$\begin{aligned} \mu_{\mathrm{LDLS}} &= 0.267(3)\,\mathrm{eV} \\ \tilde{\sigma}_{\mathrm{LDLS}} &= 0.166(3)\,\mathrm{eV} \\ \zeta_{\mathrm{LDLS}} &= 0.138(17) \\ \mu_{\mathrm{A}} &= 0.00(3)^\circ \\ \sigma_{\mathrm{A}} &= 0.64(2)^\circ \end{aligned} \tag{5.8}$$

are obtained. As it can be seen in the top right panel of Fig. 5.8, the energy distribution is slightly asymmetric and cut off, as it is expected from Fig. 5.7. The width of the angular distribution is defined at a source magnetic field of 42 mT, which corresponds to the magnetic field at the rear section right after the post-acceleration electrodes at $z = -50.91\,\mathrm{m}$.

The same analysis is repeated for a transmission function measurement using the UV laser. Unfortunately, the transmission function measurements using the pulsed UV laser are much more affected by noise than the measurements with the LDLS, which is due to the reduced light stability as well as due to the existence of detector pile-up (see Chap. 6). In this case, the best fit values

$$\begin{aligned} \mu_{\mathrm{laser}} &= 0.253(2)\,\mathrm{eV} \\ \tilde{\sigma}_{\mathrm{laser}} &= 0.081(5)\,\mathrm{eV} \\ \zeta_{\mathrm{laser}} &= -0.076(50) \\ \mu_{\mathrm{A}} &= 0.0(2)^\circ \\ \sigma_{\mathrm{A}} &= 0.65(7)^\circ \end{aligned} \tag{5.9}$$

are obtained at $\chi^2/N_{\mathrm{dof}} = 23.71(24)$, with the results being shown in the bottom row of Fig. 5.8. It can be seen, that the width of the energy distribution of the electrons generated with the UV laser is about a factor of two smaller as for the LDLS. This is related to the larger wavelength of 266 nm[21], which is closer to the work function of $\Phi_{\mathrm{em}} = 4.44\,\mathrm{eV}$ of the golden photocathode (compare Fig. 5.7). Furthermore, the light of the laser is monoenergetic compared to the 10 nm broad bandwidth of the LDLS (after the monochromator), which broadens the shape of the energy spectrum. Thus, the energy distribution of the electron beam generated with the UV laser can be approximated by a Gaussian, not only since the shape parameter $\zeta$ is over a factor of four times smaller but also because a smaller fraction of the low energy tail of the distribution is cut off at 0 eV.

In addition to the Peaberry fits a simple error function fit is performed to both datasets. The error function

$$\begin{aligned} T_{\mathrm{erf}}(E_{\mathrm{s}}, A, \mu_{\mathrm{erf}}, \sigma_{\mathrm{erf}}, A_{\mathrm{bg}}) &= \frac{A}{2} \cdot \left[1 + \mathrm{erf}\left(\frac{E_{\mathrm{s}} - \mu_{\mathrm{erf}}}{\sqrt{2} \cdot \sigma_{\mathrm{erf}}}\right)\right] + A_{\mathrm{bg}} \\ \text{with } \mathrm{erf}(x) &= \frac{2}{\sqrt{\pi}} \int_0^x \exp\left(-x'^2\right) \mathrm{d}x' \end{aligned} \tag{5.10}$$

is the most simple fit model, which is only an approximation for the case of a vanishing angular distribution and a perfectly Gaussian energy distribution. Advantage of the error function fit is that no additional information on magnetic fields are required to construct the fit model, as is the case for the Peaberry model. Comparing both fit results in Fig. 5.8, a significant difference in the case of the measurement with the LDLS is visible in the residuals, due to the deviation of the energy distribution from a Gaussian. In the case of

[21] The photon energy is $h\nu = 4.66\,\mathrm{eV}$ for the laser and 4.96 eV for the LDLS at 250 nm

the error function fit to the transmission function using the laser, the error function fit gives nearly the same results.

The best fit parameters for the position and the width of the error function fit are

$$\begin{aligned} \mu_{\mathrm{erf}}^{\mathrm{LDLS}} &= 0.263(1)\,\mathrm{eV} \quad \mu_{\mathrm{erf}}^{\mathrm{laser}} = 0.213(4)\,\mathrm{eV} \\ \sigma_{\mathrm{erf}}^{\mathrm{LDLS}} &= 0.142(1)\,\mathrm{eV} \quad \sigma_{\mathrm{erf}}^{\mathrm{laser}} = 0.087(3)\,\mathrm{eV}\,. \end{aligned} \tag{5.11}$$

For a comparison of the width of the energy distributions obtained from the Peaberry model and the error function fit, the width $\tilde{\sigma}$ of the generalised Gaussian distribution implemented in the Peaberry model need to be converted into the width $\sigma$ of a standard Gaussian distribution according to the formula provided in Ref. [Beh17]

$$\sigma = \frac{\tilde{\sigma}}{\zeta} \cdot \sqrt{\mathrm{e}^{\zeta^2-1}\left(\mathrm{e}^{\zeta^2}-1\right)}\,, \tag{5.12}$$

which gives the values

$$\sigma_{\mathrm{LDLS}} = 0.168(4)\,\mathrm{eV} \quad \sigma_{\mathrm{laser}} = 0.082(7)\,\mathrm{eV}\,. \tag{5.13}$$

The value of $\sigma_{\mathrm{erf}}^{\mathrm{LDLS}}$ is about 15 % smaller since the energy distribution of the electron gun is not perfectly Gaussian distributed. For the case of the energy distribution of the laser, both results agree well within the parameter uncertainties. Thus, the error function fit is a suitable fit model for transmission functions using the laser as light source. For transmission function fits to measurement data using the LDLS as light source the Peaberry model is recommended.

### 5.3.2 Rate and rate stability

Before the photoelectron source was installed at the rear section, it was tested at a test setup, where rates of >100 kcps were measured with the LDLS as light source [Sac20]. However, after installation of the photoelectron source at the rear section, the maximum rate decreased by nearly a factor of 100 for a yet undetermined reason. A decrease due to a reduced light intensity or a change in the work function of the photocathode could be excluded as possible causes. By increasing the light intensity, as it is possible in the case of the laser, it is still possible to obtain electron rates of $>10^4$ cps. However, as the light output of the LDLS cannot be further increased, the rate is currently limited to approximately 1500 cps.

Due to the reduced rate of the electron gun it is not possible to use the active stabilisation of the light intensity with the NoiseEater. Because of the coupling efficiency of the NoiseEater, the light intensity would be further reduced to approximately 55 % of the initial intensity, which would lead to a further decrease of the electron rate. Thus, the light intensity for both light sources is affected from drifts, which directly translates into drifts of the electron rate. The correlation of the light intensity and the electron rate can be seen in Fig. 5.9, where a rate measurement of the electron gun using the laser as light source is overlayed with the readout of the photodiode. The rate and the readout of the photodiode are highly correlated with a correlation coefficient of $\kappa = 0.96$. Due to the strong correlation, a correction of the rate by the intensity value of the photodiode in the analysis of the measurement data is possible. In order to obtain as many data points as possible, the diode reading interval is set to 10 Hz and the average of ten sensor values is written to the KATRIN database[22] with a 1 s interval.

For the correction of the light intensity drift, the light intensity can be retrieved from the database and the measured detector rate can then be divided by the relative deviation

[22] KATRIN number `111-AAI-0-2601-0001`

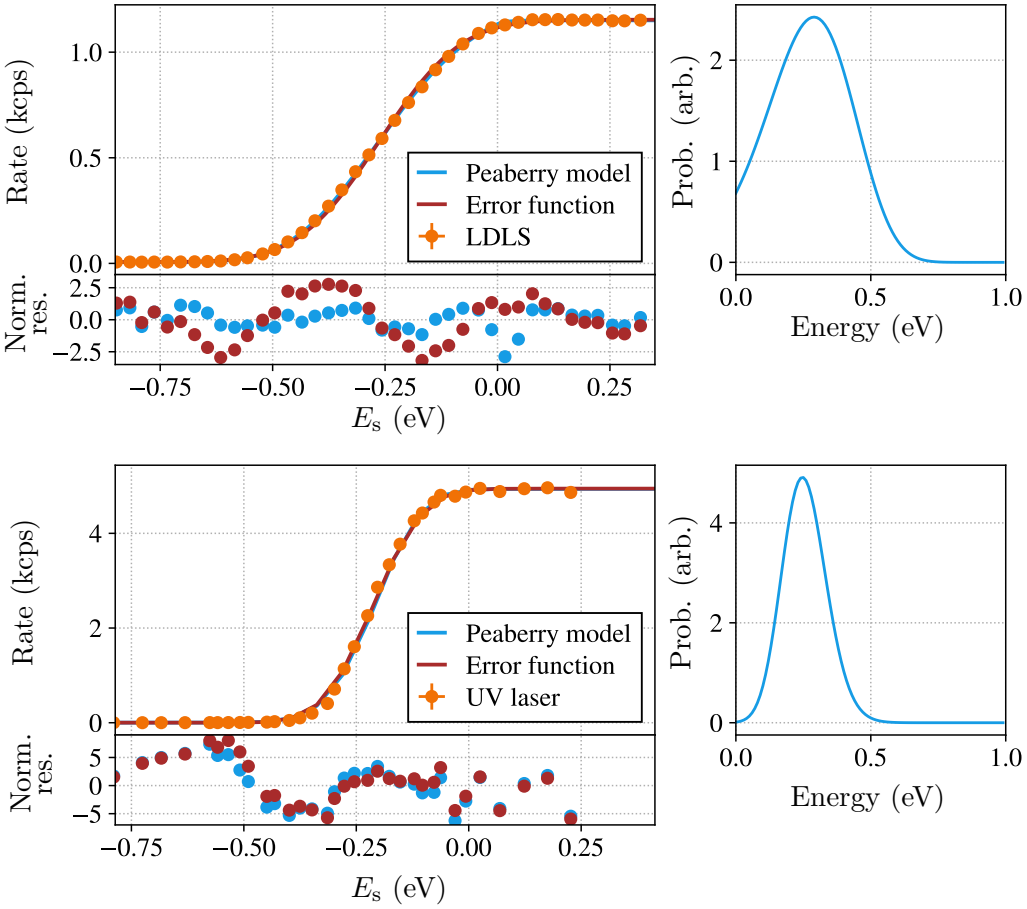


Figure 5.8: **Top:** High-statistics transmission function measurement using the LDLS as light source including fits with the detailed Peaberry model as well as a simple error function model. The Peaberry model fits the data slightly better ($\chi^2/N_{\mathrm{dof}} = 1.23(20)$) than the simple error function fit ($\chi^2/N_{\mathrm{dof}} = 2.71(20)$). The width of the energy distribution obtained from the Peaberry fit (right panel) is 166 meV. For a better presentation, the measurement data is shifted by 2.496 eV so that the edge position matches zero.
**Bottom:** Transmission function measurement using the UV laser as light source with both a Peaberry model fit and an error function fit. As the measurements with the pulsed UV laser suffer from the lower rate stability and require a dedicated pile-up correction, the transmission function measurements are less precise. Thus, both the Peaberry fit and the error function fit give nearly similar results. The width of the energy distribution from the Peaberry model fit is 81 meV. For a better presentation, the measurement data is shifted by 2.086 eV so that the edge position matches zero.

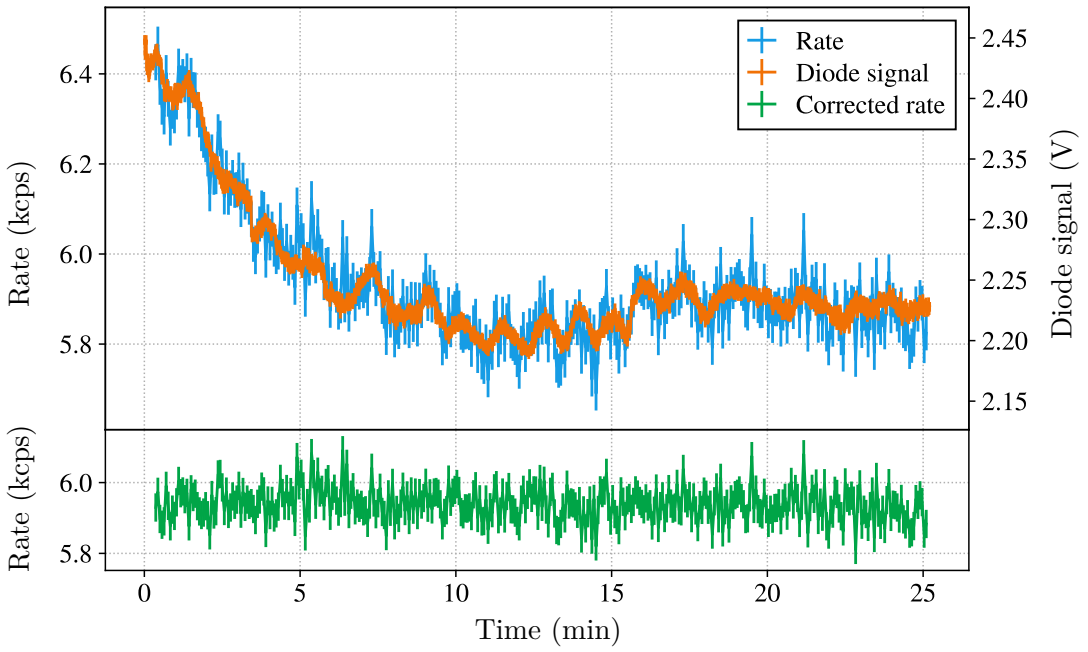


Figure 5.9: Rate trend of the electron gun using the UV laser at 100 kHz overlayed with the monitored light intensity. For demonstration, a time window during the warm-up of the laser was chosen, where the drift of the light intensity is more prominent. The rate and the light intensity follow the same trend. Correcting the data by the light intensity compensates the long-term drifts and reduces the periodic oscillations.

of the light intensity to the average intensity. An example of the rate after correction is included in Fig. 5.9. As it can be seen, the correction approach allows one to compensate for both the (periodic) short term instabilities as well as the long term drift of the light intensity. However, the monitoring of the light intensity has a Gaussian uncertainty of 0.4 % on very short time scales (see Fig. A.4), which has to be considered if the correction is applied to short measurement intervals ($\mathcal{O}(1\,\mathrm{s})$).

# 6. Pile-up reconstruction for the pulsed electron beam

The photoelectrons of the electron gun can be generated by using either the LDLS or the pulsed UV laser. The former is a continuous wave light source, which generates a Poisson distributed beam of electrons. However, using the pulsed UV laser generates a pulsed beam of electrons, where the generation time of the electrons is constrained by the pulse width of the laser (i.e. <18 ns (FWHM)). Due to the short pulse width, the electrons from the same light pulse arrive nearly simultaneously at the FPD. As the pulse width is smaller than the time resolution of the detector (L=1.6 µs), the electrons are counted as one event. This detector pile-up has the effect, that the measured rate at the detector is decreased and does not correspond to the actual electron rate of the beam.

The amount of pile-up events depends on the number of electrons which are generated from one light pulse. The latter depends on the electron rate of the beam as well as the pulse frequency $f_{\mathrm{P}}$. From the measured rate $R_{\mathrm{FPD}}$ at the FPD it is possible to estimate the average number of electrons generated from one light pulse

$$\hat{\mathcal{S}} = \frac{R_{\mathrm{FPD}}}{f_{\mathrm{P}}} \,. \tag{6.1}$$

Thus, the signal loss due to detector pile-up increases with increasing rate and decreasing pulse frequency.

Besides the dependency on the electron rate, the loss due to pile-up events is additionally dependent of the surplus energy. The energy dependency of the pile-up loss is caused by a complex interaction of the retarding potential of the main spectrometer, the energy loss due to scatterings inside the source, and the signal shaping method of the detector DAQ. An introduction to the signal shaping of the FPD DAQ and the corresponding energy dependency of the detector pile-up is provided in Sec. 6.1.

When performing response function measurements, the most prominent distortion is visible right at the transmission edge. As it can be seen in Fig. 6.1, the pile-up causes a peak-like structure, which is unphysical for integral measurements. However, the pile-up does not only influence the region close to the transmission edge but also the region at higher surplus energy, where scattered electrons are transmitted. Thus, it is essential to correct for these distortions in order to reconstruct the actual electron rate before the measurement data can be analysed.

The correction approach using look-up tables as well as the required simulation framework for the generation of the latter will be discussed in detail in Sec. 6.2.

The pile-up correction is of particular importance for the the analysis of the energy-loss function, which are discussed in Chaps. 7.2 and 8, since the response functions were measured by using the pulsed UV laser. Thus, the following discussion of the pile-up

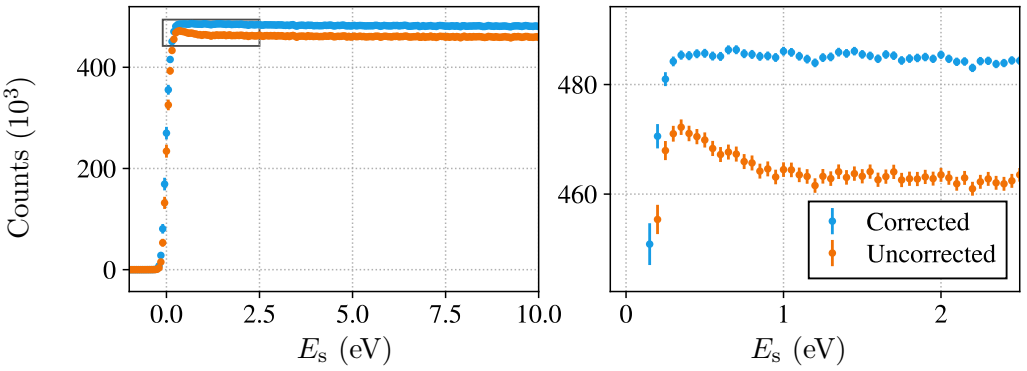


Figure 6.1: The figure shows a transmission function measurement using the pulsed UV laser. A detail view of the upper part of the transmission function (indicated by the rectangle) is shown on the right. As it can be seen, there is a decrease of more than 2 % of the events visible, where the transmission function reaches full transmission. This decrease is unphysical for integral measurements and is caused by detector pile-up of the pulsed electron beam. By applying the pile-up correction, as described in Sec. 6.2, the expected shape of the response function can be restored.

correction method focusses on these measurements, where a pulse rate of $f_P = 120\,\text{kHz}$ and 100 kHz was used.

## 6.1 Inter-arrival time dependency of the signal shaping

The event signal from the charge deposition in the Si-wafer of the FPD is processed with a three-stage trapezoidal filter [ABB+15][1] with an integration time (the so-called shaping time) $L = 1.6\,\mu\text{s}$ in order to obtain the event time and the event energy $E_{\text{FPD}}$. Multiple electrons arriving within the shaping time only cause one event trigger and are thus counted as the same event but with an accordingly higher event energy. The number of events, which are counted as one event, is defined as the event multiplicity. For monoenergetic electrons, a basic approach of determining the event multiplicity is to locate the peaks of $n$-fold electron energy in the event energy histogram and to weight the entries of the $n$-th peak by $n$. However, the influence of the retarding potential as well as the energy losses due to scattering with the source gas cause specific distributions of the inter-arrival times of the electrons, where the determined event energy becomes ambiguous, which is illustrated in Fig. 6.2. Thus, the peaks in the energy histogram overlap, which does not allow for a proper multiplicity estimation only based on the event energy $E_{\text{FPD}}$. Furthermore, the contribution to the overlapping regions is not constant, but changes with the surplus energy causing energy dependent distortions of the response function measurements. The four elementary cases, for which the ambiguity of the event energy is differently pronounced, are explained in the following for the simplest case of two electrons. However, similar applies for pile-up events including more than two electrons.

- $E_{\text{kin}} \approx qU_{\text{ret}}$
  Within a narrow energy interval close to the transmission edge, the filter potential causes a strong retardation of the electrons, since the kinetic energy of the electrons is transferred into potential energy. Due to the energy resolution of the electron gun (see Chap. 5), electrons generated from the same light pulse will have slightly different

[1] The detector system was initially only equipped with a two-stage trapezoidal filter, but a third filter stage was added in 2017 for better pile-up reconstruction

kinetic energies. Hence, the electron with less kinetic energy has a larger time-of-flight than the one with higher energy, which can cause a spread of the inter-arrival time $\delta t$ by several tens of microseconds (see Fig. 6.5). Thus, the electrons from the same pulse will not arrive at the detector within the shaping time, i.e. $\delta t \gg L$ (see left column of Fig. 6.2), and will only cause detector pile-up if the electrons are coinciding with electrons from other pulses. Therefore, each event triggers the detector individually and the event energy is properly determined, as is shown in the top panel of Fig. 6.3.

- $E_{\mathrm{kin}} \gtrsim qU_{\mathrm{ret}}$
  With rising kinetic energy, the retardation becomes smaller and so the difference in the inter-arrival times. For an energy window starting approximately 100 meV above the transmission edge, the inter-arrival time of the electrons from one pulse reaches the point, where $\delta t \approx L$. If this is the case, the two electrons trigger the system only once but the event energy obtained from the trapezoidal filter is ambiguous for different event multiplicities (see middle column of Fig. 6.2). This causes a smearing of the two-fold pile-up peak in the event energy histogram, which make the peaks overlap (see second top panel of Fig. 6.3).
- $E_{\mathrm{kin}} \gg qU_{\mathrm{ret}}$
  If the surplus energy is further increased, the flight time differences due to the retardation become negligible. Thus, all electrons from the same pulse arrive at the detector with inter-arrival times $\delta t \ll L$. In this case, the system is triggered once, but the event energy corresponds to the $n$-fold electron energy (see right column of Fig. 6.2), causing discrete peaks in the energy event histogram (see second lower panel of Fig. 6.3).
- Scattering with source gas
  For surplus energies $E_{\mathrm{s}}$ above the excitation threshold, the energy loss $\Delta E$ due to scattering with the source gas can result in the two transmission conditions $\tilde{E}_{\mathrm{kin}} = E_{\mathrm{kin}} - \Delta E \approx qU_{\mathrm{ret}}$ and $\tilde{E}_{\mathrm{kin}} = E_{\mathrm{kin}} - \Delta E \gtrsim qU_{\mathrm{ret}}$. As all unscattered electrons still fulfil the condition of $E_{\mathrm{kin}} \gg qU_{\mathrm{ret}}$, all three transmission conditions with different pile-up properties exist simultaneously. As shown in the bottom panel of Fig. 6.3, the $n$-fold pile-up-peaks are smeared out to lower energies, and even show secondary peaks du to the scattering.

In order to estimate the event multiplicity especially for measurements with non-empty source, a more robust pile-up reconstruction is required than the simple peak-weighting method.

Since a third trapezoidal filter is installed, it is possible to obtain further informations on the signal shape, such as the so-called bipolar width $w_{\mathrm{bi}}$, which is the time distance between the two zero crossings of the third trapezoidal filter signal. The bipolar width is connected to the flat-top width of the first filter stage, which itself is connected to the inter-arrival time of the electrons of the detector, as illustrated in Fig. 6.2.

Taking into account this additional information on the event signal shape, the event energy histogram can be expanded by another dimension. This allows one to better resolve the ambiguities between regions of different event multiplicities, as it is shown in Fig. 6.4. Due to the formation of discrete structures in the $E_{\mathrm{FPD}}$-$w_{\mathrm{bi}}$-plane, it is possible to provide a multiplicity estimate $\hat{\mathcal{M}}(E_{\mathrm{FPD}}, w_{\mathrm{bi}})$ based on the location inside the two dimensional plot. The determination of $\hat{\mathcal{M}}(E_{\mathrm{FPD}}, w_{\mathrm{bi}})$ is based on dedicated flight time and detector simulations, which are described in the following section.

## 6.2 Generation of the look-up table

The method of using a two-dimensional look-up table including an event multiplicity estimate $\hat{\mathcal{M}}(E_{\mathrm{FPD}}, w_{\mathrm{bi}})$ was first developed by S. Enomoto (University of Washington)

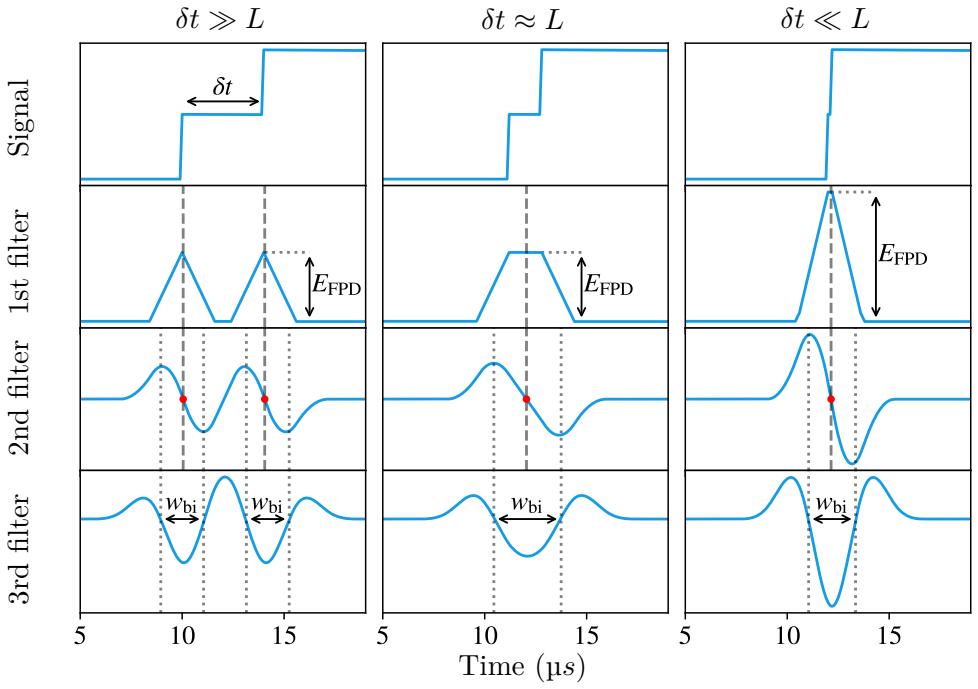


Figure 6.2: Example of the pulse shaping with the bipolar shaping trapezoidal filter system of the DAQ of the FPD. The event signal (top) is processed with a first trapezoidal filter (second row from the top) to obtain the event energy $E_{\mathrm{FPD}}$ from the height of the trapezium. The time, where to evaluate the signal (dashed lines) of the first filter stage is obtained from the second trapezoidal filter (third row from the top), as the zero crossing (red dot) defines the event trigger. By evaluating the position of the extrema of the second filter stage, additional information on the signal shape can be obtained. The time difference of the two extrema, the so-called bipolar width $w_{\mathrm{bi}}$, provides information of the flat-top width of the first filter signal, which is related to the inter-arrival time of the electrons. In order to determine the position of the extrema, a third trapezoidal filter stage is required, where $w_{\mathrm{bi}}$ is obtained from the time between the zero crossings (dotted lines). Depending on the inter-arrival time of the electrons, the events will trigger the system twice (left column) or only once (middle and right column). For electrons arriving with inter-arrival times $\delta t \approx L$, the height of the trapezium is similar to to the height of the individually triggered events. Thus, the multiplicity cannot be properly estimated using only the event energy.

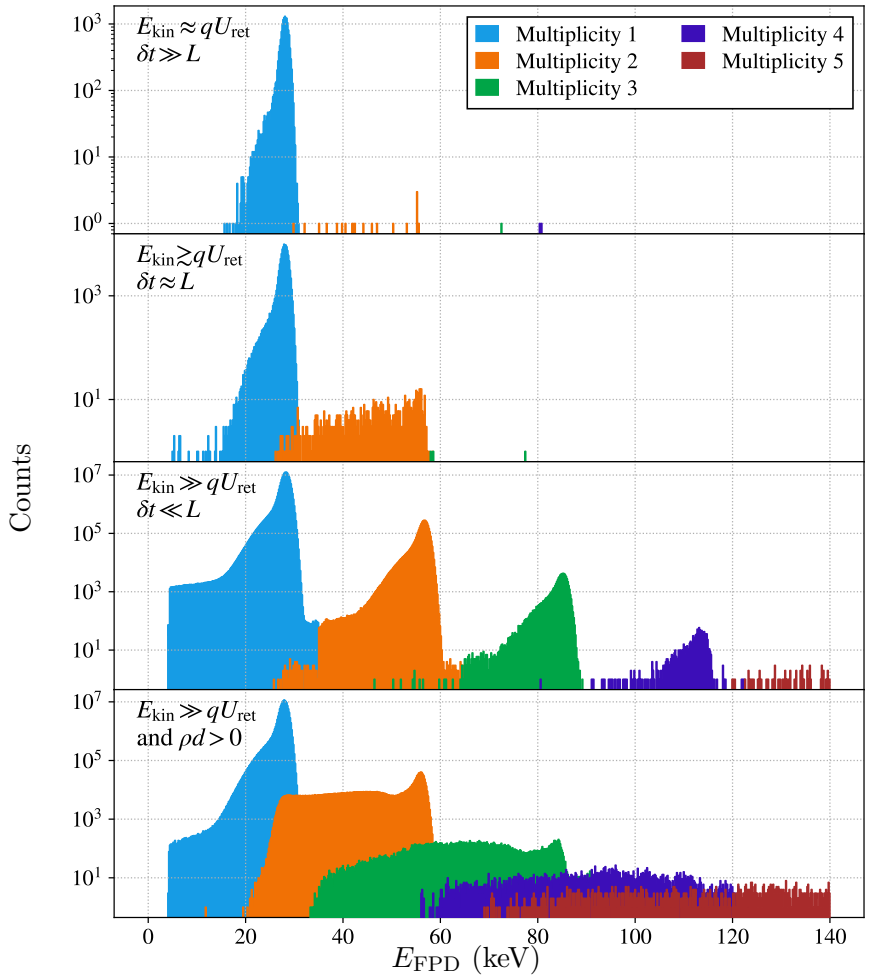


Figure 6.3: Histograms of the event energies $E_{\mathrm{FPD}}$ obtained from measurements at different surplus energies. The colours indicate the event multiplicity, which is determined with the pile-up reconstruction approach explained in 6.2.
**1st row:** The kinetic energy $E_{\mathrm{kin}}$ is approximately the same as the retarding potential $U_{\mathrm{ret}}$. Therefore, small differences in the initial kinetic energy of the electrons cause large flight time differences. Thus, electrons from the same pulse arrive at the FPD individually and only the one-fold energy peak is visible.
**2nd row:** The kinetic energy is about 100 meV larger than $U_{\mathrm{ret}}$. This causes the flight time differences to be similar to the shaping time, which causes ambiguities of $E_{\mathrm{FPD}}$. Thus, the second energy peak is smeared out to the left and overlaps with the first peak.
**3rd row:** The kinetic energy is about 50 eV larger than $U_{\mathrm{ret}}$. The inter-arrival time of the electrons from the same pulse is smaller than the shaping time. This causes discrete peaks, also for multiplicities $\mathcal{M} \geq 2$.
**4th row:** In the case of a non-empty source and for energies above the threshold energy of elastic scattering, all the three effects above appear at the same time. This causes very broad and distorted energy peaks, which overlap significantly.

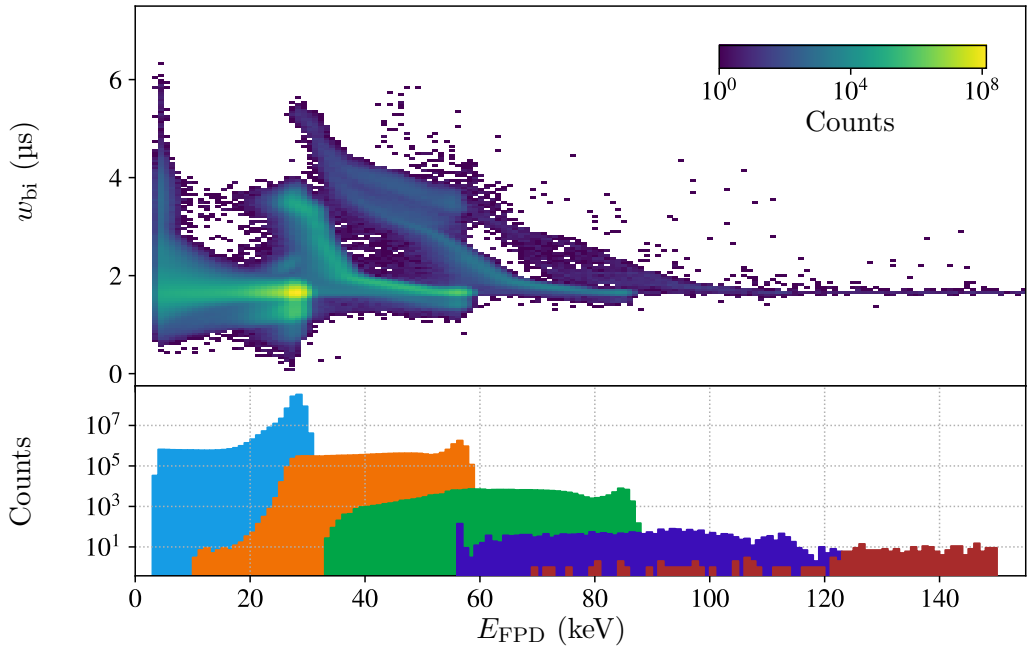


Figure 6.4: Event energy histogram in unipolar (bottom) and bipolar (top) mode. Due to the additional information on the bipolar width $w_{\mathrm{bi}}$, the event energy histogram on the bottom can be expanded by another dimension, which allows one to dissolve the ambiguities of the event energy. The histogram contains all events from the response function scans in the range of $E_{\mathrm{s}} = [-5, 55]\,\mathrm{eV}$ at a column density of 88 % $\rho_0 d$ (see Tab. 7.1). As surplus energies $E_{\mathrm{s}} \gg qU_{\mathrm{ret}}$ dominate, the shape of the energy histogram is similar to the histogram shown in the bottom plot of Fig. 6.3.

[CEN17]. In this first approach, the look-up table was compiled by detector simulations using the inter-arrival time distributions obtained from measurements with the pulsed UV laser at $f_\mathrm{P} = 20\,\mathrm{kHz}$ (neglecting the influence of scattering).

As the response function measurements described in Chap. 7 and 8 were carried out at non-empty source and with a pulse frequency of $f_\mathrm{P} = 120\,\mathrm{kHz}$ and $100\,\mathrm{kHz}$, the correction method has to be adapted in order to match the individual measurement settings. In order to be independent of the measurement of the inter-arrival time distributions, a simulation framework is developed, which allows one to obtain inter-arrival time distributions for different settings of the pulse rate as well as the source density. The simulations of the flight time as well as the inter-arrival time distributions, which will be described in Secs. 6.2.1 and 6.2.2, are required as input for the simulation of the detector response. The simulations of the detector response are performed with the DRIPS framework, which emulates the response of the detector system for a list of incident electron. Given the list of incident electrons, the amount of electrons triggering one detector event can be determined. The detector simulation and the final generation of the look-up table will be discussed in Sec. 6.2.3.

### 6.2.1 Flight time simulations

The flight time of the electrons from the electron gun to the detector can be simulated with the Kassiopeia particle tracking framework [FGT+17], which is part of the KASPER analysis software. The Kassiopeia framework allows one to track charged particles inside of electromagnetic fields. For the purpose of the tracking, two options exist, which are exact tracking and adiabatic tracking. The exact tracking performs a full calculation of the charged particles cyclotron motion along the magnetic field line, whereas the adiabatic tracking only computes the motion of the guiding centre of the cyclotron motion along the magnetic field line. The exact solution requires more steps for the calculation and is thus slower than the adiabatic tracking. Since the kinetic energy of the e-gun electrons is close to the tritium endpoint and the surplus energies are small, the electrons are guided adiabatically through the experimental setup. Hence, the adiabatic tracking provides valid simulation results and is thus chosen for the following simulations.

The flight time of the electrons is dependent on three parameters, namely the surplus energy $E_\mathrm{s}$, the retarding potential of the main spectrometer $U_\mathrm{ret}$, and the pitch angle $\theta$. As the retarding potential in the analysing plane is decreasing towards the centre of the vessel due to the potential depression of the inner electrodes, the flight times are depending on the trajectory of the electrons inside the main spectrometer vessel. From the measurements it is known that the electron beam hits the detector at detector pixel 3, which is the bottom right bullseye pixel. However, the exact position of the beam within the borders of the pixel is unknown and thus the trajectory inside the main spectrometer. In order to determine the best matching trajectory through the main spectrometer, four trajectories were simulated which would all end on pixel 3, distributed to the centre and the three pixel corners, respectively. Figure 6.5 shows the flight time functions $\tau(E_\mathrm{s}, \theta = 0°, U_\mathrm{ret} = 18\,575\,\mathrm{V})$ compared to the flight times as obtained from measurements. In order to compensate small offsets of the flight time simulations and the data for both the flight time and the surplus energy, a least square fit is performed with the two offset parameters $\tau_\mathrm{offset}$ and $E_\mathrm{s}^\mathrm{offset}$as free parameters. Although all simulations are in good agreement with the measurement data, the best agreement is obtained for the simulations at pixel corner 2, which is located at the bottom of the pixel. The two offset parameters for the best-fit result of the latter are

$$\tau_\mathrm{offset} = 0.946\,\mu\mathrm{s} \quad \text{and} \quad E_\mathrm{s}^\mathrm{offset} = -0.005\,\mathrm{eV}\,. \tag{6.2}$$

The offset of $\tau_\mathrm{offset} = 0.946\,\mu\mathrm{s}$ between the simulations and the measurement data can be

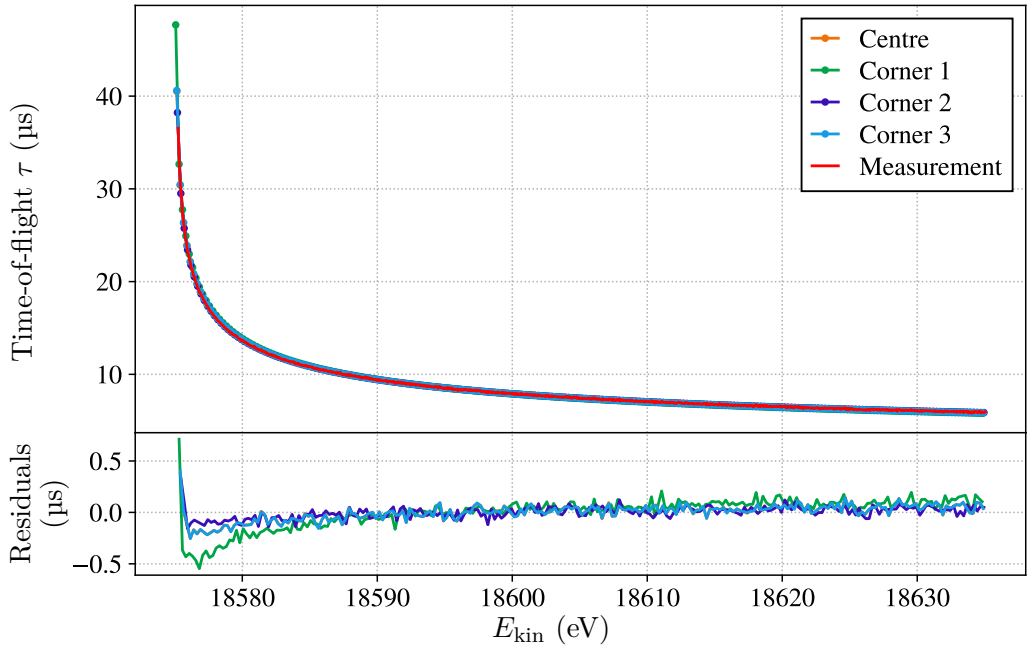


Figure 6.5: Results of the flight time simulations for different positions on the detector pixel 3 compared to measurement data obtained from ToF measurements (see Ref. [Rod]). All curves agree well, but the best agreement is obtained for trajectories ending at the pixel corner 2 (bottom corner). The residuals are below 0.1 µs except for the first data point as curves diverge and the uncertainties become large.

caused due to delays of the devices. These delays, which are on the order of 1 µs [Sac20], are not considered in the simulations.

Knowing the trajectory inside the retarding potential allows one to generate a two-dimensional flight time map $\tau(E_{\mathrm{s}}, \theta, U_{\mathrm{ret}} = 18\,575\,\mathrm{V})$ as a function of the surplus energy $E_{\mathrm{s}}$ and the pitch angle $\theta$, as shown in the bottom plot of Fig. 6.6. The pitch angle is defined at a magnetic field of 42 mT, which corresponds to the magnetic field right after the post-acceleration system of the electron gun ($z = -50.91$ m). The simulation settings are summarised in Tab. 6.1.

### 6.2.2 Arrival time simulations

In order to generate the list of incident electrons while performing simulations of the detector response using the DRIPS framework (see Sec. 6.2.3), arrival time distributions must be passed to the simulation program. These arrival time ($t_a$) distributions can be compiled by using the flight time simulations.

The shape of the arrival time distribution is depending on multiple factors, which are the surplus energy, the energy distribution and the angular distribution of the electrons, as well as the column density inside the source. The dependency on the column density is caused by the energy loss due to scattering, which results in a change of the surplus energy and thus influences the flight times according to Fig. 6.5.

In order to obtain the arrival time histograms for a defined surplus energy $E_{\mathrm{s}}$ of the electron gun, a multi-stage Monte Carlo simulation is required. At the first sampling stage, the initial electron properties, i.e. the initial kinetic energy $E_{\mathrm{ini}}$ of the photoelectrons and

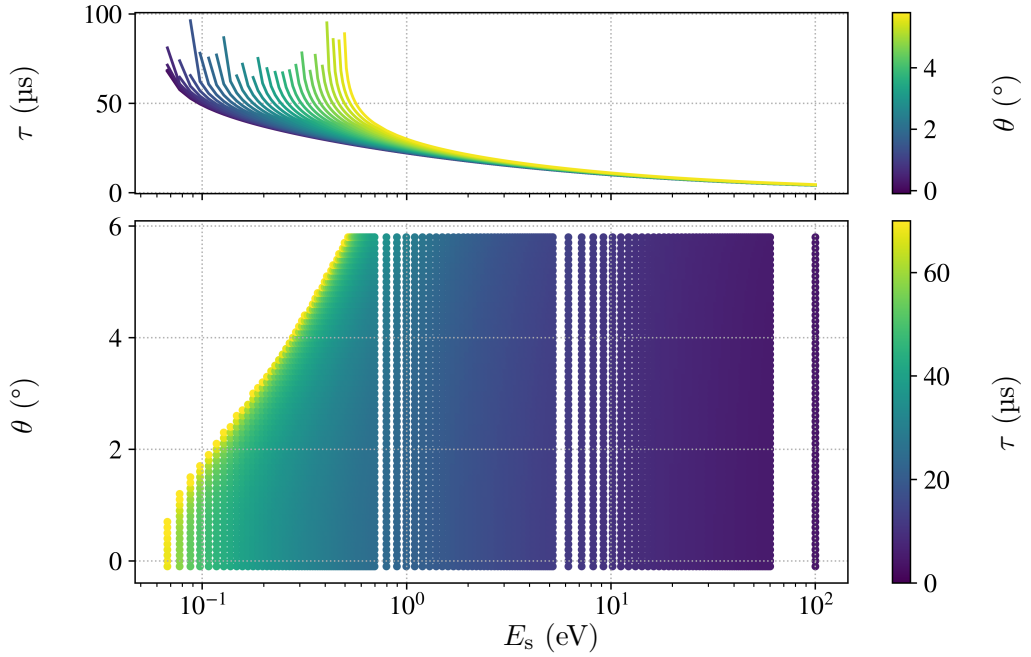


Figure 6.6: Results of the flight time simulations. The top panel shows the results projected to the $E_s$-$\tau$-plane with the colours indicating the corresponding pitch angle of the electron beam. Due to the finite energy resolution of the main spectrometer, the transmission edge (i.e. the asymptotic part) shifts towards higher energies with increasing pitch angle. The bottom panel shows the projection in the $E_s$-$\theta$-plane, with the colours indicating the time-of-flight $\tau$. The pitch angle $\theta$ is defined at a magnetic field of 42 mT after the post-acceleration system of the electron gun ($z = -50.91$ m).

Table 6.1: Overview of the settings of the Kassiopeia simulations for the construction of the flight time function $\tau(E_s, \theta, U_{ret})$.

| Parameter | Value |
|---|---|
| Main spectrometer potential $U_{ret}$ | −18 575 V |
| Pre-spectrometer potential $U_{PS}$ | −10 kV |
| Magnetic field along beam line | 70% of nominal |
| Analysing plane setting | 1.4 G |
| Electron energy $E_{kin}$ | 18 574.5 eV to 18 675 eV |
| Pitch angle $\theta$ | −0.1° to 5.8° |
| Initial magnetic field | 42 mT |
| Start position | $z = -50.91$ m |
| Terminator | FPD wafer |
| Final position | Corner 2 of FPD pixel 3 |
| Tracking | adiabatic |

the pitch angle $\theta$ are drawn. In this case, both the energy distribution and the angular distribution are assumed to be Gaussian with the shape parameters

$$\mu_{\mathrm{E}} = 0.57\,\mathrm{eV} \quad \sigma_{\mathrm{E}} = 0.07\,\mathrm{eV} \tag{6.3}$$

and

$$\mu_{\theta} = 0^{\circ} \quad \sigma_{\theta} = 0.7^{\circ}\,. \tag{6.4}$$

The values of the energy distributions differ from the values provided in Eq. (5.9), as they were determined from an early and less precise analysis. However, as it is shown in Fig. 6.7, the simulation results agrees very well with measurement data.

In the next sampling step, the interaction with the source gas is simulated. Depending on the mean number of scatterings $\mu_0 = \rho d \sigma_{\mathrm{inel}}$, a sampling is performed to simulate whether the electron scatters or not. If the particle scatters, another sampling stage is required to obtain the energy loss $\Delta E$ from the scattering. As it does not matter if $\Delta E$ is transferred in one or multiple scatterings, $\Delta E$ is randomly drawn from the sum of the $n$-fold energy-loss functions $f_n(\Delta E)$ each weighted with the scattering probability $P_n(\mu)$. The required parametrisation of the energy-loss function for the construction of the probability distribution is obtained from a preliminary result of the analytical fit to the response functions in Chap. 7, which were corrected for pile-up by using the look-up table[2] of S. Enomoto. The final surplus energy $E_{\mathrm{s}}^{\mathrm{final}}$, is then defined as the sum of the chosen surplus energy $E_{\mathrm{s}}$ and the initial kinetic energy of the electrons $E_{\mathrm{ini}}$ minus the energy loss due to scattering $\Delta E$, i.e.

$$E_{\mathrm{s}}^{\mathrm{final}} = E_{\mathrm{s}} + E_{\mathrm{ini}} - \Delta E\,. \tag{6.5}$$

If $E_{\mathrm{s}}^{\mathrm{final}}$ is greater than zero, the flight time is determined from the flight time map $\tau(E_{\mathrm{s}}^{\mathrm{final}}, \theta)$ and stored in the histogram, otherwise the particle is considered as reflected by the spectrometer potential and a new sampling is performed.

An exemplary set of arrival time histograms at different surplus energies is displayed in Fig. 6.7. In order to demonstrate the validity of the simulations, the arrival times as obtained from measurements are shown.

### 6.2.3 Detector simulation and decomposition

The arrival time histograms are used as input for the detector simulations performed with the DRIPS framework. The DRIPS framework is included in the KASPER software package and allows one to simulate the detector response for electrons arriving at the FPD. The framework emulates the characteristic properties of the FPD system, such as energy resolution, detector noise, or deadlayer effect. Multiple predefined input types exist, such as `Random` (i.e. Poisson distributed), `Pattern` or `Pulse`. The latter is used for the simulation of the pulsed electron beam and allows the detector rate $R_{\mathrm{FPD}}$, the pulse frequency $f_{\mathrm{P}}$, the pulse width, and the arrival time distribution to be defined as input parameters.

The DRIPS program generates a list of incident events by sampling from the Poisson probability of generating $\mathcal{S}$ electrons per light pulse, with the average value $\hat{\mathcal{S}}$ being estimated according to Eq. (6.1), For each of the generated electrons, the creation time is sampled from the pulse width followed by a sampling of the arrival time from the input distribution, which is added to the creation time. For each of the electrons in the list, the charge deposition in the detector wafer and the signal shaping with the trapezoidal filter system is simulated. The final output of the DRIPS simulations is similar to the real detector data, including the timestamps of the event triggers, the event energy $E_{\mathrm{FPD}}$, and the bipolar width $w_{\mathrm{bi}}$. An exemplary bipolar histogram obtained from the simulations

[2] `PileupMap-Sts3aEgun-20181113.ktf`

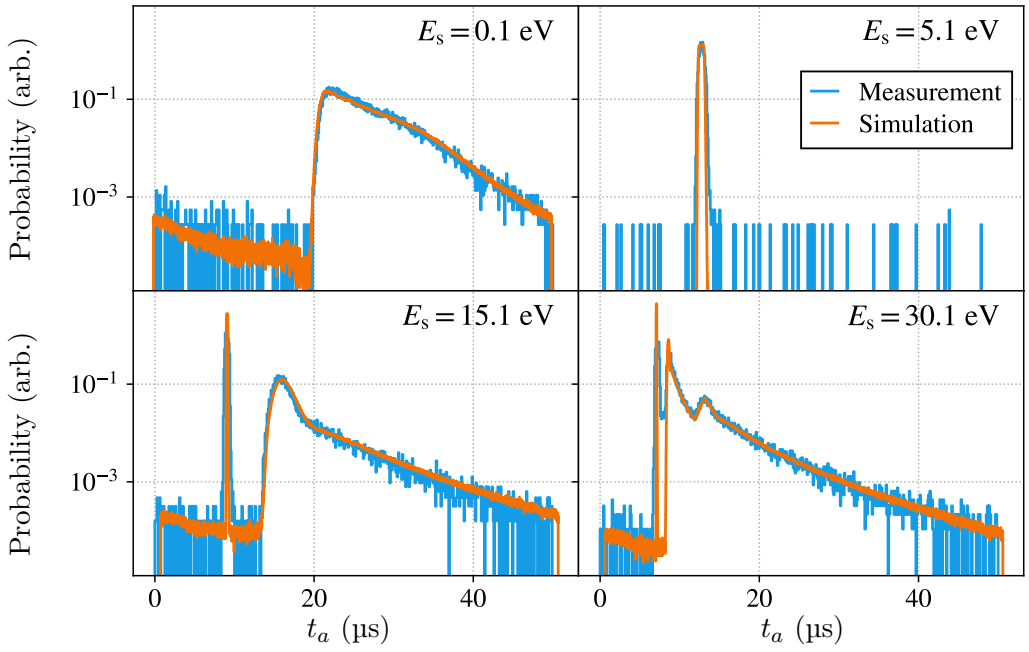


Figure 6.7: Arrival time histograms obtained from measurement data at 85 % $\rho_0 d$ (i.e. $\mu = 1.54$) and from simulations using a laser pulse frequency of $f_P = 20$ kHz. For very small surplus energies, the arrival histogram is a broad peak, which becomes more narrow with rising surplus energy (top row). For a non-empty source (bottom row), a contribution due to scattered electrons exists above the threshold energy of inelastic scattering. The scattered electrons have a broad distribution compared to the narrow peak of unscattered electrons. The histograms are drawn with a modulus of 50 µs of the x-axis which is defined by the repetition rate of the laser. The histograms are drawn for the energy interval of $E_s \pm 0.5$ eV.

($\mu = 1.65$, $f_\mathrm{P} = 120\,\mathrm{kHz}$) is displayed in Fig. 6.8 together with measurement data using the same setting. The simulation data shows the same discrete structures in the $E_\mathrm{FPD}$-$w_\mathrm{bi}$-plane as the measurement data. However, the measurement data has a larger smearing along the y-axis, which is caused by the noise of the FPD system (e.g. flicker noise). Unfortunately it is currently not possible to include both the noise as well as deadlayer effects in the simulation program at the same time. Thus, the noise is not included and only the more dominant deadlayer effects are simulated. The latter cause the visible smearing along the x-axis.

Based on the simulation data it is possible to determine the multiplicity $\hat{\mathcal{M}}$ of the output events by comparing it with the list of incident events. The multiplicity of the events is determined as the amount of incident electrons arriving within the time window $L = 1.6\,\mu\mathrm{s}$ around the timestamps of the event triggers. Each multiplicity value is written to the look-up table for the corresponding pair of $E_\mathrm{FPD}$ and $w_\mathrm{bi}$ of the output events. The look-up table consists of $200 \times 150$ bins covering the parameter space of $E_\mathrm{FPD} = [0, 200]$ keV and $w_\mathrm{bi} = [0, 7.5]$ µs. An exemplary look-up table is shown in Fig. 6.8 for the settings of $\mu = 1.65$ and a pulse frequency of $f_\mathrm{P} = 120\,\mathrm{kHz}$ (which corresponds to the laser setting for the measurements in Sec. 7).

As ambiguities between the regions of different multiplicities still exist even in the two dimensional expansion (see Fig. A.6), the look-up table is modified to provide a probability distribution of $\hat{\mathcal{M}}$ for each pair of $E_\mathrm{FPD}$ and $w_\mathrm{bi}$. The probability distributions of these overlapping regions changes as a function of the surplus energy, since both the values of $E_\mathrm{FPD}$ and $w_\mathrm{bi}$ are energy dependent (comp. Figs. 6.3 and 8.17). In order to take this energy dependency into account, it is required to simulate a look-up table for each surplus energy value of the individual response function measurements.

In the case of the response function measurements for the determination of the energy-loss function (see Tabs. 7.1 and 8.2), the response functions each consist of more than 1000 energy bins. As it is not feasible to pass this large number of look-up tables to the analysis program, an average look-up table is compiled for each response function. The process of generating the look-up tables is illustrated in Fig. 6.9. The influence of the energy independent look-up table on the reconstructed shape of the response function is investigated in detail in Sec. 8.5, where the systematic uncertainty is determined to be $<0.11\,\%$.

Using the compiled look-up tables, the multiplicity $\hat{\mathcal{M}}$ for each detector event is determined during the processing of the measurement data. By weighting the detector events with the corresponding multiplicity value, the actual electron rate can be restored, as illustrated in Fig. 6.1 for the case of the transmission function measurement. The pile-up corrected transmission function follows the expected shape and does not show any visible artefacts.

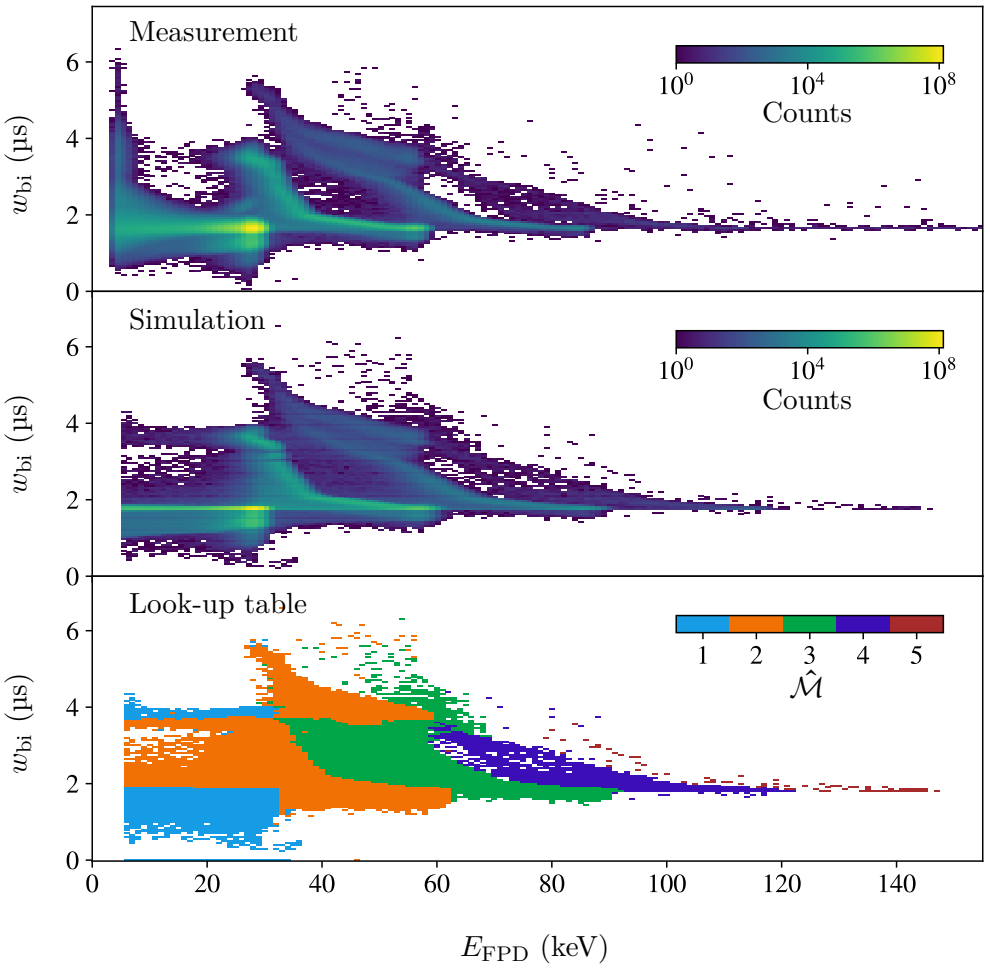


Figure 6.8: Bipolar histogram as obtained from measurement data (top) ($\mu = 1.65$, $f_{\mathrm{P}} = 120\,\mathrm{kHz}$) and simulations (middle). The simulation data shows the same discrete structures as the measurement data. From the simulation data, a look-up table (bottom) is compiled containing the event multiplicity estimate $\hat{\mathcal{M}}(E_{\mathrm{FPD}}, w_{\mathrm{bi}})$.

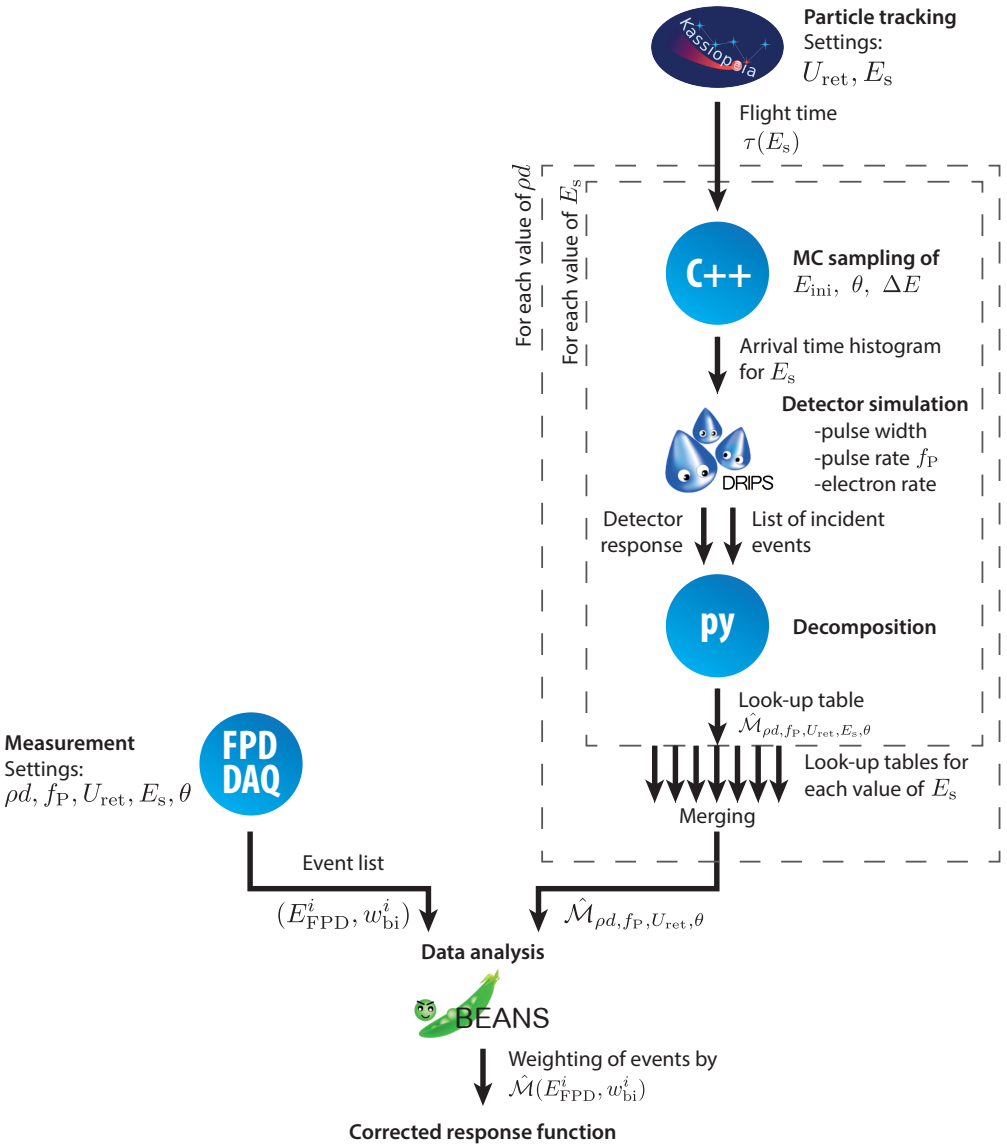


Figure 6.9: Simulation steps needed for the generation of the multiplicity look-up table. For each response function measurement at different source density and different laser pulse rates a look-up table has to be created with the corresponding setting.

# 7. Measurement of the energy-loss function of $D_2$

The energy loss of the signal electrons due to scattering with the source gas inside the WGTS is one of the main systematics of KATRIN. As discussed in Sec. 4.3, the scattering causes a distortion of the response function of the experimental setup and thus distorts the shape of the measured β-spectrum. These shape distortions can be considered in the construction of the fit model. However, this requires a precise description of the energy-loss function.

In order to reach the sensitivity goal of $m(\nu_e) = 0.2\,\mathrm{eV}$, the total systematic uncertainty budget must not exceed a value of $\sigma^{\mathrm{tot}}_{\mathrm{sys}}(m^2_\nu) \leq 17 \times 10^{-3}\,\mathrm{eV}^2$ for the observable of $m^2_\nu$. As defined in the design report [KAT05], the contribution to the systematic uncertainty budget of KATRIN from the uncertainties of the energy-loss function must not exceed the limit of $\sigma^{\mathrm{eloss}}_{\mathrm{sys}}(m^2_\nu) < 7.5 \times 10^{-3}\,\mathrm{eV}^2$.

A measurement strategy to obtain the energy-loss function with the required precision from dedicated measurements at KATRIN was already proposed in the design report and is described in more detail in Ref. [HHW+17]. The proposed measurement approach is based on a deconvolution of the energy-loss function from response function measurements at three different column densities and a reference measurement at zero column density. According to Ref. [HHW+17], the resulting precision of the deconvolved energy-loss function meets the requirements of KATRIN and leads to a systematic shift of $\Delta m^2_\nu = 5.3(5) \times 10^{-3}\,\mathrm{eV}^2$. However, further investigations of N. Trost [Tro19] showed that the deconvolution method is strongly depending on statistical noise. The reported precision in Ref. [HHW+17] was however obtained by performing only one single Monte Carlo simulation. By simulating 10000 measurements and performing a deconvolution for each simulated sample, the systematic shift of $\Delta m^2_\nu = -12.5(31) \times 10^{-3}\,\mathrm{eV}^2$ was found [Tro19]. However, in both cases only the systematic shift was considered and the uncertainty $\sigma^{\mathrm{eloss}}_{\mathrm{sys}}(m^2_\nu)$ on the observable was not taken into account. Hence, a detailed investigation of the measurement approach yielding both the systematic shift as well as the uncertainty of $m^2_\nu$ is required to determine the actual quality of the deconvolution method. In order to test the measurement approach and to improve the measurement and analysis strategy, measurements with deuterium as source gas were performed in summer/fall 2018.

Since the measurement conditions were different than expected, the measurement strategy of the response functions had to be adapted and only a data set with reduced statistics was obtained. Due to the reduced statistics, the deconvolution results, which will be discussed in Sec. 7.3.1, did not meet the expectations. Thus, a new analysis approach was developed, which reduced the remaining uncertainty on $\sigma(m^2_\nu)$ by about a factor of 30 compared to the SVD deconvolution. The new analysis approach, which will be discussed in Sec. 7.3.2, is to fit an analytical model to the measurement data including a semi-empirical parametrisation of the energy-loss function. Compared to the SVD deconvolution method,

which is developed to include only integral response functions, the analytical fit approach also allows differential response functions to be included in the analysis. Thus, the data set for the analytical fit was extended by a novel differential response function measurement. The differential measurement approach was proposed by Prof. Dr. Ch. Weinheimer (University of Münster) and the measurement and the data analysis were carried out by R.Sack [Sac20], C. Rodenbeck [Rod], and V. Hannen (University of Münster). As part of a collaborative work, a parametrisation is obtained from a combined fit using both the integral and differential data, which will be discussed in Sec. 7.3.3.

The quality of the obtained energy-loss functions obtained from both the deconvolution as well as the analytical fit approach will be discussed in Sec. 7.4.

## 7.1 Measurement approaches

The energy-loss function of the signal electrons scattering off the source gas can be investigated by measurements of the response function of the quasi-monoenergetic and angular-selective electron beam of the electron gun.

However, the response function of the electron gun, which will be discussed in Sec. 7.1.1, is a superposition of $n$-fold scattered electrons and includes a convolution with the transmission function of the electron gun. In order to extract the energy-loss function from the measurement data, sophisticated analysis tools are required, which consider the contribution from multiple scattered electrons and the shape of the transmission function.

The two analysis approaches, which will be used for the analysis of the measurement data, are a deconvolution approach as well as an analytical fit approach. Both approaches are explained in detail in the following sections.

### 7.1.1 Response function of the electron gun

Based on the theoretical description of the response function for the isotropic source in Eq. (4.38), the response function of electrons generated with the electron gun can be derived. The major difference of the electrons from the electron gun and the β-electrons is that the electron gun is located behind the source. Hence, the photoelectrons pass the entire WGTS. Moreover, the source is angular selective, which allows one to select a vanishing pitch angle. In this special case the mean number of scatterings $\mu$ becomes independent of both $z$ and $\theta$ so that

$$\mu = \rho d \sigma \,. \tag{7.1}$$

With $\mu$ being independent of $z$ and $\theta$, the probability for $n$-fold scattering in Eq. (4.34) simplifies to

$$P_n(\mu) = \frac{\mu^n}{n!} \exp\left(-\mu\right) \,. \tag{7.2}$$

The contribution to the response function of $n$-fold scattered electrons can be described by the scattering functions

$$\begin{aligned}
\epsilon_0(U_{\mathrm{ret}}, E_{\mathrm{s}}) &= T_{\mathrm{e}}(U_{\mathrm{ret}}, E_{\mathrm{s}}) \\
\epsilon_1(U_{\mathrm{ret}}, E_{\mathrm{s}}) &= T_{\mathrm{e}}(U_{\mathrm{ret}}, E_{\mathrm{s}}) \otimes f(\Delta E) \\
\epsilon_2(U_{\mathrm{ret}}, E_{\mathrm{s}}) &= T_{\mathrm{e}}(U_{\mathrm{ret}}, E_{\mathrm{s}}) \otimes f(\Delta E) \otimes f(\Delta E) \\
\epsilon_3(U_{\mathrm{ret}}, E_{\mathrm{s}}) &= T_{\mathrm{e}}(U_{\mathrm{ret}}, E_{\mathrm{s}}) \otimes f(\Delta E) \otimes f(\Delta E) \otimes f(\Delta E) \\
&\dots
\end{aligned} \quad , \tag{7.3}$$

where $T_{\mathrm{e}}(U_{\mathrm{ret}}, E_{\mathrm{s}})$ is the transmission function of the electron gun (see Eq. (5.7)).

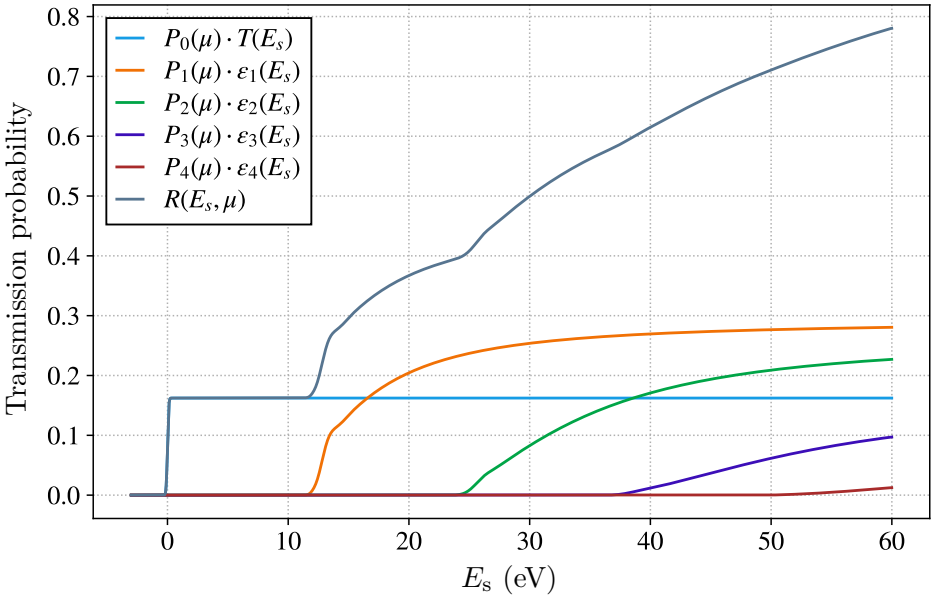


Figure 7.1: Theoretical response function $R(E_s, \mu)$ according to Eq. (7.4) for the nominal column density of $\rho_0 d = 5 \times 10^{21}\,\mathrm{m}^{-2}$. The response function is the sum of the transmission function $T(E_s)$ and the scattering functions $\epsilon_n(E_s)$ each weighted by the probability for $n$-fold scattering $P_n(\mu)$. Up to four-fold scattering contributes to the response function below the surplus energy of $E_s = 60\,\mathrm{eV}$.

Thus, the response function of the electron gun can be written as the sum of the scattering functions each weighted with the probability of $n$-fold scattering

$$R(U_{\mathrm{ret}}, E_s, \mu) = \sum_{n=0} P_n(\mu) \cdot \epsilon_n(U_{\mathrm{ret}}, E_s)\,. \tag{7.4}$$

An exemplary shape of the response function with the contributions of the scattering functions is displayed in Fig. 7.1.

The shape of the response function can be investigated either by keeping the electron energy at a constant value and by changing the retardation potential of the main spectrometer or by keeping the main spectrometer voltage constant and by modifying the electron energy. The two approaches give nearly the same results for scan ranges in the order of several 10 eV and for pitch angles around zero as the energy dependence of $\theta_{\mathrm{max}}(E)$ in Eq. (5.7) can be neglected. The functions $R(U_{\mathrm{ret}}, E_s, \mu)$, $T_e(U_{\mathrm{ret}}, E_s)$, and $\epsilon_n(U_{\mathrm{ret}}, E_s)$ are therefore written only as functions of the surplus energy, i.e. $R(E_s, \mu)$, $T_e(E_s)$, and $\epsilon_n(E_s)$. However, changing the kinetic energy of the electrons influences the inelastic cross section (see Eq. (4.10)), which has to be considered when performing response function scans at non empty source.

### 7.1.2 Deconvolution

The approach of deconvolving the energy-loss function from response function measurements is based on the work of Hannen et al. [HHW+17]. This measurement approach uses response function measurements a different column densities, in order to deconvolve the energy-loss function from the measurement data. Benefit of this measurement approach is, that the obtained energy-loss function is independent of any model.

Two different deconvolution methods were investigated in Ref. [HHW+17], which are the so-called stabilized biconjugate gradient method (Bi-CGSTAB) and the singular value decomposition (SVD). Since it was shown in Ref. [HHW+17] that the SVD deconvolution performs better than the Bi-CGSTAB deconvolution, only the method of the SVD deconvolution will be introduced in the following.

The deconvolution of the energy-loss function from the measurement using the SVD approach is performed in two consecutive steps. The first step is to extract the single scattering function from the response function measurements. This step is followed by the deconvolution step, where the transmission function, i.e. the energy resolution of the measurement, is deconvolved from the scattering function in order to obtain the energy-loss function. The algorithm of these two steps is summarised in the following.

The complete inversion and SVD algorithm is part of the KEloss package, which is included in the KASPER framework.

**Extraction of the single scattering function**

As it is displayed in Fig. 7.1, the response function for the electron gun is a superposition of the $n$-fold scattering function. In order to extract the single scattering function, it is required to perform response function measurements at three different (non-zero) column densities[1].

For these three measurements at different values of $\rho d$ (i.e. $\mu_{1,2,3} = \rho_{1,2,3} d\sigma_{\mathrm{inel}}$), a system of linear equations

$$\begin{aligned} R(E_\mathrm{s},\mu_1) - P_0(\mu_1)\cdot T_\mathrm{e}(E_\mathrm{s}) &= P_1(\mu_1)\cdot\epsilon_1(E_\mathrm{s}) + P_2(\mu_1)\cdot\epsilon_2(E_\mathrm{s}) + P_3(\mu_1)\cdot\epsilon_3(E_\mathrm{s}) \\ R(E_\mathrm{s},\mu_2) - P_0(\mu_2)\cdot T_\mathrm{e}(E_\mathrm{s}) &= P_1(\mu_2)\cdot\epsilon_1(E_\mathrm{s}) + P_2(\mu_2)\cdot\epsilon_2(E_\mathrm{s}) + P_3(\mu_2)\cdot\epsilon_3(E_\mathrm{s}) \\ R(E_\mathrm{s},\mu_3) - P_0(\mu_3)\cdot T_\mathrm{e}(E_\mathrm{s}) &= P_1(\mu_3)\cdot\epsilon_1(E_\mathrm{s}) + P_2(\mu_3)\cdot\epsilon_2(E_\mathrm{s}) + P_3(\mu_3)\cdot\epsilon_3(E_\mathrm{s}) \end{aligned} \tag{7.5}$$

can be set up, which can be expressed as matrix equation

$$\vec{R} - \vec{P_0}\cdot T_\mathrm{e}(E_\mathrm{s}) = \mathbf{P}\cdot\vec{\epsilon} \quad \text{with} \quad \mathbf{P} = \begin{pmatrix} P_1(\mu_1) & P_2(\mu_1) & P_3(\mu_1) \\ P_1(\mu_2) & P_2(\mu_2) & P_3(\mu_2) \\ P_1(\mu_3) & P_2(\mu_3) & P_3(\mu_3) \end{pmatrix} . \tag{7.6}$$

The vector $\vec{\epsilon}$ can be obtained by multiplying Eq. (7.6) with the inverse matrix $\mathbf{P}^{-1}$, i.e.

$$\vec{\epsilon} = \mathbf{P}^{-1}\cdot\left(\vec{R} - \vec{P_0}\cdot T_\mathrm{e}(E_\mathrm{s})\right) . \tag{7.7}$$

The inverse matrix $\mathbf{P}^{-1}$ is found by using the Gauss-Jordan algorithm provided in the ROOT software package [BR97].

From this inversion, the first three scattering functions can be obtained, which follow the shape of the scattering functions as included in Fig. 7.1.

**Deconvolution of the energy-loss function**

In order to obtain the energy-loss function from the single-scattering function

$$\epsilon_1(E_\mathrm{s}) = T(E_\mathrm{s}) \otimes f(\Delta E) , \tag{7.8}$$

[1] The required number of response functions is defined by the measurement interval. If the measurement interval is (significantly) larger than the threshold energy of $n$-fold scattering, also the contribution of the $n$-fold scattering function has to be considered. According to Eq. (7.5), the equation system considering the $n$-fold scattering function requires $n$ different response functions. However, it was shown in Ref. [HHW+17] that it is sufficient to consider up to three-fold scattering for the proposed measurement interval $E_\mathrm{s} < 50\,\mathrm{eV}$.

a deconvolution with the transmission function $T(E_\mathrm{s})$ is required. The shape of the latter is obtained from the reference measurement at empty source.

As the response function is measured at $N$ discrete energy intervals $U_i$, the convolution in Eq. (7.8) is

$$\epsilon_1(E - qU_i) = \sum_{j=1}^{N} T_\mathrm{e}(E - qU_i - \Delta E_j) f(\Delta E_j)\,, \tag{7.9}$$

which can be written as an $N \times N$ matrix equation

$$\vec{\epsilon_1} = \mathbf{T}_e \cdot \vec{f}\,. \tag{7.10}$$

The matrix $\mathbf{T}_e$ is lower triangular, i.e.

$$\mathbf{T}_e = \begin{pmatrix} T_\mathrm{e}(E_\mathrm{s}^1) & 0 & & & \cdots & 0 \\ T_\mathrm{e}(E_\mathrm{s}^2) & T_\mathrm{e}(E_\mathrm{s}^1) & 0 & & \cdots & 0 \\ T_\mathrm{e}(E_\mathrm{s}^3) & T_\mathrm{e}(E_\mathrm{s}^2) & T_\mathrm{e}(E_\mathrm{s}^1) & 0 & \cdots & 0 \\ \vdots & \vdots & \vdots & \vdots & \ddots & \vdots \\ T_\mathrm{e}(E_\mathrm{s}^N) & T_\mathrm{e}(E_\mathrm{s}^{N-1}) & T_\mathrm{e}(E_\mathrm{s}^{N-2}) & T_\mathrm{e}(E_\mathrm{s}^{N-3}) & \cdots & T_\mathrm{e}(E_\mathrm{s}^1) \end{pmatrix}, \tag{7.11}$$

with $E_\mathrm{s}^i = E - qU_i$. The approach of obtaining $\vec{f}$ by multiplying Eq. (7.10) with the inverse matrix $\mathbf{T}_e^{-1}$ is unfortunately not possible, as $\mathbf{T}_e$ is close to being singular and cannot be inverted numerically [HHW+17].

A common method for solving matrix equations similar to Eq. (7.10) with the matrix being singular or very close to singular is the singular value decomposition (SVD). The SVD method is based on the theorem that any $M \times N$ matrix $\mathbf{A}$ with $M \geq N$ can be written as the product of an $M \times N$ column-orthogonal matrix $\mathbf{U}$, an $N \times N$ diagonal matrix $\mathbf{W}$ with the elements $w_i \geq 0$ being the singular values, and the transpose of an $N \times N$ orthogonal matrix $\mathbf{V}$ [P+07]

$$\mathbf{A} = \mathbf{U} \cdot \mathbf{W} \cdot \mathbf{V}^T = \mathbf{U} \cdot \begin{pmatrix} w_1 & & & 0 \\ & w_2 & & \\ & & \ddots & \\ 0 & & & w_N \end{pmatrix} \cdot \mathbf{V}^T\,. \tag{7.12}$$

The inverse of the equation above can be written as

$$\mathbf{A}^{-1} = \mathbf{V} \cdot \mathbf{W}^{-1} \cdot \mathbf{U}^T = \mathbf{V} \cdot [\mathrm{diag}(1/w_i)] \cdot \mathbf{U}^T\,, \tag{7.13}$$

as $\mathbf{U}$ and $\mathbf{V}$ are orthogonal.

The transformation is only valid if the singular values are non zero, otherwise the division would cause errors. Already for small non zero values division can cause numerical rounding errors, which would give numerically unstable results. An approximation for $\vec{f}$ can still be found by setting all elements of $\mathbf{W}^{-1}$ to zero, where singular values $w_i$ are below a threshold $w_\mathrm{thr}$. The result is the so-called pseudoinverse matrix $\widetilde{\mathbf{A}}^{-1}$.

The solution of Eq. (7.10) thus is

$$\vec{f} \approx \widetilde{\mathbf{T}}_e^{-1} \cdot \vec{\epsilon_1} = \mathbf{V} \cdot \widetilde{\mathbf{W}}^{-1} \cdot \mathbf{U}^T \cdot \vec{\epsilon_1}\,. \tag{7.14}$$

However, $w_\mathrm{thr}$ is a free parameter and the best value of the latter has to be chosen depending on the input data. In the case of the deconvolution of the energy-loss function, the best value of $w_\mathrm{thr}$ is determined by using Monte Carlo simulations, which allows for a comparison

of the deconvolution result with the input energy-loss model. In Ref. [HHW$^+$17], the best deconvolution result is obtained at a threshold value of $w_{\mathrm{thr}} = 0.3\,\%$.

The results from the deconvolution process using measurement data with $D_2$ as source gas is discussed in detail in Sec. 7.3.1.

### 7.1.3 Analytical fit

A second approach of obtaining the energy-loss function from response function measurements is to perform a fit to the data by constructing a fit model including an analytical description of the energy-loss function. By performing a $\chi^2$ or negative Poisson-likelihood minimization with the parameters of the energy-loss function included as free parameters, the shape of the energy-loss function can be obtained. This method was already applied in the measurements of Aseev et al. and Abdurashitov et al. [ABB$^+$00, A$^+$17], the results of which are discussed in Sec. 4.2.

The crucial point of this approach is that the method is dependent on the choice of a suitable model, which describes the shape of the energy-loss function sufficiently well. In Refs. [ABB$^+$00, A$^+$17] the shape of the energy-loss function, as provided in Eq. (4.32) and (4.33), was purely empirical and only based on their measurement data. Based on the measurement data taken at KATRIN, an improved semi-empirical model was developed by V. Hannen and R. Sack [Sac20].

The new semi-empirical model is a piecewise model that uses three Gaussian kernels to describe the contributions from the three dominant electronic excitation states $2p\sigma\,^1\Sigma_u^+$, $2p\pi\,^1\Pi_u$, and $3p\pi\,^1\Pi_u$ (comp. Fig. 4.2) and an ionisation tail based on the BED model (see Eq. (4.28)).

The junction point is defined by the ionisation threshold energy $E_{\mathrm{ion}}$ (see Eq. (4.25)), which has to be chosen according to the used hydrogen isotope. The transition between the two functions is chosen to be continuous, which defines the amplitude of the BED tail. The model function can be written as

$$f(\Delta E, a_{1,2,3}, m_{1,2,3}, \sigma_{1,2,3}) = \begin{cases} \sum_{j=1}^{3} a_j \cdot \exp\left(-\frac{(\Delta E - m_j)^2}{2\sigma_j^2}\right) & \Delta E \leq E_{\mathrm{ion}} \\ \frac{f(E_{\mathrm{ion}})}{f_{\mathrm{BED}}(E_{\mathrm{ion}})} \cdot f_{\mathrm{BED}}(\Delta E)) & \Delta E > E_{\mathrm{ion}} \end{cases}, \tag{7.15}$$

and is fully defined by nine free parameters only, namely the amplitude $a_j$, position $m_j$, and width $\sigma_j$ of each of the three Gaussian kernels.

This new energy-loss model is used to construct the response function model as described in Eq. (7.4). Besides the nine energy-loss function parameters
$\vec{\mathcal{P}} = (a_1, m_1, \sigma_1, a_2, m_2, \sigma_2, a_3, m_3, \sigma_3)$, three nuisance parameters are required. The two parameters $A$ and $A^{\mathrm{bg}}$ are required for the normalisation of the signal component and the background component, respectively. The third nuisance parameter is the average number of scatterings $\mu = \rho d \sigma_{\mathrm{inel}}$.

As it will be discussed in detail in Sec. 8.2.1, the background component of the response function measurements is not flat but follows the shape of an integral response function. The reason for this energy dependency of the background rate is that the background electrons are being generated on the photocathode, very likely due to ion impact, and are then accelerated with the same kinetic energy as the signal electrons. However, their initial energy distribution is different compared to the energy distribution of the photoelectrons. With the energy distribution parameters $\mu_{\mathrm{E}}^{\mathrm{bg}}$ and $\sigma_{\mathrm{E}}^{\mathrm{bg}}$ as provided in Eq. (8.2), the shape of the background component $R^{\mathrm{bg}}\left(E_{\mathrm{s}}, \mu, \mu_{\mathrm{E}}^{\mathrm{bg}}, \sigma_{\mathrm{E}}^{\mathrm{bg}}, \vec{\mathcal{P}}\right)$ can be constructed as an integral response function (see Eq. (7.4)). In this case, the response function is constructed by

using an error function (see Eq. (5.10)) with the shape parameters defined by $\mu_{\mathrm{E}}^{\mathrm{bg}}$ and $\sigma_{\mathrm{E}}^{\mathrm{bg}}$ as transmission function, i.e. $T_{\mathrm{bg}}(E_{\mathrm{s}}, \mu_{\mathrm{E}}^{\mathrm{bg}}, \sigma_{\mathrm{E}}^{\mathrm{bg}}) = T_{\mathrm{erf}}(E_{\mathrm{s}}, A = 1, \mu_{\mathrm{E}}^{\mathrm{bg}}, \sigma_{\mathrm{E}}^{\mathrm{bg}}, A_{\mathrm{bg}} = 0)$.

Thus, the fit model for one response function is

$$\begin{aligned} R\left(E_{\mathrm{s}}, A, \mu, A^{\mathrm{bg}}, \vec{\mathcal{P}}\right) =& A \cdot \left(\sum_{n=0}^{n_{\max}} P_n(\mu)\epsilon_n(E_{\mathrm{s}}, \vec{\mathcal{P}})\right) \\ &+ A^{\mathrm{bg}} \cdot R^{\mathrm{bg}}\left(E_{\mathrm{s}}, \mu, \mu_E^{\mathrm{bg}}, \sigma_E^{\mathrm{bg}}, \vec{\mathcal{P}}\right) , \end{aligned} \tag{7.16}$$

with $\epsilon_n(E_{\mathrm{s}}, \vec{\mathcal{P}})$ being constructed using the analytical description of the energy-loss function $f(\Delta E, \vec{\mathcal{P}})$ (see Eq. (7.15)). The amount of scattering functions $n_{\max}$, which have to be considered in the construction of the fit, depends on the measurement interval of the response functions. In contrast to the deconvolution method, it is possible to consider all contributing scattering functions independent of the number of measured response functions. For an upper measurement range of $E_{\mathrm{s}} = 55\,\mathrm{eV}$, up to four-fold scattering is considered.

## 7.2 Response function measurements

First energy-loss measurements were performed in summer/fall 2018, when the circulation of gas inside the WGTS and the gas flow retention was first tested with deuterium as part of the so-called STS-IIIa measurement campaign [BBS+17]. The goal of the energy loss measurements with deuterium was to test the measurement principle as well as the available analysis approaches in order to obtain a first energy-loss function. The latter was required specially for the determination of the column density (see Ref. [Mar20]).

The initial measurement and deconvolution method described in Ref. [HHW+17], requires response function measurements at four different column densities (0 %, 20 %, 60 %, and 100 % $\rho_0 d$) in the range of 18 550 eV to 18 605 eV. The response functions should be measured with a step size of 0.1 V resulting in a total of 2200 measurement setpoints. At each measurement point, a total of $10^7$ electrons from the electron gun need to be emitted in order to reach the required statistical uncertainty. Thus, the measurement time is strongly depending on the electron rate of the electron gun. For an expected rate of $5 \times 10^4$ cps, which was achieved at a previous test [Sac20], a net measurement time of at least 122 h would be required. Although the required measurement is already more than five days, this time does not yet include the time, which is required to set the retarding potential of the main spectrometer and to reach stable voltage conditions. Including approximately 15 s to set each voltage point, the total measurement time was expected to require six to seven days. Hence, the measurement approach requires stable measurement conditions over several days and an electron rate $>5 \times 10^4$ cps. However, the measurement conditions did not meet these requirements, especially in terms of the required electron rate. Thus, the data taking as well as the processing of the measurement data had to be adapted accordingly, which will be discussed in Sec. 7.2.1.

The processing of the measurement data is described in Sec. 7.2.2.

### 7.2.1 Measurement approach

Due to some yet unknown reason, the electron rate of the electron gun is below the expectations of >10 kcps. Using the LDLS at its maximum rate setting (250 nm at a bandwidth of 10 nm) the electron gun provides a beam of only $1.5 \times 10^3$ cps [Sac20]. With this low rate, the measurements of the four response functions would require more than 24 weeks of measurement time, which makes the measurement impossible to be carried out as initially proposed. Additionally, rate drifts on the order of 0.2 %/h were observed

Table 7.1: Overview of the measurement settings during the response function measurements in integral mode with $D_2$ as source gas.

| Parameter | Value |
|---|---|
| Light source | InnoLas Mosquitoo 266nm pulse laser |
| Pulse frequency $f_P$ | 120 kHz |
| Trigger | external |
| Diode current | 6 A |
| Pitch angle | 0° |
| Rate | 11.8 kcps, 5.9 kcps, 11.7 kcps, and 11.4 kcps |
| Column density | 0 %, 5 %, 35 %, and 88 % of $\rho_0 d$ |
| $D_2$ purity | 96 % |
| Analysing plane setting | 1.4 G |
| Scanning strategy | Ramping of $U_{em}$; $U_{ret} = -18\,525$ V =const. |
| Scan range | $E_s$ =−5 V to 55 V |
| Ramping speed | 33.16 mV s$^{-1}$ |
| Bin width | 0.05 eV |
| Run length | 1807 s |

during the commissioning of the electron gun, which were not correlated with the drift of the light intensity. If these drifts occurred during a multi-day measurement, the resulting response function could be severely distorted. Thus, not only an increase in rate but also an optimisation of the scanning strategy is required to obtain measurement uncertainties below 0.1 %.

The modifications of the measurement approach are discussed in the following. An overview of the measurement settings is provided in Tab. 7.1.

**Light source**

In order to increase the electron rate of the electron gun, the measurements were performed with the pulsed UV laser instead of the LDLS. As the laser can provide a much higher light intensity, rates in the order of $10^4$ cps to $10^6$ cps can be achieved, depending on the laser settings [Beh17]. The limiting factor for the electrons rate is the performance of the FPD at high rates, as it is optimised for single electron detection. If the rates are too high, an overload of the preamplifier can happen, which would cause a irretrievable signal loss. Thus, a rate of 50 kcps per pixel should not be exceeded.

But even for electron rates below this threshold, the measurements are affected by detector pile-up. Especially when using the pulsed UV laser (pulse width >18 ns FWHM), the detector pile-up is higher compared to the constant wave light source, i.e. the LDLS, as electrons generated from the same light pulse commonly arrive at the detector with time differences being in the same order as the pulse width (see Chap. 6). In order to reduce the probability of multiple electrons being generated from the same light pulse a high pulse frequency of 120 kHz was chosen. At a moderately chosen electron rate of about 12 kcps, the average number of electrons generated per light pulse is 0.1, which results in about 5 % of pile-up events. For the runs at 5 % $\rho_0 d$, which were performed at the very end of the measurements, a drop in the light intensity by a factor of two was detected. The drop in the light intensity, causing a corresponding decrease in rate, can only be explained by a malfunction of the laser's optical components or the optical fibres, since the laser was operated with identical settings as for the other measurements.

**Scanning strategy**

The intrinsic rate drift, which occurred during the commissioning, would result in large uncertainties if each of the response functions was measured in one single scan. The impact of the drift on the response functions can be reduced by performing several shorter scans, where the scanning direction is alternated, so that the drifts (partly) cancel out when merging the measurements. At a drift of $0.2\,\%\,\mathrm{h}^{-1}$, a scanning length of 0.5 h is required to keep the uncertainties below 0.1 % for each of the scans. However, the waiting time, which is required to set the 550 voltage setpoints, would already exceed this timescale by far. Thus, the scanning strategy has to be optimised. In order to avoid the waiting times while the voltages at the main spectrometer and the electron gun stabilise, the method of continuous ramping was introduced. Instead of keeping the electron gun energy fixed and performing a scan with the filter voltage of the main spectrometer, the response function measurement can also be performed by keeping the filter potential fixed and changing the electron energy[2].

Setting the voltages only for the emission electrode of the electron gun is fast and multiple setpoints per second can be transmitted. Thus, a continuous ramping option was implemented into the controller (cRIO), which allows the voltage points to be set with a frequency of 2.78 Hz to obtain a smooth triangular voltage curve (see Fig. 7.2). For a more precise monitoring of the voltage ramps of the emission electrode voltage, the measurement interval of the Fluke 8846A DVM was decreased from the standard interval of 10 s to 1 s. With a measurement interval of 1 s in the 1000 V range, the device has a precision of 1 meV. The reading of the Fluke 8846A over the period of four up and down scans is displayed in Fig. 7.2, to demonstrate the perfect triangular shape.

Since the ramping of the emission electrode voltage was directly controlled via the cRIO, a proper synchronisation of the run control (i.e. the ORCA system) is not provided. Thus, the automated starting and stopping of the 1807 s long measurement runs is not completely synchronous with the turning points of the voltage ramp. In order to add a safety margin to the required data range of −5 eV to 50 eV, the upper limit of the scan range is extended to 55 eV, resulting in a scanning speed of $s = \pm 33.16\,\mathrm{mV\,s^{-1}}$.

The available measurement time of six days was split between the measurements at different column density according to the number of scans provided in Tab. 7.2. Due to the tight schedule of the STS-IIIa measurement campaign it was not possible to perform exact the same number of scans for at each column density setpoint. Especially for the measurements at empty source only one night of measurement time was available.

**Source configuration**

In addition to the integral response function measurements, a new measurement approach was tested, which allows the response functions to be measured in a differential way (see Ref. [Sac20]). As the proposed measurement demanded for a low column density of approximately 10 % in order to reduce the amount of multi-fold scatterings, the column density values of the integral measurements were adjusted in a way that the differential measurements could be performed right after the integral response function measurements at the lowest column density.

Out of this reason, the column density setpoints (in addition to the measurements at empty source) were chosen to be 15 %, 50 %, and 100 % of the nominal column density. Since

[2] As the inelastic scattering cross section $\sigma_{\mathrm{inel}}$ is energy dependent (see Eq. (4.10)), this measurement approach is only valid for small changes of the kinetic energy. For the scan range extending to 55 eV (60 eV as in the case for the measurements described in Sec. 8), a change of the cross section of 0.25 % (0.27 %) is expected from Eq. (4.9), which must be considered in the data analysis.

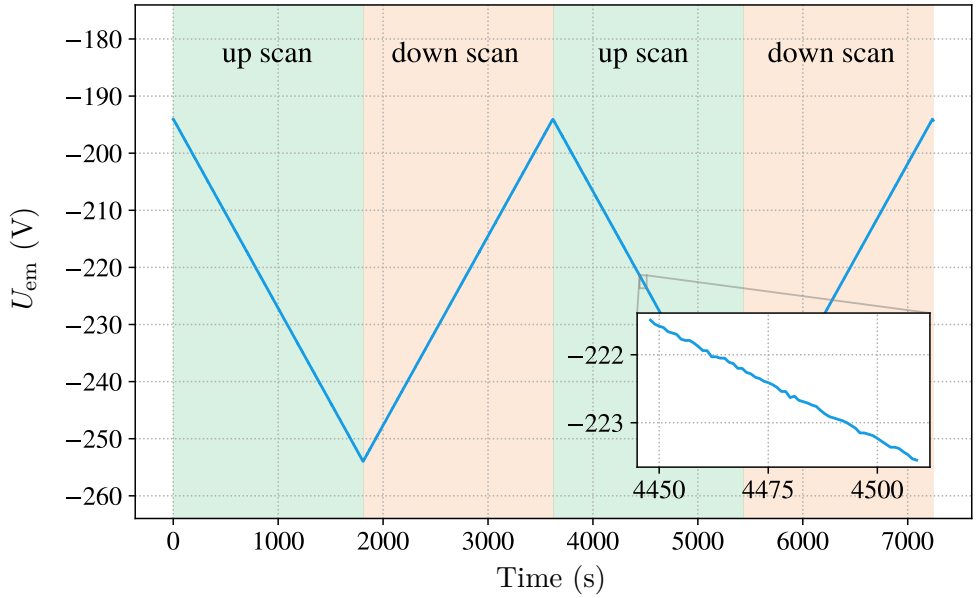


Figure 7.2: Read back of the Fluke 8846A DVM while continuously ramping the emission electrode voltage $U_{\mathrm{em}}$ of the electron gun. The ramping speed of the triangular curve is $s = \pm 33.16\,\mathrm{mV\,s^{-1}}$. The voltage points have a spread of 7.0 meV with respect to a linear fit to each of the ramps. The terminology up scans and down scans refers to the increase/decrease of the kinetic energy, which has the opposite sign as $U_{\mathrm{em}}$.

the inlet system was not yet fully calibrated, the actual values of the column density were smaller than the setpoints. The actual values of 5 %, 35 %, and 88 % were determined from the nuisance parameters $\mu_i = \rho_i d \sigma_{\mathrm{inel}}$ of the best-fit result (see Sec. 7.3.2).

#### Other configurations

As the electron gun is set to a pitch angle of approximately 0°, the width of the transmission function is dominated by the width of the energy distribution of the electron gun (comp. Chap. 5). The nevertheless non-vanishing angular distribution broadens the transmission function. In order to reduce the broadening, the magnetic field at the analysing plane was set to a 1.4 G setting instead the regular 2.7 G setting, which improves the energy resolution by approximately 5 %. This reduced magnetic field setting can only be used for measurements of the electron gun close to the symmetry axis of the main spectrometer, as the 191 T cm$^2$ flux tube becomes larger than the diameter of the spectrometer. Thus, electrons being guided on the outer region of the flux tube hit the spectrometer wall and are not transmitted. Even smaller magnetic field settings could be used for on-axis measurements with the electron gun. However, dedicated simulations are required to determine the currents of the individual coils of the LFCS (see e.g. Ref. [Erh16]). At the time of the measurement, the lowest available magnetic field setting was the 1.4 G setting.

### 7.2.2 Data processing

Due to the changed measurement strategy, up to 90 scans at each column density setting were performed, which need to be processed individually before being merged to one response function. An important part of the data processing is the binning of the data. The binnning is required, since the scans were not divided into subruns at a defined surplus

energy, as it is usually done, but they were taken as one single run covering the entire continuous voltage ramp of the emission electrode voltage. Furthermore, the single scans need to be corrected for the drifts of the light intensity and the pile-up correction (see Sec. 6) has to be applied in order to correct for the shape distortions of the response functions.

The processing of the raw measurement data is performed by using the BEANS software package, which is part of the KASPER framework. The BEANS analysis framework allows one to easily access both measurement data of the FPD as well as the continuously recorded sensor data of the monitoring devices all along the beamline.

The data processing is explained step-by-step in the following.

### Binning

In order to obtain discrete surplus energy values from the continuously ramped electron energy of the electron gun, a binning process is required.

As defined in Eq. (5.2), the surplus energy of the electron gun is defined by the difference of the inner electrode potential and the emission electrode offset voltage plus an additional offset due to the potential depression and work function differences. The offset due to the potential depression and the work function differences are expected to be constant over the measurement time and thus cause only a constant shift of the response function, which is corrected when merging the individual runs. For the binning of the continuous voltage ramp it is therefore only necessary to consider the voltage difference of the emission electrode $U_{\mathrm{em}}$ and the inner electrode system $U_{\mathrm{ie}}$. Unfortunately, the inner electrode voltage supply had a malfunction, which lowered the voltage stability. Thus, drifts and jumps of 40 meV occurred during the scan, which is investigated in detail in Ref. [Sac20]. An example of the observed drifts of the inner electrode voltage is shown in Fig. 7.3.

In order to obtain the timestamps for the boundaries of each energy bin $t(E_{\mathrm{s}})$, the inverse of the function

$$E_{\mathrm{s}}(t) = q \cdot (U_{\mathrm{em}}(t) - U_{\mathrm{ie}}(t)) \tag{7.17}$$

has to be found. For this purpose, both the slow control values $U_{\mathrm{em}}(t)$ and $U_{\mathrm{ie}}(t)$ are fit with a linear and quintic function, respectively. With this method, the surplus energy can be determined with a standard deviation of $\sigma(E_{\mathrm{s}}) = 7.0\,\mathrm{meV}$ (see Fig. A.7).

The data is first binned with a bin width of 10 mV, which allows for a better energy calibration of the individual response functions in order to compensate the energy offset due to the potential depression and the work function differences. In the merging process, the data is then rebinned to the final 50 mV binning.

### Light intensity and pile-up correction

Two corrections of systematic effects can be directly performed within the BEANS analysis code. The first essential correction step contains the pile-up reconstruction on an event basis. The pile-up correction is an essential part of the analysis in order to compensate for the up to 5 % of event losses due to detector pile-up. As the loss of signal electrons is not constant over the scanning range, distortions of the response function would be the result. The dedicated pile-up reconstruction, as introduced in Chap. 6, allows one to estimate the event multiplicity $\hat{\mathcal{M}}$ based on the event energy $E_{\mathrm{FPD}}$ and the bipolar width $w_{\mathrm{bi}}$, which is obtained from the trapezoidal filter system of the FPD for each of the event signals.

The second reconstruction step is the correction for drifts of the light intensity of the laser (see Secs. 5.2.2 and 5.3.2). The correction is performed on a subrun basis, using the

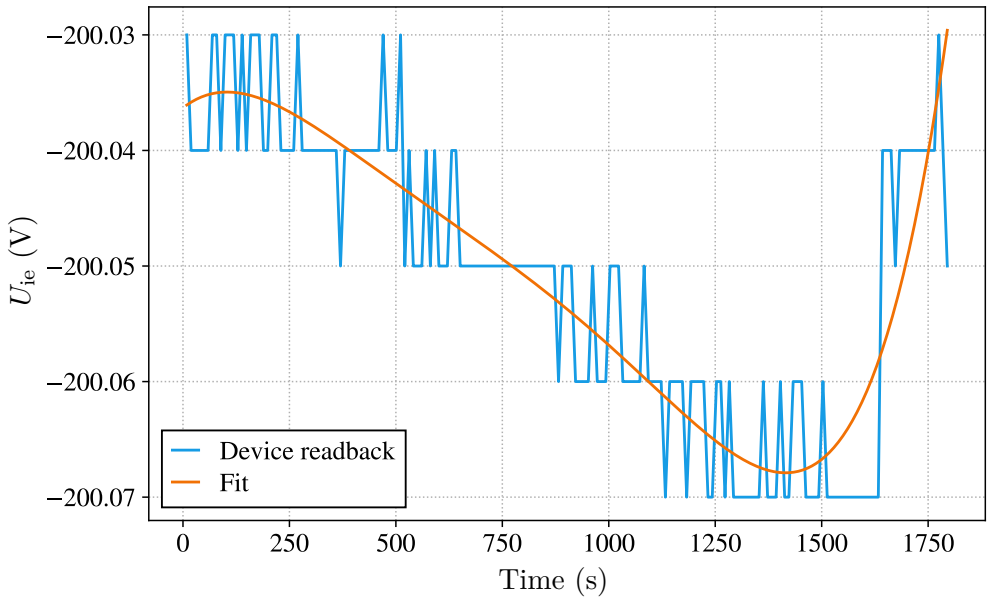


Figure 7.3: Exemplary course of the inner electrode voltage $U_{\mathrm{ie}}$ during run 43418. The readback of the voltage supply shows a continuous drift of up to 40 mV, followed by a jump of the same order during one run. A fifth-degree polynomial is fitted to the data to approximate the drift by an analytical function.

continuously recorded intensity values of the photodiode[3], which is connected with a fibre splitter to the output of the laser (see Fig. 5.3).

Both correction steps are described in the following.

- **Pile-up correction**
  For the measurements at each of the different column density settings, a dedicated look-up table is generated from simulations (see Chap. 6) and is used in the analysis.

  The data is corrected by weighting each detector event with the corresponding multiplicity estimate determined from the look-up table. Where a remaining ambiguity of the event multiplicity exits, the multiplicity is drawn from the provided probability distribution $\hat{\mathcal{M}}(E_{\mathrm{FPD}}, w_{\mathrm{bi}})$ instead of only selecting the most probable value.

  The impact of the pile-up correction is visible in Fig. 7.4, where the pile-up corrected and the pile-up uncorrected response functions are shown. The differences show a complex structure, which agrees with the predictions of Fig. 6.3. The differences reach up to 5 %. Due to the significant shape distortion especially in the region where the scattered electrons contribute to the response function, the determination of the energy-loss function from the response functions would be impossible without the pile-up correction.

- **Diode correction**
  The correction of the drifts of the light intensity of the laser are performed as described in Sec. 5.3.2.

  However, the intensity values $I$ need to be interpolated from the 1 s readout intervals of the photodiode, since the subrun length of the 10 mV bins is about 0.3 s and thus

[3]KATRIN number `111-AAI-0-2601-0001`

smaller than the sensor reading interval. The obtained number of events $N$ of each bin is then corrected by the relative intensity deviation with respect to the average intensity $\langle I \rangle$ over the length of the run

$$\tilde{N} = N \cdot \frac{\langle I \rangle}{I} \,. \tag{7.18}$$

Since the intensity monitoring system has a Gaussian uncertainty of $\sigma_\mathrm{I} = 0.4\,\%$ when using the pulsed laser, the uncertainty on the readout values is propagated via Gaussian error propagation during the correction (see Sec. A.1). Hence, the resulting uncertainties of the data points are not purely Poissonian anymore and thus need to be propagated via Gaussian error propagation in the following steps.

**Merging**

The individually processed runs are merged into one single response function. Due to the energy offset caused by the voltage depression of the inner electrode system and the differences of the work function between the photocathode and the main spectrometer, an energy calibration of each scan is required. To do so, the position of each transmission function is determined from an error function fit yielding the position parameter $\mu_\mathrm{erf}$. The entire response function is then shifted by the value of $\mu_\mathrm{erf}$ so that the centre of the transmission function (i.e. $\mu_\mathrm{erf}$) is located at zero. As the data is binned in 10 meV steps, a linear interpolation between the bin values is applied in order to shift the data points with higher precision than the bin size. This interpolation is required, since the binning scheme has to be the same for all runs in order to merge the data.

The entries of the individual runs for each bin are then summed up and rebinned to 50 meV bin width, with the bin centres being located at $(...; -50; 0.0; 50; 100; ...)\,\mathrm{meV}$[4]. During the interpolation, summation, and rebinning, the uncertainties are propagated to obtain the uncertainty $\sigma_\mathrm{N}$ on the data points (see Sec. A.1).

Due to the uncertainty on the continuously ramped surplus energy $\sigma(E_\mathrm{s}) = 7.0\,\mathrm{mV}$, an uncertainty on the surplus energy values of the data point has to be taken into account. In order to convert the uncertainties on the surplus energy into uncertainties on the counts, the slope of the response functions for each data point is required, which is determined from the slope of the two neighbouring data points. The additional uncertainty on the counts is obtained by multiplying the slope with $\sigma(E_\mathrm{s})$. This uncertainty is then added quadratically with $\sigma_\mathrm{N}$ to obtain the final uncertainty

$$\sigma_\mathrm{tot} = \sqrt{\sigma_\mathrm{N}^2 + \left(\sigma(E_\mathrm{s}) \cdot s_i\right)^2} \,, \tag{7.19}$$

which is described in more detail in Sec. A.1. The additional contribution to the uncertainty has the largest influence at the middle of the transmission function (i.e. $E_\mathrm{s} = 0\,\mathrm{eV}$).

The number of scans and the total amount of emitted electrons per 50 meV bin are listed in Tab. 7.2. The final response functions are displayed in Fig. 7.4, with the influence of the energy loss due to scattering with the source gas being clearly visible. However, each of the response functions show a decrease of approximately 1.5 % of the counts right after the transmission edge, which is not expected in integral measurements. The origin of this rate decrease is still unresolved. Possible causes could be the pile-up reconstruction or that the beam was partly obstructed by the off-axis aperture inside the rear section. Such energy

[4] The correct choice of the binning pattern is important especially with the analysis of the measurement data by performing a analytical fit. If the bin centres are chosen to be at $(...; -75; -25; 25; 75; ...)\,\mathrm{meV}$ , the output of the discrete convolutions is shifted by half the bin width.

Table 7.2: Overview of the key properties of the integral response functions, which were measured at four different column densities with $D_2$ as source gas. The mean number of scatterings $\mu$, the number of scans $\Sigma$, the average rate of the electron gun $R_{\mathrm{egun}}$ as well as the total emitted number of electrons $N_{\mathrm{tot}}$ per 50 meV bin are provided for each column density setting. A data range of −3 eV to 50 eV is chosen to be the quality selected region.

| Column density / $\rho_0 d$ | $\mu$ | $\Sigma$ | $R_{\mathrm{egun}}$ /(kcps) | $N_{\mathrm{tot}}$ |
|---|---|---|---|---|
| 0 % | 0.00 | 27 | 11.8 | $4.8 \times 10^5$ |
| 5 % | 0.095 | 90 | 5.9 | $8.0 \times 10^5$ |
| 35 % | 0.64 | 71 | 11.6 | $1.3 \times 10^6$ |
| 88 % | 1.60 | 89 | 11.4 | $1.5 \times 10^6$ |

dependent obstructions have been observed during other measurements and can be caused due to the energy dependency of the $\vec{E} \times \vec{B}$ drift inside the dipole electrodes at the rear section.

## 7.3 Determination of the energy-loss function

Two different analysis approaches exist for the determination of the energy-loss function from the measured response functions, which are introduced in Sec. 7.1. Both the deconvolution approach as well as the analytical fit, which will be discussed in Secs. 7.3.1 and 7.3.2, use the same set of response functions shown in Fig. 7.4.

Besides the integral response functions, an additional differential response function is available, which was measured by making use of the time-of-flight (ToF) of the electrons. This differential measurement was analysed by R. Sack (University of Münster), with a detailed description of the measurement approach and the data analysis being available in Ref. [Sac20]. A brief introduction to the measurement approach is provided in Sec. 7.3.3.1. This differential response function is included in the analytical fit, the result of which is discussed in Sec. 7.3.3. The fit to the combined data set using only two of the three integral response functions and the differential response function is also discussed in Ref. [Sac20]. The results presented in Sec. 7.3.3 are obtained from a fit including all three available integral response functions. Moreover, the processing of both the integral and the differential data as well as the fit model were improved.

### 7.3.1 Deconvolution

The response functions shown in Fig. 7.4 can be used to deconvolve the energy-loss function from the measurement data by using the SVD deconvolution method, as described in Sec. 7.1.2. The deconvolution of the energy-loss function from the set of integral response functions was first carried out by K. Debowski in his master's thesis [Deb19]. However, the deconvolution result discussed in Ref. [Deb19] were obtained from a preliminary data set. With the enhanced pile-up correction and data processing discussed in Chap. 6 and Sec. 7.2.2, the quality of the data set presented in this work further improved. Thus, a re-analysis of the data using the SVD deconvolution is required, which is discussed in the following.

Before the deconvolution can be performed, the optimal value of the threshold parameter $w_{\mathrm{thr}}$ has to be determined. The latter is influenced by the statistics and the column density settings of the response functions as well as by the size of the voltage steps. In addition to the differences of the statistics and the column density compared to Ref. [HHW$^+$17] (resulting from the measurement conditions) also the size of the voltages steps was modified.

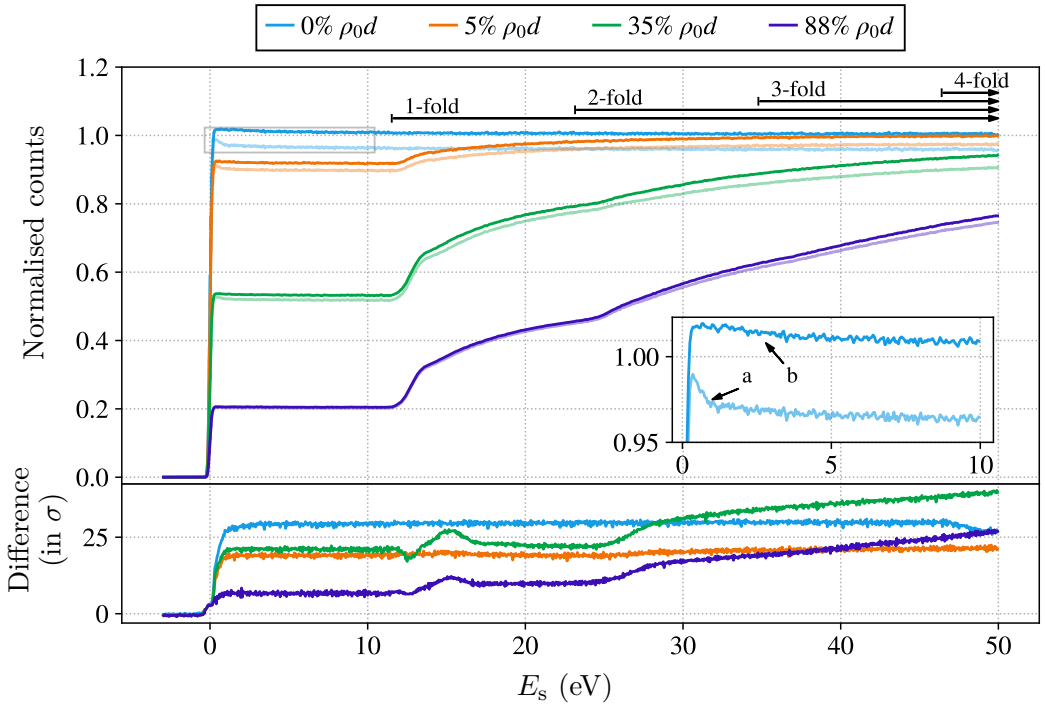


Figure 7.4: Overview of the measured response functions after processing the data as described in Sec. 7.2.2. The contributions of $n$-fold scatterings to the transmission function are visible and are indicated with the arrows at the top. For a better presentation, the response functions are normalised so that the amount of unscattered electrons (i.e. the plateau region $E_s = [1\,\text{eV}, 10\,\text{eV}]$) equals the scattering probability $P_0(\mu_i)$. For each of the pile-up corrected response functions, the corresponding response function without correction is drawn with reduced opacity. A significant signal loss of up to 5 % due to pile-up events is visible, which is depending on the rate of transmitted electrons (compare the differences at the plateau region). The difference between the uncorrected and the corrected response functions (relative to the uncertainty $\sigma$ of the data points ) is drawn in the bottom panel. The detail view in the top panel shows the upper region of the transmission function measured at empty source. Besides the distortion of the uncorrected response function (arrow a), there is a distortion of the corrected response function visible (arrow b). The decrease of the counts above the transmission edge $0 \lesssim E_s \lesssim 3$ by approximately 1.5 % is not expected for integral data. This distortion is also visible in the other response functions.

The latter was chosen to be 50 mV instead of the initially proposed 100 meV steps, since it was shown in Ref. [Deb19], that a smaller binning improves the deconvolution results.

The optimal value of $w_{\mathrm{thr}}$ can only be determined from Monte Carlo simulations. After $w_{\mathrm{thr}}$ has been determined, the energy-loss function can be deconvolved from the measurement data.

**Determination of $w_{\mathrm{thr}}$**

In order to determine the optimal value of $w_{\mathrm{thr}}$, Monte Carlo simulations of the measurements are performed by using the KEloss framework. Based on the parameters listed in Tab. 7.2 a total of 1000 response functions for each column density are simulated with the energy losses due to inelastic scattering being sampled from the literature-based Glück model (see Sec. 4.2). Each of the simulated response functions is then deconvolved using the SVD deconvolution algorithm of the Keloss framework, as explained in Sec. 7.1.2. The deconvolutions are carried out for different values of $w_{\mathrm{thr}}$ in the range of 0.3 % to 1.7 % in steps of 0.1%. A selection of three of the deconvolution results for a selected set of threshold values are shown in Fig. 7.5 together with the $1\sigma$ belt of the complete set of simulations. The result shows a decrease of noise with increasing $w_{\mathrm{thr}}$. But as the noise is decreased systematic oscillations become dominant for values above $w_{\mathrm{thr}} = 1.1\,\%$. Furthermore, the height of the peak of the electronic excitation states, decreases with increasing values of $w_{\mathrm{thr}}$.

In order to determine the threshold value, where the input model and the deconvolution result agree best, the Euclidean norm between the vector of data points from the input model $\vec{f}_{\mathrm{i}}(\Delta E)$ and the deconvolution result $\vec{f}_{\mathrm{d}}(\Delta E)$ is calculated. As shown in Fig. 7.6, a minimum is obtained at a threshold value of $w_{\mathrm{thr}} = 1.1\,\%$. The new determined value is more than three times larger than the initially proposed threshold value of $w_{\mathrm{thr}} = 0.3\,\%$, which is a result of the reduced statistics of the measurement data.

**Deconvolution**

Before the actual deconvolution can be performed, the three scattering functions $\epsilon_n$ are extracted from the three response function measurements at non-empty source. The obtained scattering functions are shown in the middle row of Fig. 7.7, together with the scattering function obtained from the inversion of the simulation data.

Comparing the scattering functions of the measurement data to the scattering functions from the MC simulations, a distortion of all three scattering functions in the range of 0 eV to 10 eV is visible. The reason for this distortion can be explained by the systematic distortions of the response functions next to the transmission edge (see detail b in Fig. 7.4). However, the effect is least prominent for $\epsilon_1$. As only the scattering function $\epsilon_1$ is required for the deconvolution step, the deconvolution can still be performed.

The energy-loss function is deconvolved from the single scattering function using the SVD deconvolution with the determined threshold value of $w_{\mathrm{thr}} = 1.1\,\%$. The deconvolution result for the measurement data is shown in the bottom row of Fig. 7.7.

As expected from the simulations, the deconvolution result shows one dominant peak, which can be assigned to the electronic excitation states. The peak is located at 12.78(3) eV and has a height of $0.22(1)\,\mathrm{eV}^{-1}$, which is determined by fitting a Gaussian kernel to the tip of the peak. However, the other parts of the deconvolved energy-loss function are affected by the periodic oscillations, which does not allow to determine the exact shape of the ionisation tail.

The energy-loss function shows a large negative and unphysical oscillation around $\Delta E = 0\,\mathrm{eV}$. This structure is very likely caused by the distortion of the response function close to the

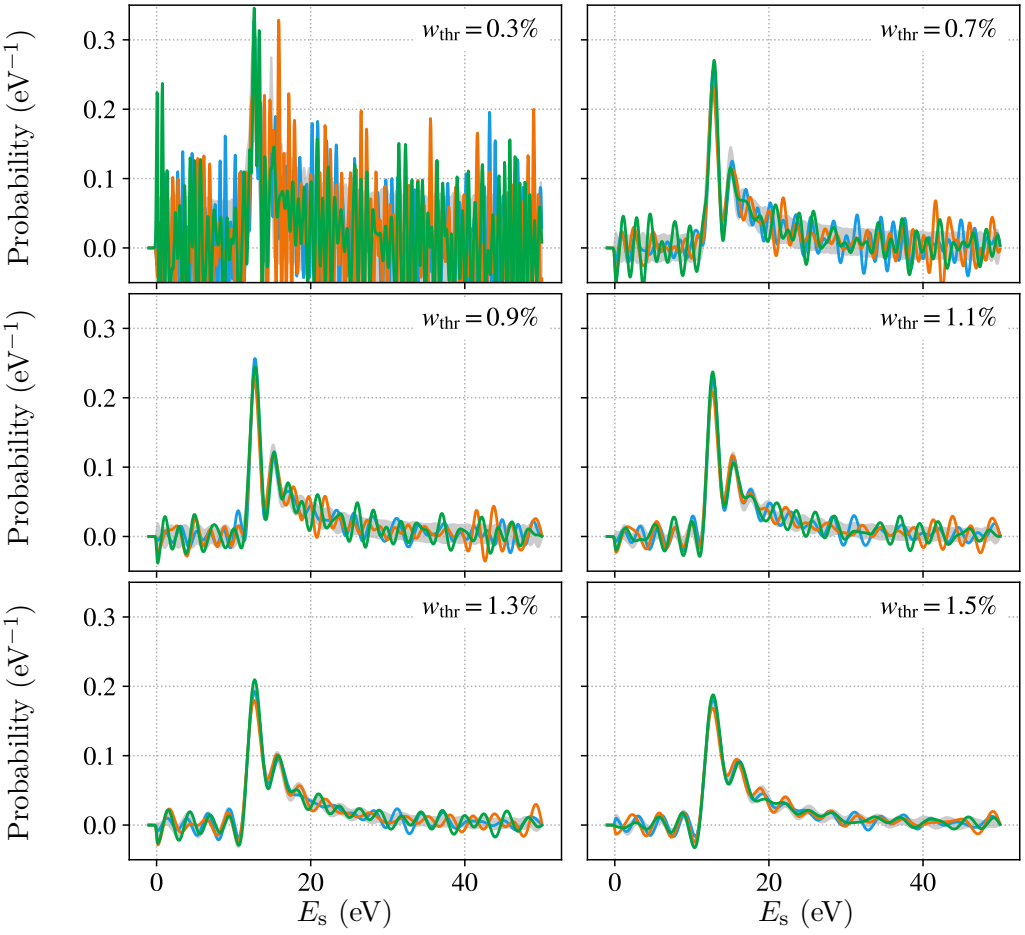


Figure 7.5: Deconvolution results using MC data for different values of $w_{thr}$. For each value of $w_{thr}$ three arbitrary chosen deconvolution results are displayed as well as the $1\sigma$ interval of the total amount of 1000 deconvolution results (grey). The noise as well as the $1\sigma$ uncertainty decreases with increasing $w_{thr}$. For values above $w_{thr} = 1.1\,\%$ systematic oscillation become dominant, which is visible in the oscillating shape of the $1\sigma$ band. Furthermore, the increase of the threshold value causes a decrease of the height of the peak of the electronic excitation states.

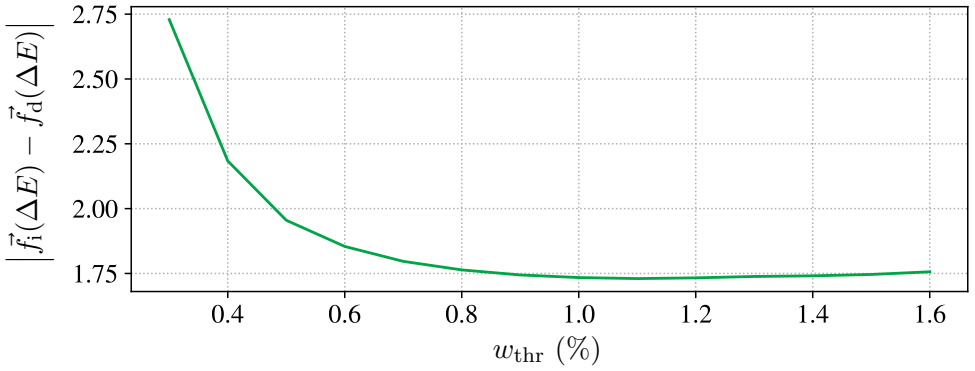


Figure 7.6: Euclidean norm of the difference between the shape of the input model and the deconvolution result of the energy-loss function for different threshold values $w_{\mathrm{thr}}$. A minimal difference between the two models is obtained at a value of $w_{\mathrm{thr}} = 1.1\,\%$.

transmission edge. Although the single scattering function seems to be unaffected from this systematic effect, the final deconvolution step uses the transmission function measured at empty source, which again is affected from this systematic.

Comparing the deconvolution result with the existing empirical Abdurashitov et al. model [A$^+$17], the height and position of the first excitation peak agrees well with the corresponding mean 12.80(4) eV and amplitude 0.25(2) eV of the Gaussian part of the Abdurashitov et al. model, which is displayed in Fig. 7.8. For a better comparison of the shape of the ionisation tail, the periodic oscillations are damped by applying a floating average of 5 eV to the data above the ionisation threshold energy of $E_{\mathrm{ion}}(\mathrm{D}_2) = 15.470\,\mathrm{eV}$. The smoothed ionisation tail is included in Fig. 7.8, where it can be seen that the average shape of the ionisation tail is in agreement with the model of Abdurashitov et al..

The deconvolution results will be compared with the results of the analytical fit in Sec. 7.4, where the resulting uncertainty on the KATRIN observable $m_\nu^2$ is discussed.

### 7.3.2 Fit to the integral response functions

A different analysis approach than the initially proposed method of SVD deconvolution is to perform a combined fit to the measurement data with the fit model including an analytical description of the energy-loss function as discussed in Sec. 7.1.3. This analysis approach was already applied in the analyses of Aseev et al. and Abdurashitov et al. [ABB$^+$00, A$^+$17].

However, the determination of the energy-loss function from a fit is model dependent and it is thus important to chose a suitable model. As discussed in Sec. 4.2 there are different models available including the empirical parametrisations of Aseev et al. and Abdurashitov et al. as well as the literature based energy-loss model for deuterium of N. Trost [Tro19]. In principle, both models could be used as energy-loss function models for the construction of the fit function to the integral response functions. However, the shapes of the models do not agree well with the measurement data, which can be demonstrated by comparing or fitting the models to the differential response function data (comp. Figs. A.8 and A.9). The semi-empirical energy-loss function model of Eq. (7.15), which was developed based on the KATRIN measurement data, describes the data much better and is thus used for the fit to the integral response functions.

Since three response functions at different column densities are available, a combined fit to the three response functions is carried out yielding the shape parameters of the energy-loss function model.

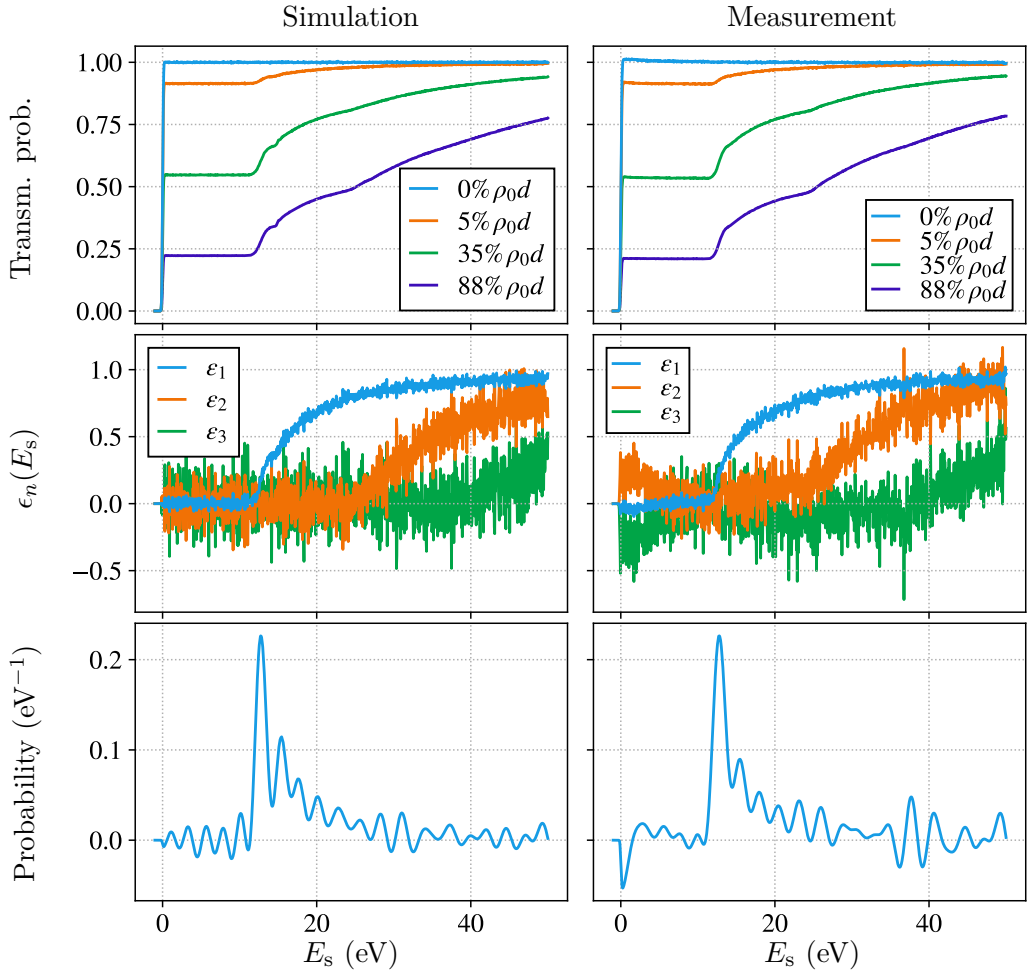


Figure 7.7: Deconvolution results for MC data (left) and the actual measurement data (right). The top row shows the transmission function used for the deconvolution. In the case of the measurement data, the response functions shows a small slope towards the transmission edge, which is very likely an artefact of the pile-up reconstruction. The middle row shows the extracted scattering functions for one-fold to three-fold scatterings. The scattering functions of the measurement data show a similar distortion towards 0 eV as the response functions. The bottom row shows the deconvolution results for $w_{\mathrm{th}} = 1.1\,\%$.

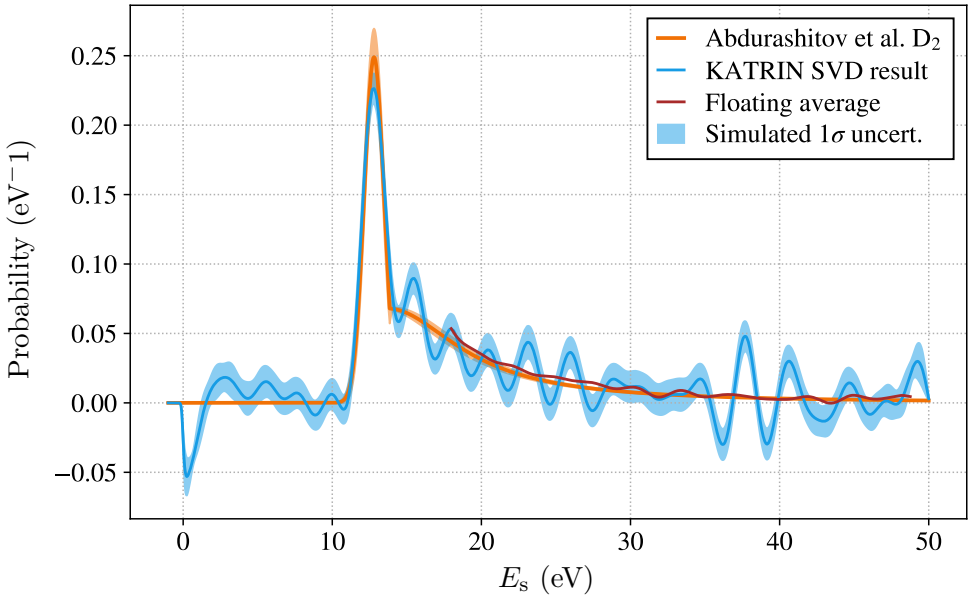


Figure 7.8: Result of the SVD deconvolution including the $1\sigma$ uncertainty interval as obtained from MC simulations. The position and height of the excitation peak agrees well with the Abdurashitov et al. model [A+17], but for higher energies, the shape of the energy-loss function is superimposed by systematic oscillations. By applying a floating average to the data with a window size of 5 eV for the region above the ionisation threshold energy of $E_{\mathrm{ion}}(\mathrm{D}_2) = 15.470\,\mathrm{eV}$, the shape of the ionisation tail can be reconstructed. The smoothed ionisation tail agrees well with the measurements of Abdurashitov et al..

The construction of the combined fit function as well as the obtained measurement results are discussed in the following sections.

#### 7.3.2.1 Fit model and likelihood function

Although it is possible to fit the response functions individually, one would obtain three different sets of best fit values for the included energy-loss function parameters. Thus, a combined fit is preferred, where the fit result gives only one set of energy-loss function parameters, which matches all three data sets the best. In order to determine this best fit value, a likelihood function needs to be constructed, which will be minimised. The fit model for each response function is generated using the fit function in Eq. (8.1), which is defined by the nine energy-loss function parameters $\vec{\mathcal{P}}$ as well as three nuisance parameters for the signal amplitude $A_i$, the average number of scatterings $\mu_i$, and the background amplitude $A_i^{\mathrm{bg}}$. However, the fit function in Eq. (8.1) is only valid if the kinetic energy of the electrons is constant. Due to the scanning strategy, which was used for the response function measurements, the kinetic energy of the electrons was continuously changed. Thus, the fit model has to be corrected.

Furthermore, the transmission function has to be defined in order to construct the fit model and to calculate the likelihood function.

**Fit model**

The change of the kinetic energy of the electrons during the response function measurements causes both a change in the shape of the model of the ionisation tail as well as a change of the inelastic cross section.

The change of the shape of the BED model (see Eq. (4.28)), causes a distortion of the ionisation tail on the order of $10^{-5}$, as it can be seen in Fig. 7.9.

The more dominant effect is the change of the inelastic cross section $\sigma_{\mathrm{inel}}(E_{\mathrm{kin}}^{\mathrm{nr}})$ (see Eq. (4.9). As the kinetic energy is increased by 55 eV, the cross section decreases by 0.25 % (see Fig. 7.9). This systematic decrease influences the probability distribution for $n$-fold scattering $P_n(\mu)$ (see Eq. (4.34)) and thus causes a distortion of the response function.

Both effects can be considered in the construction of the fit model.

In order to correct for the change of $\sigma_{\mathrm{inel}}(E_{\mathrm{kin}}^{\mathrm{nr}})$, the ratio of the cross section at the transmission function (i.e. $E_{\mathrm{kin}} = qU_{\mathrm{ret}}$) and at the surplus energy of $E_{\mathrm{s}}$ is calculated by using Eq. (4.9). As Eq. (4.9) requires the non-relativistic kinetic energy, the relativistic kinetic energy has to be first converted to the non-relativistic energy according to Eq. (4.4), which is indicated by the index nr. This ratio of the two cross sections as a function of the surplus energy

$$\delta\sigma_{\mathrm{inel}}(\mathrm{E_s}) = \frac{\sigma_{\mathrm{inel}}\left((qU_{\mathrm{ret}} + E_{\mathrm{s}})_{\mathrm{nr}}\right)}{\sigma_{\mathrm{inel}}\left((qU_{\mathrm{ret}})_{\mathrm{nr}}\right)} \tag{7.20}$$

is drawn in Fig. 7.9. This scaling function is then used to correct the value of the scattering probabilities $P_n(\mu)$ for each surplus energy, i.e.

$$P_n(\mu, E_{\mathrm{s}}) = P_n(\mu \cdot \delta\sigma_{\mathrm{inel}}(E_{\mathrm{s}}))\,. \tag{7.21}$$

Similar as for the correction of the cross section, a scaling function for the shape of the ionisation tail

$$\delta f_{\mathrm{BED}}(E_{\mathrm{s}}, E_{\mathrm{kin}}) = \begin{cases} 1 & E_{\mathrm{s}} \leq E_{\mathrm{ion}} \\ \frac{f_{\mathrm{BED}}(E_{\mathrm{s}}, qU_{\mathrm{ret}}+E_{\mathrm{s}})}{f_{\mathrm{BED}}(E_{\mathrm{s}}, qU_{\mathrm{ret}})} \cdot \frac{f_{\mathrm{BED}}(E_{\mathrm{ion}}, qU_{\mathrm{ret}})}{f_{\mathrm{BED}}(E_{\mathrm{ion}}, qU_{\mathrm{ret}}+E_{\mathrm{s}})} & E_{\mathrm{s}} > E_{\mathrm{ion}} \end{cases} \tag{7.22}$$

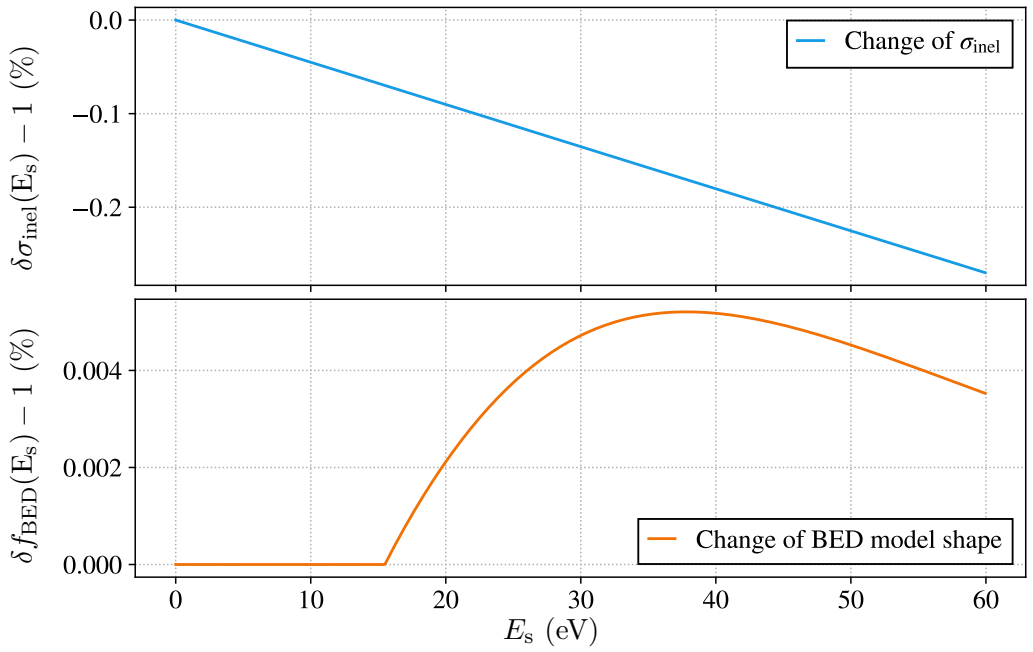


Figure 7.9: Relative changes of $\sigma_{\mathrm{inel}}(T)$ (top) and $f_{\mathrm{BED}}(E_{\mathrm{s}}, E_{\mathrm{kin}})$ (bottom) due to the change of the kinetic energy of the electrons during the measurements of the response functions.

is calculated, which is shown in Fig. 7.9. The second factor in the equation is required to ensure the continuity of the energy-loss function at the junction point $\Delta E = E_{\mathrm{ion}}$. This scaling function $\delta f_{\mathrm{BED}}(E_{\mathrm{s}}, E_{\mathrm{kin}})$ is used to correct the shape of the energy-loss function $f(\Delta E, \vec{\mathcal{P}})$, which gives

$$\tilde{f}(\Delta E, \vec{\mathcal{P}}) = f(\Delta E, \vec{\mathcal{P}}) \cdot \delta f_{\mathrm{BED}}(E_{\mathrm{s}}, E_{\mathrm{kin}})\,. \tag{7.23}$$

The fit function for the $i$-th data set thus becomes

$$\begin{aligned} R_i\left(E_{\mathrm{s}}, A_i, \mu_i, A_i^{\mathrm{bg}}, \vec{\mathcal{P}}\right) =& A_i \cdot \left(\sum_{n=0}^{4} P_n(\mu_i, E_{\mathrm{s}})\tilde{\epsilon}_n(E_{\mathrm{s}}, \vec{\mathcal{P}})\right) \\ &+ A_i^{\mathrm{bg}} \cdot R_i^{\mathrm{bg}}\left(E_{\mathrm{s}}, \mu_i, \mu_E^{\mathrm{bg}}, \sigma_E^{\mathrm{bg}}, \vec{\mathcal{P}}\right)\,, \end{aligned} \tag{7.24}$$

with $\tilde{\epsilon}_n(E_{\mathrm{s}}, \vec{\mathcal{P}})$ being the $n$-fold scattering functions (comp. Eq. (7.3)) using $\tilde{f}(\Delta E, \vec{\mathcal{P}})$ instead of $f(\Delta E, \vec{\mathcal{P}})$. The same corrections are applied to the integral background component $R_i^{\mathrm{bg}}\left(E_{\mathrm{s}}, \mu_i, \mu_E^{\mathrm{bg}}, \sigma_E^{\mathrm{bg}}, \vec{\mathcal{P}}\right)$.

### Transmission function model

The scattering functions $\tilde{\epsilon}_n(E_{\mathrm{s}}, \vec{\mathcal{P}})$ in Eq. (7.24) describe the contribution of the $n$-fold scattered electrons to the response function. The scattering functions are constructed by convolving the energy-loss function $n$ times with itself in order to describe the probability distribution for the energy loss from $n$ scatterings. In order to take the transmission properties of the electrons in the main spectrometer into account, a convolution with the transmission function of the electron gun $T_{\mathrm{e}}(E_{\mathrm{s}})$ is required (comp. Eq. (7.3)). Hence, the construction of the fit function requires a precise model of the transmission function. In principle, $T_{\mathrm{e}}(E_{\mathrm{s}})$ can be analytically described by an error function (see Sec. 5.3) and the shape properties can be obtained from a fit to the reference measurement at empty source.

But due to the distortions of the response function close to the transmission edge (see Fig. 7.4), the approximation of the transmission function with an error function results in significant structures in the residuals (see Fig. A.10). Thus, no analytical function is used, but the fit function is constructed by directly using the measurement data of the reference measurement at empty source. This has the benefit, that no model is required to describe the distortions. However, it has to be considered that the fit function is also affected by statistical fluctuations, which causes a systematic increase of the $\chi^2$. By performing Monte Carlo simulations of the measurement and the analysis, it can be shown that an increased value of $\chi^2/N_{\mathrm{dof}} = 1.91(6)$ is expected.

**Likelihood function**

Since the uncertainties on the data points of the response function measurements are not Poisson distributed but follow a Gaussian distribution due to the correction of the photo diode and the uncertainties on the surplus voltage (see Sec. 7.2.2), a $\chi^2$ function instead of a negative Poisson-likelihood function is used for the minimisation.

The $\chi^2$ function is

$$\chi^2\left(\sum_i^3 \left\{A_i, \mu_i, A_i^{\mathrm{bg}}\right\}, \vec{\mathcal{P}}\right) = \sum_i^3 \sum_{E_\mathrm{s}} \left(\frac{y_i(E_\mathrm{s}) - R_i\left(E, A_i, \mu_i, A_i^{\mathrm{bg}}, \vec{\mathcal{P}}\right)}{\sigma_\mathrm{i}(E_\mathrm{s})}\right)^2 , \tag{7.25}$$

with $y_i(E_\mathrm{s})$ and $\sigma_\mathrm{i}(E_\mathrm{s})$ being the measurement value and the uncertainty at the energy value $E_\mathrm{s}$ of the $i$-th data set and $R_i\left(E_\mathrm{s}, A_i, \mu_i, A_i^{\mathrm{bg}}, \vec{\mathcal{P}}\right)$ the corresponding value of the fit model. Using the function value at the bin centre for the calculation of the likelihood function is only an approximation, since the binning of the continuous voltage scans actually requires the calculation of the integral of the fit function within the bin edges. However, with a very fine binning, the inhomogeneity of the data and the fit model within the bin edges becomes negligible. The validity of this approximation for a binning of 50 meV can be confirmed by dedicated Monte Carlo simulations, which are described in Sec. 8.5.3.

A pull term

$$p = \left[\left(\int_0^{E_{\max}} f(E)\ \mathrm{d}E - 1\right) \cdot 10^4\right]^2 \tag{7.26}$$

is added to the $\chi^2$ function in order to ensure that the resulting energy-loss function is properly normalised to 1 over the integration range $E = [0, E_{\max}]$ with a precision of $10^{-4}$. The upper boundary $E_{\max} = 0.5 \cdot (E_{\mathrm{kin}} - E_{\mathrm{ion}}(D_2))$ is defined by the limit of the ionisation tail (see Sec. 4.1.2.3).

For the combined fit of the three integral response functions, a total of 18 free parameters need to be minimised. Since the rate as well as the measurement times were not identical for the individual data sets, their signal amplitudes are different. For a more convenient choice of the initial parameters of the normalisation constant $A_i$ and $A_i^{\mathrm{bg}}$, the data sets are normalised so that the last data point within the fit range equals 1. The normalisation constants are provided in Tab. A.2.

For the construction of the fit model and the combined likelihood function, a dedicated python fitting module is developed. The aim of the `fitter` module is to provide a modular fitting program, which allows one to add any amount of response functions with the possibility to individually set basic properties, such as the fit range of the transmission function model of the data sets. The `fitter` module uses `iminuit` [DPD+20], which is a python binding of the MINUIT2 C++ library [JR75]. By using `iminuit`, it is possible to

access MIGRAD, which is a fast and robust minimisation algorithm. Hence, the latter will be used for the minimisation of the $\chi^2$ function.

An introduction to the `fitter` module is provided in Sec. A.2.

#### 7.3.2.2 Fit result

For the combined $\chi^2$ fit of the three integral response functions, a fit range of $E_\mathrm{s} = [-1, 50]$ eV is chosen, which results in a total of 3060 data points contributing to the likelihood function. The statistics of each of the data points above the transmission edge range from $10^5$ counts to $10^6$ counts (see Tab. 7.2).

The best fit result for the successful minimisation[5] of the 18 free parameters with MIGRAD is displayed in Fig. 7.10 together with the normalised residuals of each of the data points. Since the fit model is constructed by using the transmission function measurements at empty source, the distortions of the response functions close to the transmission edge (comp. Fig. 7.4) is considered. This makes the fit function agree better with the measurement data compared to a fit result using an analytical transmission function shown in Fig. A.10, where deviations of the residuals of more than $2.5\sigma$ are visible. However, even when using the measurement data to construct the fit function, structures in the residuals remain visible. Especially in the range below 30 eV, the residuals of all data sets are first shifted upwards and are then systematically shifted downwards, before the residuals level out around zero for $E_\mathrm{s} > 30$ eV.

The deviations in the residuals for regions below the excitation threshold energy of approximately 11 eV can only be caused due to differences between the shape of the response function and the transmission function measured at empty source. Since the structures in the residuals continue smoothly in the region above the excitation threshold, the deviations are very likely caused due to the differences in the transmission function measurement and not due to the shape of the empirical model of the energy-loss function.

The goodness of fit can be tested by dividing the obtained minimum of the $\chi^2$ value by the degrees of freedom, as the sum of $n$ normal distributed variables follows a $\chi^2$ distribution with the expectation value $n$ (see e.g. Ref. [Lis17]). Thus, if $\chi^2/N_\mathrm{dof}$ deviates significantly from 1, either the fit model or the uncertainties of the data points do not match the measurement data. Since the variance of the $\chi^2$ distribution is $2N_\mathrm{dof}$ and can be approximated by a Gaussian for large $N_\mathrm{dof}$, the $1\sigma$ interval of $\chi^2/N_\mathrm{dof}$ is calculated as $\sqrt{2/N_\mathrm{dof}}$.

With a minimum $\chi^2$ value of $\chi^2 = 5138.23$ at a total of 3060 data points and 18 free fit parameters, a reduced $\chi^2$ value of

$$\frac{\chi^2}{N_\mathrm{dof}} = \frac{5163.36}{3042} = 1.70(3) \tag{7.27}$$

is obtained. As it is expected from the Monte Carlo simulations, the value of $\chi^2/N_\mathrm{dof}$ is increased due the construction of the fit model by using measurement data. However, the obtained value is slightly smaller than the expected value of 1.91(6) as obtained from Monte Carlo simulations.

The obtained best-fit parameters for the nine energy-loss function parameters as well as the nine nuisance parameters are provided in Tab. 7.3. Figure 7.11 displays the resulting shape of the energy-loss function together with the model of Abdurashitov et al.. Due to the semi-empirical model consisting of three Gaussian kernels and the theoretical BED model

[5] In order to verify that MIGRAD converged to the global minimum, the fit was repeated 1000 times with the initial parameters being randomised.

(see Eq. (4.28)) for the ionisation tail, the obtained energy-loss function provides a good description of the shape for energies above 12 eV. Thus, the width of the $1\sigma$ uncertainty band included in Fig. 7.11 is below $10^3\,\mathrm{eV}^{-1}$. For the ionisation tail, the shape of which is described from the theoretical BED model (see Eq. (4.28)), the uncertainty becomes even smaller, as it is only depending on the uncertainty on the amplitude at the ionisation threshold energy.

However, for the left side of the second Gaussian kernel describing the main contribution of the $2p\pi\,^1\Pi_u$ states, it is visible that the integral measurement data does not allow the shape to be determined with as high precision as for the other regions. Hence, the $1\sigma$ uncertainty band expands by about a factor of five compared to the uncertainty above this region. Furthermore, the Gaussian kernel, which is used with the intention to approximate the $2p\sigma\,^1\Sigma_u^+$ states, is detached from the main Gaussian kernel. However, this detached Gaussian is not expected from the detailed measurements of J. Geiger and the literature-based model shown in Figs. 4.2 and 4.3.

Comparing the measurement result to the model of Abdurashitov et al., it can be seen that the semi-empirical KATRIN model with the three Gaussian kernels allows for a better resolution of the molecular excitation states especially between 13.5 eV and the ionisation threshold energy $E_{\mathrm{ion}}(D_2) = 15.470\,\mathrm{eV}$ [WJH99]. Furthermore, a significant difference of $0.03\,\mathrm{eV}^{-1}$ between the height of the electronic excitation peaks is visible. This discrepancy is likely caused by using only one Gaussian kernel for the approximation of the molecular excitation states in the Abdurashitov et al. model. As multiple groups of electronic excitations states exist (see Fig. 4.2), the Gaussian kernel is broadened in order to take also these contributions into account. Due to the normalisation, the height of the Gaussian is reduced. The best method to compare the uncertainties of the two models is to compare the width of the $1\sigma$ uncertainty band. By calculating the area of the uncertainty band it can be shown that the uncertainty of the new KATRIN model is over a factor of 20 times smaller than the uncertainty of the Abdurashitov et al. model.

Two additional properties of the obtained energy-loss function can be investigated to prove the quality of the measurement result. The first property is the correct normalisation of the energy-loss function and the second is the mean energy loss.

Due to the included pull term (see Eq. (7.26)) in the likelihood function, the integral of the energy-loss function evaluates to

$$\int_0^{E_{\max}} f(E)\ \mathrm{d}E = 1.0 \tag{7.28}$$

and the mean energy loss $\langle \Delta E \rangle$ is

$$\langle \Delta E \rangle_{\mathrm{int}}^{\mathrm{D_2}} = 30.64(1)\,\mathrm{eV}\,. \tag{7.29}$$

The value of the mean energy loss is about 0.4 eV larger than calculated value from the Abdurashitov et al. $D_2$ parametrisation

$$\langle \Delta E \rangle_{\mathrm{Abd.}}^{\mathrm{D_2}} = 30.19(2)\,\mathrm{eV}\,. \tag{7.30}$$

The quality of the obtained energy-loss function with regard to the propagated uncertainty on $m_\nu^2$ is discussed in Sec. 7.4.

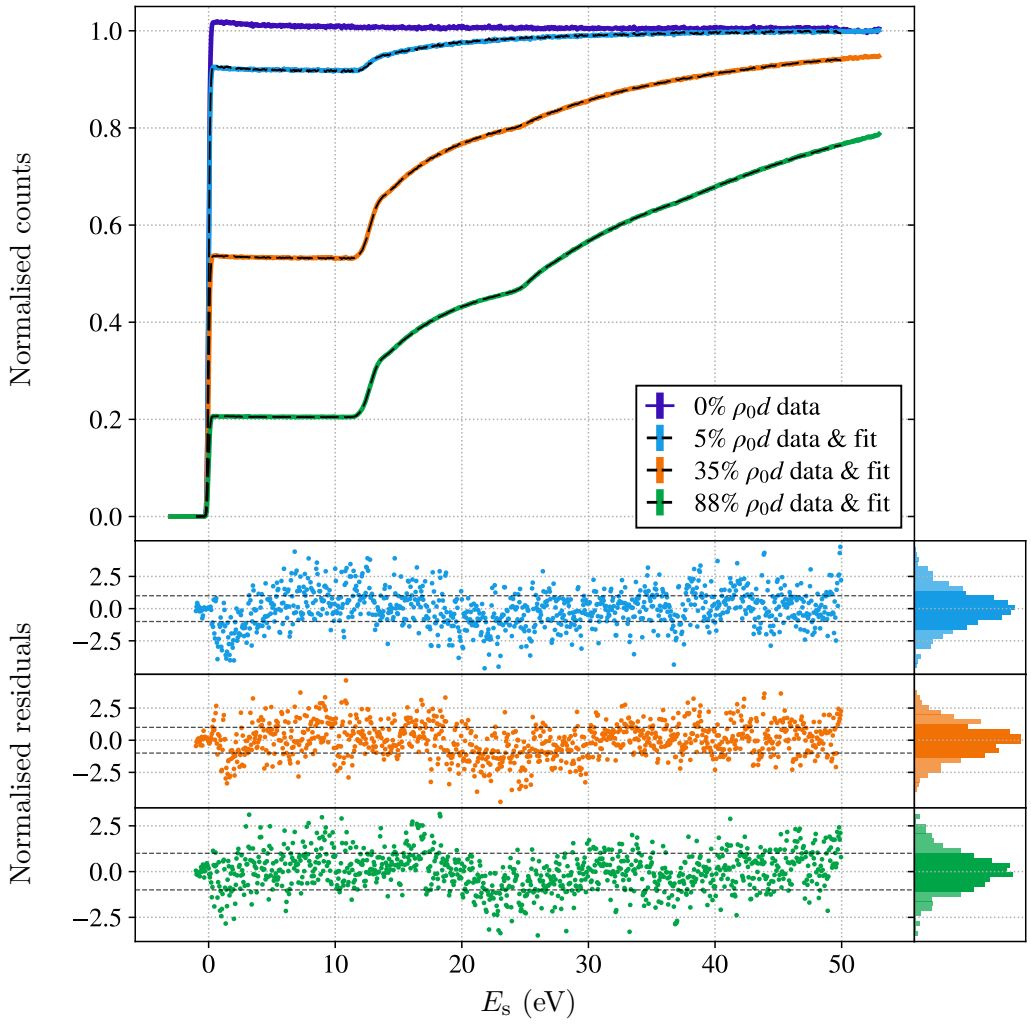


Figure 7.10: Combined fit to the integral response functions for $D_2$ together with the normalised residuals $(y_{\text{data}} - y_{\text{fit}}) \cdot \sigma^{-1}$. The histograms on the right show the distribution of the residuals, with the shaded area indicating the $1\sigma$ range. The normalised residuals show a systematic deviation of about $1\sigma$ in the range of $E_s = [0, 30]$ eV, although the fit model is constructed by using the transmission function data of the 0 % $\rho_0 d$ measurement (see Sec. 7.3.2.1). Due to the construction of the fit function using measurement data, the spread of the residuals is increased, since both the fit function as well as the measurement data are affected by statistical fluctuations. The broadening of the residuals decreases with increasing column density (see histograms on the right), as the contribution of unscattered electrons decreases and since the noise reduces with the convolution process. Due to the broadening, an increased value of $\chi^2/N_{\text{dof}} = 1.70(3)$ is obtained.

Table 7.3: Parameters for the energy-loss function (see Eq. (7.15)) of molecular deuterium and the nuisance parameters as obtained from a combined $\chi^2$ fit to the integral response functions. Due to the normalisation of the data sets before executing the fit, the parameters $A_i$ and $A_i^{\mathrm{bg}}$ are not in absolute units but scaled according to the factors provided in Tab. A.2. The obtained values of $\mu_i$ allow to determine the column density inside the source during the measurements, which corresponds to the values provided in Tab. 7.1. The covariance and correlation matrices for the subset of the nine energy-loss function parameters are provided in Fig. 7.12.

| Parameter | Unit | Value | $\sigma_{\mathrm{fit}}$ |
|---|---|---|---|
| $a_1$ | $\mathrm{eV}^{-1}$ | 0.040 40 | 0.001 31 |
| $m_1$ | eV | 11.7227 | 0.0190 |
| $\sigma_1$ | eV | 0.084 01 | 0.002 76 |
| $a_2$ | $\mathrm{eV}^{-1}$ | 0.271 086 | 0.000 221 |
| $m_2$ | eV | 12.716 40 | 0.001 67 |
| $\sigma_2$ | eV | 0.495 884 | 0.000 424 |
| $a_3$ | $\mathrm{eV}^{-1}$ | 0.074 175 3 | 0.000 046 0 |
| $m_3$ | eV | 14.880 68 | 0.001 56 |
| $\sigma_3$ | eV | 1.086 44 | 0.001 64 |
| | | Nuisance parameters | |
| $A_5$ | | 1.003 237 8 | 0.000 055 9 |
| $\mu_5$ | | 0.094 730 | 0.000 102 |
| $A_5^{\mathrm{bg}}$ | | 0.000 000 0 | 0.000 020 1 |
| $A_{35}$ | | 1.054 041 8 | 0.000 093 6 |
| $\mu_{35}$ | | 0.640 465 | 0.000 127 |
| $A_{35}^{\mathrm{bg}}$ | | 0.000 011 2 | 0.000 010 6 |
| $A_{88}$ | | 1.269 691 | 0.000 236 |
| $\mu_{88}$ | | 1.595 378 | 0.000 216 |
| $A_{88}^{\mathrm{bg}}$ | | 0.000 037 5 | 0.000 029 2 |

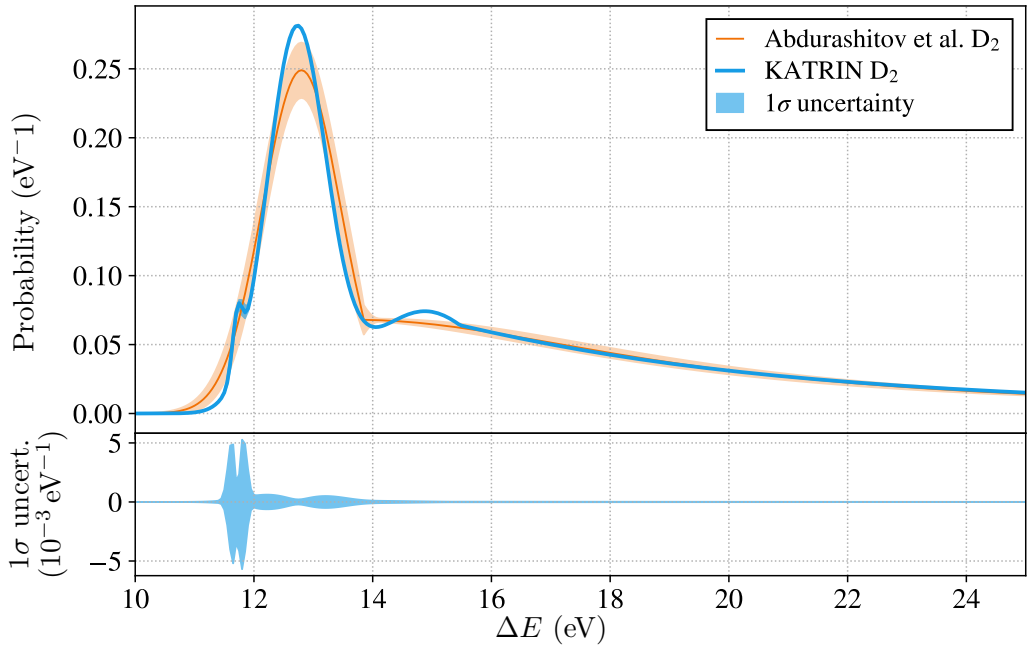


Figure 7.11: Energy-loss function as obtained from the fit to the $D_2$ integral measurement data. With the new semi-empirical energy-loss function model (see Eq. (7.15)) a very detailed description especially in the range of $\Delta E > 12\,\mathrm{eV}$ is obtained, where the $1\sigma$ uncertainty band is below $10^{-3}\,\mathrm{eV}^{-1}$. For the energy range below 12 eV, it can be seen that the shape properties of the first Gaussian kernel are less precise determined from the minimiser. Thus, the $1\sigma$ uncertainty band expands by a factor of five. The first Gaussian kernel is slightly detached from the main peak, which is not expected (comp. Fig. 4.2). Compared to the empirical model of Abdurashitov et al., both the shape as well as the model uncertainties were improved.

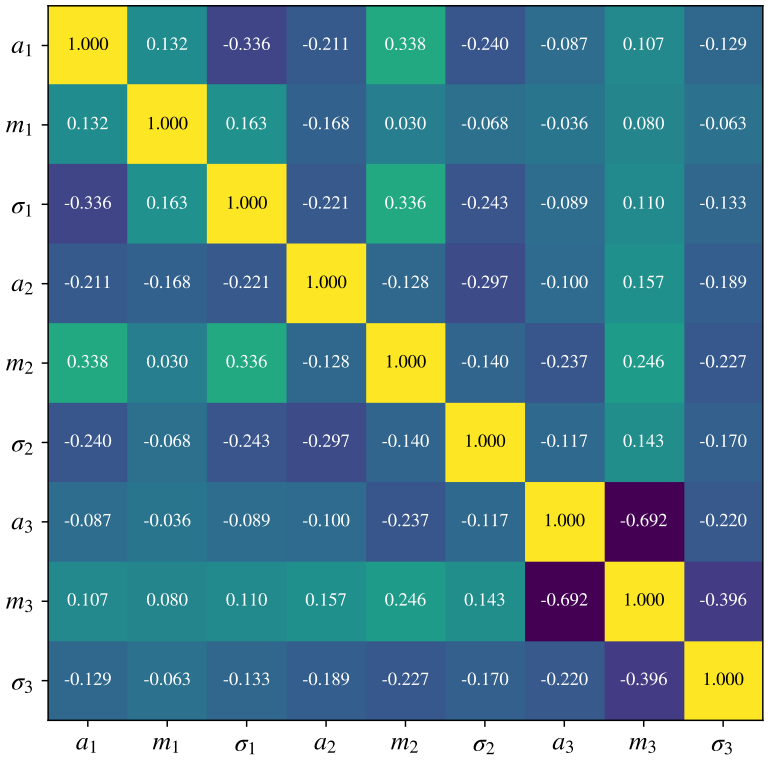


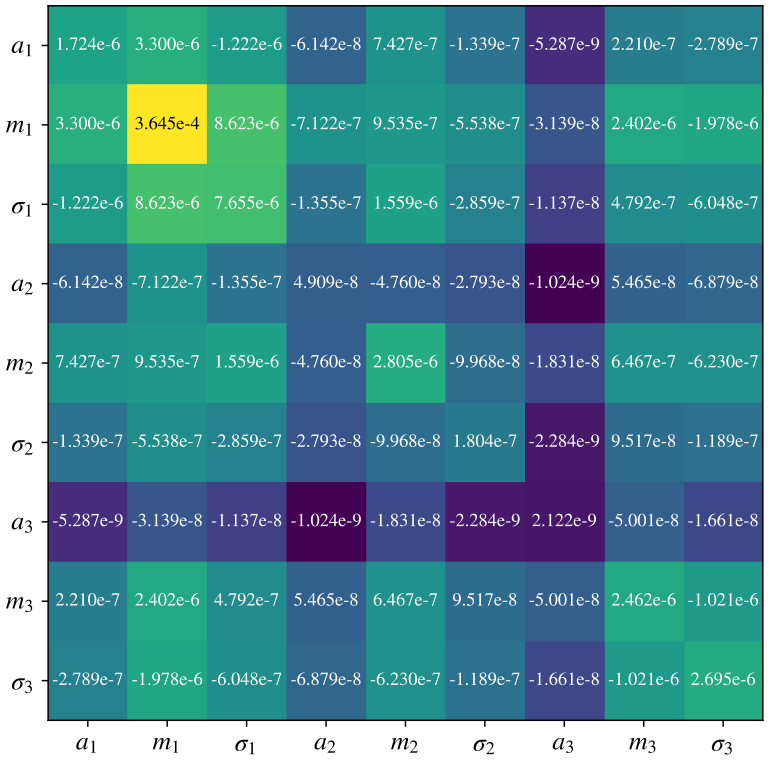


Figure 7.12: Correlation matrix (top) and covariance matrix (bottom) for the energy-loss function parameters in Tab. 7.3 as obtained from the $\chi^2$ fit to the integral response functions of molecular deuterium.

### 7.3.3 Combined fit using integral and differential data

In addition to the measurement of the response functions in integral mode, a novel differential measurement approach was tested during the STS-IIIa measurement campaign. The differential measurement approach was proposed by Prof. Ch. Weinheimer (University of Münster) and was performed and analysed by R. Sack [Sac20]. In order to make full use of the available information of both data sets, a combined fit to both the integral data sets as well as the differential data was developed together with V. Hannen, R. Sack, and C. Rodenbeck. A brief introduction to the differential measurement approach and the obtained data is provided in Sec. 7.3.3.1. The integration of the differential data into the fit as well as the discussion of the obtained fit results is discussed in Secs. 7.3.3.2 and 7.3.3.3.

#### 7.3.3.1 Differential measurement data

As it is described in Sec. 5.2, the pulsed UV laser can be triggered externally with a function generator, which allows for a synchronisation of the light pulses with the DAQ of the FPD. If the timestamp of the light pulse is known, the time difference between the generation of the light pulse and the arrival time at the detector can be determined, which allows one to measure the time-of-flight of the electrons.

Due to the retardation inside the main spectrometer potential, the flight time is depending on the surplus energy of the electrons, as it is shown in Fig. 6.5. The flight times diverge for electrons with $E_\mathrm{s} \approx 0\,\mathrm{eV}$ and flight times of $>30\,\mu\mathrm{s}$ are expected.

If the source is filled with gas, an energy loss $\Delta E$ due to scattering of the signal electrons with the source gas is possible. Thus, even for surplus energies $E_\mathrm{s} > 0\,\mathrm{eV}$, the reduced kinetic energy of the signal electron after the scattering can again fulfil the condition $\tilde{E}_\mathrm{s} = E_\mathrm{s} - \Delta E \approx 0\,\mathrm{eV}$ and the electrons again have large flight times compared to the unscattered electrons.

By selecting only the events with the time-of-flight being larger than a selected threshold value, an integral response function can be turned into a differential response function, as it is possible to select only scattered electrons fulfilling the condition $\Delta E \approx E_\mathrm{s}$.

However, it is only possible to measure the flight time as a modulus of the time ${f_\mathrm{P}}^{-1}$ between the laser pulses, since the electrons arriving at the detector cannot be assigned to a defined light pulse. In order to obtain the largest possible analysis window, the laser has to be operated at a low pulse frequency. In contrast to the integral measurements, where a very high pulse frequency of 120 kHz is used (in order to reduce the detector pile-up), the response function measurements for the differential analysis were performed with a pulse rate of 20 kHz. This setting results in an analysis window of 50 µs. The distribution of the flight times as a function of the surplus energy are shown in Fig. 7.13.

The measurement was performed in the same manner as in the case of the integral response functions (see Sec. 7.2), i.e. the retarding energy was set to a fixed potential of $U_\mathrm{ret} = 18\,325\,\mathrm{V}$ and the emission electrode voltage $U_\mathrm{em}$ was continuously ramped on the voltage interval of $-194\,\mathrm{V}$ to $-254\,\mathrm{V}$. These 1807 s long scans were repeated alternatingly in up and down direction. The measurement was performed at the same column density of $5\,\%\ \rho_0 d$ as during the integral measurement. After processing the data and selecting only the events with a time-of-flight in the range from 35 µs to 50 µs, the differential response function in Fig. 7.13 is obtained. The window of the ToF cut differs to the data set used in Ref. [Sac20], where the analysis window was chosen to be 30 µs to 50 µs. Reason for this difference is that the data set was re-analysed by V. Hannen (University of Münster) in order to apply the same analysis procedure as for the tritium measurements, which are discussed in Sec. 8. This re-analysis also includes an additional event multiplicity cut, which is introduced in Ref. [Rod] in order to improve the signal-to-background ratio

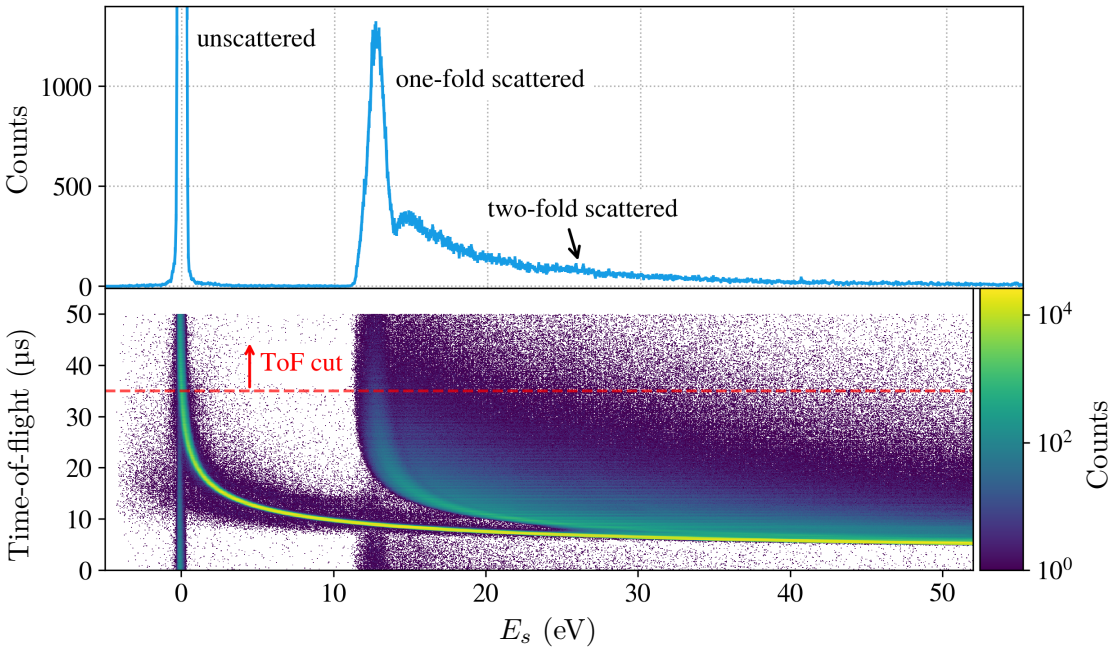


Figure 7.13: The differential response function in the upper panel is obtained by applying a ToF cut on the flight time distribution as shown on the bottom panel. Similar to the integral response function, the response function is a superposition of $n$-fold scattering functions. Since the column density was only 5 % $\rho_0 d$, the probability of two-fold scattering is only $P_2 = 0.45\,\%$ and thus only a small contribution of the two-fold scattered electrons is visible in the range of 25 eV. The large peak of unscattered electrons at $E_s = 0$ eV is cut off for better representation. The data shown in this figure was provided by Ref. [Sac20].

especially in the range of the ionisation tail. The characterisation of this background as well as the influences of the multiplicity cut on the background shape are discussed in detail in Sec. 8.2.

#### 7.3.3.2 Combined fit model

In order to perform a combined fit to both the integral data and the differential response function, the likelihood function for the integral data set (see Eq. (7.25)) has to be extended to include the differential fit function.

The differential fit function is constructed in the same way as in Eq. (8.1), but instead of using the integral transmission function $T_e(E_s)$, the differential transmission function $T_d(E_s)$ is used, which is given by the peak of unscattered electrons on the interval of $E_s = [-1, 1]$ eV.

In contrast to the fit model used in Ref. [Sac20], the flat background component is replaced with a more complex model. As it is discussed in Sec. 8.2, the background component follows the shape of an integral response function even after applying the ToF cut, since the background events are not correlated with the trigger signal of the laser. By introducing the event multiplicity cut (see Sec. 8.2 and Ref. [Rod]) the background can be reduced. However, the event multiplicity cut causes a distortion of the shape of the background component, which can be only obtained from simulations. The background shape used for the analysis of the deuterium data is shown in Fig. 7.14.

The fit function for the differential measurements is thus

Table 7.4: Overview of the measurement and analysis settings for the response function measurement in differential mode using $D_2$ as source gas.

| Parameter | Value |
|---|---|
| Light source | InnoLas Mosquitoo 266nm pulse laser |
| Pulse frequency $f_P$ | 20 kHz |
| Trigger | external |
| Diode current | 7 A |
| Pitch angle | 0° |
| Rate | 7 kcps |
| Column density | 5 % of $\rho_0 d$ |
| $D_2$ purity | 96 % |
| Analysing plane setting | 1.4 G |
| Scanning strategy | Ramping of $U_{em}$; $U_{ret} = -18\,525$ V =const. |
| Scan range | $E_s$ =−5 V to 55 V |
| Ramping speed | 33.16 mV $s^{-1}$ |
| Run length | 1807 s |
| Number of scans | 12 |
| Bin width | 0.05 eV |
| ToF selection | 35 µs to 50 µs |

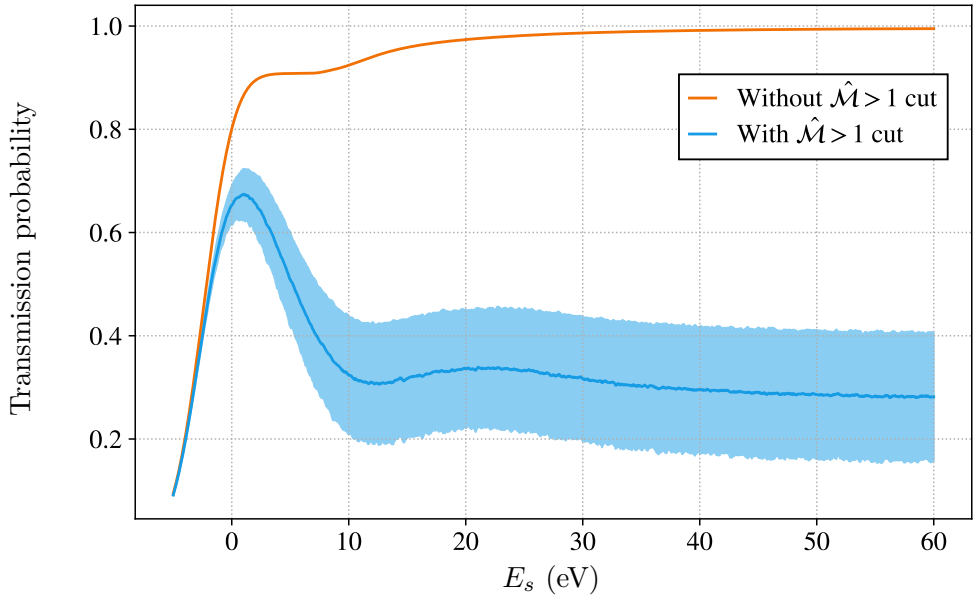


Figure 7.14: Simulated background model for the differential energy loss measurements after applying the multiplicity $\hat{\mathcal{M}} > 1$ cut for a column density of 5 % $\rho_0 d$ of $D_2$. The shaded area indicates the $1\sigma$ uncertainty interval caused by the uncertainty on the initial cluster size $\hat{\mathcal{S}}$ of the background events as determined in Sec. 8.2. The data was provided by Ref. [Sch20].

$$R_i\left(E_\mathrm{s}, A_i, \mu_i, A_i^\mathrm{bg}, \vec{\mathcal{P}}\right) = A_i \cdot \left(\sum_{n=0}^{4} P_n(\mu_i, E_\mathrm{s})\bar{\epsilon}_n^\mathrm{d}(E_\mathrm{s}, \vec{\mathcal{P}})\right) + A_i^\mathrm{bg} \cdot B(E_\mathrm{s}, \mu_i, \hat{\mathcal{M}} = 1)\,, \tag{7.31}$$

with $\bar{\epsilon}_n^\mathrm{d}(E_\mathrm{s}, \vec{\mathcal{P}})$ being the differential scattering functions. The latter are constructed similar as in Eq. (7.3) but by using the differential transmission function $T_\mathrm{d}(E_\mathrm{s})$ of the electron gun after applying the ToF cut. In order to correct for the change of the kinetic energy, the same corrections as discussed in Sec. 7.3.2.1 are applied to both the signal component as well as the background component. Similar to the integral fit function, three nuisance parameters $A_i$, $\mu_i$, and $A_i^\mathrm{bg}$ are required. Again, a normalisation of the data sets is carried out before the fit is performed. In the case of the differential data, the data is divided by the integral of the data points within the selected fit range. The normalisation constant is provided in Tab. A.2.

The fit range is chosen to be 8 eV to 53 eV since no information on the energy-loss function is included in the differential data below the threshold energy of one-fold scattering. Furthermore, it is possible to determine the amplitude of the background component from the signal level between the peak of unscattered electrons and the one-fold scattered electrons. Thus, it is not required to fit the entire response function as in the case of the integral measurement data.

#### 7.3.3.3 Combined fit results

With the differential data set included, the minimisation of 21 free parameters, i.e. the nine energy-loss parameters as well as the twelve nuisance parameters, is required. By adding the differential data set, the number of data points increases to 3960 resulting in the number of degrees of freedom of $N_\mathrm{dof} = 3939$. The best fit result, as shown in Fig. 7.15, is obtained at a value of

$$\frac{\chi^2}{N_\mathrm{dof}} = 1.57(2)\,, \tag{7.32}$$

which is again larger than one. Similar as in the case of the fit using only the integral data, this increase of the $\chi^2$ value is caused by using the measurement data to construct the fit model. Monte Carlo simulations of the combined fit show that a value of $\chi^2/N_\mathrm{dof} = 1.71(5)$ would be expected. The value of $\chi^2/N_\mathrm{dof} = 1.57(2)$ is again smaller than the expected value but the difference is only 0.14 compared to 0.21 when fitting only the integral response functions. Thus, the goodness of fit improved by adding the differential data. The residuals of the differential data in Fig. 7.15 do not show any visible structure. However, the structures in the residuals for the integral data are still remaining and did not improve significantly.

The obtained best-fit parameters for the energy-loss function, as well as for the nuisance parameters are available in Tab. 7.5, with the covariance and correlation matrices for the subset of the energy-loss function parameters provided in Fig. 7.16.

Similar as for the fit result using only integral data, the resulting energy-loss function is normalised to 1 by the pull term yielding a mean energy loss of

$$\langle \Delta E \rangle_\mathrm{comb}^{\mathrm{D_2}} = 30.63(1)\,\mathrm{eV}\,, \tag{7.33}$$

which is in good agreement with the value obtained from the integral data fit in Eq. (7.29) and the value for the Abdurashitov et al. parametrisation in Eq. (7.30). The resulting energy-loss function is shown in Fig. 7.17. It is visible that the combined fit result provides

Table 7.5: Parameters for the energy-loss function (see Eq. (7.15)) of molecular deuterium and the nuisance parameters as obtained from a combined $\chi^2$ fit to both integral and differential data. The covariance and correlation matrices for the subset of the nine energy-loss function parameters are provided in Fig. 7.16.

| Parameter | Unit | Value | $\sigma_{\text{fit}}$ |
|---|---|---|---|
| $a_1$ | $\text{eV}^{-1}$ | 0.034 38 | 0.002 19 |
| $m_1$ | eV | 11.7935 | 0.0158 |
| $\sigma_1$ | eV | 0.1660 | 0.0130 |
| $a_2$ | $\text{eV}^{-1}$ | 0.273 67 | 0.001 17 |
| $m_2$ | eV | 12.729 97 | 0.003 69 |
| $\sigma_2$ | eV | 0.482 82 | 0.004 23 |
| $a_3$ | $\text{eV}^{-1}$ | 0.074 659 | 0.000 383 |
| $m_3$ | eV | 14.874 62 | 0.008 55 |
| $\sigma_3$ | eV | 1.0734 | 0.0262 |
| Nuisance parameters: integral | | | |
| $A_5$ | | 1.003 234 0 | 0.000 057 8 |
| $\mu_5$ | | 0.094 724 | 0.000 103 |
| $A_5^{\text{bg}}$ | | $1 \times 10^{-14}$ | 0.000 019 8 |
| $A_{35}$ | | 1.054 016 | 0.000 108 |
| $\mu_{35}$ | | 0.640 433 | 0.000 137 |
| $A_{35}^{\text{bg}}$ | | 0.000 011 3 | 0.000 010 6 |
| $A_{88}$ | | 1.269 618 | 0.000 300 |
| $\mu_{88}$ | | 1.595 307 | 0.000 261 |
| $A_{88}^{\text{bg}}$ | | 0.000 038 2 | 0.000 029 5 |
| Nuisance parameters: differential | | | |
| $A_5$ | | 11.128 | 0.430 |
| $\mu_5$ | | 0.099 49 | 0.004 12 |
| $A_5^{\text{bg}}$ | | 0.000 235 2 | 0.000 057 7 |

a better approximation of the $2p\sigma\,^1\Sigma_u^+$ states by the first Gaussian kernel, as the peak is less detached and the uncertainties in this region are about a factor of three times smaller than in the integral fit result. However, the $1\sigma$ uncertainty is slightly increased for the energy range above 12 eV, which is an indication that the integral data and the differential data differ slightly in their shape. Comparing the integral of the uncertainty band, the uncertainty of the combined fit increased by a factor of 1.3. Although the uncertainties are increased, the combined fit result is considered to be better than the result for the fit using only the integral data, since both measurements approaches are influenced by different systematic uncertainties, such as the pile-up correction in the integral case and the flight time measurement in the differential case. Thus, systematic distortions of the resulting energy-loss function due to the systematic uncertainties of the data sets are expected to be reduce in a combined fit. The quality of this measurement result with respect to the KATRIN requirements is further discussed in Sec. 7.4.

A detailed discussion of the systematic effects of the measurement approach including detailed Monte Carlo simulations are available in Sec. 8.5 as part of the tritium measurements described in Chap. 8.

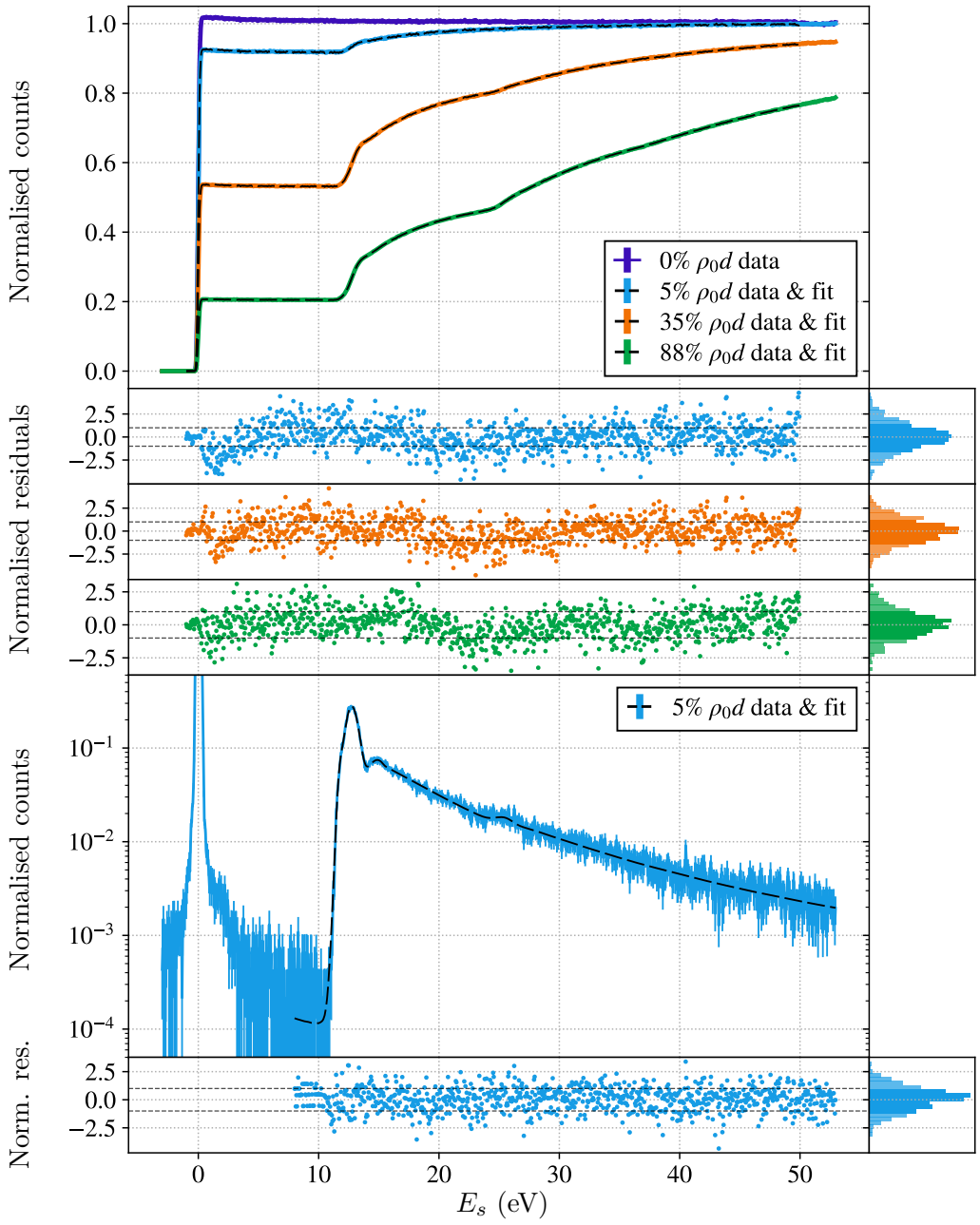


Figure 7.15: Best fit result of a combined $\chi^2$ fit including both integral and differential response functions. The normalised residuals are drawn below the response functions with the corresponding colours. The structures in the residuals of the integral data is still visible, whereas no structure in the residuals of the differential data is visible. With the differential data set included, a value of $\chi^2/N_{\mathrm{dof}} = 1.57(2)$ is obtained.

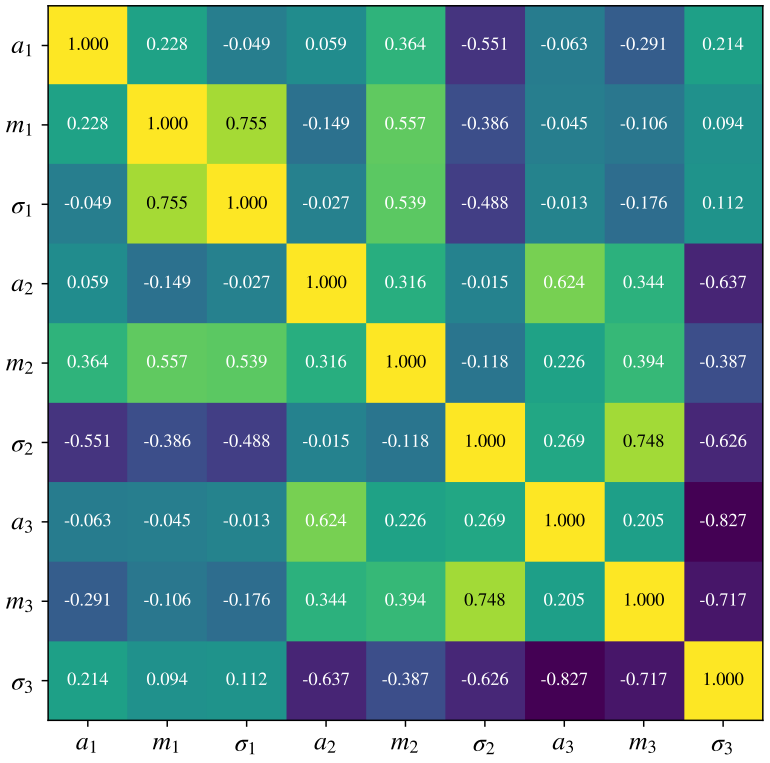


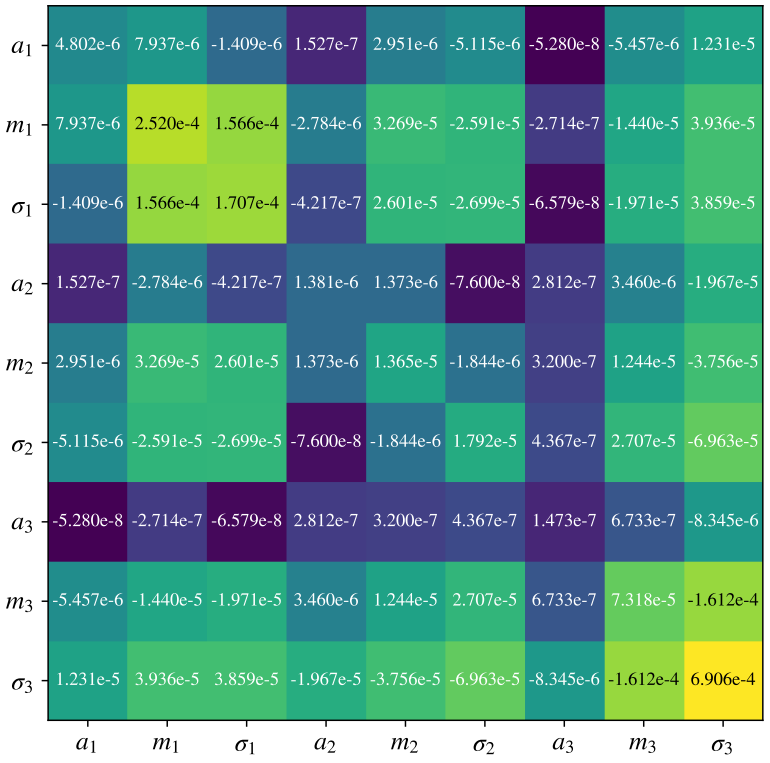


Figure 7.16: Correlation matrix (top) and covariance matrix (bottom) for the energy-loss function parameters in Tab. 7.5 as obtained from the combined $\chi^2$ fit to integral and differential response functions for molecular deuterium.

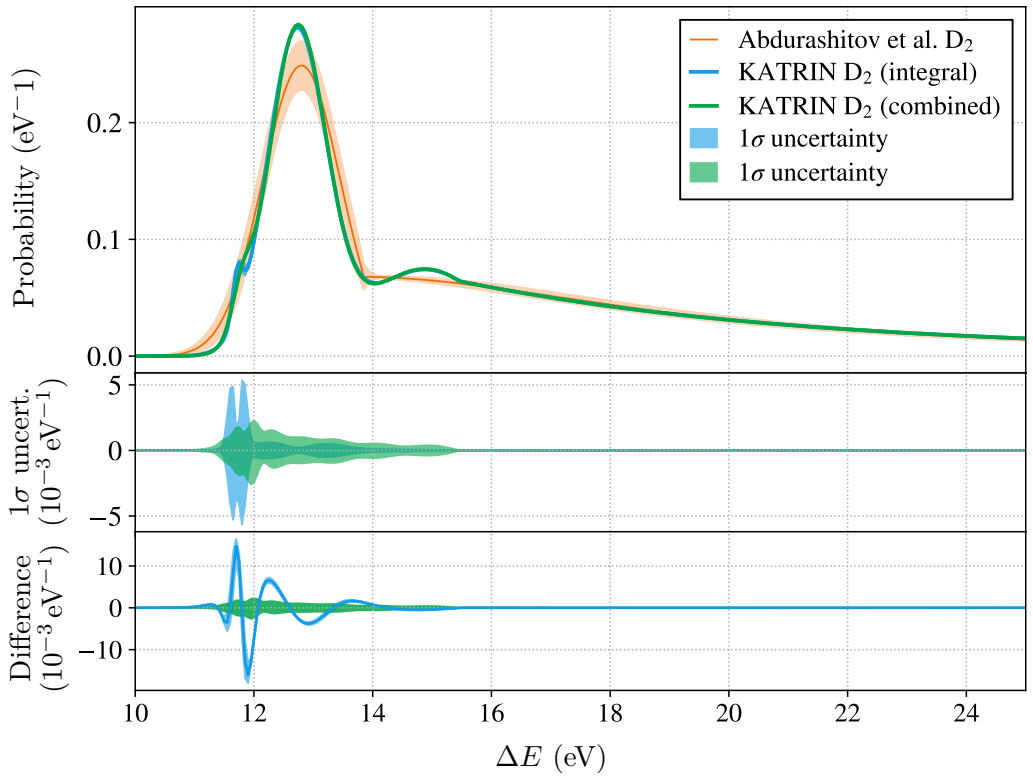


Figure 7.17: The energy-loss function as obtained from the combined fit of both integral and differential response function measurements compared to the fit result when using only the integral data, and the model of Abdurashitov et al. [A+17]. Compared to the fit result using only the integral data, the combined fit result provides a better description of the shape in the range of 11.5 eV to 12 eV, which is visible in the reduced width of the $1\sigma$ interval (middle row). The differences between the two models become minute above the ionisation threshold, which can be seen in the bottom plot.

## 7.4 Comparison of the measurement approaches

Two different analysis approaches were used for the determination of the energy-loss function from response function measurements using $D_2$. The SVD deconvolution (see Sec. 7.3.1) as well as the analytical fit to the the integral response function (see Sec. 7.3.2) use exactly the same data set, which thus allows for a direct comparison of the quality of the measurement results. Furthermore, it is possible to investigate the difference of the measurement results of the combined fit using only integral data and the fit using also the differential response function (see Sec. 7.3.3). The three different energy-loss function models are shown in Fig. 7.18. The comparison of the energy-loss function model obtained from the SVD deconvolution result and the energy-loss model obtained from the analytical fit including only the integral data set shows a significant difference of both the shape and the uncertainty of the model. Besides the systematic oscillations of the deconvolution results, the comparison also shows that the height of the dominant electronic excitation peak is reduced by more than 20 %. Both systematic effects are artefacts of the deconvolution (comp. Fig. 7.5) and depend on the value of the free parameter $w_{\mathrm{thr}}$. Although the optimal value of $w_{\mathrm{thr}} = 1.1\,\%$ was determined by dedicated simulations, the discrepancy remains significant. The shape of the analytical fit result does not suffer from these systematic uncertainties and is more robust, as it also allows one to take systematic uncertainties of the data into account not only in form of the uncertainties of the data points but also by corrections of the fit model. Besides the difference is the shape of the two energy-loss functions, it can also be seen that the $1\sigma$ uncertainty band of the analytical fit approach is on average a factor of 30 smaller than the uncertainty band of the deconvolution result. Especially in the region of the ionisation tail, where the shape is described by the BED model, the analytical fit result outperforms the uncertainty of the deconvolution result by more than a factor of 300.

The validity of the energy-loss function model obtained from the analytical fit to the integral response functions is verified with the result of the combined fit using also the differential response function. As discussed in Sec. 7.4, the results obtained from the analytical fits agree well although there is a deviation visible for energies below 12 eV. Hence, the analytical fit approach is considered to be a very robust analysis method for the determination of the energy-loss function from response function measurements, as it is not affected by the systematic uncertainties of the deconvolution. Furthermore, the analytical fit approach is less influenced by statistical fluctuations of the count rate than the deconvolution approach, which results in significantly smaller uncertainties of the obtained models.

In order to determine whether the quality of the different measurement results meets the KATRIN requirement, it is required to investigate the impact of the model uncertainties on the observable $m_\nu^2$. This propagation of the model uncertainties is performed by Monte Carlo simulations of the measurement of the β-spectrum, which will be discussed in the following.

### Uncertainty of the fit approach

For the investigation of the uncertainties of the analytical fit results the so-called covariance matrix approach is used. In the case of the covariance matrix approach, the parameter uncertainties of the energy-loss function propagated by constructing a covariance matrix $C_\beta$ of the β-spectrum. This covariance matrix can then be used in the calculation of the likelihood function, which increases the parameter uncertainties of the observable $m_\nu^2$.

In order to construct the covariance matrix $C_\beta$, a total of 10000 tritium spectra are simulated while the parameters of the energy-loss function are randomly drawn from a multivariate

normal distribution taking into account the covariance matrix $C_{\vec{\mathcal{P}}}$ of the energy-loss function parameters as provided in Fig. 7.12 and 7.16, respectively. The covariance between the $i$-th and $j$-th data point of the β-spectrum is calculated for the $n = 10000$ samples according to

$$C_{\beta,\mathrm{ij}} = \frac{1}{n}\sum_{k}^{n}\left(N_i^k - \bar{N}_i\right)\left(N_j^k - \bar{N}_j\right), \tag{7.34}$$

with $N_i^k$ and $N_j^k$ being the counts of the corresponding data point of the $k$-th sample and $\bar{N}_i$ and $\bar{N}_j$ being the average value of the given data points. The generation of the covariance matrix is included in the KaFit framework.

The covariance matrix $C_\beta$ can then be considered in the calculation of the $\chi^2$ function according to

$$\chi^2 = \sum_{i,j=1}^{k}(N_i - y_i)C^{-1}_{\beta,\mathrm{ij}}(N_j - y_j), \tag{7.35}$$

with $k$ being the number of data points and $y_i$ and $y_j$ being the fit model value at the $i$-th and $j$-th data point (see e.g. Ref. [Lis17]). By adding the covariance matrix, the $\chi^2$ function is broadened, which leads to an increase of the parameter uncertainty of the observable $m_\nu^2$. In order to determine the increase of the parameter uncertainty, a fit to MC simulation data has to be performed once using the covariance matrix $C_\beta$ and once without the covariance matrix. The statistical uncertainty $\sigma_{\mathrm{stat}}$ is obtained from the fit to the simulation data without $C_\beta$ included, whereas the fit to the simulated data including $C_\beta$ gives the total uncertainty $\sigma(m_\nu^2)_{\mathrm{tot}}$ including the statistical and systematic uncertainty. Under the condition that the statistical and systematic uncertainties contribute quadratically to the total uncertainty, i.e. $\sigma_{\mathrm{tot}} = \sqrt{\sigma_{\mathrm{stat}}^2 + \sigma_{\mathrm{sys}}^2}$, the systematic uncertainty $\sigma_{\mathrm{sys}}(m_\nu^2)$ is obtained by a quadratic subtraction

$$\sigma_{\mathrm{sys}}(m_\nu^2) = \sqrt{\sigma_{\mathrm{tot}}(m_\nu^2) - \sigma_{\mathrm{stat}}(m_\nu^2)}. \tag{7.36}$$

Although the uncertainty $\sigma_{\mathrm{stat}}$ of the fit without the covariance matrix $C_\beta$ is called the statistical uncertainty, it is important to point out, that there is no statistical noise included in the simulation (commonly called an Asimov data set [CCGV11]), which allows one to directly assess the statistical mean.

Three different simulations are performed with the following settings:

- The parametrisation of Tab. 7.3 (integral fit result) and the corresponding covariances $C_{\vec{\mathcal{P}}}$ from Fig. 7.12 are used to generate the covariance matrix $C_\beta^{\mathrm{int}}$ for the tritium spectrum. In order to determine $\sigma_{\mathrm{tot}}^{\mathrm{int}}(m_\nu^2)$ and $\sigma_{\mathrm{stat}}^{\mathrm{int}}(m_\nu^2)$, a spectrum is simulated using the best-fit values of Tab. 7.3. This spectrum is fit by constructing the fit model with the same energy-loss function parameters but once with and once without including $C_\beta^{\mathrm{int}}$ in the likelihood function. This allows one to determine $\sigma_{\mathrm{sys}}^{\mathrm{int}}(m_\nu^2)$ from the resulting uncertainties $\sigma_{\mathrm{tot}}^{\mathrm{int}}(m_\nu^2)$ and $\sigma_{\mathrm{stat}}^{\mathrm{int}}(m_\nu^2)$.
- The parametrisation of Tab. 7.5 (combined fit result) and the corresponding covariances $C_{\vec{\mathcal{P}}}$ from Fig. 7.16 are used to generate the covariance matrix $C_\beta^{\mathrm{comb}}$ for the tritium spectrum. In order to obtain $\sigma_{\mathrm{tot}}^{\mathrm{comb}}(m_\nu^2)$ and $\Delta m_{\nu^2,\mathrm{comb}}$, a spectrum is simulated using the best fit values of Tab. 7.3. This spectrum is fit by constructing the fit model with the same energy-loss function parameters but once with and once without including $C_\beta^{\mathrm{comb}}$ in the likelihood function. This allows one to determine $\sigma_{\mathrm{sys}}^{\mathrm{comb}}(m_\nu^2)$ from the resulting uncertainties $\sigma_{\mathrm{tot}}^{\mathrm{comb}}(m_\nu^2)$ and $\sigma_{\mathrm{stat}}^{\mathrm{comb}}(m_\nu^2)$.
- In the two upper cases it is not possible to investigate a possible shift of $\Delta m_\nu^2$, as the simulation model and the fit model are the same. However, the two models show

Table 7.6: Parameter settings of the Monte Carlo propagation for the determination systematic uncertainty on $m_\nu^2$ due to the uncertainties of the energy-loss function results, as discussed in Secs. 7.4 and 8.6.

| Parameter | Setting |
|---|---|
| Column density | $5 \times 10^{21}\,\mathrm{m}^{-2}$ |
| Measurement time distribution | KNM2 (v0) |
| Measurement time | 3 y |
| Statistical fluctuations | No |
| Magnetic field configuration | regular 6.3 G |
| Endpoint | 18 573.7 eV |
| Background | 0.202 cps |
| Fit range | [18533, 18709] eV |

differences in the shape, which can be considered as a systematic uncertainty. In order to determine the shift of $\Delta m_\nu^2$ due to the shape differences, the parametrisation of Tab. 7.3 (integral fit result) is used to simulate the spectrum, but the fit model is constructed by using the best-fit values of Tab. 7.5 (combined fit results) as well as the covariance matrix $C_\beta^{\mathrm{comb}}$ of the β-spectrum of the latter. This gives the shift of the observable $\Delta m_\nu^2$ due to the differences in the energy-loss function parametrisations.

For the simulations of the β-spectrum, the measurement settings were chosen to be similar as for the KATRIN neutrino-mass measurement campaign 2 (KNM2), with a measurement time extrapolated to three years at a nominal column density of $\rho_0 d = 5 \times 10^{21}\,\mathrm{m}^{-2}$ (see Tab. 7.6).

The obtained uncertainties from the propagation are:

$$\begin{aligned} \sigma_{\mathrm{sys}}^{\mathrm{int}}(m_\nu^2) &= 2.1 \times 10^{-3}\,\mathrm{eV}^2 \\ \sigma_{\mathrm{sys}}^{\mathrm{comb}}(m_\nu^2) &= 2.8 \times 10^{-3}\,\mathrm{eV}^2 \\ \Delta m^2_{\nu,\,\mathrm{int/comb}} &= 0.04 \times 10^{-3}\,\mathrm{eV}^2\,. \end{aligned} \tag{7.37}$$

From the results can be seen that the systematic uncertainty on the neutrino mass $\sigma_{\mathrm{tot}}^{\mathrm{int}}(m_\nu^2)$ and $\sigma_{\mathrm{tot}}^{\mathrm{comb}}(m_\nu^2)$ both meet the requirements of $7.5 \times 10^{-3}\,\mathrm{eV}^2$. As expected from the comparison of the uncertainty band of the energy-loss functions (see Fig. 7.17), the value of $\sigma_{\mathrm{sys}}^{\mathrm{comb}}(m_\nu^2)$ is about a factor of 1.35 larger than the value of $\sigma_{\mathrm{sys}}^{\mathrm{int}}(m_\nu^2)$ . The systematic shift due to the differences of the shape cause only a negligible shift, which is about two orders of magnitude smaller compared to the uncertainties. However, this shift gives only the relative shift between the models and does not cover a systematic shift that could be included in both parametrisations of the energy-loss function. In order to asses this shift, a full propagation of systematics would be required. However, this is only performed for the tritium measurements described in Chap. 8, where it is shown, that the measurements are dominated by the the statistical uncertainty.

**Uncertainty of the SVD devonvolution approach**

In order to propagate the uncertainties of the deconvolution result, an ensemble test using the KEloss framework is performed. Similar as for the construction of the uncertainty band of the deconvolution result (see Sec. 7.3.1), a set of 1000 simulations of the response function measurements are performed including statistical fluctuations of the count rate. The simulations are then deconvolved, yielding different deconvolution results due to the

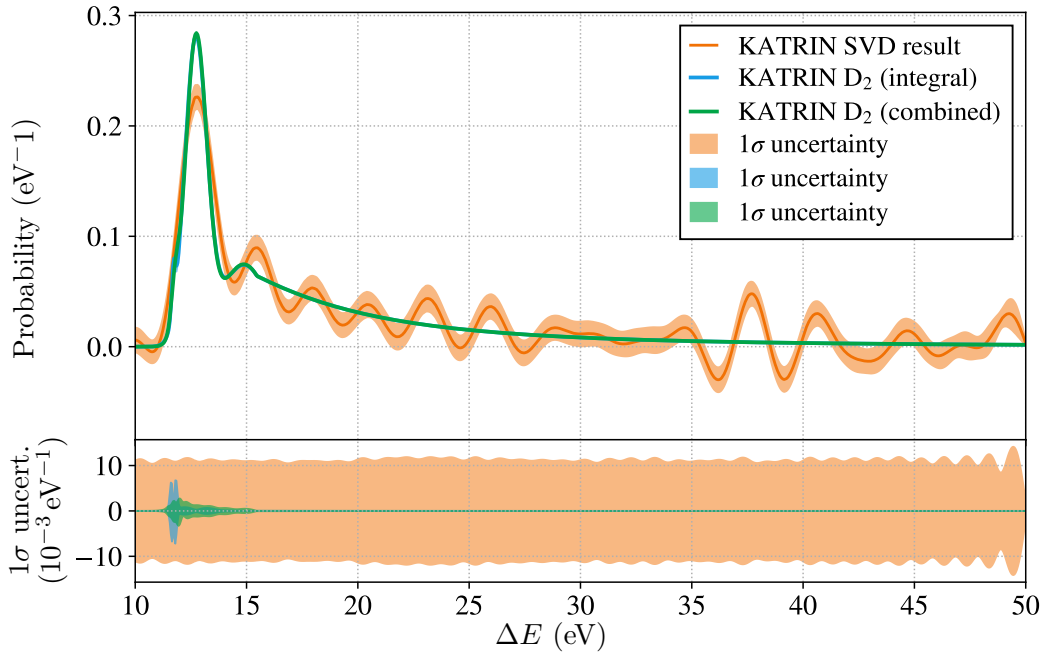


Figure 7.18: Energy-loss functions for molecular deuterium as obtained from the SVD deconvolution and the analytical fit approach. The results of the analytical fit to both the integral data and the combined data set agree well. However, a significant difference between the fit results and the deconvolution result is visible. The deconvolution result is not only affected by systematic oscillations, but also the height of the peak approximating the electronic excitation states is significantly smaller. The uncertainty bands of the individual results are displayed in the bottom panel. The uncertainty of the fit result is across almost the full energy range $\Delta E$ considered here more than a factor of 100 smaller than for the deconvolution.

statistical uncertainty of the data set. In a second simulation step, 1000 MC tritium β-spectrum scans are simulated assuming a neutrino mass of $m(\nu_e) = 0\,\mathrm{eV}$. The spectra are generated by using the same energy-loss function (i.e. the Glück model as shown in Fig. 4.3), which was used as input model for the response function simulations during the deconvolution process. For the simulations, the measurement settings were chosen to be similar as for the KATRIN neutrino-mass measurement campaign 2 (KNM2), with a measurement time extrapolated to three years at a nominal column density of $\rho_0 d = 5 \times 10^{21}\,\mathrm{m}^{-2}$ (see Tab. 7.6). Furthermore, no statistical fluctuations of the count rates were included in the simulations.

The simulation data is then fit with $m_\nu^2$ being a free parameter, but by constructing the response function with the energy-loss function obtained as output of the deconvolution. Since no statistical fluctuation of the count rate is included in the simulations of the β-spectrum, the only differences between the latter and the fit function are caused by the difference in the energy-loss models. Thus, the deviation of $m_\nu^2$ to zero is caused by shape difference of the energy-loss function.

The obtained parameter distribution of $m_\nu^2$ is shown in Fig. 7.19. The width $\sigma(m_\nu^2)$ and the median position $\Delta m_\nu^2$ of the distribution are

$$\sigma_{\mathrm{sys}}^{\mathrm{SVD}}(m_\nu^2) = 0.097\,\mathrm{eV}^2 \quad \text{and} \quad \Delta m^2_{\nu,\,\mathrm{SVD}} = -0.028\,\mathrm{eV}^2\,. \tag{7.38}$$

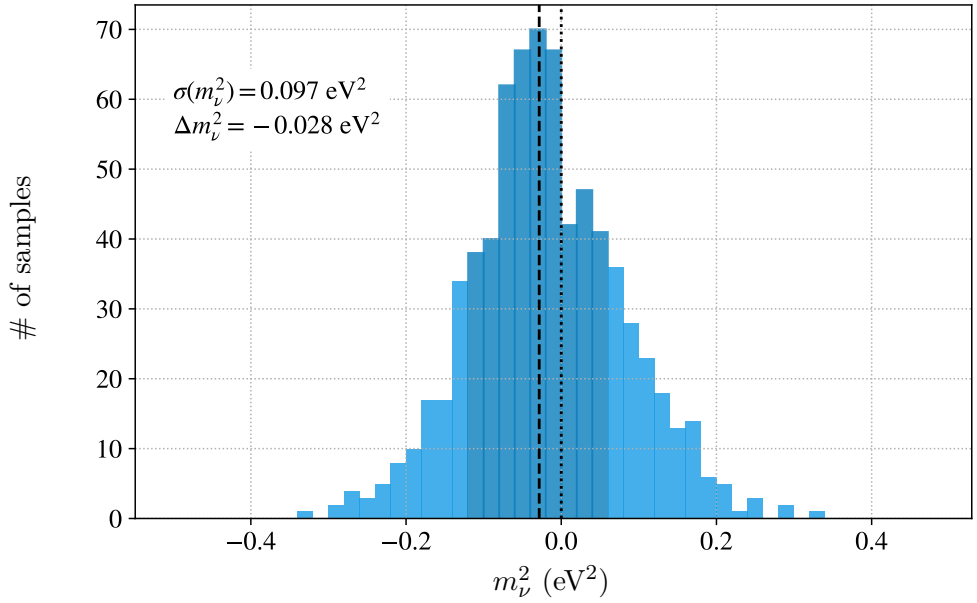


Figure 7.19: Parameter distribution of $m_\nu^2$ as obtained from the Monte Carlo propagation of 1000 deconvolution result of the energy-loss function (see Sec. 7.3.1). The distribution has a width of $\sigma_{\mathrm{sys}}^{\mathrm{SVD}}(m_\nu^2) = 0.097\,\mathrm{eV}^2$ (indicated by the shaded area) and shows a systematic shift of the median (dashed line) of $\Delta m_{\nu,\mathrm{SVD}}^2 = -0.028\,\mathrm{eV}^2$ compared to the input value $m_\nu^2 = 0\,\mathrm{eV}^2$ (dotted line) of the simulation.

The obtained uncertainty is about 25 times larger than the uncertainty obtained from the combined analytical fit and thus exceeds the KATRIN requirements of $\sigma_{\mathrm{sys}}^{\mathrm{eloss}}(m_\nu^2) < 7.5 \times 10^{-3}\,\mathrm{eV}^2$ by more than one order of magnitude.

Besides the investigations of the uncertainty of the deconvolution approach based on Monte Carlo simulations, it is also possible to directly compare the deconvolution result to the more reliable results of the analytical fit. Due to the shape differences caused by the systematic oscillations and the reduced height of the electronic excitation peak, a systematic shift of

$$\Delta m_{\nu,\mathrm{SVD/fit}}^2 = 0.084\,\mathrm{eV}^2 \tag{7.39}$$

is obtained. This value is located slightly above the upper limit of the $1\sigma$ interval of the distribution obtained from the ensemble test of the deconvolution approach (see Fig. 7.19).

**Conclusion**

From the comparison of the two analysis methods, it can be concluded that the approach of fitting an analytical model to the measurement data performs at least 25 times better than the deconvolution approach.

Although the advantages of the deconvolution approach are to obtain a model independent measurement result, the deconvolution process requires the free threshold parameter $w_{\mathrm{thr}}$, which can only be determined by simulations with respect to a reference model. The same applies to the determination of the uncertainty of the measurement result, which can only be obtained from Monte Carlo simulations.

With the new semi-empirical energy-loss model, a detailed description of the energy-loss function exists. The uncertainties due to the fit model are therefore minute. Furthermore,

the analytical fit directly provides parameter uncertainties and correlations. Thus, the analysis with the analytical fit is preferred for future measurements.

## 7.5 Summary

A first measurement of the energy-loss function for electrons scattering off molecular deuterium inside the source of KATRIN were discussed in this chapter. The measurement was based on response function measurements using a photoelectron source, in order to generate monoenergetic and angular-selected electrons with (relativistic) kinetic energies close to the tritium endpoint energy.

Given the conditions of the experimental setup, the initially proposed measurement approach (see Ref. [HHW+17]) was adapted. By establishing a measurement method, where the surplus energy of the electron gun was continuously ramped, it was possible to perform repeated response functions measurements in alternating directions in order to compensate the influence of systematic drifts of the column density and the electron rate.

Two different analysis approaches were used in order to determine the energy-loss function from the response function measurements shown in Fig. 7.4. The first approach used the method of SVD deconvolution (see Sec. 7.1.2) and the second approach was to perform a fit to the measurement data including an analytical description of the energy-loss function (see 7.1.3).

The result of the deconvolution, as shown in Fig. 7.8, is strongly affected by the reduced statistics of the measurements and thus shows large periodic oscillations, which are an artefact of the deconvolution method. Better results were obtained from the analytical fit including the new semi-empirical energy-loss model. Besides the analysis of the integral response function, the data set was extended by including a novel differential response function. Both results of the analytical fit approach provide a very detailed description of the energy-loss function (see Fig. 7.18), with the $1\sigma$ uncertainty interval being on average more than a factor of 100 smaller than the uncertainty band of the deconvolution approach.

The quality of the two analysis approaches was further investigated with respect to the uncertainty on the KATRIN observable $m_\nu^2$. From the propagation of the model uncertainties, the systematic uncertainties

$$\sigma_{\mathrm{sys}}^{\mathrm{SVD}}(m_\nu^2) = 97 \times 10^{-3}\,\mathrm{eV}^2 \tag{7.40}$$

for the SVD deconvolution result as well as

$$\begin{aligned} \sigma_{\mathrm{sys}}^{\mathrm{int}}(m_\nu^2) &= 2.1 \times 10^{-3}\,\mathrm{eV}^2 \quad \text{(using only integral data)} \\ \sigma_{\mathrm{sys}}^{\mathrm{comb}}(m_\nu^2) &= 2.8 \times 10^{-3}\,\mathrm{eV}^2 \quad \text{(using integral and differential data)} \end{aligned} \tag{7.41}$$

for the two results of the analytical fit approach were obtained. Thus, the analytical fit approach performs more than 30 times better than the result of the SVD deconvolution approach. Both results of the analytical fit approach meet the KATRIN requirements of $\sigma_{\mathrm{sys}}^{\mathrm{eloss}}(m_\nu^2) < 7.5 \times 10^{-3}\,\mathrm{eV}^2$. However, the uncertainty of the fit result increased with adding the differential data to the fit, which indicates a systematic difference between the differential data and the integral data. The result of the combined fit is thus considered to be more robust than the result obtained from the fit using only integral data.

The first precision measurements of the energy-loss function of deuterium with the experimental setup of KATRIN was crucial for the improvement of the measurement approach. Based on the differential response function data, the semi-empirical energy-loss function model was developed, which allowed for a combined fit using both integral and differential

response functions. This measurement approach can be used for the following measurement of the energy-loss function of tritium.

For a further optimisation of the measurement approach, the following improvements will be considered for the tritium measurements:

- Split measurement time equally between differential and integral measurements to include more differential data sets.
- Reduce rate in integral measurements to lower detector pile-up and to remove the systematic structure near the transmission edge.
- Use analytical transmission function for the construction of the fit model.

# 8. Measurement of the energy-loss function of $T_2$

After the first measurement of the energy-loss function using molecular deuterium as source gas in fall 2018, measurements were carried out with molecular tritium during the first KATRIN neutrino-mass measurement campaign (KNM1) in spring 2019.

As discussed in Chap. 7, the analysis approach of performing an analytical fit to the response functions performs better than the method of SVD deconvolution. Furthermore, the combined analysis using both integral and differential response functions seemed to give more reliable results than the analysis using only integral data. Hence, the total available measurement time of approximately four days during the KNM1 campaign was split equally between measurements in integral and differential measurement mode and the measured response functions are analysed with the analytical fit approach.

Section 8.1 describes the measurement strategy and the processing of the obtained integral response functions. As the data taking of the response functions in differential mode and the corresponding data processing is covered by the PhD thesis of C. Rodenbeck [Rod], it will not be discussed in detail here.

Since an increased background rate is visible in the measurement data compared to the deuterium measurements, dedicated background measurements were performed to determine the origin and the shape properties of the background component. Both the measurements as well as the integration of the background component into the fit model are described in Sec. 8.2.

The results of the combined fit using both the integral and differential data sets are discussed in Sec. 8.3.

In order to investigate the quality of the measurement result, the systematic uncertainties of the measurements are characterised in Sec. 8.4. The different sources of systematic uncertainties are used as input for the Monte Carlo simulations described in Sec. 8.5, which are performed to investigate the influence on the measurement result of the energy-loss function.

The quality of the measurement result with respect to the systematic uncertainty on the KATRIN observable $m_\nu^2$ is discussed in Sec. 8.6.

This chapter is concluded by Sec. 8.7, where the results of the first precision measurement of the energy-loss function for molecular tritium with the experimental setup of KATRIN are summarised.

It is important to point out that the analysis of the measurement data with the combined fit using both integral and differential response functions is a collaborative work with C. Rodenbeck and V. Hannen (University of Münster) as well as B. Lehnert (Lawrence Berkeley National Laboratory). However, the data processing of the integral measurement

data, the characterisation of the systematics of the measurements as well as the development of the Monte Carlo framework required to determine the impact of the systematics on the measurement result is the outcome of this of this work.

## 8.1 Measurement and data processing of the integral response functions

The strategy of the data taking and the processing of the integral response function is similar to the process of the deuterium measurements described in Sec. 7.2. However, a few improvements and changes due to slightly different measurement conditions were incorporated. An overview of the measurement settings is provided in Tab. 8.2. The relevant changes of the measurement settings and conditions compared to the deuterium measurements are discussed in the following:

- **Reduced electron rate**
  In order to reduce detector pile-up, which is expected to be the reason for the structure of the response functions near the transmission edge of the deuterium data (see Fig. 7.4), the photoelectron rate was lowered by about a factor of two compared to the deuterium measurements. Hence, the electron rate during the integral measurements were below 7 kcps. The exact values are provided in Tab. 8.2.

- **Optimised laser settings**
  The laser settings were optimised in order to operate the laser with as little pile-up as possible. Therefore, the laser was changed to be triggered internally with $f_P = 100\,\mathrm{kHz}$ and the diode current was set to 8 A. Furthermore, the light intensity was reduced to obtain the desired rates of 7 kcps by increasing the attenuation of the laser output with the internally installed attenuator.

- **Extended scan range**
  The scan range was extended to $E_\mathrm{s} = [-5, 60]\,\mathrm{eV}$ at the same run length of 1807 s resulting in a ramping speed of $35.95\,\mathrm{mV\,s^{-1}}$.

- **Increased retarding potential**
  In order to avoid a background signal of β-electrons from the tritium decay in the source, the measurements must be performed above the tritium endpoint. Therefore, the retarding potential was chosen to be $U_\mathrm{ret} = -18\,575\,\mathrm{V}$, which is 50 V more negative than for the deuterium measurements.

- **Optimised column density values**
  Since the actual column density values of the deuterium measurements were smaller than the desired values, the setpoints were adjusted so that the fraction of unscattered electrons $P_0(\mu)$ is distributed in equidistant steps, as it can be seen in Fig. 8.2.

- **Correction of $U_\mathrm{ie}$**
  Although the faulty voltage supply of the inner electrode (see Fig. 7.3) was exchanged after the deuterium measurements, large drifts of $U_\mathrm{ie}$ appeared due to a malfunction of the air conditioning of the main spectrometer building. The malfunction caused a periodically oscillation of the building temperature with a period time of 1.6 h and an amplitude of 0.2 °C. These temperature instabilities caused similar periodic oscillations of the inner electrode voltage, which is shown in Fig. 8.1. In order to correct for these drifts during the binning of the measurement data (see Eq. (7.17)), the course of $U_\mathrm{ie}(t)$ during one scan is fit with a sine function.

As listed in Tab. 8.1, between 26 to 31 up and down scans were carried out for the column density settings of 0 %, 41 %, and 86 % of $\rho_0 d$, However, for the measurement at 14 % $\rho_0 d$ only a reduced amount of 14 scans is available, since a wrongly triggered safety interlock of the high-voltage system aborted the measurements during the night.

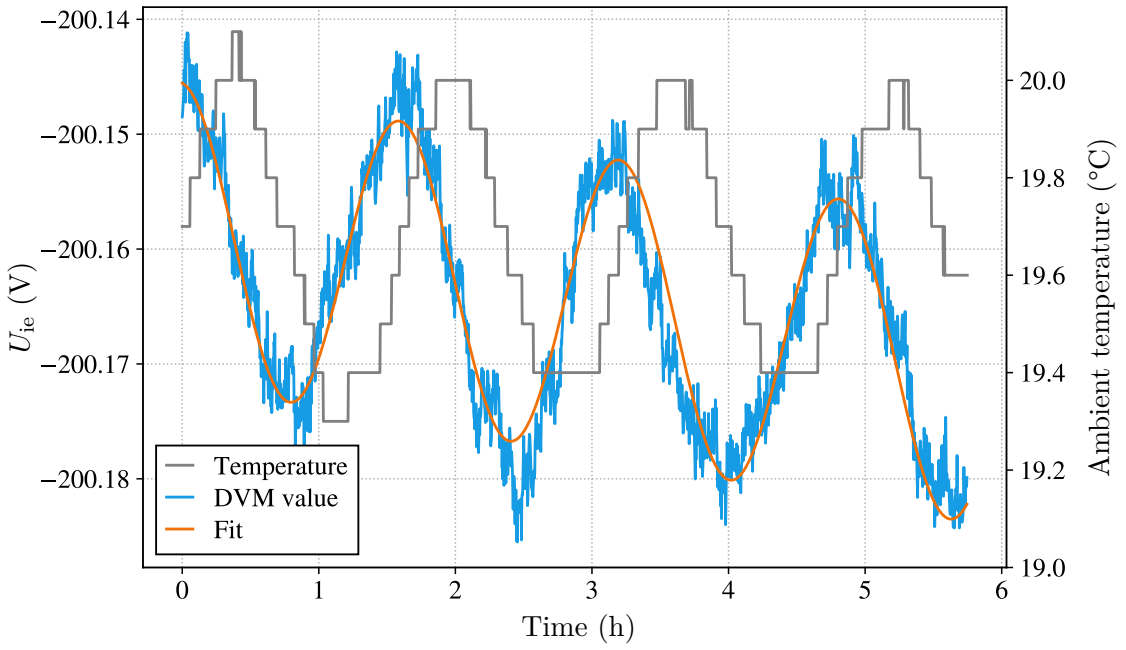


Figure 8.1: Due to a malfunction of the air conditioning of the main spectrometer building, the ambient temperature inside the building was oscillating. As the temperature stability influences the stability of the voltage supply, the inner electrode voltage $U_{ie}$ was oscillating with a period time of 1.6 h and an amplitude of 13 meV. The course can be approximated with a sine function.

The individual runs were processed in the same way as described in Sec. 7.2, including the correction of the light intensity and the detector pile-up by using dedicated look-up tables for each of the response functions. The look-up tables are obtained from the simulations described in Chap. 6 taking into account the column density value, the electron rate, and the pulse rate of the laser. Similar to the processing of the deuterium data, the individual scans were merged by first shifting the middle of the transmission function to 0 eV and then summing up the counts of all scans. The final response functions are shown in Fig. 8.2. Compared to the response functions measured with deuterium (see Fig. 7.4), there are no systematic distortions of the shape close to the transmission function edge visible. Thus, the reduction of the electron rate and the adjustments of the laser settings improved the measurement results. However, the statistics of the integral response functions is decreased by nearly a factor of ten compared to the response function measurements for deuterium (compare Tabs. 8.1 and 7.2), since both the electron rate and the measurement time were reduced by about a factor of two and three, respectively. Thus, the focus of this chapter is on the combined analysis including both the integral and differential data. The combined fit result is discussed in detail Sec. 8.3. The analysis results using only the integral response functions are provided in Sec. A.3 in the appendix.

## 8.2 Characterisation of the background component

As discussed in detail in Ref. [Rod], an increased background signal is visible in the differential measurements using tritium compared to the response function measurements with deuterium. In order to determine the origin of this background and to investigate the shape properties of the background component, dedicated background measurements were carried out, which are described in Sec. 8.2.1. The determination of the shape properties of the background component is very important to set up an appropriate model of the

Table 8.1: Overview of the key properties of the integral response functions, which were measured at four different column densities with $T_2$ as source gas. The mean number of scatterings $\mu$, the number of scans $\Sigma$, the average rate of the electron gun $R_{\text{egun}}$ as well as the total emitted number of electrons $N_{\text{tot}}$ per 50 meV bin are provided for each column density setting. A data range of $-1$ eV to 56 eV is chosen to be the quality selected region.

| Column density / $\rho_0 d$ | $\mu$ | $\Sigma$ | $R_{\text{egun}}$ /(kcps) | $N_{\text{tot}}$ |
|---|---|---|---|---|
| 0 % | 0.00 | 28 | 5.3 | $1.9 \times 10^5$ |
| 14 % | 0.25 | 14 | 5.8 | $1.0 \times 10^5$ |
| 41 % | 0.75 | 26 | 6.5 | $2.2 \times 10^5$ |
| 86 % | 1.56 | 31 | 6.8 | $2.7 \times 10^5$ |

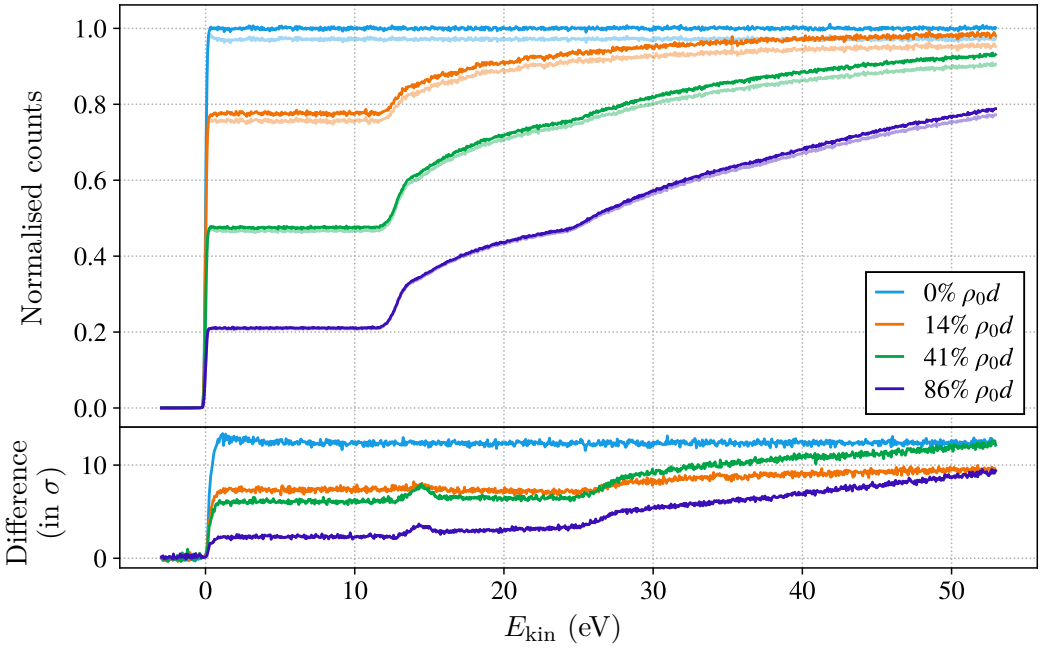


Figure 8.2: Overview of the measured integral response functions for $T_2$. For each data set, the corresponding data without pile-up correction is drawn as shaded lines. With the reduced electron rate and the optimised laser settings, the amount of pile-up events is below 3 %. As shown in the bottom plot, the differences between the corrected and the uncorrected response functions are up to $10\sigma$, which would cause significant residuals in the fit result. Due to the adjusted column density values, the number of unscattered electrons (i.e. the height of the plateau in the region $E_{\text{s}} = [1, 10]$ eV) is now distributed in equidistant steps.

Table 8.2: Overview of the measurement settings during the response function measurements in integral and differential mode with $T_2$ as source gas.

| Parameter | Integral | Differential |
|---|---|---|
| Light source | ——— InnoLas Mosquitoo 266nm pulse laser ——— | |
| Pulse frequency $f_P$ / kHz | 100 | 20 |
| Trigger | internal | external |
| Diode current / A | 8 | 7 |
| Pitch angle / ° | 0 | 0 |
| Rate / kcps | 5.3, 5.8, 6.5, 6.8 | 5.8;7.3;6.3;9.5 |
| Column density / % of $\rho_0 d$ | 0, 14, 41, 86 | 15, 22, 39, 84 |
| $T_2$ purity / % | 95 | 95 |
| WGTS temperature / K | 30 | 30 |
| Analysing plane setting / G | 1.4 | 1.4 |
| Scanning strategy | ——— Ramping of $U_{em}$; $U_{ret} = -18\,575$ V =const. ——— | |
| Scan range $E_s$ / eV | [-5,60] | [-5,60] |
| Ramping speed / mV s$^{-1}$ | 35.95 | 35.95 |
| Bin width / eV | 0.05 | 0.05 |
| Run length / s | 1807 | 1807 |
| ToF cut / µs | - | 35-50 |

background in order to take the background component into account in the construction of the fit function.

In order to reduce the background component in the differential measurement data and to improve the signal-to-background ratio, the so-called multiplicity $\hat{\mathcal{M}} > 1$ cut is introduced in Ref. [Rod]. The multiplicity $\hat{\mathcal{M}} > 1$ cut makes use of the different event multiplicities of the signal electrons and the background events after applying the ToF cut. Since the background electrons arrive in clusters at the detector, it is possible to discriminate them from the signal electrons based on the reconstructed electron multiplicity of the event signal of the FPD. As it will be demonstrated in Sec. 8.2.2, the $\hat{\mathcal{M}} > 1$ cut does not reduce the background by a constant factor but causes an energy dependentd distortion of its shape. In order to consider the distorted background shape in the fit function, simulations are required, which are described in Sec. 8.2.2.2

### 8.2.1 Determination of the background shape

The background measurements were performed with the same scanning strategy as for the energy loss measurements and with the same measurement settings as listed in Tab. 8.2 but with the light source turned off.

Three measurements were carried out, covering one measurement at empty source and two measurements with column densities of 22 % and 84 % $\rho_0 d$, which are shown in Fig. 8.3.

As it is visible by the course of the measurement data, the background follows the same shape as the integral response functions. Thus, the background electrons must be produced at the same electric potential as the signal electrons. One very likely theory for the background process is that positive ions are accelerated in the electric fields of the electron gun, which then impinge on the photocathode and thereby emit secondary electrons. These secondary electrons are then accelerated to the same kinetic energies as the signal electrons. Although the acceleration energy of the background electrons is the same as for the signal electrons, the initial energy distribution is expected to deviate from the energy distribution of the photoelectrons. In order to determine the initial energy distribution, a combined

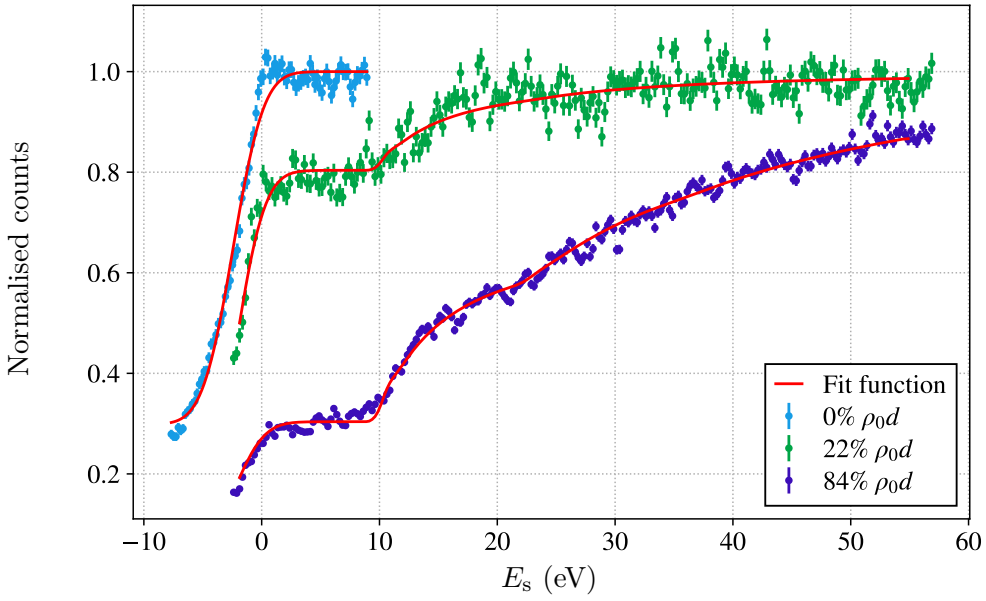


Figure 8.3: The figure shows the measured background rate as a function of the surplus energy. The background component follows the shape of an integral response function. An integral response function is fit to the data to determine the shape properties of the initial energy distribution of the secondary electrons. For the measurement at empty source, the scan range was chosen to be $E_s = [-10, 10]$ eV in order to cover only the transmission function, since no scattering is expected.

$\chi^2$ fit to the three background response functions is performed. In the fit model of the background shape

$$\begin{aligned} R_i^{\mathrm{bg}}\left(E_{\mathrm{s}}, A_i, \mu_i, A_i^{\mathrm{flat}}, \mu_{\mathrm{E}}^{\mathrm{bg}}, \sigma_{\mathrm{E}}^{\mathrm{bg}}\right) =& A_i \cdot (P_0(\mu_i) \cdot T_{\mathrm{bg}}(E_{\mathrm{s}}, \mu_{\mathrm{E}}^{\mathrm{bg}}, \sigma_{\mathrm{E}}^{\mathrm{bg}}) \\ &+ P_1(\mu_i) \cdot T_{\mathrm{bg}}(E_{\mathrm{s}}, \mu_{\mathrm{E}}^{\mathrm{bg}}, \sigma_{\mathrm{E}}^{\mathrm{bg}}) \otimes f(\Delta E, \vec{\mathcal{P}}) \\ &+ P_2(\mu_i) \cdot T_{\mathrm{bg}}(E_{\mathrm{s}}, \mu_{\mathrm{E}}^{\mathrm{bg}}, \sigma_{\mathrm{E}}^{\mathrm{bg}}) \otimes f(\Delta E, \vec{\mathcal{P}}) \otimes f(\Delta E, \vec{\mathcal{P}}) \\ &+ \ldots) \\ &+ A_i^{\mathrm{flat}}\,, \end{aligned} \tag{8.1}$$

the energy-loss function parameters $\vec{\mathcal{P}}$ are fixed to preliminary evaluated values of the energy-loss function (listed in Tab. A.3) and the two free parameters $\mu_{\mathrm{E}}^{\mathrm{bg}}$ and $\sigma_{\mathrm{E}}^{\mathrm{bg}}$ are included in order to determine the position and width of the transmission function $T_{\mathrm{bg}}(E_{\mathrm{s}}, \mu_{\mathrm{E}}^{\mathrm{bg}}, \sigma_{\mathrm{E}}^{\mathrm{bg}})$. Again, an error function (see Eq. (5.10)) is used as model for the transmission function $T_{\mathrm{bg}}(E_{\mathrm{s}}, \mu_{\mathrm{E}}^{\mathrm{bg}}, \sigma_{\mathrm{E}}^{\mathrm{bg}})$, i.e. the energy distribution of the background component is assumed to be Gaussian and the impact of the angular distribution is neglected. Besides the background component, which is investigated, an additional flat background component with amplitude $A_i^{\mathrm{flat}}$ can exist. The latter is caused from the background processes inside the main spectrometer.

The best fit result, as shown in Fig. 8.3, is obtained at a reduced $\chi^2$ value of $\chi^2/N_{\mathrm{dof}} = 3.315(62)$ and thus does not agree very well with the expectations of $\chi^2/N_{\mathrm{dof}} = 1$, which is caused by the very simple approximation of the energy distribution by using a Gaussian distribution. From the fit result, the shape parameters of the energy distribution

$$\mu_{\mathrm{E}}^{\mathrm{bg}} = -2.42(3)\,\mathrm{eV} \quad \sigma_{\mathrm{E}}^{\mathrm{bg}} = 2.04(4)\,\mathrm{eV} \quad cov(\mu_{\mathrm{E}}^{\mathrm{bg}}, \sigma_{\mathrm{E}}^{\mathrm{bg}}) = -4.39 \times 10^{-4}\,\mathrm{eV}^2 \tag{8.2}$$

are obtained.

From the fit result it can be seen, that the initial energy distribution of the background electrons is located at 2.42(3) eV and has an energy spreads of 2.04(4) eV. Compared to the initial energy distribution of the photoelectrons (comp. Tab. 8.5), the initial energy distribution of the background electrons is shifted towards higher energies and has a more than 20 times larger width. Especially in the case of the transmission function of the measurement at empty source, it can be seen that using an error function is only a basic approximation, as the transmission function has a broader tail towards lower surplus energies and is very sharp at the upper edge of the transmission function. This asymmetric shape is expected from the asymmetric shape of secondary electrons emitted from ion impact (see e.g. Ref. [Weh66]), which supports the theory that the background is caused by ions. However, the development of a more suitable model of the energy distribution would require measurements with higher statistics focussing only on the energy window $E_{\mathrm{s}} = [-15, 5]$ eV.

The different energy distribution of the background events thus causes a shift and broadening of the integral shaped background component, which adds to the shape of the signal electrons. Due to this difference, it is required to include the background shape even in the integral measurements, although the signal-to-background ratio is only on the order of $10^{-3}$. However, the influence on the differential data set is much larger, as the ToF cut is ineffective in the case of the randomly timed background events. Hence, applying the ToF cut does not turn the integral background spectrum into a differential spectrum as in the case of the signal electrons. Consequently, the background component has still an integral shape and only the amount of background electrons is reduced by a factor of 3.34, as the acceptance window of the ToF cut is set to 35 µs to 50 µs. It is therefore essential to include

an integral shaped background component to the differential fit function, similar as for the integral measurements. However, when applying the multiplicity cut, the shape of the background component is distorted, as it will be discussed in the following section. Thus, the shape cannot be modelled with an integral response function but has to be obtained by simulations.

### 8.2.2 Multiplicity cut

The signal-to-background ratio at the tail region of the differential response functions can drop below one, especially in the case of small column densities, where there is nearly no contribution from $n$-fold scattered electrons. In order to improve the signal-to-background ratio, the multiplicity $\hat{\mathcal{M}} > 1$ cut was introduced by C. Rodenbeck [Rod], based on the observation that the background electrons form clusters in time resulting in detector events with large values of $\hat{\mathcal{M}}$. By rejecting all events with $\hat{\mathcal{M}} > 1$ during the data analysis it is possible to reduce the amount of background events without significantly influencing the shape of the signal component. The occurrence of electron clusters can be explained by the theory of ions generating the background by impinging on the photocathode. The ions penetrate the metal and collide with the lattice atoms and the nearly free valence-band electrons (see e.g. [BAF79]). Due to the energy transfer between the ion and the electron, it is possible for the latter to exit the solid. Depending on the ion energy and the mass of the ion, multiple electrons can be emitted. Baragiola et al. [BAF79] and Veje [Vej82] report an average value of 1.09 electrons being emitted from 20 keV $H_2^+$ ions impinging on a gold target as well as 3.02 for 30 keV $HeH^+$ ions. From these results it is expected, that the ejected number of elections per ion event is Poisson distributed with the mean initial cluster size $\hat{\mathcal{S}}$ being in the range of 1.09 to 3.02.

The existence of these cluster events can be proven by investigating the multiplicity distributions of the background measurements, which are available in Fig. 8.4. The distributions show that a significant amount of the background events arrive at the detector in clusters with multiplicities up to $\hat{\mathcal{M}} = 7$ and above. As the count rate is only about 10 cps, no pile-up would be expected if the arrival times of the electrons were Poisson distributed.

This is in strong contrast to the event multiplicity distribution of the differential measurement data after applying the ToF cut. In the case of the differential response function measurements, the measurement data is rather unaffected by pile-up events, i.e. nearly all the events have a multiplicity of $\hat{\mathcal{M}} = 1$, since only the scattered electrons are selected by applying the ToF cut. Thus, to generate $n$-fold pileup events, $n$ electrons from one pulse would have to scatter off the source gas and would have to loose nearly the same amount of energy in order to arrive simultaneously at the detector, which is very unlikely. As it will be discussed in Sec. 8.4.6, the probability for event multiplicities $\hat{\mathcal{M}} > 1$ is below $10^{-3}$.

The efficiency of the background reduction by applying the $\hat{\mathcal{M}} > 1$ cut can be demonstrated using the background measurements. As it is shown in Fig. 8.5, the multiplicity cut removes about half of the background events and thus improves the signal to background ration by a factor of two. However, as it is also visible that the background does no longer follow the shape of an integral response function but is significantly distorted. Three important shape properties are visible, which are explained in the following:

- $E_s < 10\,\text{eV}$:
  A peak is visible at the transmission edge of the (initial) integral response function. This structure can be explained similar as in Fig. 6.3. Right at transmission edge the flight time differences become large for the electrons from one ion impact due to the broad energy distribution of the electrons. Consequently, the electrons arrive individually, i.e. $\hat{\mathcal{M}} = 1$, at the detector and the multiplicity cut is ineffective. With

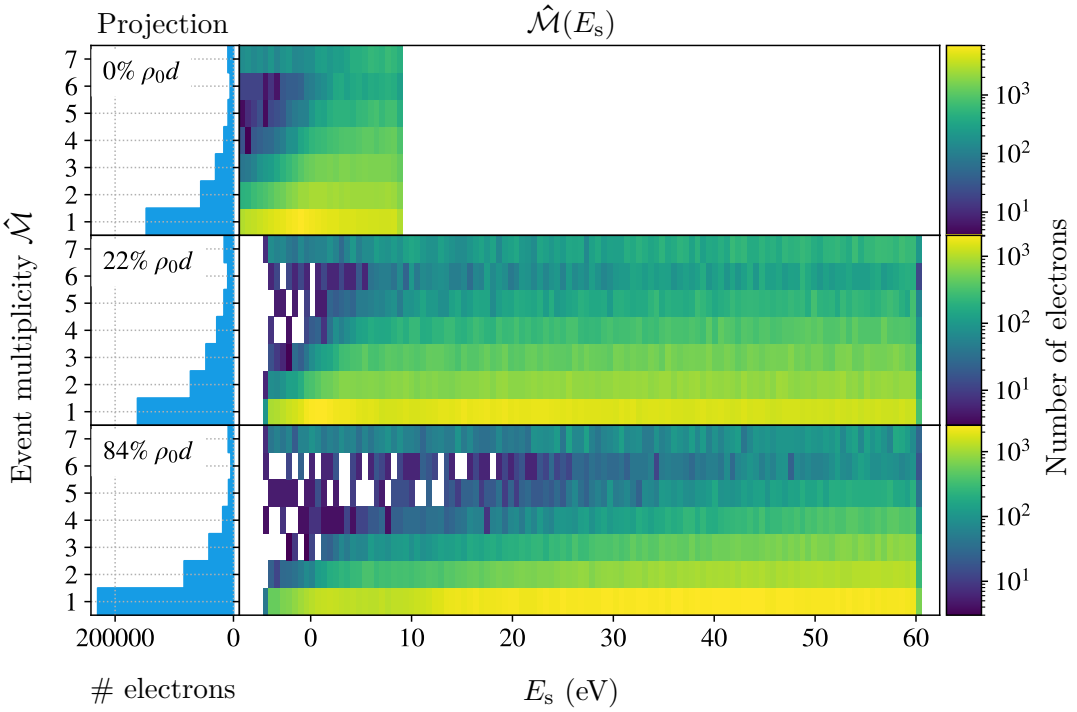


Figure 8.4: Multiplicity distributions of the background measurements at three different column densities (see Fig. 8.3). The right panels show the multiplicity distribution as a function of the surplus energy $E_s$. The left panels show the projected multiplicity distribution of each measurement independent of the surplus energy. From the multiplicity distributions it can be seen that the ion impacts causes a significant amount of electron clusters with $\hat{\mathcal{M}} > 1$. With non-empty source, the multiplicity distribution between $\hat{\mathcal{M}} = 1$ and $\hat{\mathcal{M}} > 1$ events changes as a function of the surplus energy even above the transmission edge (for a detail view see Fig. A.11).

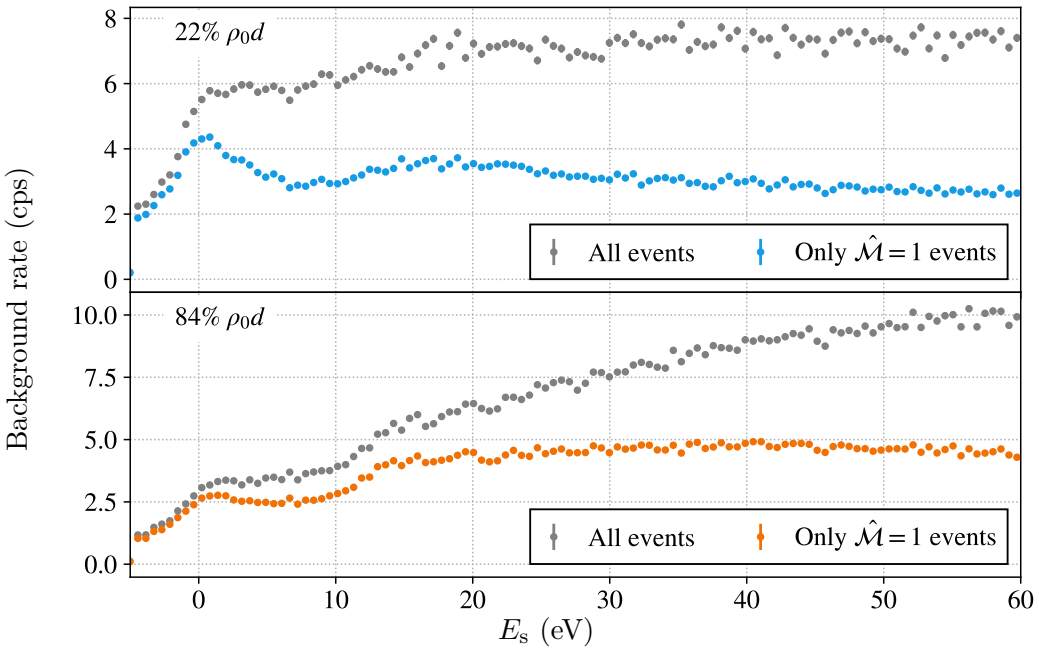


Figure 8.5: Background rate as a function of the surplus energy $E_s$ before and after applying the multiplicity $\hat{\mathcal{M}} > 1$ cut. The efficiency of the cut is dependent on the column density and the surplus energy. Thus, the shape of the background is distorted compared to the initial integral response function shape. Above a surplus energy of 30 eV the background is reduced by approximately a factor of two. Comparing the response functions with and without multiplicity cut, it can be seen that also the rate stability improved by applying the cut.

rising energy, the flight time differences shrink and thus the multiplicity increases, which makes the multiplicity cut becomes more effective with increasing surplus energy.

- $E_s$ =10 eV to 30 eV:
  An increase in the background shape with applied $\hat{\mathcal{M}} > 1$ cut is visible. This is the region where the one-fold scattered electrons contribute predominantly to the signal. As the electrons scatter, they lose a certain amount of their kinetic energy and are thus stronger retarded in the spectrometer potential. Hence, they do not arrive with the other electrons from the same ion impact, but as single electrons. The efficiency of the multiplicity cut is therefore less effective at regions, where large amounts of scattered electrons are transmitted. This can be seen by comparing the reduction of the 22 % $\rho_0 d$ measurement with the 85 % $\rho_0 d$ measurement. In the case of the former, the reduction is nearly a factor of two whereas the reduction is only about 25% for the latter.

- $E_s > 30$ eV:
  For higher surplus energies, the background shape with applied $\hat{\mathcal{M}} > 1$ cut flattens out as the surplus energy of the dominantly single-scattered electrons becomes larger than 10 eV. Comparing this with the flight time curve in Fig. 6.5, it is obvious that the flight time differences due to the retardation in the main spectrometer become minute. Thus, all electrons from one ion event arrive at the detector within the shaping time and the efficiency of the cut increases.

Due to the complex shape of the background after the multiplicity cut, it is necessary to implement a suitable background model in the fit, which considers the shape distortions of

the background due to the multiplicity $\hat{\mathcal{M}} > 1$ cut.

However, only two background measurements were carried out with matching column density setting of the differential response function measurements. It is therefore not possible to construct a background model from the measurement data for each of the four differential response function. Hence, it is required to obtain the shape of the background component from dedicated simulations. An important input for the simulations is the mean initial cluster size $\hat{\mathcal{S}}$ of the background process. An estimate of the mean initial cluster size $\hat{\mathcal{S}}$ can be obtained from the measurement data.

Both the determination of $\hat{\mathcal{S}}$ as well as the simulations to determine the shape of the background component after applying the $\hat{\mathcal{M}} > 1$ cut were carried out by C. Schwachtgen as part of his master's thesis [Sch20] and will be summarised in Sec. 8.2.2.1 and 8.2.2.2, respectively.

#### 8.2.2.1 Determination of the initial cluster size

One important property of the background is the mean initial cluster size $\hat{\mathcal{S}}$ of the background events, i.e. the average amount of electrons being emitted from one ion impact on the photocathode. In order to determine the distribution of $\hat{\mathcal{S}}$, the distributions of $\hat{\mathcal{M}}$ for the background scans at 22 % and 84 % $\rho_0 d$, as shown in Fig. 8.4, and another dedicated 2.5 h measurement (run `60820`) at a fixed surplus energy of $E_\mathrm{s} = 10\,\mathrm{eV}$ at empty source are investigated. The additional scans at empty source shown in the top plot of Fig. 8.4 are not evaluated since the more precise measurements at the fixed surplus energy exist.

The direct determination of the distribution of the mean initial cluster size from the measurement data is not possible, as the distributions of the event multiplicity $\hat{\mathcal{M}}$, as shown on the left side of Fig. 8.4, are affected by both the scattering and the retarding potential (as previously discussed). However, it is possible to simulate the impact of both the retarding potential and the inelastic scattering on the initial distribution of the cluster size in order to obtain the multiplicity distribution as measured at the detector. The simulation output can then be used to perform a fit to the measured multiplicity distributions.

Since the measurements at non-empty source were performed in the scanning mode, the simulations require to be carried out on the same measurement range of $E_\mathrm{s} = [-5, 60]\,\mathrm{eV}$ with a fine step size, which was chosen to be 0.05 eV to match the binning of the other analyses.

The simulations are performed by using the flight time simulations framework, which was developed to generate the multiplicity look-up table in Chap. 6. However, the last and time consuming detector simulation using the DRIPS framework is not carried out. In order to save calculation time, the detector simulations are simplified and the multiplicities are determined directly in the C++ program of the flight time simulations.

To do so, the amount $n$ of electrons generated from one ion event is drawn from a Poisson distribution with the expectation value being the mean cluster size $\hat{\mathcal{S}}$. For each of the $n$ electrons, the initial energy is drawn from a Gaussian distribution with the shape parameters being defined by the fit results in Eq. (8.2). The angular dependency is neglected and $\theta$ is fixed to 0°, since the broad energy distribution dominates the spread of arrival times. At the pitch angle of 0.7° (at 42 mT), which corresponds to the angular spread of the electron gun (comp. Eq. (5.8)), the energy resolution of the main spectrometer in the 1.4 G setting causes a broadening of less than 10 meV, which is two orders of magnitude smaller than the width of the initial energy distribution.

Depending on the initial surplus energy $E_\mathrm{s}$ and the sampled energy losses due to inelastic scatterings $\Delta E$ inside the source (see Sec. 6.2.2), the arrival time for each electron is

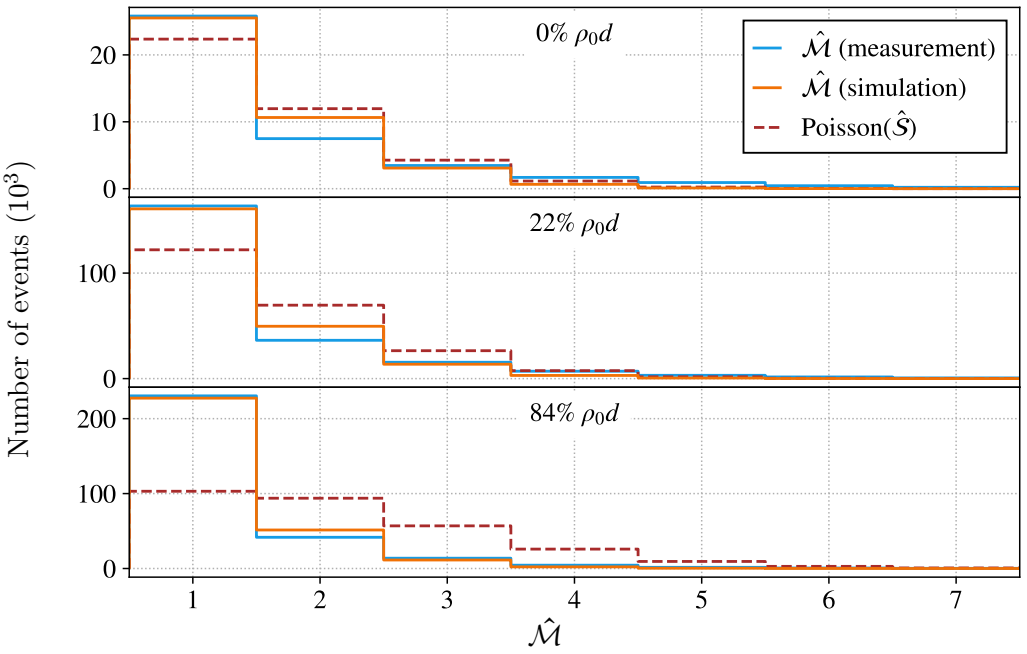


Figure 8.6: Distribution of $\hat{\mathcal{M}}$ as obtained from measurements together with the best fit results of the initial mean cluster size $\hat{\mathcal{S}}$. The simulations agree well with the measurements, except for the amount of two-fold scattered electrons, which is increased compared to the measurements. The differences might be caused by the simplified multiplicity estimation, which is carried out directly in the flight time simulation program, instead of performing a full detector response simulation with the DRIPS framework. The corresponding Poisson distribution for the best fit value of $\hat{\mathcal{S}}$ for each measurement is included to demonstrate the different shape between the initial distribution and the measured distribution at the FPD.

determined from the flight time map provided in Fig. 6.6. The list of the arrival times of the $n$ electron events is then analysed and the amount of electrons arriving within the shaping time $L = 1.6\,\mu s$ is determined. Of course this does not include the characteristic properties of the focal plane detector system and is only a basic simulation model.

The resulting multiplicity histograms for each surplus energy are then merged into one histogram similar as drawn on the left side of Fig. 8.4.

In the case of the 0 % $\rho_0 d$ measurement at fixed surplus energy only one simulation at $E_s = 10\,\text{eV}$ is required.

The simulated distributions of the final event multiplicities $\hat{\mathcal{M}}_{\text{sim}}(\hat{\mathcal{S}})$ are then used to perform a fit to the distributions of $\hat{\mathcal{M}}_{\text{data}}$ by varying $\hat{\mathcal{S}}$. The parameter settings used for the simulations are summarised in Tab. 8.3. The $\chi^2$ fits can be either carried out individually or a combined fit can be performed.

The best-fit results for both the individual fits and the combined fit are

$$\begin{aligned}
&0\,\%\ \rho_0 d\text{:} && \hat{\mathcal{S}} = 1.07(24)\\
&22\,\%\ \rho_0 d\text{:} && \hat{\mathcal{S}} = 1.14(28)\\
&84\,\%\ \rho_0 d\text{:} && \hat{\mathcal{S}} = 1.82(28)\\
&\text{weighted mean:} && \hat{\mathcal{S}} = 1.30(38)\\
&\text{combined fit:} && \hat{\mathcal{S}} = 1.34(16)
\end{aligned} \tag{8.3}$$

with the individual best-fit results being shown in Fig. 8.6. It can be seen, that the simulated histograms agree well with the measurement data except for the amount of multiplicity 2 events, where an excess is visible. The excess can have different causes. Possible reasons could be the simplified determination of the event multiplicity in the simulations or the small differences in the shape of the energy distribution, as the latter is approximated with a Gaussian. Another possible reason for this deviation could be that the initial distribution of the cluster size is not perfectly Poisson distributed.

Furthermore, it is visible that the obtained values of $\hat{\mathcal{S}}$ increase with the column density. However, the background mechanism due to ion impact is expected to be independent of the column density, as the amount of secondary electrons generated from one ion impact is expected to be only dependent on the kinetic energy of the ion. A possible reason for the increase of the multiplicity could be the increasing probability of coincidences of several ion events as the ion rate increases, which thus generates events with larger multiplicity. The simulations however do not cover the coincidence of multiple ions. Thus, the deviations of $\hat{\mathcal{S}}$ are a systematic uncertainty of the measurements. For the average value of $\hat{\mathcal{S}}$, both the combined fit and the weighted mean of the individual fit results is provided. Both values agree well within the uncertainties. However, the uncertainty of the weighted mean is twice as large as the uncertainty obtained from the combined fit and thus covers the individual fit results better. In order to be more conservative, the value of the weighted mean

$$\hat{\mathcal{S}} = 1.30(38) \tag{8.4}$$

is used for the simulations of the background shape after applying the $\hat{\mathcal{M}} > 1$ cut.

The obtained value of $\hat{\mathcal{S}} = 1.30(38)$ is in agreements with the value $\hat{\mathcal{S}} = 1.09$ for 20 keV $H_2^+$ ions impinging on a gold surface as reported by Baragiola et al. [BAF79], which supports the theory that the background is generated from ion impact.

#### 8.2.2.2 Simulations of the background shape after multiplicity cut

In order to determine the shape of the background component after applying the multiplicity $\hat{\mathcal{M}} > 1$ cut, the same simulation framework as described in Chap. 6 is used.

In a first simulation step, the arrival time histograms are simulated for surplus energies in the range of $E_s = [-5, 60]$ eV in 0.05 eV steps using the determined parameters of the energy distribution of Eq. (8.2). Since the shape of the arrival time histograms is dependent on the column density, the simulations need to be carried out for each column density setting of the differential response functions. A summary of the simulation settings is provided in Tab. 8.3. The arrival time histograms are then used for the simulation of the detector response using DRIPS. For the sampling of the initial amount of background electrons from a Poisson distribution, the determined mean cluster size of Eq. (8.4) is used. The simulated detector output for each surplus energy (and column density setting) is then analysed with the multiplicity look-up table[1] to determine the event multiplicities $\hat{\mathcal{M}}$ at the detector.

By accepting only the $\hat{\mathcal{M}} = 1$ events, the shapes of the background components after the $\hat{\mathcal{M}} > 1$ cut is obtained, which are displayed in Fig. 8.7. Since the simulated background shapes are dependent on the value of the mean cluster size $\hat{\mathcal{S}}$, the simulations are repeated for the $1\sigma$ limits of $\hat{\mathcal{S}}$, which are included in the figure.

In order to verify the simulation results it is possible to compare the simulations at the column density values of 22 % and 84 % $\rho_0 d$ with the shape of the background measurements

[1] For the analysis of the differential response function measurements, the look-up table `PileupMap-Sts3aEgun-20181113.ktf` by S. Enomoto is used (see Ref. [Rod]). Thus, the same look-up table is used to determine the multiplicity of the simulation data.

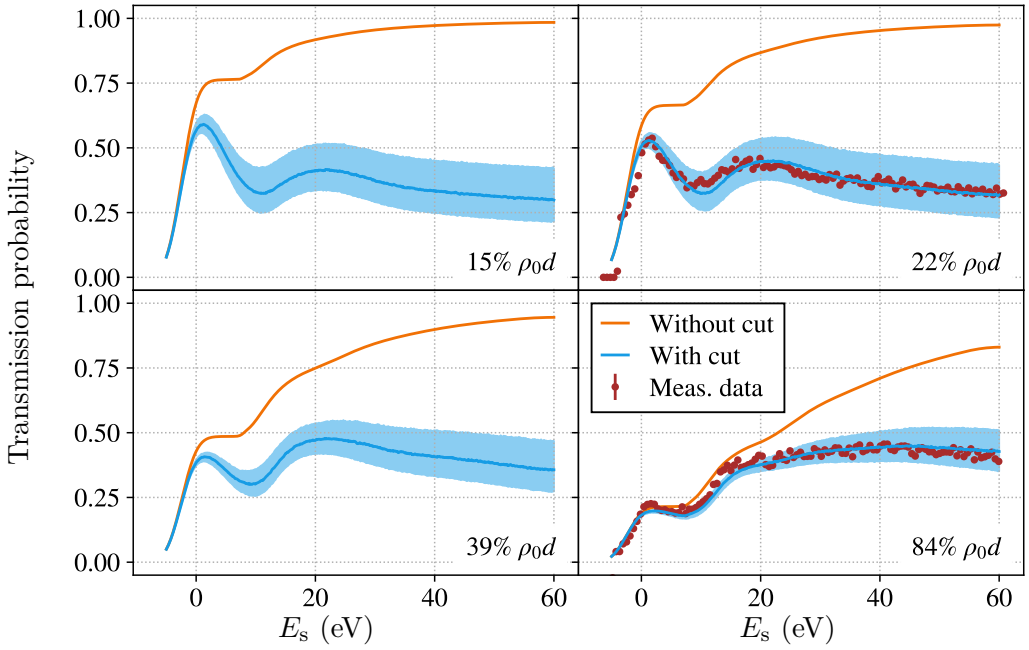


Figure 8.7: Simulations of the shape of the background component after $\hat{\mathcal{M}} > 1$ cut for the column densities of the differential response function measurements. The shaded area indicates the $1\sigma$ uncertainty interval caused by the uncertainty on the cluster size $\hat{\mathcal{S}}$. The simulated curves are used as background model $B(E_s, \mu, \hat{\mathcal{M}} = 1)$ for the construction of the differential fit function (see Eq. (7.31)). The simulations at 22 % and 84 % $\rho_0 d$ are in good agreement with the shape of the background measurements after applying the $\hat{\mathcal{M}} > 1$ cut (no data is available for 15 % and 39 % $\rho_0 d$). Figure adapted from [Sch20].

after the $\hat{\mathcal{M}} > 1$ cut is applied (see Fig. 8.5). The simulation results agree well with the measurements and only minor shape differences exist, especially where the one-fold scattered electrons start to contribute to the signal. A possible reason for these small shape differences could be the uncertainty on the shape of the initial energy distribution of the background events in Eq. (8.2), as similar deviations are visible in Fig. 8.3.

## 8.3 Combined fit result

In order to determine the shape of the energy-loss function of molecular tritium, a combined $\chi^2$ fit is performed to a data set including the integral response functions (see Sec. 8.1) as well as differential response functions. The differential data set is provided by C. Rodenbeck [Rod] and was obtained using the same measurement approach as described in Sec. 7.3.3. This data set consists of four differential response function, which were measured at similar non-zero column densities than in the integral case. As no reference measurement at empty source is required, an additional measurement at 22 % $\rho_0 d$ is included. The measurement and analysis settings of the differential data set are listed in Tab. 8.2.

The fit function is constructed in the same manner as for the combined fit to the deuterium data (see Sec. 7.3.3.2), which results in a total of 30 free parameters. Again, nine of the parameters are required for the energy-loss function model (see Eq. (7.15)) and the other 21 parameters are nuisance parameters, which are the amplitude $A_i$, the average number of scatterings $\mu_i$ and the background amplitude $A_i^{\mathrm{bg}}$ for each of the seven data sets. Compared to the combined fit to the deuterium data, the number of free parameters increased by nine nuisance parameters, as three more differential response functions were added.

Table 8.3: Overview of the simulation settings for the investigations of the multiplicity cut. Column one and two provide the simulation settings for the simulations discussed in Sec. 8.2.2. The third column summarises the settings of the simulations described in Sec. 8.4.6.

| | Determination of $\hat{\mathcal{S}}$ | Distortion of background component | Distortion of signal component |
|---|---|---|---|
| Energy range | $E_s = 10\,\text{eV}$ for 0% $\rho_0 d$ meas.; $E_s = [-5, 60]$ eV in 0.05 eV steps otherwise | $E_s = [-5, 60]$ eV in 0.05 eV steps | $E_s = [-5, 60]$ eV in 0.05 eV steps |
| $\rho d$ / % of $\rho_0 d$ | 0; 22; 84 | 15; 22; 39; 84 | 15; 22; 39; 84 |
| $\mu_E$ / eV | 2.42 | 2.42 | 0.0 |
| $\sigma_E$ / eV | 2.04 | 2.04 | 0.090 |
| $\mu_A$ / ° | 0 | 0 | 0 |
| $\sigma_A$ / ° | 0 | 0 | 0 |
| $\hat{\mathcal{S}}$ | observable | 1.30(38) | 0.35 |
| ToF selection / µs | - | - | 35-50 |
| Determination of $\hat{\mathcal{M}}$ | comparison with $L = 1.6\,\mu\text{s}$ directly in flight time simulation | DRIPS and `PileupMap-Sts3aEgun-20181113.ktf` | comparison with $L = 1.6\,\mu\text{s}$ directly in flight time simulation |

In contrast to the deuterium data, the integral response functions do not show a systematic distortion close to the transmission function edge, as the amount of pile-up events was reduced by decreasing the electron rate and optimising the laser settings. It is therefore possible to describe the transmission function with an analytical function instead of constructing the fit function by using the measurement data (comp. 7.3.2.1). The artificial increase of the $\chi^2$ value due to the additional statistical noise in the fit function can thus be avoided. In order to obtain the transmission function properties, an error function fit (see Eq. (5.10)) to the 0 % $\rho_0 d$ is performed in the range of $E_s = [-1, 5]$ eV, the best-fit result of which is shown in Fig. 8.8. The obtained shape parameters are

$$\begin{aligned} \mu_E &= -0.2(22)\,\text{meV} & \mu_E &= 90(1)\,\text{meV} \\ A &= 204\,861(49) & A_{bg} &= 23(3)\,. \end{aligned} \tag{8.5}$$

As it can be seen from the residuals drawn in the bottom panel of Fig. 8.8, only minor deviations exist between the measurement data and the simple transmission function model. These deviations cause a slightly increased value of $\chi^2/N_{dof} = 1.74(13)$. For the region above the transmission edge, the flat residuals verify, that no distortion of the transmission function exists, as in the case of the deuterium data.

The fit range of the combined fit to the data set is chosen to be $[-1, 56]$ eV for the integral data set and $[10, 56]$ eV for the differential data set, resulting in a total of 7100 data points. The best-fit result, as shown in Fig. 8.9, is obtained at a value of

$$\frac{\chi^2}{N_{dof}} = 1.133(17)\,. \tag{8.6}$$

Similar as for the fit to the deuterium data, the fit to the tritium data was repeated 1000

times with the initial parameters being randomised to ensure that MIGRAD converged to the global minimum. Compared to the deuterium results in Sec. 7.3.3, not only the goodness of fit improved significantly, i.e. $\chi^2/N_{\mathrm{dof}}$ is close to one, but also the residuals show nearly no structures. Especially in the case of the integral response functions the structures could be eliminated with the improvement of the measurement settings and by using the analytical transmission function model.

Although the value of $\chi^2/N_{\mathrm{dof}}$ is very close to one, it does not fully agree with one within the uncertainties of the $\chi^2$ distribution. This deviation can in principle have two reasons. The first reason is that the energy-loss function model has an empirical part, which approximates the complex shape of the electronic excitation states by three Gaussians (see Eq. (7.15)). Thus, small deviations between the data and the model can exist, which causes a small increase of the $\chi^2$ value. Another cause, which can contribute to the increased $\chi^2$ value, are underestimated or yet unconsidered systematic effects. These systematic effects can cause a larger uncertainty (i.e. spread) of the data points. Since structures in the residuals are minute, it is possible to consider the increased uncertainty of the data points by rescaling the $\chi^2$ function so that the $\chi^2/N_{\mathrm{dof}}$ equals one. This corresponds to a scaling of the uncertainty of the data points by the corresponding scaling factor. Consequently, the parameter uncertainties of the fit result increase, which allows for a more conservative estimation of the uncertainties. The parameters of the best-fit result do not change with the rescaling. The best-fit parameters as well as the uncertainties from the fit with $\chi^2/N_{\mathrm{dof}} = 1.133(17)$ and $\chi^2/N_{\mathrm{dof}} = 1$ are provided in Tab. 8.4 with the correlation matrix as well as the covariance matrix for the subset of the nine energy-loss function parameters provided in Figs. 8.10 and A.12. The obtained shape of the energy-loss function is available in Fig. 8.11 together with the $1\sigma$ uncertainty bands for both sets of parameter uncertainties. As it can be seen, the rescaling causes a minute increase of the uncertainty band.

The energy-loss function is again well normalised to an area of 1.0 with a precision of $10^{-4}$ due to the pull term and has a mean energy loss of

$$\langle \Delta E \rangle_{\mathrm{T_2}} = 30.79(1)\,\mathrm{eV}\,. \tag{8.7}$$

The value is 150 meV larger than the value of $\langle \Delta E \rangle_{\mathrm{comb}}^{\mathrm{D_2}}$, which can be explained by the differences of the shape. Especially the position $m_2$ of the second Gaussian kernel is shifted by approximately 70 meV compared to the deuterium result. Besides this difference, it is also visible in Fig. 8.11 that the width of the Gaussians decreased, which agrees with the expectations of a less broad splitting of the excitation states due to the vibrational excitations. As discussed in Sec. 4.1.2, vibrational excitations split the lines from electronic transitions into sets of lines (comp. Figs. 4.1 and 4.2). The width of the splitting is dependent on the mass of the molecules and decreases with increasing mass (comp. Eq. (4.15)).

Due to the improved data quality of the integral data, the $1\sigma$ uncertainty interval drawn below the energy-loss function decreased by nearly a factor of two in the range blow $E_{\mathrm{s}} = 14.5\,\mathrm{eV}$. Above the energy of 14.5 eV, the uncertainty of the deuterium model is smaller than for the tritium model by about a factor of 1.2. The improvement in the region below 14.5 eV can be explained with the increased amount of differential repose functions, which allow for a better determination of the shape parameters of the three Gaussians. A possible explanation for the increase of the uncertainty for the ionisation tail could be the reduced statistics of the integral measurements compared to the deuterium measurements. The statistical uncertainty in the integral measurement data in the region of the ionisation tail decreases due to the integral form (the opposite applies to the differential data), which reduces the statistical uncertainty on the amplitude of the ionisation tail. By reducing the statistics of the integral data set, also the sensitivity is reduced.

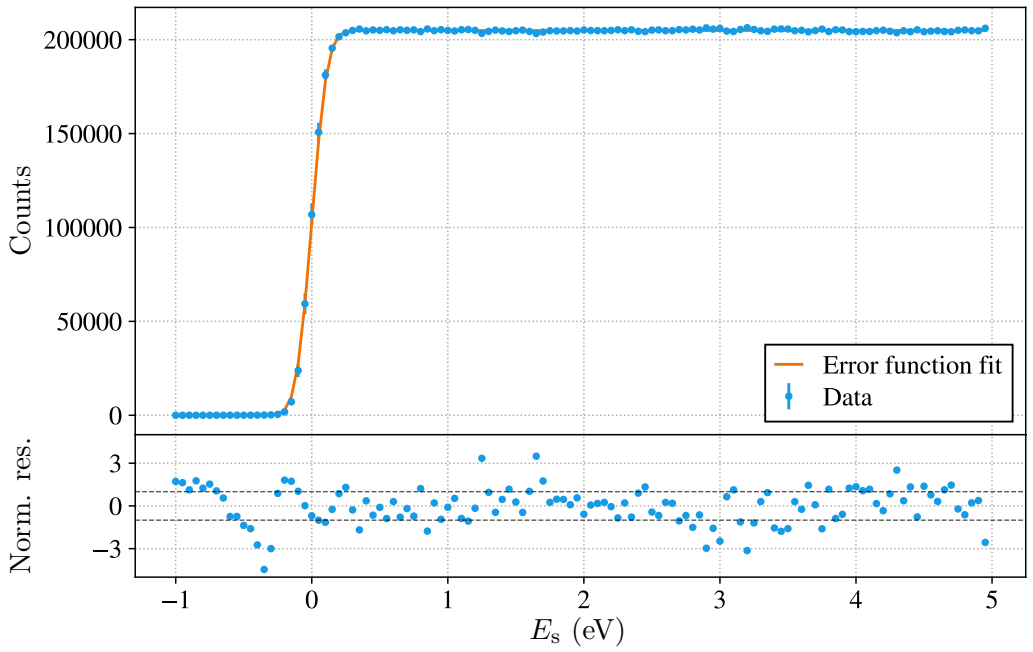


Figure 8.8: Transmission function of the reference measurement at empty source including an error function fit. The residuals are drawn in the bottom panel. Small structures in the residuals are visible especially for the region $E_s < 0\,\text{eV}$, where the influence of the shifted and broadened background component (comp Fig. 8.3) increases. For the region above $E_s = 0\,\text{eV}$, the residuals show no significant structure. The fit confirms that the data is not systematically distorted above the transmission edge as in the case of the $D_2$ measurements (comp. Fig. 7.4).

However, the provided parameter uncertainties obtained from the fit represent only the statistical uncertainties. In order to access the systematic uncertainties of the measurement a full propagation of systematic uncertainties is required. The characterisation of the individual systematic effects of the measurement as well as the investigations of their impact on the measurement result is described in the next section.

Comparing the new KATRIN $T_2$ model to the existing Aseev et al. $T_2$ model, significant differences in the shape are visible in Fig. 8.11. Besides the too broad peak approximating the shape of the electronic excitations also the position is shifted by about 200 meV towards lower energies. Although the isotopes are different, the Abdurashitov et al. $D_2$ model agrees better with the KATRIN $T_2$ model. Thus, the validity of the Aseev et al. model can not be confirmed. A further comparison of the models with respect to the resulting uncertainty on the observable $m_\nu^2$ is provided in Sec. 7.3.

## 8.4 Characterisation of systematics

A large benefit of the determination of the energy-loss function by performing a fit to the measurement data is that the uncertainty for the individual fit parameters (see Tab. 8.4) can be calculated from the likelihood function. However, with the used $\chi^2$ function, as described in Eq. (7.25), only the provided uncertainties of the data points can be considered. Some systematic effects, such as the uncertainty of the light intensity and the uncertainty on the surplus energy during the continuous scans, are already considered by converting these systematic uncertainties into additional uncertainties of the data points (see Sec. A.1).

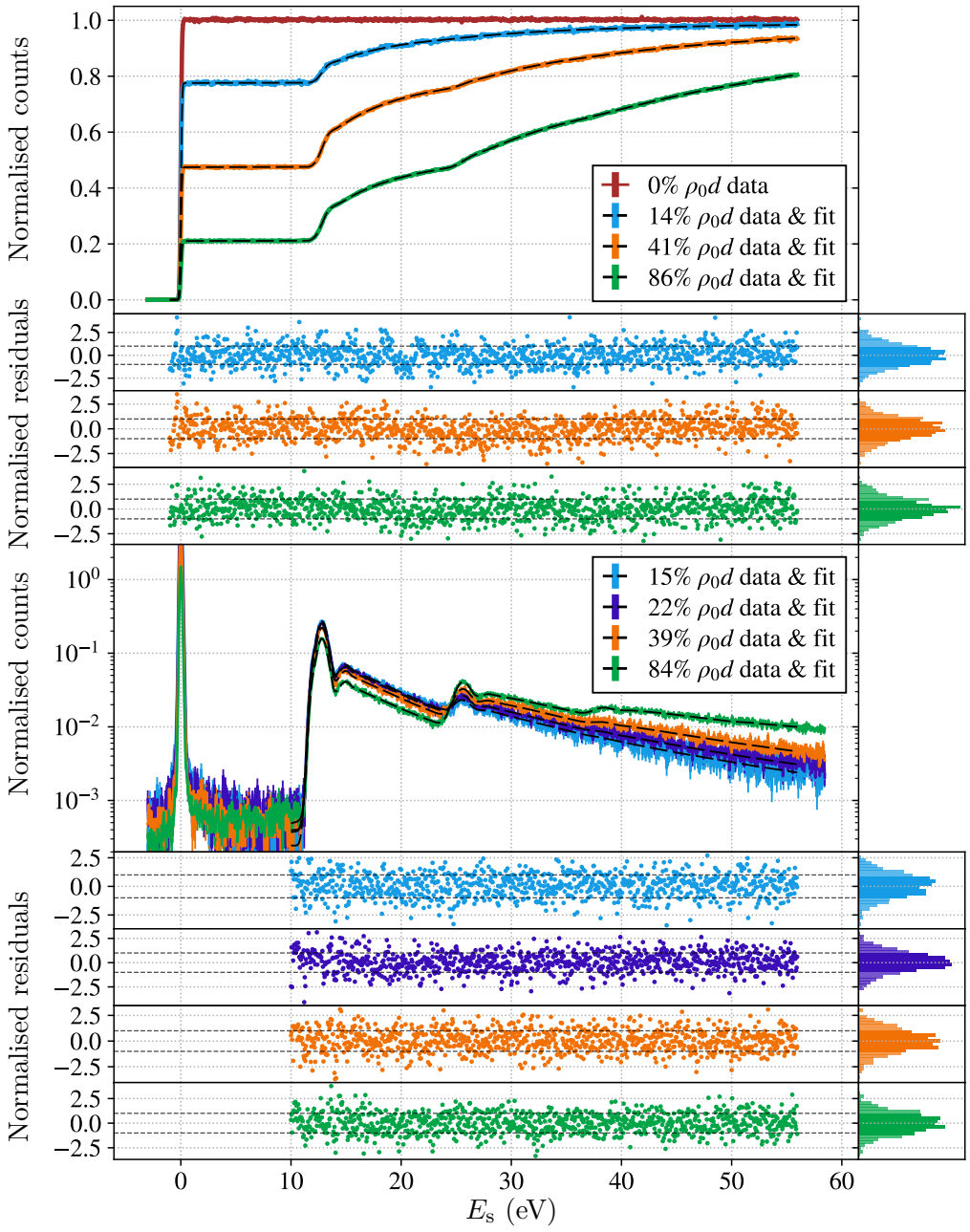


Figure 8.9: Best-fit result of a combined $\chi^2$ fit to both the integral data as well as the differential data. The residuals, which are drawn below each data set in the corresponding colours, show no significant structures for both data sets. The $1\sigma$ limit is indicated by the dashed lines. For each set of residuals, the distribution is provided on the right with the shaded area indicating the $1\sigma$ interval. The best-fit result is obtained at a value of $\chi^2/N_{\mathrm{dof}} = 1.133(17)$.

Table 8.4: Parameters for the energy-loss function (see Eq. (7.15)) of molecular tritium and the nuisance parameters as obtained from a combined $\chi^2$ fit to both integral and differential data. The best-fit result is obtained at a value of $\chi^2/N_{\mathrm{dof}} = 1.133(17)$. In addition to the parameter uncertainties for this $\chi^2$ value, parameter uncertainties are provided in the last column for a rescaled value of $\chi^2/N_{\mathrm{dof}} = 1$. Due to the normalisation of the data sets before executing the fit, the parameters $A_i$ and $A_i^{\mathrm{bg}}$ are not in absolute units but scaled according to the factors provided in Tab. A.2. From the values of $\mu_i$, the column density inside the source during the measurements can be calculated, the values of which are provided in Tab. 8.2. The covariance and correlation matrices for the subset of the nine energy-loss function parameters are provided in Figs. 8.10 and A.12.

| Parameter | Unit | Value | $\sigma_{\mathrm{fit}}$ | $\sigma_{\mathrm{fit}}$ $(\chi^2/N_{\mathrm{dof}} = 1)$ |
|---|---|---|---|---|
| $a_1$ | $\mathrm{eV}^{-1}$ | 0.032 80 | 0.001 13 | 0.001 20 |
| $m_1$ | eV | 11.918 91 | 0.007 82 | 0.008 33 |
| $\sigma_1$ | eV | 0.183 60 | 0.006 54 | 0.006 96 |
| $a_2$ | $\mathrm{eV}^{-1}$ | 0.295 704 | 0.000 635 | 0.000 676 |
| $m_2$ | eV | 12.804 59 | 0.001 99 | 0.002 12 |
| $\sigma_2$ | eV | 0.467 65 | 0.002 04 | 0.002 17 |
| $a_3$ | $\mathrm{eV}^{-1}$ | 0.075 746 | 0.000 345 | 0.000 368 |
| $m_3$ | eV | 14.967 70 | 0.003 80 | 0.004 05 |
| $\sigma_3$ | eV | 0.9073 | 0.0120 | 0.0127 |
| | | Nuisance parameters: integral | | |
| $A_{14}$ | | 1.019 459 | 0.000 160 | 0.000 170 |
| $\mu_{14}$ | | 0.253 850 | 0.000 293 | 0.000 312 |
| $A_{14}^{\mathrm{bg}}$ | | 0.000 288 5 | 0.000 034 5 | 0.000 036 7 |
| $A_{41}$ | | 1.065 223 | 0.000 195 | 0.000 207 |
| $\mu_{41}$ | | 0.745 165 | 0.000 284 | 0.000 303 |
| $A_{41}^{\mathrm{bg}}$ | | 0.000 626 1 | 0.000 039 9 | 0.000 042 5 |
| $A_{86}$ | | 1.235 140 | 0.000 398 | 0.000 424 |
| $\mu_{86}$ | | 1.557 345 | 0.000 408 | 0.000 434 |
| $A_{86}^{\mathrm{bg}}$ | | 0.003 032 2 | 0.000 096 2 | 0.000 102 |
| | | Nuisance parameters: differential | | |
| $A_{15}$ | | 4.4967 | 0.0573 | 0.0610 |
| $\mu_{15}$ | | 0.269 13 | 0.004 29 | 0.004 57 |
| $A_{15}^{\mathrm{bg}}$ | | 0.000 439 8 | 0.000 065 7 | 0.000 069 9 |
| $A_{22}$ | | 3.1964 | 0.0261 | 0.0277 |
| $\mu_{22}$ | | 0.405 62 | 0.004 76 | 0.005 07 |
| $A_{22}^{\mathrm{bg}}$ | | 0.000 642 5 | 0.000 064 9 | 0.000 069 1 |
| $A_{39}$ | | 2.158 11 | 0.007 85 | 0.008 36 |
| $\mu_{39}$ | | 0.718 04 | 0.004 73 | 0.005 04 |
| $A_{39}^{\mathrm{bg}}$ | | 0.000 586 1 | 0.000 052 9 | 0.000 056 3 |
| $A_{84}$ | | 1.608 15 | 0.004 50 | 0.004 79 |
| $\mu_{84}$ | | 1.523 52 | 0.005 25 | 0.005 59 |
| $A_{84}^{\mathrm{bg}}$ | | 0.001 061 5 | 0.000 057 3 | 0.000 061 0 |

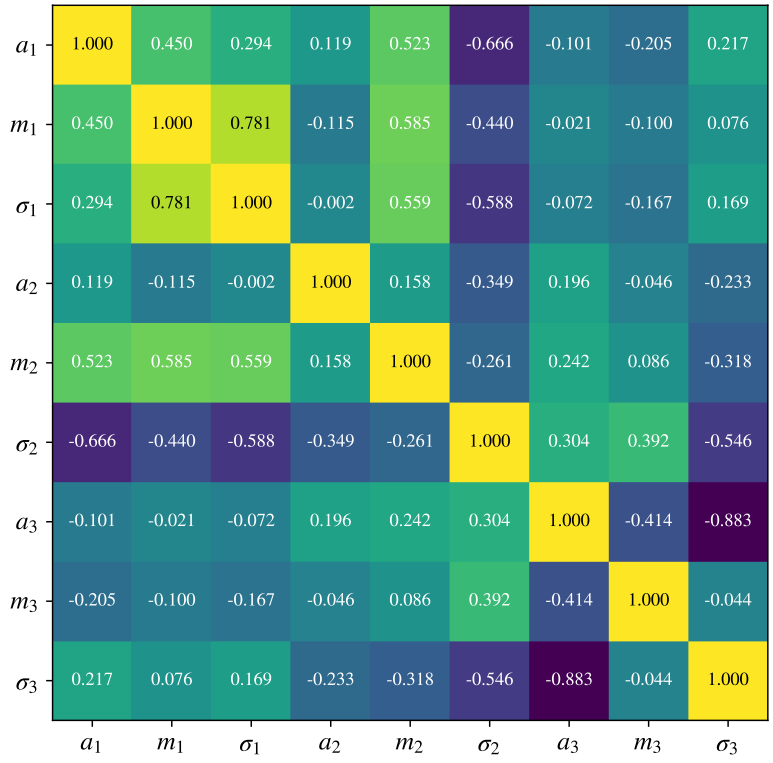


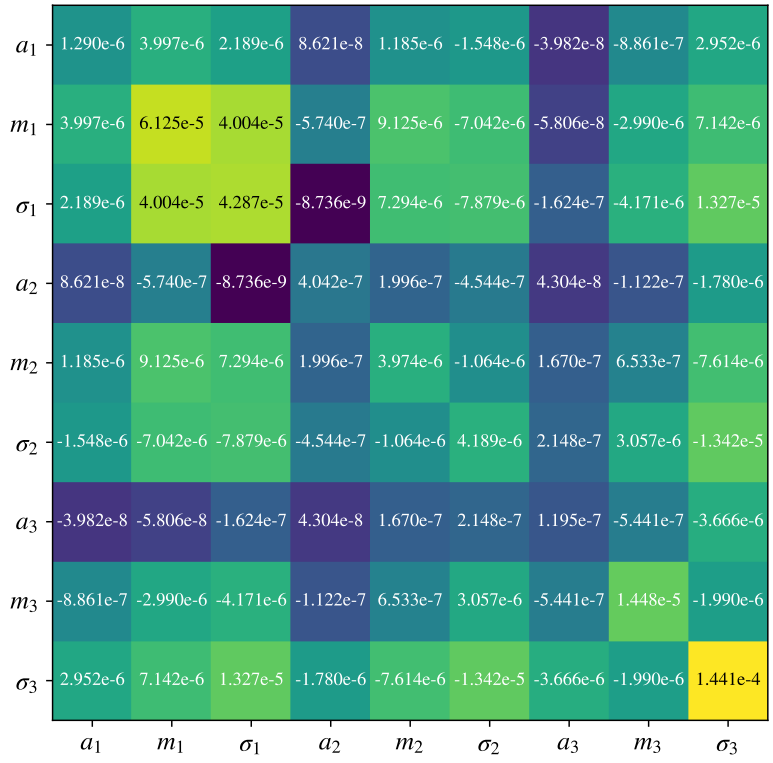


Figure 8.10: Correlation matrix (top) and covariance matrix (bottom) for the energy-loss function parameters in Tab. 8.4 as obtained from the combined $\chi^2$ fit to integral and differential response functions for molecular tritium.

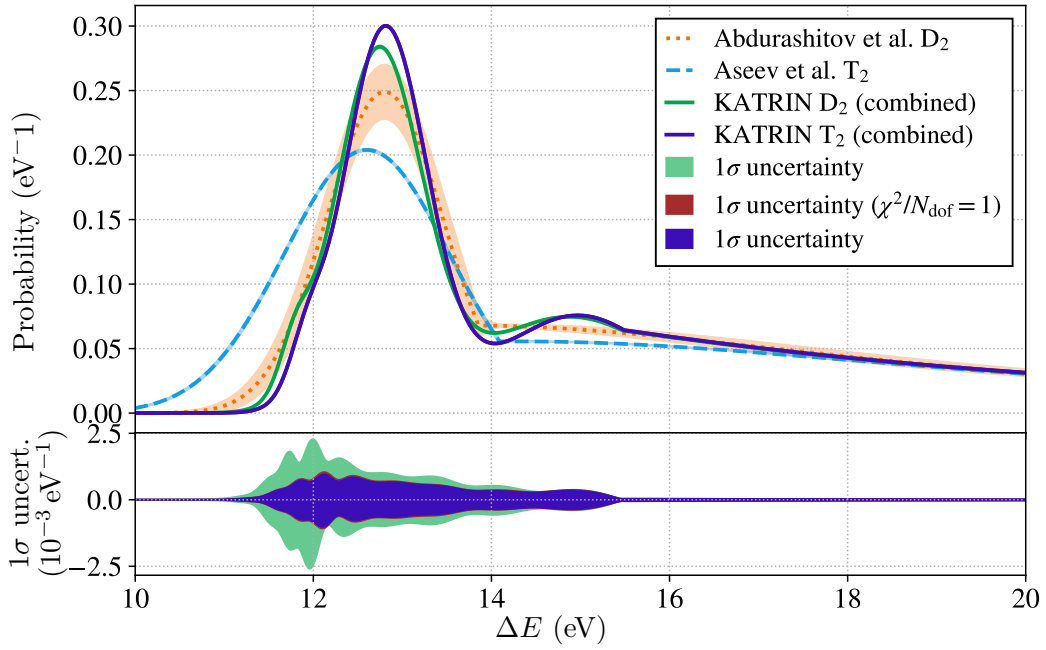


Figure 8.11: Shape of the energy-loss function as obtained from the combined fit of both integral and differential response functions for molecular tritium. The $1\sigma$ uncertainty band is additionally drawn in the bottom panel, as it is not visible in the top panel. Besides the uncertainty band from the fit result with $\chi^2/N_{\mathrm{dof}} = 1.133(17)$, the uncertainty band from the rescaled fit with $\chi^2/N_{\mathrm{dof}} = 1$ is included (red). The increase of the uncertainty due to the rescaling is minute. For comparison, the results of Aseev et al. ($T_2$) and Abdurashitov et al. ($D_2$) as well as the KATRIN $D_2$ result are included. It is visible that the KATRIN $T_2$ result agrees better with the Abdurashitov et al. $D_2$ model than with the actual $T_2$ model of Aseev et al.. Compared to the KATRIN $D_2$ result, the electronic excitation peak is slightly narrower and thus higher, which is expected due to a less strong vibrational splitting of the electronic excitation sates (see Sec. 4.1.1). The $1\sigma$ uncertainty interval improved in the region $E_{\mathrm{s}} < 12.5\,\mathrm{eV}$. However, above $E_{\mathrm{s}} = 14.5\,\mathrm{eV}$ the uncertainty band of the tritium result is on average a factor of 1.2 larger than the uncertainty band of the deuterium result.

Other systematic uncertainties exist, which have not yet been taken into account. The uncertainties can be caused either directly from uncertainties of the the measurement conditions, such as drifts of the column density and the rate of the electron gun, or they can be caused by applied corrections, such as the pile-up correction (see Chap. 6) and the multiplicity cut (see Sec. 8.2.2). These systematics cause distortions of the measured response function, which thus causes parameter shifts and an increase of the uncertainties of the best-fit result of the energy-loss function.

Since the energy-loss function is used to construct the fit model of the neutrino-mass fit, the additional parameter uncertainties and shifts propagate into uncertainties and shifts of the observable $m_\nu^2$. It is therefore very important to characterise all the systematic effects, which influence the result of the energy-loss model. If the systematics are well characterised, their influence on the measurement result of the energy-loss function as well as on the neutrino-mass measurements can be investigated by performing Monte Carlo simulations (see Secs. 8.5 and 8.6).

In the following, the known sources of systematic uncertainties are described, which result from the condition of the energy-loss function measurements and the data processing.

### 8.4.1 Column density stability

The tritium inlet flow is constantly monitored with a throughput sensor[2] located in front of the injection capillaries of the WGTS. With a calibration table provided by A. Marsteller [Mar20], it is possible to convert the inlet flow into column density values. This allows for a real-time monitoring of the column density during the measurements with the values shown in Fig. 8.12. Especially in the case of the 41 % $\rho_0 d$ measurements, a drift of the column density occurred. The column density decreased with a slope of $0.148(1)\,\%\,\mathrm{h}^{-1}$ during the measurements of the integral response functions and $0.190(1)\,\%\,\mathrm{h}^{-1}$ during the measurements of the differential response functions. The drift was caused by traces of methane freezing to the inner walls of the injection capillaries, which reduced the conductivity of the latter. The methane was generated by radiochemical reactions of the tritium with the carbon of the stainless steel, as the loops system and the WGTS were exposed to a large tritium throughput for the first time during the KNM1 measurements. The effect was reduced after the 41 % $\rho_0 d$ measurements by warming up the system to 100 K in order to remove the frozen methane while continuing with the tritium circulation to reduce the carbon on the surface. After this purging process, the stability could be improved by a factor of ten during the 86 % $\rho_0 d$ measurements.

As the drift of the column density influences the average number of scatterings $\mu$ and thus the scattering probabilities $P_n(\mu)$, the response functions are distorted. In the case of $P_0$, the drift during the 41 % $\rho_0 d$ measurements causes a distortion of 0.07 % over the time span of one scan, i.e 1807 s. However, the influence on the merged response function is reduced, as the scans were taken in alternating directions.

### 8.4.2 Rate stability

Long-term drifts of the rate of the electron gun can occur, which are not connected to the drift of the light intensity. These drifts can be caused e.g. due to a drift of the work function of the photocathode or due to the degradation of the thickness of the photocathode by ion impact.

The stability can be obtained directly from the data by monitoring the amount of unscattered electrons for each of the individual scans. In the case of the integral measurements, the

[2] mks MASS-FLO® meter Type 179A, KATRIN number `610-RFY-8-0206`

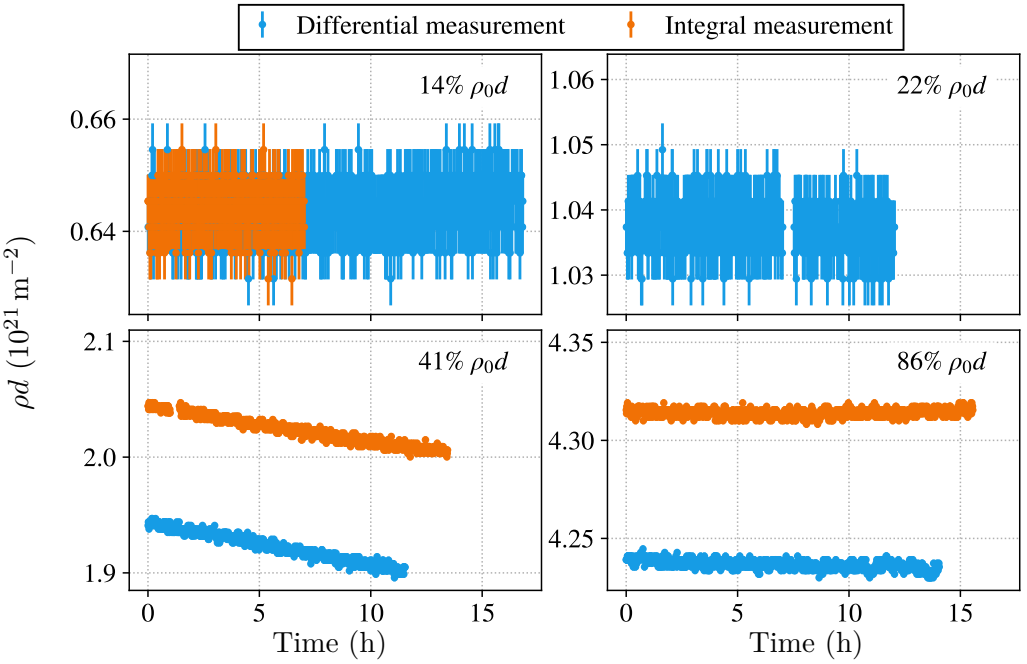


Figure 8.12: Monitoring of the column density with a throughput sensor installed in front of the injection capillaries of the WGTS for the seven response function measurements at non-empty source. For the measurements at 22 % $\rho_0 d$ only differential measurements were performed. During the measurements at 41 % $\rho_0 d$ a drift of the column density of 0.15 % h$^{-1}$ for the integral and 0.19 % h$^{-1}$ for the differential data is observed, which was caused by a reduction of the conductivity of the injection capillaries as methane was freezing on the inside of the injection capillaries.

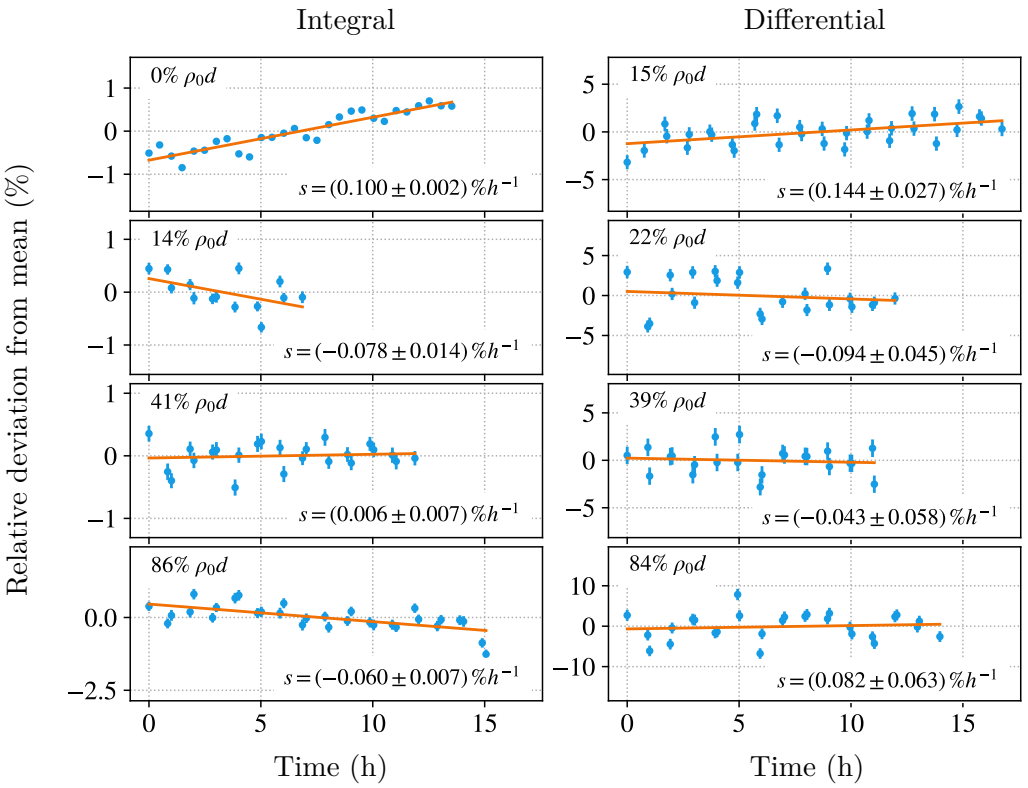


Figure 8.13: Rate stability (relative to the average rate) of both integral and differential measurements. The data points are obtained from monitoring the amount of unscattered electrons. The relative slopes $s$, which are obtained from a linear fit (orange), are provided in each panel.

average counts per bin in the plateau region, i.e. $E_\mathrm{s} = [1, 10]$ eV, is used as monitoring point, whereas for the differential measurement the total amount of counts of the peak of unscattered electrons in the range of $E_\mathrm{s} = [-1, 1]$ eV is used. Similar investigations were already carried out in Ref. [Sch20]. However, in Ref. [Sch20] the amount of unscattered electrons of the differential data was determined from the height of the peak of unscattered electrons which has a larger uncertainty than considering the integral of the peak. Thus, the rate stability was re-analysed as described in the following.

The amount of unscattered electrons is not only depending on the the light intensity, but it is also depending on the probability for zero-scattering and thus depending on the column density. In order to determine the stability of the electron rate, the electron rate must be first corrected for drifts of the column density. This is done by scaling the rate with the relative deviation of the column density within the analysis window (i.e. the plateau region or the peak of unscattered electrons) to the overall average during all scans at the same column density setpoint.

The monitoring points for each of the eight data sets are shown in Fig. 8.13 together with the relative slopes (in $\%\,\mathrm{h}^{-1}$) obtained from a linear fit to the data. The overall drift reaches up to 2.2 % in the case of the 14 % $\rho_0 d$ measurements. However, only the relative drift within the time of one scan causes systematic distortion of the response function, which is smaller than 0.07 %. The impact on the merged response function is further reduced, as the scans were taken in alternating directions.

Table 8.5: Shape parameters $\mu_E$ and $\sigma_E$ of the transmission functions, as obtained from error function fits to the integral response functions in the range of $E_s = [-1, 5]$ eV. The covariance of the two parameters is provided in the last column.

| Column density / $\rho_0 d$ | $\mu_E$ / meV | $\sigma_E$ / meV | $cov(\mu_E, \sigma_E)$ /meV$^2$ |
|---|---|---|---|
| 0% | −0.2(22) | 90(1) | 0.748 |
| 14% | 0.3(23) | 91(2) | 0.976 |
| 41% | −0.6(23) | 89(2) | 0.871 |
| 86% | 0.4(25) | 91(2) | 1.032 |

### 8.4.3 Transmission function shape

The transmission function, which is used to construct the fit model, is obtained from the error function fit (see Eq. (5.10)) to the response function measurement at empty source. Therefore, it is important to verify that the transmission functions of the measurements at non-empty source have the same shape properties. For this purpose, all transmission functions are fit in the same range of $E_s = [-1, 5]$ eV as for the fit in Fig. 8.8. The obtained shape parameters $\mu_E$ and $\sigma_E$ , as listed in Tab. 8.5 do not deviate significantly and agree well within the parameter uncertainties. However, it is visible that the determined positions $\mu_E$ have an uncertainty of approximately 2 meV. This uncertainty has to be considered as uncertainty on the energy calibration of the data sets, since an error function fit was used for the energy calibration, i.e. for shifting the transmission function to zero (see Sec. 7.2.2).

### 8.4.4 Measurement strategy

The continuous ramping of the high voltage causes a systematic broadening of the measured response function when binning the data to discrete energy values. This broadening is not considered in the fit model. Thus, deviation between the binned response function and the fit model evaluated at the bin centre $E_s$ can exist, if either the shape of the fit model or of the shape of the data is inhomogeneously distributed within the bin of width $\Delta E_{bin}$, i.e.

$$\left\langle N\left(E = \left[E_s - \frac{\Delta E_{bin}}{2}, E_s + \frac{\Delta E_{bin}}{2}\right]\right)\right\rangle \neq N(E_s)\,. \tag{8.8}$$

However, in the case of the very fine binning of 50 meV and the smooth fit model, the effect is minute, as it will be shown in Sec. 8.5.

Furthermore, the continuous ramping causes a decrease of the inelastic cross section $\sigma_{inel}(E)$ by 0.27 % within the scan range of 60 eV (see Eq. (4.10)). As discussed in Sec. 7.3.2.1, the fit model is corrected to take the systematic distortion of the response function into account.

### 8.4.5 Pile-up correction

As it is visible in Fig. 8.2, the uncorrected integral measurement data is strongly affected by shape distortions due to detector pile-up, which reach up to 3%. The pile-up affected measurement data is corrected using the dedicated look-up tables obtained from simulations, which are described in Chap. 6.

The look-up tables have two major uncertainties. The first uncertainty is the signal loss due to undercoverage of the look-up table. This means, that the look-up table does not contain multiplicity information for the entire parameter space of $E_{FPD}$ and $w_{bi}$. It is therefore possible, that events have a combination of $E_{FPD}$ and $w_{bi}$, which is not defined, i.e. the event's multiplicity evaluates as zero.

The second systematic uncertainty is that the look-up table is not energy dependent. As described in detail in Chap. 6, the individual look-up tables obtained at different surplus energies are merged into one global look-up table. This has no influence on the regions, where there is no ambiguity of $\hat{\mathcal{M}}(E_{\mathrm{FPD}}, w_{\mathrm{bi}})$ for the same pair of $E_{\mathrm{FPD}}$ and $w_{\mathrm{bi}}$. But for the regions where overlaps exist, the ratio between the overlapping multiplicities changes slightly with the surplus energy. Thus, using the energy independent look-up table causes small distortions of the resulting response functions, which need to investigated.

The analyses for both systematic uncertainties are described in the following.

**Signal loss due to undercoverage**

The distribution of events from the integral response function measurements, which are not covered by the look-up table are shown in Fig. 8.14. Especially in the case of the measurement at empty source, it can be seen that the majority of the lost events are located close to the parameter space covered by the look-up table. As discussed in Sec. 6.2.3, the simulations of the detector response do not cover the noise of the electronics and thus a smearing along the $w_{\mathrm{bi}}$-axis is missing. The look-up table is thus slightly smaller than the distribution of the measurement data, which causes the losses. This effect is reduced for the measurements at non-empty source, as scattered events cause a more complex structure in the $E_{\mathrm{FPD}}$-$w_{\mathrm{bi}}$-plane, which enlarges the area of the look-up table. Thus, the probability for event loss decreases significantly. However, it can be seen, that with increasing column density the amount of events with large values of $E_{\mathrm{FPD}}$ and $w_{\mathrm{bi}}$ increases. This discrepancy with the simulations is however not visible in case of the deuterium measurements at 88 % $\rho_0 d$, as shown in Fig. 6.8. The difference can be explained with the existence of the background, which has larger event multiplicities than the signal electrons (comp. Sec. 8.2.2.1) and thus are not covered by the simulations.

As the distribution of the events within the $E_{\mathrm{FPD}}$-$w_{\mathrm{bi}}$-plane changes as a function of the energy (comp. Fig. 8.17) the event loss has to be investigated as a function of the surplus energy. To do so, the untagged and thus lost events of each energy bin of the response function are summed up. The multiplicity of the lost events is estimated based on the value of $E_{\mathrm{FPD}}$, i.e. the multiplicity corresponds to the ratio of the event energy and the initial kinetic energy of the electrons[3]. In this calculation the additional energy increase $E_{\mathrm{PAE}} = 10\,\mathrm{keV}$ due to the post-acceleration electrode of the FPD as well as the width of the peaks $\delta w = 2.5\,\mathrm{keV}$ due to the energy resolution of the detector need to be considered. The formula for this simplified multiplicity estimation thus is

$$\hat{\mathcal{M}}(E_{\mathrm{FPD}}) = \left\lceil \left| \frac{E_{\mathrm{FPD}} - E_{\mathrm{PAE}} - \delta w}{E_{\mathrm{kin}}} \right| \right\rceil . \tag{8.9}$$

As discussed in Chap. 6, the multiplicity estimation considering only $E_{\mathrm{FPD}}$ cannot resolve the overlap in the energy histograms (see Fig. 6.3). However, the systematic uncertainty between the completely uncorrected response functions and the pileup corrected response functions using the look-up table was determined to be smaller than 3 % (see Fig. 8.2). Thus, the uncertainty due to the pile-up correction considering only $E_{\mathrm{FPD}}$ is below 3 %, which is sufficient for this analysis.

The relative event losses as a function of the surplus energy are shown in Fig. 8.15. As expected from Fig. 8.14, only small losses on the order of $10^{-4}$ exist for the measurements at 41% and 86% $\rho_0 d$. The losses increase with decreasing column density and the largest event loss of up to 0.08 % is obtained for the measurement at empty source.

[3] This is the basic pile-up correction approach, which is also briefly discussed in Sec. 6. For this correction it is assumed that $n$ electrons arriving at the detector simultaneously cause a $n$ times larger value of $E_{\mathrm{FPD}}$.

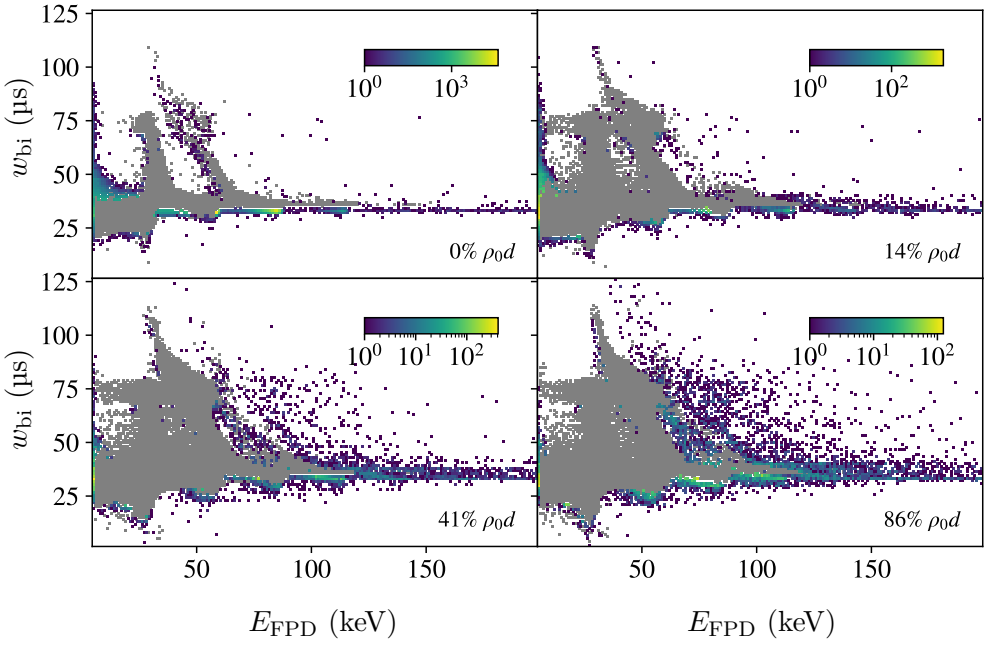


Figure 8.14: Distribution of the lost events due to undercoverage of the look-up table. The colour indicates the absolute number of events per bin. The area of the look-up table is indicated with the grey area. Especially in the case of the measurement at empty source, it can be seen, that the majority of events it lost due to the reduced width in the direction of $w_{\mathrm{bi}}$, which is caused from the missing noise in the simulations (see discussion in Sec. 6.2.3). For the measurements at non-empty source, additionally events are lost, which have large values of $E_{\mathrm{FPD}}$ and $w_{\mathrm{bi}}$.

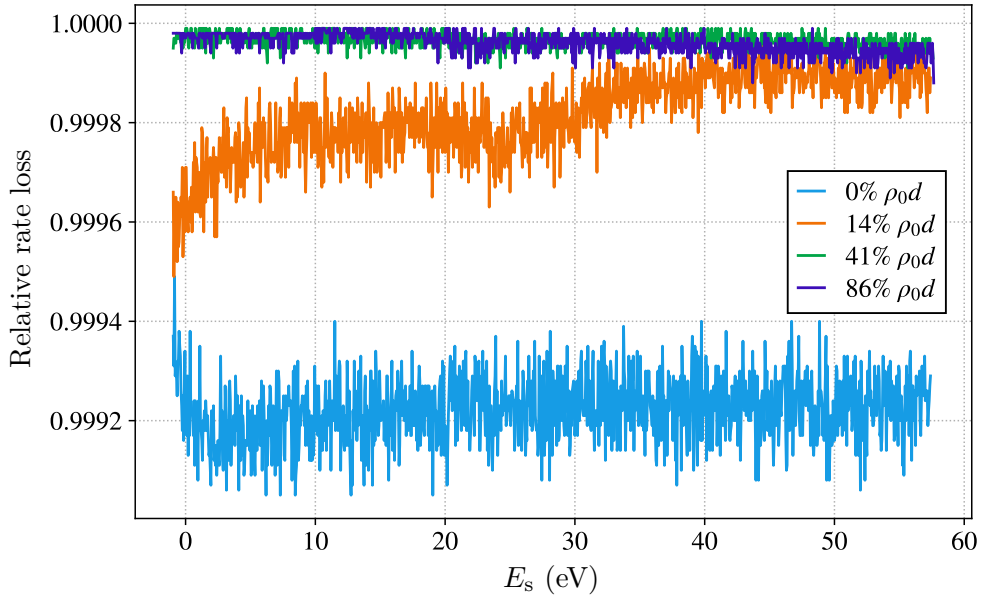


Figure 8.15: Relative rate losses due to undercoverage of the multiplicity look-up table. The largest rate loss is observed for the measurement at empty source and 14% $\rho_0 d$. Although the absolute losses reach up to approximately 0.08 %, the relative peak-to-peak deviations, which must be considered as uncertainty in the measurement of the energy-loss function, are below 0.05 %.

However, the absolute losses are irrelevant for the measurement of the energy-loss function, since a constant rate offset is absorbed by the free fit parameter $A_i$. Thus, only the relative deviation is relevant, as this distorts the shape of the response function. For the most affected measurements at 0% and 14% $\rho_0 d$, the relative peak-to-peak deviation is smaller than 0.05 %.

**Shape distortions due to energy independent look-up table**

In order to investigate the shape distortions due to the energy independent look-up table, response functions were simulated with the DRIPS framework mimicking the response function measurements as listed in Tab. 8.2. For each energy bin $E_s = [-5, 60]$ eV of the response functions, DRIPS simulations are carried out, which are configured with the corresponding electron rate at the given surplus energy, the pulse rate of the laser, and the arrival time histogram for the given surplus energy and column density setting. The arrival time histograms (comp. Fig. 6.7) were already available from the generation of the look-up table, described in Chap. 6. The output of the DRIPS simulations, which emulates the detector response, is then reconstructed using the energy independent look-up table. By determining the difference between the initial amount of simulated electrons and the amount of reconstructed electrons, it is possible to determine the reconstruction efficiency as a function of the surplus energy.

The reconstruction efficiency and the statistical uncertainty at each surplus energy value is drawn in Fig. 8.16. The figure shows that the correction with the energy independent look-up table causes an offset in all data sets of approximately 0.87 %. Again, this constant offset does not affect the analysis, and only the relative deviations are relevant.

The curves show two very characteristic properties. The first property is that the curves at non-empty source decrease for surplus energies $E_s \geq 10$ eV with increasing surplus energies.

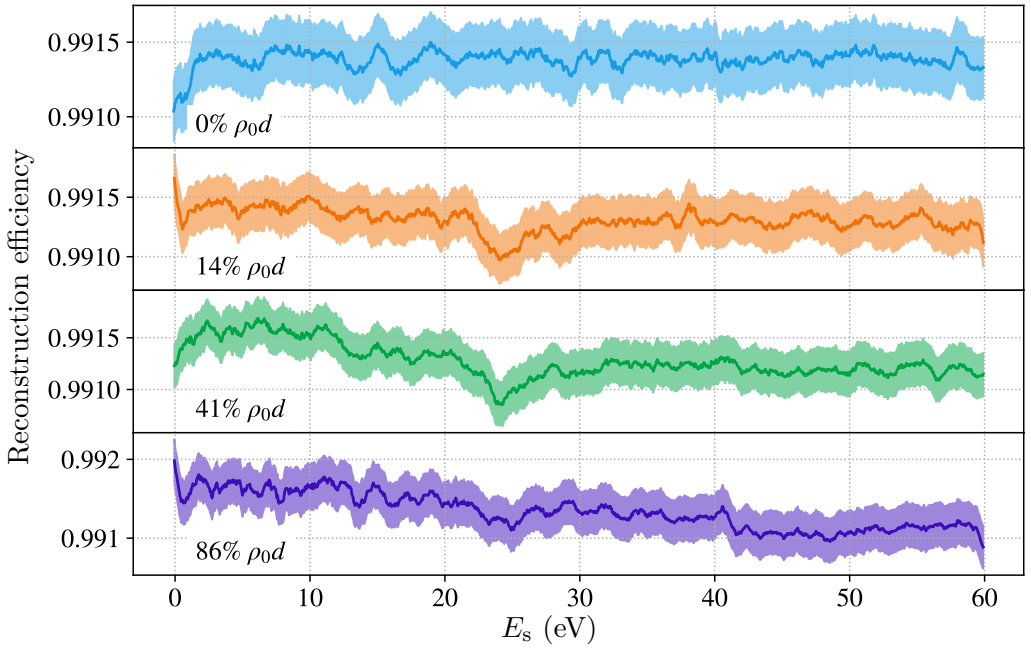


Figure 8.16: The curves show the reconstruction efficiency of the pile-up reconstruction using an energy independent multiplicity look-up table. The shaded area indicate the statistical uncertainty of the simulations. For the measurements at non empty source, a decrease of the efficiency with increasing surplus energy is visible, as more scattered electrons are transmitted. Furthermore, a bump at approximately 25 eV is visible, which is caused by two-fold scattered electrons.

The second property is the existence of a bump on the energy interval $E_s = [20, 30]$ eV.

The slope can be explained since the amount of scattered electrons increases with the surplus energy. These scattered electrons are stronger retarded than the unscattered electrons and thus arrive at the detector with a time delay. As illustrated in Fig. 6.2, the delayed arrival of the scattered electrons causes larger flat-top widths of the processed event signals, if the electrons arrive still within the shaping time of the detector. As it can be seen in Fig. 8.17, the scattering causes events with $w_{bi} \gtrsim 2\mu s$. As the amount of events with $w_{bi} \gtrsim 2\,\mu s$ changes as a function of the surplus energy (comp. Fig. 8.17), the ratio between the regions with remaining ambiguous multiplicities (comp. Fig. A.6) is not constant. Thus, a small misinterpretation of the event properties exists, which is depending on the surplus energy.

A similar explanation holds for the systematic bump on the energy interval $E_s = [20, 30]$ eV. This bump is located at the energy region, where two-fold scattering takes place. These two-fold scattered electrons cause events with $w_{bi} \lesssim 1.6\,\mu s$ in the energy range of $E_s = [20, 30]$ eV (comp. Fig. 8.17). Again this local change of the population inside the $E_{FPD}$-$w_{bi}$-plane is not covered by the energy independent lookup-table, which causes a wrong estimation of the multiplicity.

Since both effects increase with the amount of scattered electrons, the most significant deviation is obtained at the measurement at 86 % $\rho_0 d$ with a peak-to-peak deviation of 0.11 %.

### 8.4.6 Multiplicity cut

Besides the distortion of the spectral shape of the background component, the $\hat{\mathcal{M}} > 1$ cut can also distort the shape of the signal component, which has to be determined.

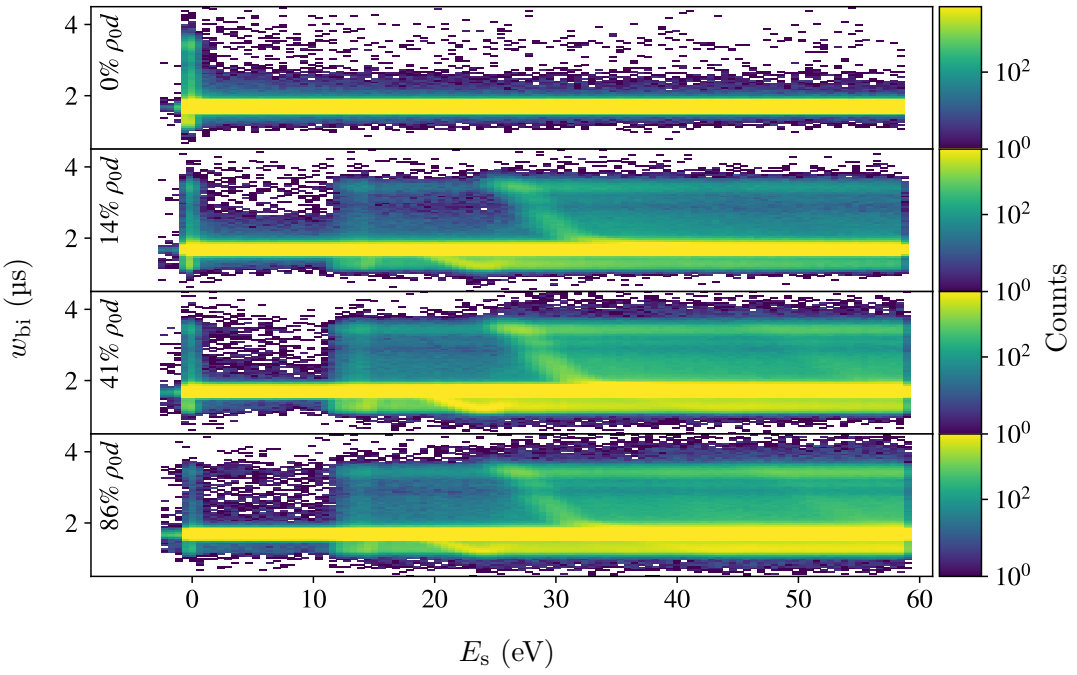


Figure 8.17: Distributions of the bipolar width $w_{\mathrm{bi}}$ as a function of the surplus energy $E_{\mathrm{s}}$ for the integral response function measurements at different column densities (see Fig. 8.2). If no scattering takes place, the events populate the regions of higher bipolar width only in the region right at the transmission edge and are otherwise located in a compact band at around $w_{\mathrm{bi}} = 1.6\,\mu\mathrm{s}$. In the case of a non-empty source, there is a significant contributions of events with $w_{\mathrm{bi}} > 1.6\,\mu\mathrm{s}$ above the excitation threshold energy of approximately 11 eV. Above the threshold energy of two-fold scattering (i.e. $E_{\mathrm{s}} \approx 22\,\mathrm{eV}$), a significant contribution of events with $w_{\mathrm{bi}} \lesssim 1.6\,\mu\mathrm{s}$ is observed.

Unfortunately, the distortion cannot be investigated using measurement data, since no background free measurements are available, which would allow a precise determination of the amount of signal electrons with $\hat{\mathcal{M}} > 1$.

Therefore, the loss of signal electrons can only be determined from simulations. The simulations described in the following were carried out by master's student Christophe Schwachtgen [Sch20]. A first approach is made by simulating the response functions similar as for the determination of the background shape, i.e. by first generating flight time histograms and then carrying out DRIPS simulations. However, the amount of events with $\hat{\mathcal{M}} > 1$ above the threshold energy for inelastic scattering is on the order of $10^{-4}$. Since a total of 1300 simulations are required for each column density, it is not possible to obtain sufficient high statistics, as the duration of the DRIPS simulations would exceed tens of thousands of cpu hours. The simulations can be speed up by skipping the DRIPS simulations and by determining the event multiplicity directly in the flight time simulations, as it was done in the simulations to determine the initial mean cluster size $\hat{\mathcal{S}}$ described in Sec. 8.2.2.2. The simulation is configured with the properties of the electron gun in the ToF mode, i.e. with an energy distribution of $\mu_{\mathrm{E}} = 0.09\,\mathrm{eV}$ and the initial amount of electrons from one pulse $\hat{\mathcal{S}} = 0.35$, as summarised in Tab. 8.3. Again, a list of arrival times at the detector is simulated for each of the electrons being generated from the same light pulse. In order to include the ToF cut, only the events with flight times in the range $\tau = [35, 50]$ µs are accepted. By determining the amount of electrons arriving within the shaping time $L = 1.6\,\mu\mathrm{s}$, the event multiplicity is obtained, which is however only a simplified model of the actual detector DAQ. This process is repeated until a total amount of $10^5$ electrons is reached.

By determining the fraction of the events with multiplicities $\hat{\mathcal{M}} > 1$, the curves in Fig. 8.18 are obtained.

As it is visible, the fraction of events with $\hat{\mathcal{M}} > 1$ is proportional to the shape of the differential response function. This is caused by the fact, that the probability for the coincidence of one scattered electron with another scattered electron within the shaping time $L$ is proportional to the probability of losing the same amount of energy as the first electron. Since it does not matter if the energy loss is caused by one-fold or $n$-fold scattering, the shape of the probability distribution is proportional to the shape of the differential response function, i.e. the sum of the $n$-fold scattering functions. For the peak of unscattered electrons, the distortions on the signal component of the response function are in the range of 1 % to 4 %, which reduces to below 0.1 % for the region above the threshold energy of inelastic excitation.

## 8.5 Monte Carlo propagation of systematic uncertainties

Given the list of systematic uncertainties in Sec. 8.4, their influence on the obtained fit result in Sec. 8.3 has to be investigated.

In the case of the energy-loss function measurements, this is done by performing Monte Carlo simulations. The analysis approach of performing Monte Carlo simulations in order to investigate the impact of the systematics on the measurement result is explained in Sec. 8.5.1.

In order to carry out the simulations, a dedicated Monte Carlo framework was developed, which allows one to easily generate so-called Monte Carlo twins of the measurement data including all known systematic effects. The generation of these Monte Carlo twins using the Monte Carlo framework as well as the integration of the systematics into the simulations is discussed in Sec. 8.5.2.

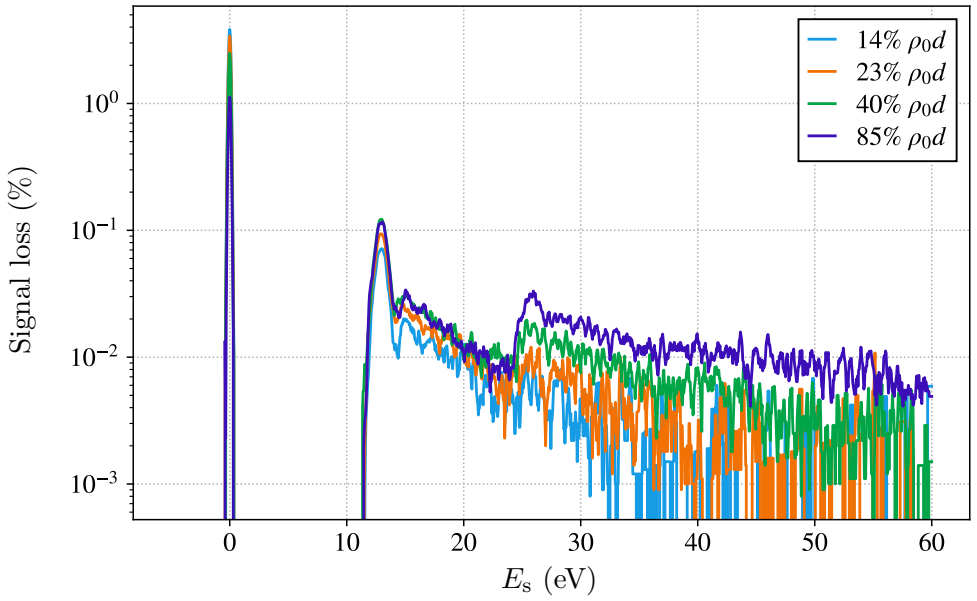


Figure 8.18: Simulated relative signal loss when applying the $\hat{\mathcal{M}} > 1$ cut to the differential measurement data. As it can be clearly seen, the probability of electrons coinciding with other scattered electrons (or just transmitted electrons in the case of the peak of unscattered electrons) clearly scales with the rate. Thus, about 4 % of the electrons at the peak of unscattered electrons arrive at the detector with event multiplicities $\hat{\mathcal{M}} > 1$, which are thus rejected from the $\hat{\mathcal{M}} > 1$ cut. This amount of $\hat{\mathcal{M}} > 1$ events decreases to below 0.1 % for the scattered electrons. The shown data was provided by Ref. [Sch20].

Table 8.6: Overview of the systematic uncertainties of the response function measurements for $T_2$.

| | Integral data | | | | Differential data | | | |
|---|---|---|---|---|---|---|---|---|
| | 0 % $\rho_0 d$ | 14 % $\rho_0 d$ | 41 % $\rho_0 d$ | 86 % $\rho_0 d$ | 15 % $\rho_0 d$ | 22 % $\rho_0 d$ | 39 % $\rho_0 d$ | 84 % $\rho_0 d$ |
| Rate drift / % $h^{-1}$ | 0.100(2) | −0.078(14) | 0.006(7) | −0.060(7) | 0.144(27) | −0.094(45) | −0.043(58) | 0.082(63) |
| Column density drift / % $h^{-1}$ | - | 0.005(5) | −0.1482(4) | 0.0011(1) | 0.017(1) | −0.019(1) | −0.190(1) | −0.0078(1) |
| Background shape properties | | | | | | | | |
| position and width / eV | $\mu_E^{bg} = 2.42(3)$ eV and $\sigma_E^{bg} = 2.04(4)$ eV for all runs | | | | | | | |
| Pile-up correction / % (peak-to-peak) | 0.1 | 0.07 | 0.09 | 0.09 | - | - | - | - |
| Multiplicity cut | | | | | | | | |
| max. background shape uncertainty / % | - | - | - | - | 42 | 38 | 32 | 20 |
| max. signal shape distortion / % | - | - | - | - | 3.8 | 3.4 | 2.5 | 1.1 |
| Transmission function model | | | | | | | | |
| position / meV | −0.2(22) | 0.3(23) | −0.6(23) | 0.4(25) | - | - | - | - |
| width / meV | 90(1) | 91(2) | 89(2) | 91(2) | - | - | - | - |
| Uncertainty on $U_{em}$ / mV | 7 mV for all runs | | | | | | | |

The results of the Monte Carlo simulations will be discussed in Sec. 8.5.3 including a systematics breakdown, which allows the impact of each systematics to be determined individually.

### 8.5.1 Analysis approach

The approach of the Monte Carlo simulations is to generate Monte Carlo twins of the measurement data taking into account all known statistical and systematic uncertainties of the measurement. The Monte Carlo twins can then be analysed with the same fitting program, as developed for the analysis of the measurement data. Since the input parameters of the Monte Carlo twins are known, it is possible to investigate differences between the input parameters and the output parameters of the analysis of the measurement data.

In the case of the energy-loss function measurements, the eight response functions are constructed by using the new KATRIN $T_2$ parametrisation as provided in Tab. 8.4, which are denoted the initial parameters $\vec{\mathcal{P}}_{\mathrm{ini}}$. For the purpose of the Monte Carlo simulations it is assumed, that this model is (close to) the ideal energy-loss function of the KATRIN experiment. The response functions are then modified according to the characterised systematics discussed in Sec. 8.4. The sets of Monte Carlo twins are then fit with the same fit model as used for the analysis, which gives the set of output parameters $\vec{\mathcal{P}}_{\mathrm{out}}$. The comparison of $\vec{\mathcal{P}}_{\mathrm{ini}}$ and $\vec{\mathcal{P}}_{\mathrm{out}}$ allows one to determine differences in the parameters, which are induced by the statistical and systematic uncertainties.

Since the systematics have uncertainties it is not sufficient to generate only one Monte Carlo twin data set, but a large amount of simulations are required, where the parameters of the systematic effects are randomised according to their uncertainty. By fitting each of the data sets, parameter distributions of $\vec{\mathcal{P}}_{\mathrm{out}}$ are obtained, which do not only reveal the shifts on the parameters but also uncertainties on the latter from the width of the distributions. This method of generating and analysing a large amount of data sets while varying the parameters is called ensemble test.

With the Monte Carlo simulations it is possible to investigate each systematic effect individually and to compile a systematics breakdown, i.e. the contribution of each of the individual systematics to the total systematic uncertainty $\sigma_i^{\mathrm{sys}}$. Furthermore it is possible to select, whether statistical fluctuations of the count rate are included or not. This allows one to determine the contribution of the statistical parameter uncertainties $\sigma_i^{\mathrm{stat}}$ as well as the contribution of the systematic uncertainties $\sigma_i^{\mathrm{sys}}$ to the overall uncertainty of the measurements.

### 8.5.2 Generation of MC twin data sets

The generation of Monte Carlo twins requires to simulate response function with the same properties than the measurements, i.e. mimicking both the systematic and statistical uncertainties. Especially for the implementation of the different systematic uncertainties, the response function need to be modified according to sensor data and other inputs.

In order to construct the response function and to modify them easily, a response function generator module was developed, which is described in Sec. A.4.

The systematic effects listed in Tab. 8.6 need to be included in the Monte Carlo simulation of the response function, if the effect is not yet considered in the processing of the measurement data, such as the uncertainty from the diode correction as well as the uncertainty on $E_{\mathrm{s}}$.

In the following, the expressions scan level, response level, and campaign level will be used to identify the sampling level of the individual systematic uncertainties. The expressions are defined as follows:

- *Scan level*
  The values are randomly drawn for each of the individuals scans contributing to the final response function.
- *Response level*
  The values are only randomised once for the response function measurements at the same column density setting, i.e. all scans contributing to the final response function use the same value.
- *Campaign level*
  The values are only randomised once for the simulations covering the entire data set of the eight response functions.

The considered systematic uncertainties in the Monte Carlo simulation are:

- **Column density drift**
  The column density during every single scan is approximated with a first order polynomial, with the slope being determined from a fit to the column density values shown in Fig. 8.12. The slope is randomised according to the parameter uncertainty on the scan level. In order to implement the drift of the column density, the average number of scatterings $\mu$ is scaled according to the slope and thus becomes a function of the surplus energy $E_\mathrm{s}$. The response function is thus recalculated for each value of $E_\mathrm{s}$, since the scattering probabilities $P_n\left(\mu(E_\mathrm{s})\right)$ are changing. In order to mimic the alternating scan direction, the slope is inverted in the case of down scans.
- **Rate drift**
  In order to include the rate drift, the response functions of the individual scans are scaled according to the rate drifts determined in Fig. 8.13. The slope value is randomly drawn from the uncertainties on the response level. The slopes are varied according to the parameter uncertainty. In order to mimic the alternating scan direction, the slope is inverted in the case of down scans.
- **Transmission function model**
  Since the transmission function is approximated by an error function while constructing the fit function (see Sec. 8.3), the uncertainties on the shape parameters in Tab. 8.6 need to be taken into account. The shape parameters of the individual response functions are randomised on the response level taking into account the correlation between the width and the position.
- **Binning**
  The effect due to the binning of the data into discrete voltage bins is approximated by calculating the response function with a 2.5 meV binning. These fine-binned response functions are then rebinned to the regular 50 meV binning by calculating the average within each 50 meV bin.
- **Pile-up correction**
  The distortions of the response function due to the pile-up correction method using the energy independent look-up table of the multiplicity estimate $\hat{\mathcal{M}}(E_\mathrm{s}, w_\mathrm{bi})$ are implemented by multiplying the single response function with the two reconstruction efficiency curves provided in Fig. 8.15 and 8.16. In order to take the uncertainties of the latter into account the data points of the scaling functions are randomised on the response level before applying them to each of the individual scans.
- **Background shape**
  For both the integral and differential data sets, an integral background component is generated by using the same column density values as the actual response functions as well as the background shape properties defined in Eq. (8.2). The scale of the

background component is determined from the merged measurement data, i.e. the amounts of counts per bin in the range of $E_\mathrm{s} = [-2, -1]\,\mathrm{eV}$ for the integral response functions and $E_\mathrm{s} = [5, 8]\,\mathrm{eV}$ for the differential measurement. In the case of the differential measurements, the background component is scaled with the corresponding scaling function for $\hat{\mathcal{S}} = 1.3$ to distort the background shape according to the multiplicity $\hat{\mathcal{M}} > 1$ cut.

In order to investigate the uncertainties arising from the uncertainties on the energy distribution of the shape parameters of the background component can be randomised according to the values defined in Eq. (8.2) taking into account the correlations. This is only done on the campaign level, since it is not expected that the energy distribution of the background electrons changes within the measurement. Statistical fluctuations of the count rate of the background component are sampled independently of the signal component, since the two components are of different origin.

- **Multiplicity cut**
  In order to integrate the uncertainties on the shape of the background components (see Fig. 8.7) after applying the $\hat{\mathcal{M}} > 1$ cut, the shapes need to be randomised according to the uncertainties on $\hat{\mathcal{S}}$. As these shapes can be only obtained from time-consuming simulations a look-up table of simulated scaling functions is used. For each column density value, a look-up table for the values of $\hat{\mathcal{S}}$ =0.16, 0.54, 0.8, 0.92, 1, 1.2, 1.3, 1.68, 1.8, 2.06, 2.44, 2.9, 4, 5.1, 6.2, 7.3, 8.4, and 9.5 is generated[4]. The value of $\hat{\mathcal{S}}$ is sampled from the uncertainty provided in Eq. (8.4) and the scaling function is then interpolated from the functions provided in the look-up table. These scaling functions are then applied to the simulated integral background components of the differential data set. This sampling is performed on the response level, since it is expected that $\hat{\mathcal{S}}$ does not change for one column density setting. But since differences in the individual best fit values in Eq. (8.3) are obtained for different column densities, the cluster size is randomised for each column density setting.

  Furthermore, the shape distortions of the signal component of the differential response functions (see Fig. 8.18) are integrated by multiplying the differential response functions with the scaling function $1 - s(E_\mathrm{s}, \mu_i)$, with $s(E_\mathrm{s}, \mu_i)$ being the corresponding signal loss functions provided in Fig. 8.18. Since the functions $s(E_\mathrm{s}, \mu_i)$ are affected by simulation noise on the order of $10^{-5}$, a sampling on the scan level is included to take the uncertainties of the data points into account.

The described systematics can be implemented individually or all at the same time. Furthermore, it is possible to include statistical uncertainties by sampling each point of the final response function from a Poisson distribution. However, the background component and the signal component are generated from individual processes and are thus sampled individually. A Monte Carlo twin data set is shown in Fig. 8.19 together with the underlying measurement data.

The Monte Carlo data sets are fit with the fitting framework to determine the uncertainties and possible shifts on the energy-loss function parameters induced by the included systematics, as described in Sec. 8.5.1. Since the data points of the simulated Monte Carlo twins are purely Poisson distributed, a Poisson likelihood is constructed in contrast to the Neyman's $\chi^2$ function, which is used in the analysis of the measurement data (see Sec. 8.3). The reason for using a Poisson likelihood is that the Neyman's $\chi^2$ is only valid for data with Gaussian distributed uncertainties. As the latter only applies to Poisson distributed data in the limit of large bin entries, parameter shifts can appear if the data has small

[4]The values of $\hat{\mathcal{S}}$ follow no specific pattern and the distribution is not equidistant as simulations were already available for some values of $\hat{\mathcal{S}}$.

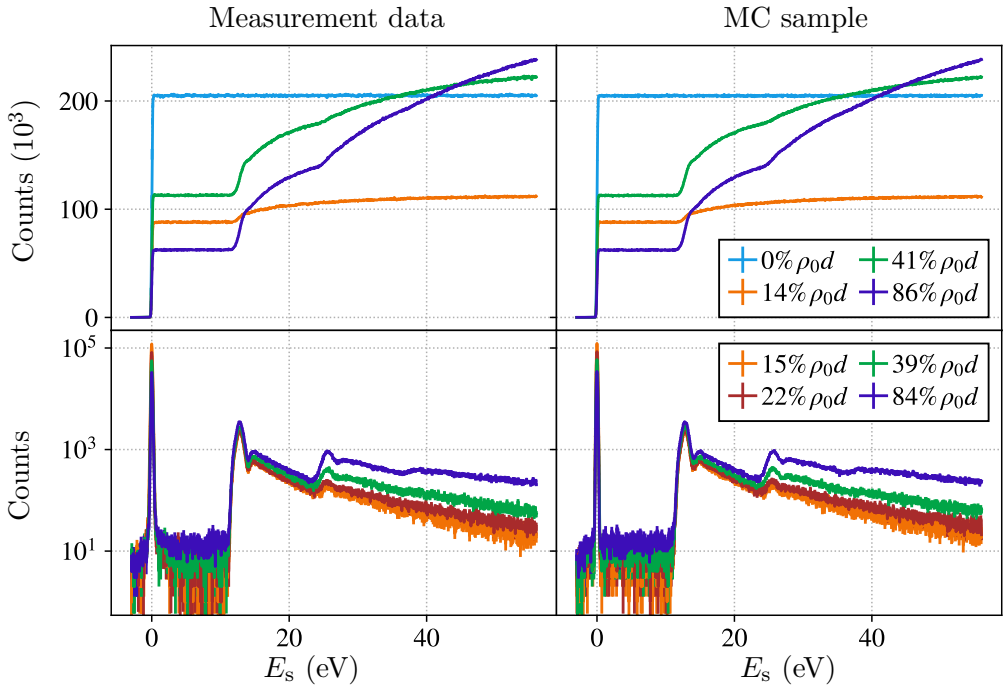


Figure 8.19: Example of one set of Monte Carlo twins of the response function measurements generated with the Monte Carlo framework. In this case only statistical uncertainties are included. The framework allows one to mimic the measurement based on the properties of the measurement data and the systematics investigated in Sec. 8.4.

bin entries (see e.g. Ref. [Lis17]). As it is visible in Fig. 8.19, the differential response functions approach zero on the left side of the electronic excitation peak as well as in the upper region of the ionisation tail in the case of small column densities. In order to avoid systematic shifts by using the Neyman's $\chi^2$, the likelihood function is constructed using the Poisson likelihood $\chi^2_\lambda$ [BC84]

$$\chi^2_\lambda\left(\sum_i \left\{A_i, \mu_i, A_i^{\mathrm{bg}}\right\}, \vec{\mathcal{P}}\right) = 2\sum_i \sum_{E_\mathrm{s}} \left( R_i\left(E_\mathrm{s}, A_i, \mu_i, A_i^{\mathrm{bg}}, \vec{\mathcal{P}}\right) - n_i(E_\mathrm{s}) + n_i(E_\mathrm{s}) \cdot \ln\left[\frac{n_i(E_\mathrm{s})}{R_i\left(E_\mathrm{s}, A_i, \mu_i, A_i^{\mathrm{bg}}, \vec{\mathcal{P}}\right)}\right]\right) \tag{8.10}$$

with $n_i(E_\mathrm{s})$ being the number of counts per bin at the given surplus energy. The index $i$ is iterated over both the differential and integral response functions. Similar to the fit to the measurement data, a pull term (see Eq. (7.26)) is integrated into the likelihood function to ensure a proper normalisation of the energy-loss function. The Poisson likelihood $\chi^2_\lambda$ follows a $\chi^2$ distribution [BC84] and thus allows for the same goodness of fit test as applied in Sec. 8.3.

### 8.5.3 Results of the MC propagation of systematic uncertainties

In order to investigate the influence of the systematics on the measurement of the energy-loss function, five different types of simulations are performed, which are explained in the following:

1. **Full Asimov data**
   The entire set of response functions are simulated with no statistical fluctuations of

the count rate and no systematics included. The data is then fit to demonstrate that the simulations and the fit functions are identical and no artificial shifts exist, i.e. $\vec{\mathcal{P}}_{\mathrm{out}} = \vec{\mathcal{P}}_{\mathrm{ini}}$. This also verifies that the minimiser is working properly. Since the fit function is constructed by using the measurement data of the peak of unscattered electrons, the fit model and the simulation data would never be identical, as the background component adds to the shape of the peak. In order to perform this cross check, the fit function must therefore be modified so that the same analytical transmission functions as for the generation of the data are used. If both the fit function and the simulated response functions use the same transmission function, it can be verified that the minimiser converges to the initial parameters $\vec{\mathcal{P}}_{\mathrm{ini}}$.

2. **Systematics breakdown**
   Each of the systematic uncertainties discussed in Sec. 8.5.2 is investigated individually to determine possible parameter shifts as well as the contribution to the systematic parameter uncertainty $\sigma_i^{\mathrm{sys}}$. For each of the systematic uncertainties a total of 10000 Monte Carlo data sets are generated with the systematic effects sampled accoding to their uncertainties. The other systematic uncertainties are excluded.

3. **All systematics (all sys.)**
   All systematics are included at the same time and all parameters are randomised according to their uncertainties. This allows one to determine the overall systematic uncertainty of the measurement. This simulation is required, since the individual systematics can influence each other especially in the case of parameter shifts. Determining the parameter shifts by adding up the individual deviations from the systematics breakdown can give different results.

4. **Only statistical uncertainties (stat. only)**
   No systematics are implemented in the simulations and only the Poisson uncertainty on the data (and the background component) is simulated. The resulting uncertainty on the parameters are the statistical uncertainty $\sigma_i^{\mathrm{stat}}$.

5. **Integration of statistical and systematic uncertainties (stat. & sys.)**
   In a last simulation both statistical uncertainties as well as all systematic uncertainties are included in the simulations. This allows one to determine the overall uncertainty of the parameters $\sigma_i^{\mathrm{tot}}$ as well as possible parameter shifts.

For each of the simulations, a total of 10000 Monte Carlo data sets are generated and each of the samples is fit.

An example of the obtained parameter distributions for the simulations including both statistical and systematic uncertainties (stat. & sys.) is provided in Fig. 8.20 and the distributions for the simulations including only systematic uncertainties as well as only statistical uncertainties are available in Figs. A.13 and A.14. In all three cases, the parameter distributions are nearly normal distributed and do not show asymmetries or multiple maxima, which would indicate local minima in the likelihood function. The $1\sigma$ range of the parameter distributions in Fig. 8.20 agree very well with the parameter uncertainties obtained from the fit to the measurement data. Furthermore, the correlations and covariances in Fig. A.15 for the parameter distributions of the stat. & sys. simulations are in good agreement with the covariances and correlations obtained from the fit to the measurement data (comp. Fig. 8.10). Consequently, the shape of the $1\sigma$ uncertainty band of the simulation, which is displayed in Fig. 8.21, agrees very well with the uncertainty band of the measurement result. Although the uncertainty band below the energy of 14 eV agrees better with the uncertainty band of the scaled (i.e. $\chi^2/N_{\mathrm{dof}} = 1$) parameter uncertainties, the uncertainty band of the latter is approximately 5 % larger than the former for energies above 14 eV. In this region, the uncertainty band of the unscaled fit result agrees better

with the simulations. Based on the comparison of the uncertainty band, it is thus not possible to favour one result or the other.

For a more convenient comparison of the parameter distributions, the median values and the standard deviations of all parameter distributions for the individual simulations are included in Fig. 8.22. In this representation it can be directly seen that the systematic uncertainty of each parameter value is at least a factor of three smaller than the statistical uncertainty. The largest contribution to this systematic uncertainty is due to the shape uncertainties on the model of the transmission function, which is used to construct the integral response functions. Besides the small increase of the parameter uncertainty, the systematics breakdown shows no significant parameter shifts due to the investigated systematics. As it is shown in Fig. 8.21, the shape of the energy-loss function differs only on the order of $10^{-4}\,\mathrm{eV}^{-1}$ compared to the shape of the input energy-loss function (using $\vec{\mathcal{P}}_{\mathrm{ini}}$). However, the systematics cause an increase of the $\chi^2$ value, which can be seen from the distribution of $\chi^2/N_{\mathrm{dof}}$ in the top right panel of Fig. 8.20. The distribution has a median of 1.09 and covers the value of $\chi^2/N_{\mathrm{dof}} = 1.133(17)$, which was obtained from the measurement. The deviation of $\chi^2/N_{\mathrm{dof}}$ from one can thus be explained from the systematic uncertainties of the measurements, which are not considered in the fit.

From the Monte Carlo simulations can be concluded, that the parameter uncertainties are dominated by the statistical uncertainty and the parameter uncertainties obtained from the stat. & sys. simulations agree very well with the parameter uncertainties obtained from the fit to the measurement data, as it can be seen from the $1\sigma$ uncertainty band displayed in Fig. 8.21. The systematics cause no significant parameter shifts, but lead to an increased $\chi^2$ value, which explains the slightly increased $\chi^2$ value with $\chi^2/N_{\mathrm{dof}} = 1.133(17)$ of the fit result. Rescaling the $\chi^2$ function for a conservative estimation of the parameter uncertainties is possible but not essential. Consequently, the Monte Carlo simulations verify the measurement results of Sec. 8.3.

## 8.6 Resulting uncertainty on KATRIN neutrino-mass measurements

With the provided parametrisation of the energy-loss function for molecular tritium in Tab. 8.4, an energy-loss model is obtained, which outperforms the available models of Aseev et al. and Abdurashitov et al..

However, it has to be verified that the uncertainties of the model parameters comply with the strict KATRIN requirements and that the resulting systematic uncertainty on $m_\nu^2$ due to the uncertainties of the energy-loss model does not exceed the limit of $\sigma_{\mathrm{sys}}^{\mathrm{eloss}}(m_\nu^2) > 7.5 \times 10^{-3}\,\mathrm{eV}^2$.

Similar to the investigations for the energy-loss function of deuterium in Sec. 7.4, the uncertainties are propagated using the covariance matrix approach.

Three different types of simulations are carried out to propagate the uncertainties of the measurement data as well as of the Monte Carlo result and to provide a comparison of the new KATRIN model to the existing models of Aseev et al. and Abdurashitov et al.. All the simulations in the following are based on the parameter settings listed in Tab. 7.6, which are based on the conditions of the experimental setup during KNM2, extrapolated to three years worth of data taking at nominal column density. Therefore, it is important to point out that the values discussed in the following have to be re-evaluated if either the measurement time or the measurement conditions change.

### Systematic uncertainty of the measurement data

The covariance matrix $C_\beta$ for the β-spectrum as measured with KATRIN is generated by simulating 10000 β-spectra based on the new KATRIN $T_2$ energy-loss function (see

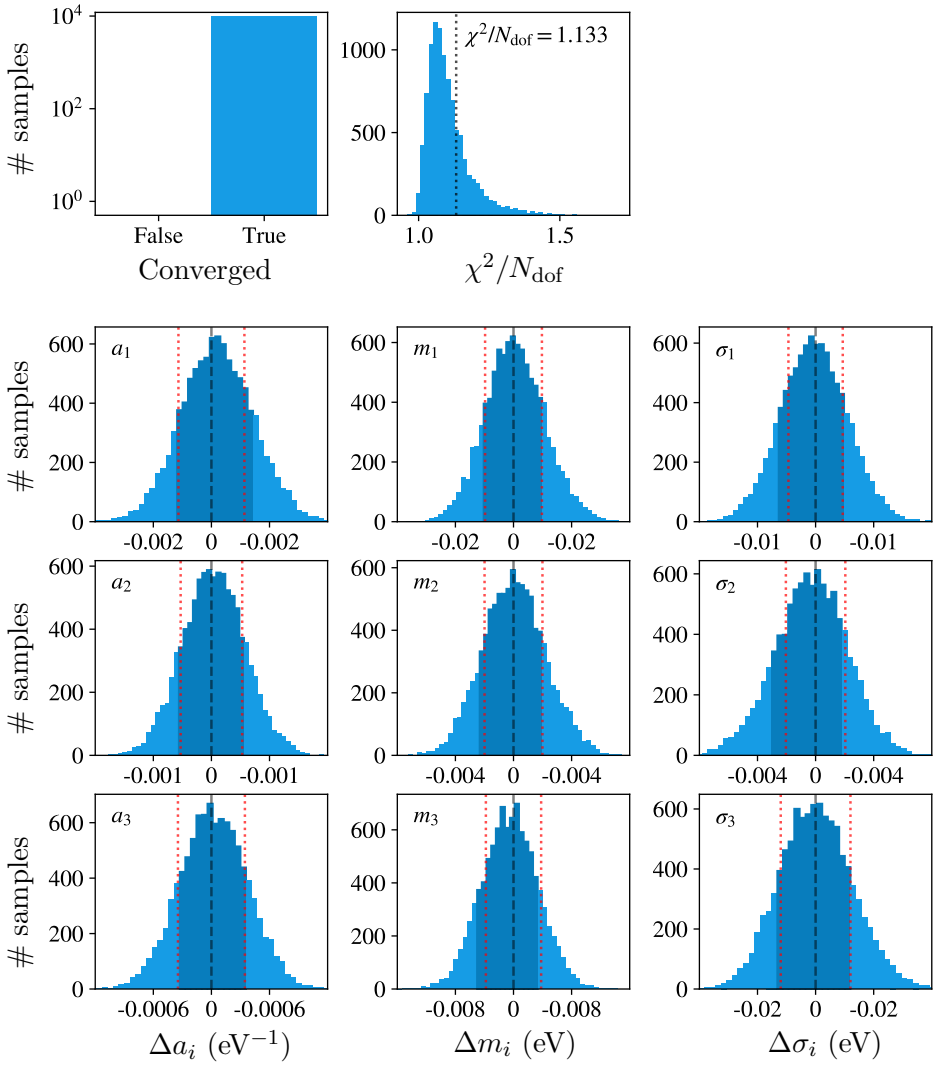


Figure 8.20: The bottom part of the figure shows the parameter distributions of the ensemble test including both systematic and statistical uncertainties. The histograms show the deviations of the parameters of the best fit results of the individual fits to the Monte Carlo data sets and the initial value, i.e. $\mathcal{P}_{i,\mathrm{MC}} - \mathcal{P}_{i,\mathrm{data}}$. The shaded area indicates the $1\sigma$ interval of the distributions. For a comparison, the parameter uncertainty $\sigma_{\mathrm{fit}}$ of the best fit result using the measurement data (comp. Tab. 8.4) is indicated by the red dotted lines. The top part of the figure shows the amount of converged fit results as well as the distribution of $\chi^2/N_{\mathrm{dof}}$. It is visible that the distribution of $\chi^2/N_{\mathrm{dof}}$ is deviating from one due to the systematic uncertainties with the median of the distribution being located at 1.09. The value of $\chi^2/N_{\mathrm{dof}} = 1.133$, as obtained from the fit to the measurement data, is indicated with the dotted line.

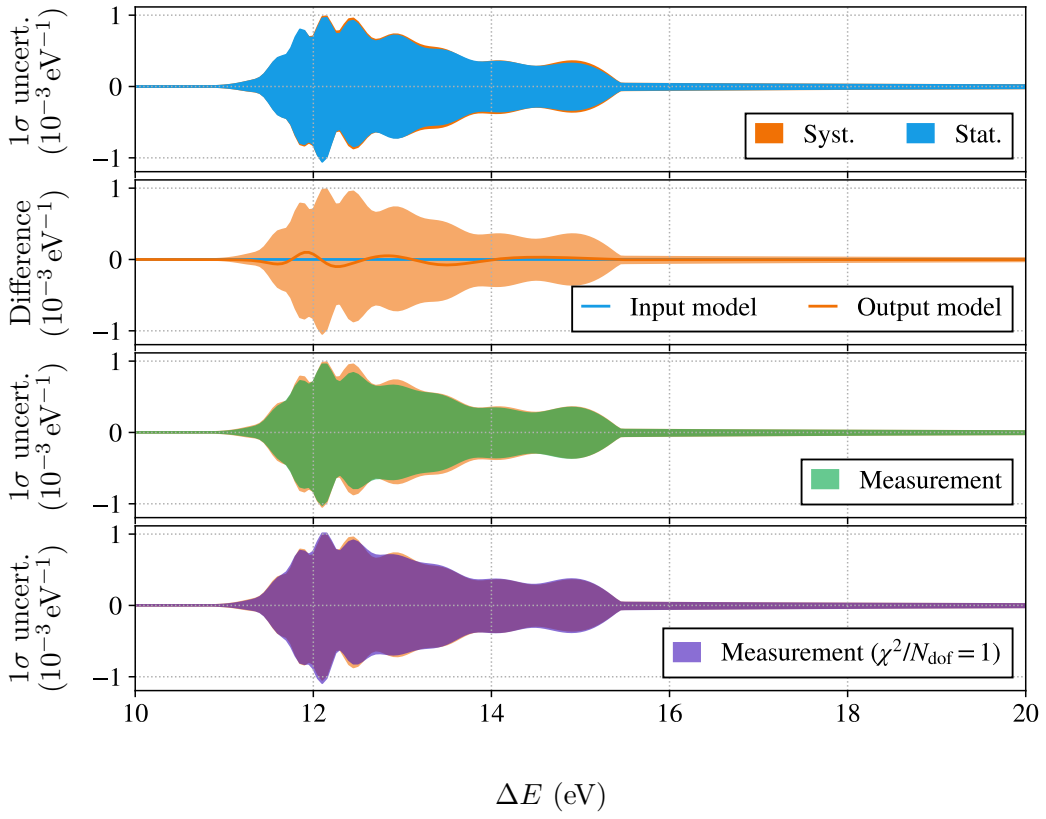


Figure 8.21: **Row one:** Shape of the uncertainty band according to the parameter distributions obtained from the Monte Carlo simulations. The contribution of the statistical uncertainty and systematic uncertainty are indicated. As expected from the systematics breakdown in Fig. 8.22, the uncertainty is dominated by the statistical uncertainty.
**Row two:** Difference between the shape of the energy-loss function $f(\vec{\mathcal{P}}_{\text{ini}})$ used to construct the Monte Carlo data sets and the average shape of the energy-loss function $f(\vec{\mathcal{P}}_{\text{out}})$ obtained from the fits to the stat. & sys. simulation data. Due to the included systematics, the energy-loss function parameter are slightly shifted, which causes a small deviation between the input model and the output model with a maximal difference of $0.1 \times 10^{-3}\,\text{eV}^{-1}$. For comparison, the uncertainty band (stat. & sys.), as obtained from the simulations, is included.
**Row three and four:** Uncertainty bands as obtained from the measurement with and without the rescaling of the $\chi^2$ function. The uncertainty band as obtained from the Monte Carlo simulations is included in orange. In the region below 14 eV, the uncertainty band agrees better with the uncertainty band for the rescaled parameter uncertainties. Above 14 eV the uncertainty band of the rescaled parameter uncertainties is 5 % larger than the simulated uncertainty band. In this region, the uncertainty band of the unscaled parameter uncertainties agrees better.

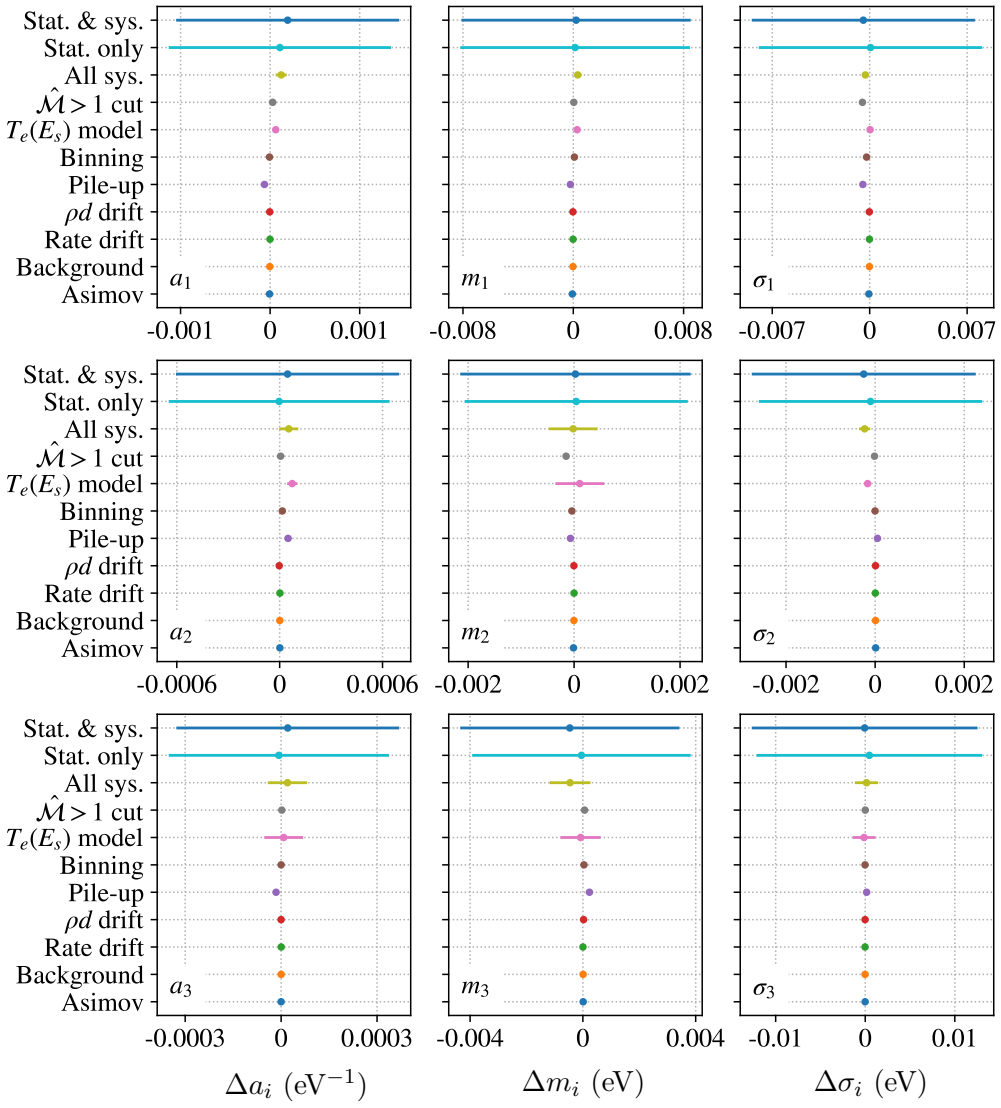


Figure 8.22: Systematics breakdown of the energy-loss function measurements. The data points show the deviation between the median of the parameter distribution and the input value of the Monte Carlo simulations. The bars indicate the standard deviation of the distributions. The largest contribution to the parameter uncertainties is obtained from the uncertainties on the transmission function shape of the integral response functions. No significant parameter shifts from the individual systematics are observed.

Tab. 8.4). For each of the simulations, the parameters are randomly drawn from the parameter uncertainties taking into account the parameter correlations provided in Fig. 8.10. The constructed covariance matrix $C_\beta$ of the β-spectrum is then used to perform a fit to simulation data, with both the fit function and the β-spectrum being generated using the KATRIN $T_2$ model.

From the broadening of the likelihood function, a systematic uncertainty of

$$\sigma_{\text{data}}(m_\nu^2) = 4.0 \times 10^{-3}\,\text{eV}^2 \tag{8.11}$$

and

$$\sigma_{\text{data},\chi^2/N_{\text{dof}}=1}(m_\nu^2) = 4.3 \times 10^{-3}\,\text{eV}^2 \tag{8.12}$$

for the rescaled parameter uncertainties is obtained, which outperforms the requirements by a factor of 1.7. Although the overall uncertainty of the energy-loss function improved compared to the deuterium result (comp. Fig. 8.11), the uncertainty of $m_\nu^2$ is about a factor 1.4 larger than the values obtained for the deuterium results (comp. Eq. (7.37)). This can be explained by the on average 1.2 times larger uncertainty band of the tritium results in the region of the ionisation tail, which is a consequence of the reduced statistics of the integral measurements (as already discussed in Sec. 8.3). As a consequence of the smaller statistical uncertainty of the measured β-spectrum for larger surplus energies, the uncertainty of the energy-loss function in the range of the ionisation tail dominates the neutrino-mass uncertainty. Hence, the uncertainty on $m_\nu^2$ is worse than for the deuterium result.

Since the same energy-loss model is used for the construction of both the β-spectrum and the fit function, it is only possible to investigate the uncertainty $\sigma_{\text{data}}(m_\nu^2)$. Possible systematic shifts of the observable $\Delta m_\nu^2$ due to systematic parameters shifts of the measured energy-loss function compared to the real energy-loss function of the experiment cannot be determined since the latter is not accessible. However, it is possible to determine these shifts by using the results of the Monte Carlo simulations.

**Systematic uncertainty obtained from the Monte Carlo simulations**

The parameters of the energy-loss function obtained from the propagation of systematics using the Monte Carlo framework allow one to investigate not only the resulting uncertainty $\sigma_{\text{MC}}(m_\nu^2)$ from the simulated parameter uncertainties but also the systematic shift $\Delta m_\nu^2$. The latter is accessible, since both the initial energy-loss function parameters $\vec{\mathcal{P}}_{\text{ini}}$ as well as the output energy-loss function parameters $\vec{\mathcal{P}}_{\text{out}}$ are available.

Similar as above, the covariance matrix $C_\beta$ is constructed by simulating 10000 β-spectra including the output model obtained from the Monte Carlo simulations and the corresponding covariances $C_{\vec{\mathcal{P}}}$ provided in Fig. A.15. The spectrum is simulated using the initial parameters $\vec{\mathcal{P}}_{\text{ini}}$ and the fit model is constructed by using the output energy-loss parameters $\vec{\mathcal{P}}_{\text{out}}$. In addition to the systematic uncertainty of

$$\sigma_{\text{MC}}(m_\nu^2) = 3.9 \times 10^{-3}\,\text{eV}^2 \tag{8.13}$$

a systematic shift of

$$\Delta m_\nu^2 = -0.5 \times 10^{-3}\,\text{eV}^2 \tag{8.14}$$

is determined. The value of $\sigma_{\text{MC}}(m_\nu^2)$ agrees well with the value of $\sigma_{\text{data}}(m_\nu^2)$. Due to the smaller statistical uncertainty of the β-spectrum measurement at higher surplus energies (see Fig. 3.3), the uncertainty of the ionisation tail of th energy-loss function has a larger influence on the resulting uncertainty on $m_\nu^2$ than the uncertainty in the region of the electronic excitation states. Consequently, the measurement result with the unscaled

parameter uncertainties agrees better with the simulation result, since the uncertainty interval in the tail region agrees better (comp. Fig. 8.21). Even with the systematic shift of $\Delta m_\nu^2 = -0.5 \times 10^{-3}\,\mathrm{eV}^2$, the uncertainty is below the limit of $\sigma_{\mathrm{sys}}^{\mathrm{eloss}}(m_\nu^2) > 7.5 \times 10^{-3}\,\mathrm{eV}^2$.

**Comparison to the results of Aseev et al. and Abdurashitov et al.**

The new KATRIN $T_2$ energy-loss function model allows one to perform a comparison of the already existing energy-loss function models of Aseev et al. and Abdurashitov et al. in order to demonstrate the systematic uncertainties, which would arise if the models were used in the neutrino-mass analysis.

To do so, the covariance matrix $C_\beta$ is constructed for the Aseev et al. $T_2$ model and the Abdurashitov et al. $D_2$ model according to the parameter uncertainties provided in Tab. 4.1. The β-spectrum is then simulated using the new KATRIN $T_2$ model and the fit function is constructed by using the model of Aseev et al. and Abdurashitov et al., respectively.

The systematic uncertainties on $m_\nu^2$ due to the uncertainty of the model parameters are

$$\sigma_{\mathrm{Aseev}}(m_\nu^2) = 48 \times 10^{-3}\,\mathrm{eV}^2 \quad \text{and} \quad \sigma_{\mathrm{Abd.}}(m_\nu^2) = 58 \times 10^{-3}\,\mathrm{eV}^2\,, \tag{8.15}$$

which exceeds the KATRIN requirements by more than a factor of seven. Furthermore, the comparison to the KATRIN $T_2$ results reveals that the two models would cause a severe systematic shift of

$$\Delta m^2_{\nu,\mathrm{Aseev}} = 372 \times 10^{-3}\,\mathrm{eV}^2 \quad \text{and} \quad \Delta m^2_{\nu,\mathrm{Abd.}} = 19 \times 10^{-3}\,\mathrm{eV}^2 \tag{8.16}$$

if they were used in the neutrino-mass analysis instead of the new KATRIN model. A graphical comparison of the shifts and uncertainties is provided in Fig. 8.23. The large shift of the Aseev et al. $T_2$ model is caused due to the significant deviation of the width and position of the Gaussian kernel approximating the electronic excitation states (see Fig. 8.11).

## 8.7 Summary

Measurements of integral response functions were carried out in order to investigate the energy-loss function of the electrons scattering off molecular tritium inside the WGTS. The energy-loss function is obtained by performing a combined $\chi^2$ fit to the measurement data including the set of differential response functions provided by Ref. [Rod].

Since a background signal is visible in the measurement data, the background component was characterised by dedicated measurements described in Sec. 8.2. The measurements show that the background component follows the shape of an integral response function similar as the signal electrons. Thus, the background electrons must be generated at the photocathode, very likely due to ion impact. Besides the general shape of the background component, the initial energy distribution parameters $\mu_{\mathrm{E}}^{\mathrm{bg}} = 2.42(3)\,\mathrm{eV}$ and $\sigma_{\mathrm{E}}^{\mathrm{bg}} = 2.04(4)\,\mathrm{eV}$ as well as the mean initial cluster size $\hat{\mathrm{S}} = 1.3(4)$ of the background events were determined from the measurement data.

These characteristic properties of the background component were used to construct the background models for the fit function. Especially in the case of the differential response function measurements, the shape of the background had to be determined from dedicated simulations, as the background component is distorted from the multiplicity $\hat{\mathcal{M}} > 1$ cut (see Fig. 8.7).

The fit to the measurement data was carried out and the best-fit result was obtained at $\chi^2/N_{\mathrm{dof}} = 1.133(17)$, with the best fit parameters provided in Tab. 8.4.

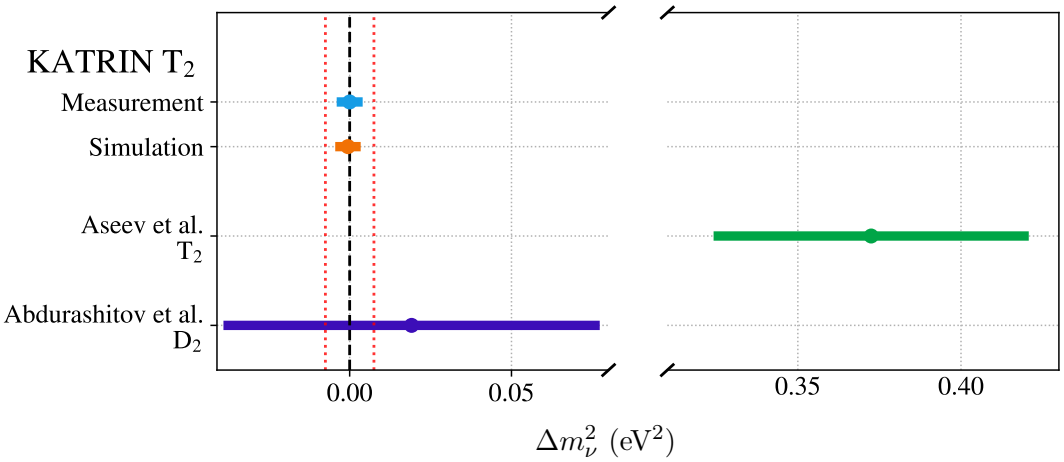


Figure 8.23: Comparison of the uncertainty on $m_\nu^2$ induced by the parameter uncertainties of the energy-loss function. The systematic uncertainty on $m_\nu^2$ resulting from the parameter uncertainties of the KATRIN $T_2$ model meets the KATRIN requirements of $\sigma_{\text{sys}}^{\text{eloss}}(m_\nu^2) < 7.5 \times 10^{-3}\,\text{eV}^2$ (red dotted lines). The propagated results of the Monte Carlo simulations shows only a minute shift of $\Delta m_\nu^2 = -0.5 \times 10^{-3}\,\text{eV}^2$. Thus, the KATRIN $T_2$ result meets the requirements. Compared to the Aseev et al. $T_2$ and the Abdurashitov et al. $D_2$ model, the uncertainties improved by over one order of magnitude.

In order to investigate the quality of the fit result, the systematic uncertainties of the measurements were characterised and used as input for Monte Carlo simulations. Based on the generation of twin Monte Carlo data sets, the uncertainties were propagated and a systematics breakdown was compiled (see Fig. 8.22). With the Monte Carlo simulations the validity of the parameter uncertainties from the fit could be verified and it was demonstrated that the parameter uncertainties provided in Tab. 8.4 are dominated by the statistical uncertainty of the measurements. Furthermore, the Monte Carlo simulations verified that the systematics do not cause significant parameter shifts.

The measurement results as well as the results from the Monte Carlo simulations were used to investigate the resulting uncertainty on the KATRIN observable $m_\nu^2$. By propagating the uncertainties on the parametrisation of the energy-loss function, a systematic uncertainty of $\sigma(m_\nu^2) = 4.0 \times 10^{-3}\,\text{eV}^2$ was determined. The result was verified with the propagation of the Monte Carlo simulation results. The small observed parameter shifts of the energy loss parametrisation cause a shift of only $\Delta m_\nu^2 = -0.5 \times 10^{-3}\,\text{eV}^2$. Considering both the statistical uncertainty and the systematic shift, the measurement result meets the KATRIN requirements of $\sigma_{\text{sys}}^{\text{eloss}}(m_\nu^2) < 7.5 \times 10^{-3}\,\text{eV}^2$.

# 9. Conclusion and Outlook

With the discovery of the neutrino oscillations in 1998 and the resulting insurmountable evidence that neutrinos must have a non-vanishing rest mass, the domain of neutrino physics beyond the standard model was entered. Since the neutrino oscillation experiments are only sensitive to the mass difference, the absolute value of the masses has to be determined with other dedicated experiments. Different measurement approaches exist in order to determine the neutrino mass, e.g. through cosmological observations, the measurement of the neutrinoless double beta decay, or the direct measurement by investigating the kinematics of the β-decay. However, up to the present day only upper limits on the neutrino mass were reported. The currently leading direct neutrino-mass experiment is the Karlsruhe Tritium Neutrino Experiment (KATRIN). It is targeted to measure the effective electron antineutrino mass by investigating the energy spectrum of the tritium β-decay, where a non-vanishing neutrino mass causes a distortion of the spectral shape close to the endpoint.

KATRIN started taking data in spring 2019 and reported an improved upper limit on the effective electron antineutrino mass of

$$m(\nu_e) < 1.1\,\mathrm{eV}\,c^{-2} \quad (90\%\text{ confidence level})$$

already from the first month of data taking [AAA+19b]. With this first result, the existing upper limit of $m(\nu_e) < 2\,\mathrm{eV}\,c^{-2}$ (95% confidence level) by the Mainz and Troitsk experiments was improved by nearly a factor of two. The sensitivity goal of $m(\nu_e) = 200\,\mathrm{meV}\,c^{-2}$ (90% confidence level) is reached after three net years worth of data, which is expected to be reached after approximately five calendar years of measuring time. In order to realise this sensitivity goal, a source activity of $10^{11}$ β-decays per second is required, resulting in the integrated source density of $5 \times 10^{21}$ molecules/m$^2$. At this high source density nearly 60 % of the signal electrons at the endpoint of the tritium spectrum undergo inelastic scatterings with the source gas. The energy loss from these scattering processes is one of the main systematics of KATRIN, as it causes a significant distortion of the measured β-spectrum. In order to take this systematic effect into account in the neutrino-mass analysis, a detailed and precise description of the probability distribution of these energy losses, the so-called energy-loss function, is required. In order to reach the neutrino-mass sensitivity goal of KATRIN, the systematic uncertainty $\sigma_{\mathrm{sys}}^{\mathrm{eloss}}(m_\nu^2)$ on the observable $m_\nu^2$ arising from the uncertainty of the energy-loss function model must not exceed the budget of $\sigma_{\mathrm{sys}}^{\mathrm{eloss}}(m_\nu^2) = 7.5 \times 10^{-3}\,\mathrm{eV}^2\,c^{-4}$. As no model meeting this requirement is available, it is essential for KATRIN to measure the energy-loss function of 18.6 keV electrons scattering off molecular tritium in-situ with the experimental setup of KATRIN.

The precision measurement of the energy-loss function of both molecular deuterium and tritium is the main topic of this thesis.

The measurement of the energy-loss function was performed by using a monoenergetic and angular selective photoelectron source. This unique photoelectron source was developed

over many years at KATRIN and was finally commissioned in fall 2018 as part of this work together with R. Sack (University of Münster) [Sac20]. The experimental work of this thesis was mainly focussed on the commissioning and characterisation of the optical setup. The optical setup consists of two light sources: the primary one is a Laser-Driven Light Source and the secondary one a pulsed UV laser. Since the light intensity stability is directly correlated with the rate stability of the photoelectron source, the stability of both light sources was characterised. Dedicated stability measurements showed that the stability of either light source exceeds the requirements of a long-term stability of less than 0.1 %. For the Laser-Driven Light Source and the UV laser, a long-term stability of 3 % and 12 % was obtained, respectively. In order to reach the stability requirements, an active intensity stabilisation was included into the optical setup. The active stabilisation system consists of a variable circular aperture, which is adjusted with a stepper motor. By using the intensity information of a photodiode connected to the light output with a fibre splitter, the intensity can be stabilised to a selected setpoint. With this active intensity stabilisation, it is possible to reach a long-term intensity stability of 0.03 %. However, the first commissioning measurements of the photoelectron source showed that the achieved rate is much below the expectations of $>10^4$ photoelectrons per second and only a rate of approximately 1500 photoelectrons per second was obtained when using the Laser-Driven Light Source. Consequently, the active stabilisation could not be used during the measurements, as the coupling efficiency of the device of 55 % would further attenuate the light yield and the resulting electron rate. Thus, the rate of the photoelectron source is affected by the intensity fluctuations of the light sources. However, it was demonstrated in this work that the recorded light intensity information from the monitoring system can be used to correct for the intensity drift during the processing of the measurement data, which became the standard correction method for all measurements with the photoelectron source. Even though not all ambitious design goals of the photoelectron source have been achieved yet, the commissioning of the latter constitutes an important contribution to the success of KATRIN, as this essential calibration and monitoring device is now available. Besides the energy-loss function measurements, the photoelectron source is extensively used e.g. for the determination of the electric and magnetic field in the analysing plane or the repeated measurement of the column density during the neutrino mass measurements.

When using the pulsed UV laser as light source, the photoelectron source generates a pulsed beam of electrons. The operation of the photoelectron source in the pulsed mode causes a significant amount of pile-up events at the detector. It was found that the rate loss due to these pile-up events is not constant but changes as a function of the surplus energy as a result of a complex interplay of the retarding potential of the main spectrometer and the energy loss due to scattering. The energy dependency causes a distortion of the response function measurements of the photoelectron source in the order of several percent. In this work, a correction approach proposed by S. Enomoto (University of Washington) was adapted for response function measurements at filled source, where the energy loss due to scattering must be considered. This dedicated pile-up correction makes use of both the event energy as well as the bipolar width of the event signal, which are obtained from the bipolar shaping trapezoidal filter system of the focal plane detector. By using the two characteristic event properties, the number of electrons triggering the same detector event can be determined from simulated look-up tables. In order to generate the multiplicity look-up tables for individual measurement settings, a complex simulation framework was developed, which allows one to perform flight time and detector response simulations taking into account the pulse rate of the laser and the source density. The improved pile-up correction developed in this work allows the systematic distortions of the response functions to be corrected with hight precision resulting in uncertainties of less than 0.1 %. This pile-up correction is essential for the success of the measurement of the energy-loss function and any other measurement being performed using the pulsed photoelectron source.

As part of this work, the precision measurement of the energy-loss function with deuterium gas inside the windowless source was performed in fall 2018 with the aim to test the measurement approach and the analysis techniques that had been developed. For this purpose, integral response function measurements at three different source gas densities and a reference measurement at empty source were performed. The measurement strategy of the response functions was improved by introducing a continuous ramping of the surplus energy. This new scanning method allowed for quick voltage scans, which can be repeated multiple times in alternating directions in order to eliminate the influence of drifts of the electron rate or the source density. These response function measurements were analysed by using a singular value decomposition (SVD) deconvolution as proposed in Ref. [HHW+17] and an analytical fit including a novel semi-empirical parametrisation of the energy-loss function. With the direct comparison of the energy-loss function models obtained from the two approaches using the same data set it was demonstrated that the result obtained from the analytical fit outperforms the deconvolution in terms of energy resolution and model uncertainties. The uncertainties of the model obtained from the analytical fit are about a factor of 100 smaller than for the deconvolution result. As the analytical fit allows one to include also differential data, the data set was extended by a differential response function. This differential response function was provided by R. Sack (University of Münster) [Sac20] and was obtained from time-of-flight measurements. With this additional data, the energy-loss function determined in this work was further refined. By performing a Monte Carlo propagation of the energy-loss model uncertainties, this work has shown that the resulting uncertainty on the KATRIN observable $m_\nu^2$ is $\sigma_{\mathrm{sys}}^{\mathrm{eloss}}(m_\nu^2) = 2.8 \times 10^{-3}\,\mathrm{eV}^2\,c^{-4}$ and thus meets the stringent requirements of $\sigma_{\mathrm{sys}}^{\mathrm{eloss}}(m_\nu^2) < 7.5 \times 10^{-3}\,\mathrm{eV}^2\,c^{-4}$. As a result, it was successfully demonstrated in this work that both the measurement strategy as well as the analysis technique of the combined fit of integral and differential data can be used for the measurement of the energy-loss function using tritium as source gas.

Based on the experience gained during the deuterium measurement and the data analysis, the first precision measurement of the energy-loss function for tritium with the experimental setup of KATRIN was performed in spring 2019. The aim of the measurements was to obtain a precise model of the energy-loss function for tritium, which can be used in the neutrino-mass analysis of KATRIN. For this purpose, four response function measurements were performed each in integral and differential mode (the latter were analysed by C. Rodenbeck (University of Münster) [Rod]). With a total amount of 30 free parameters and 7070 degrees of freedom, the best fit result was obtained at a value of $\chi^2/N_{\mathrm{dof}} = 1.133(17)$. In order to verify the fit result, all known systematic uncertainties of the measurement were characterised and a Monte Carlo framework was developed. With dedicated simulations of the entire measurement and analysis chain it could be demonstrated in this work that the measurement is dominated by the statistical uncertainty and the contribution of the systematic uncertainties to the parameter uncertainties as well as parameter shifts is negligible. From a propagation of the parameter uncertainties, a systematic uncertainty on $m_\nu^2$ of $\sigma_{\mathrm{sys}}^{\mathrm{eloss}}(m_\nu^2) = 4.0 \times 10^{-3}\,\mathrm{eV}^2\,c^{-4}$ was determined. The result was verified by propagating the results of the Monte Carlo simulations, where an uncertainty of $\sigma_{\mathrm{sys}}^{\mathrm{eloss}}(m_\nu^2) = 3.9 \times 10^{-3}\,\mathrm{eV}^2\,c^{-4}$ and a systematic shift of $\Delta m_\nu^2 = -0.5 \times 10^{-3}\,\mathrm{eV}^2\,c^{-4}$ was obtained. Hence, the quality of the energy-loss function outperforms the KATRIN requirements of $\sigma_{\mathrm{sys}}^{\mathrm{eloss}}(m_\nu^2) < 7.5 \times 10^{-3}\,\mathrm{eV}^2\,c^{-4}$ by nearly a factor of two.

Due to the unprecedented precision obtained on the energy-loss function of molecular tritium, the results of this work constitute a very important contribution to the past and future successful measurement programme of KATRIN. The novel semi-empirical parametrisation of the energy-loss function of tritium was already used during the analysis of the first neutrino-mass measurement campaign leading to the improved upper limit of $m(\nu_e) < 1.1\,\mathrm{eV}\,c^{-2}$ [AAA+19b]. As the measurement result of the energy-loss func-

tion meets the high requirements of KATRIN for the final neutrino-mass sensitivity of $m(\nu_e) = 0.2\,\mathrm{eV}\,c^{-2}$, the provided energy-loss function can be used even for the analysis of future high-statistics data sets. In order to reach the final sensitivity, KATRIN continues taking data for the next four years, thereby continuously decreasing the statistical uncertainty on the β-spectrum. If the effective electron antineutrino mass is larger than the final sensitivity of KATRIN, another major milestone in the more than 90 years long history of neutrino physics would be reached with the first determination of the neutrino mass.

# Appendix

## A.1 Propagation of uncertainty during data processing

Different corrections are applied to the measurement data during the processing. In the following, the calculations of the corrections and the corresponding propagation of the uncertainties are provided.

### Light intensity correction

The monitoring system of the light intensity of the light source of the electron gun has an relative uncertainty of $\sigma_{\mathrm{I}} = 0.4\,\%$. In order to correct for light intensity drifts, the rate is corrected with the relative deviation of the light intensity to its mean value

$$\tilde{N} = N \cdot \frac{\langle I \rangle}{I}\,, \tag{A.1}$$

with $N$ being the number of events per bin. The uncertainty of the mean is negligible and thus only the uncertainty of the sensor value is propagated in order to obtain the uncertainty of the scaling factor

$$\tilde{\sigma}_{\mathrm{I}} = \frac{\langle I \rangle}{I} \cdot \sigma_{\mathrm{I}}\,. \tag{A.2}$$

This uncertainty is propagated during the intensity correction, which gives the uncertainty of the data points

$$\sigma_{\mathrm{N}} = \sqrt{N \cdot \left(\frac{\langle I \rangle}{I}\right)^2 + \left(N \cdot \tilde{\sigma}_{\mathrm{I}}\right)^2}\,. \tag{A.3}$$

### Integration of high-voltage stability

In order to take the uncertainty of the high-voltage slope of $\sigma(E_{\mathrm{s}}) = 7.0\,\mathrm{mV}$ into account, the uncertainty on the voltage bins is converted into an uncertainty on the counts. This is done by determining the slope of the response function at each data point and by multiplying the slope with the uncertainty on the voltage reading. The slope $s_i$ at the $i$-th bin is determined by considering the two neighbouring data points

$$s_i = \frac{N_{i-1} - N_{i+1}}{2b}\,, \tag{A.4}$$

with $b$ being the bin width.

The additional uncertainty $\sigma_{\mathrm{E_s}}$ on the count rate due to the uncertainty on the voltage reading thus becomes

$$\sigma_{\mathrm{E_s}} = \sigma(E_{\mathrm{s}}) \cdot s_i\,. \tag{A.5}$$

This uncertainty is added quadratically to the uncertainty on the data points in order to obtain the total uncertainty

$$\sigma_{\mathrm{tot}} = \sqrt{\sigma_{\mathrm{N}}^2 + \sigma_{\mathrm{E_s}}^2}\,. \tag{A.6}$$

### Interpolation

For the purpose of the energy calibration of the individual data sets, the data is shifted so that the middle of the transmission function is located at $E_\mathrm{s} = 0\,\mathrm{eV}$ (see Sec. 7.2.2). As the binning pattern has to be the same for all data sets, the shift is limited by the bin width. In order to shift the response function more precisely, an interpolation between the bins is required. The interpolation is performed by expressing the shift $\delta E$ as a fraction of the bin width $b$, i.e.

$$\mathcal{F} = \frac{\delta E}{b}\,. \tag{A.7}$$

The bin entries $\tilde{N}_i$ after the energy shift are then calculated as

$$\tilde{N}_i = N_i \cdot (1 - \mathcal{F}) + N_{i+1} \cdot \mathcal{F}\,. \tag{A.8}$$

The uncertainty of the interpolated bin values is calculated according to

$$\tilde{\sigma}_\mathrm{N} = \sqrt{\sigma^2_{\mathrm{N},i} \cdot (1 - \mathcal{F}) + \sigma^2_{\mathrm{N},i+1} \cdot \mathcal{F}}\,. \tag{A.9}$$

## A.2 Usage of the fitting module

For the purpose of fitting both integral and differential response functions in order to determine the shape of the energy-loss function, the dedicated `fitter` module is available in the `elossPackage` as part of the `KATRIN-eloss` repository. The fitter module requires to be loaded and to be initialised

```
import  fitter
myFitter=fitter.elossFitter(gasType="D2")
```

with the possible `gasType` parameter values being one of the hydrogen isotopes `H2`, `D2`, or `T2`. By selecting the gas species, the ionisation energy (see Eq. (4.25)) is set accordingly in order to construct the energy-loss model.

After the initialisation of the fitter module, the individual data sets can be added with the command

```
myFitter.addIntegralData("5_runs_stacked.dat",name='5_int', label="5%
    $\rho_0 d$",filePath='./')
```

with the first required parameter being the name of the data set. The other optional parameters are an identifier (required to set response function specific parameters), a plot label, and the path of the data sets. If the parameters are not set, the file name is used for both the identifier and the plot label and the path points to the `data` directory of the `KATRIN-eloss` repository. An arbitrary amount of response functions can be added.

The transmission function is added with the command

```
myFitter.setTransmissionFunction("0_runs_stacked.dat",dataSet=None,
    filePath='./', fit=False)
```

with the file name being required. If the added transmission function should be assigned to one of the above added data sets individually, the `dataSet` parameter can be used to pass the corresponding name of the data set. If `dataSet` is not set or `None`, the loaded transmission function is valid for all above added response functions. Again, the path parameter points to the `data` directory if no dedicated path is selected. An important condition on the transmission function is that the binning has to match the binning of the corresponding data set. The data range can in fact be different if the fit range is chosen to

be smaller than the data range of both the response function and the transmission function. If the optional parameter `fit` is set to `True`, the loaded transmission function will be fit by an error function and the fit result will be used to construct the fit model.

In order to set the fit range as well the data range, the commands

```
myFitter.setIntegralFitrange(-1,50, dataSet=None)
myFitter.setIntegralDataRange(-3,53, dataSet=None)
```

are available. The first two parameters are the lower and upper boundaries of the fit range and the data range, respectively. The optional parameter `dataSet` can be used to pass the name of one of the added data sets in order to set the ranges individually. If the parameter is not set or `None`, the range is applied to all of the previously loaded data sets. The data range is only used to limit the data range in the graphical output of the fitter.

In order to implement the differential data into the `fitter` module, the initialisation similar to the integral data. For this purpose, the module provides the commands

```
myFitter.addTofData("5_tof_data.dat",name='5_tof', label="5% $\rho_0 d$
    (tof)",filePath='.')
myFitter.setZeroLossPeak("5_tof",-1,1)
myFitter.setCommonTofFitrange(8,53)
```

Again, an arbitrary amount of differential response functions with individual binning pattern (independent of the integral data) and data range can be added.

Last step of the initialisation process of the fitter module is to define the start parameter for the included minimiser (i.e. MIGRAD). This is done by setting up a dictionary containing a list of the energy-loss function parameters and lists of parameter settings for the nuisance parameters of the individual data sets.

The energy-loss function parameters are assigned to the key `elossFunctionParameters`, which must contain a list of dictionaries providing the keys `name`, `start`, `stop`, `error`, `limit`, and `fixed`. For the semi-empirical energy-loss model, as described in Eq. (7.15), nine parameters need to be initialised, which have to be ordered according to `amp1, pos1, sig1, amp2, pos2, sig2, amp3, pos3, sig3`. In the case of the empirical energy-loss model, the parameter bounds are only chosen to be non-negative. If other limits are required, the option `limits` exist, which allows one to pass a list to the minimiser containing the lower and upper parameter limits.

For the nuisance parameters of each data set, the list of parameters must include a dictionary with the parameter settings for the parameters $A_i$, $\mu_i$, and $A_i^{\mathrm{bg}}$. Again, the order of the parameters is important.

An example of the settings dictionary would be

```
#configure start parameters, step size and limits of fitter
settings={'elossFunctionParameters':[
{'name':'amp1', 'start': 3.24e-02, 'error': 0.1, 'limit':0, 'fixed':'No'},
{'name':'pos1', 'start': 1.18e+01, 'error': 0.1, 'limit':0, 'fixed':'No'},
{'name':'sig1', 'start': 1.71e-01, 'error': 0.1, 'limit':0, 'fixed':'No'},
#... amp2 pos2 sig2 ...
{'name':'amp3', 'start': 7.49e-02, 'error': 0.1, 'limit':0, 'fixed':'No'},
{'name':'pos3', 'start': 1.48e+01, 'error': 0.1, 'limit':0, 'fixed':'No'},
{'name':'sig3', 'start': 1.05e+00, 'error': 0.1, 'limit':0, 'fixed':'No'}],
'5_int':[
{'name': 'norm5_int', 'start': 1.00e+00, 'error': 0.1, 'limit': 0,
    'fixed': 'No'},
{'name': 'mu5_int', 'start': 8.81e-02, 'error': 0.1, 'limit': 0, 'fixed':
    'No'},
```

```
{'name': 'bkgAmpl5_int', 'start': 5.69e-05, 'error': 0.1, 'limit': 0,
    'fixed': 'No'}],
'5_tof':[
{'name': 'norm5_tof', 'start': 1.24e+00, 'error': 0.1,      'limit': 0,
    'fixed': 'No'},
{'name': 'mu5_tof', 'start': 9.0e+02, 'error': 0.1, 'limit': 0, 'fixed':
    'No'},
{'name': 'bkgAmpl5_tof', 'start': 2.21e-05, 'error': 0.1, 'limit': 0,
    'fixed': 'No'}]
}
```

In order to make the choice of the amplitude parameter $A_i$ more convenient, the individual data sets are normalised before executing the fit. In the case of the integral data, the response functions are scaled so that the last data point of the selected data range matches one. Thus, $A_i$ can be initialised with 1. Due to this scaling, the best fit values of $A_i$ for the different column densities will be in the order of one. In the case of the differential data, the response functions are scaled by the integral of the data points within the selected fit range.

The minimisation is executed with the command

```
myFitter.fit(settings)
```

with the settings dictionary being required as function argument.

The `fit()` function executes the minimisation of the likelihood function considering the added data sets.

An example on the usage of the fitter module is provided in the code example A.1.

```
import  fitter

path='inputDir'
myFitter=fitter.elossFitter(gasType="D2") #initialize fitter

#load files
myFitter.addIntegralData("5_runs_stacked.dat",name='5_int', label="5% $\rho_0 d$",filePath=path)
myFitter.addTofData("5_tof_data.dat",name='5_tof', label="5% $\rho_0 d$ (tof)",filePath=path)

#select transmission function
myFitter.setTransmissionFunction("0_runs_stacked.dat",filePath=path)
myFitter.setZeroLossPeak("5_tof",-1,1)

myFitter.setIntegralDataRange(-3,53) #set integral plot range
myFitter.setIntegralFitrange(-3,50) #set integral fit range
myFitter.setCommonTofFitrange(8,53) #set tof fit range

#configure start parameters, step size and limits of fitter
settings={'elossFunctionParameters':[
{'name':'amp1', 'start': 3.24e-02, 'error': 0.1, 'limit':0, 'fixed':'No'},
{'name':'pos1', 'start': 1.18e+01, 'error': 0.1, 'limit':0, 'fixed':'No'},
{'name':'sig1', 'start': 1.71e-01, 'error': 0.1, 'limit':0, 'fixed':'No'},
{'name':'amp2', 'start': 2.78e-01, 'error': 0.1, 'limit':0, 'fixed':'No'},
{'name':'pos2', 'start': 1.27e+01, 'error': 0.1, 'limit':0, 'fixed':'No'},
{'name':'sig2', 'start': 4.77e-01, 'error': 0.1, 'limit':0, 'fixed':'No'},
{'name':'amp3', 'start': 7.49e-02, 'error': 0.1, 'limit':0, 'fixed':'No'},
{'name':'pos3', 'start': 1.48e+01, 'error': 0.1, 'limit':0, 'fixed':'No'},
{'name':'sig3', 'start': 1.05e+00, 'error': 0.1, 'limit':0, 'fixed':'No'}],

'5_int':[
{'name': 'norm5_int', 'start': 1.00e+00, 'error': 0.1, 'limit': 0, 'fixed': 'No'},
{'name': 'mu5_int', 'start': 8.81e-02, 'error': 0.1, 'limit': 0, 'fixed': 'No'},
{'name': 'bkgAmpl5_int', 'start': 5.69e-05, 'error': 0.1, 'limit': 0, 'fixed': 'No'}],
'5_tof':[
{'name': 'norm5_tof', 'start': 1.24e+00, 'error': 0.1,      'limit': 0, 'fixed': 'No'},
{'name': 'mu5_tof', 'start': 9.0e+02, 'error': 0.1, 'limit': 0, 'fixed': 'No'},
{'name': 'bkgAmpl5_tof', 'start': 2.21e-05, 'error': 0.1, 'limit': 0, 'fixed': 'No'}]
}

#execute fitter
myFitter.fit(settings)
#export results
myFitter.exportFitResults('fitresults.dat')
```

Code A.1: Example usage of the `fitter` module. Any number of data sets can be added and the fit and plot ranges can be set individually. Also the transmission functions can be loaded for each data set individually, which will then be used to construct the fit function.

## A.3 Analysis using only integral response functions of $T_2$

Similar as for the deuterium data, the integral data set for tritium can be analysed without including the differential data.

The best-fit result, as shown in Fig. A.1, is obtained at $\chi^2/N_{\mathrm{dof}} = 1.173(24)$ with $N_{\mathrm{dof}} = 3402$ with the parameters provided in Tab. A.1. A comparison between the fit result using only the integral data as well as the result using both data sets is provided in Fig. A.3. Similar as for the deuterium data, the shape parameters of the first Gaussian cannot be determined with as high precision as in the combined fit. Thus, the first Gaussian is slightly detached and shows large parameter uncertainties. Furthermore, a difference in the region of the third Gaussian is visible. However, the shape of the dominant structures, such as the second Gaussian and the ionisation tail, agree well with the combined fit result.

The mean energy loss evaluates to

$$\langle \Delta E \rangle_{\mathrm{int}}^{\mathrm{T_2}} = 30.85\,\mathrm{eV}\,, \tag{A.10}$$

which is only 60 meV larger than the value for the combined analysis provided in Eq. (8.7).

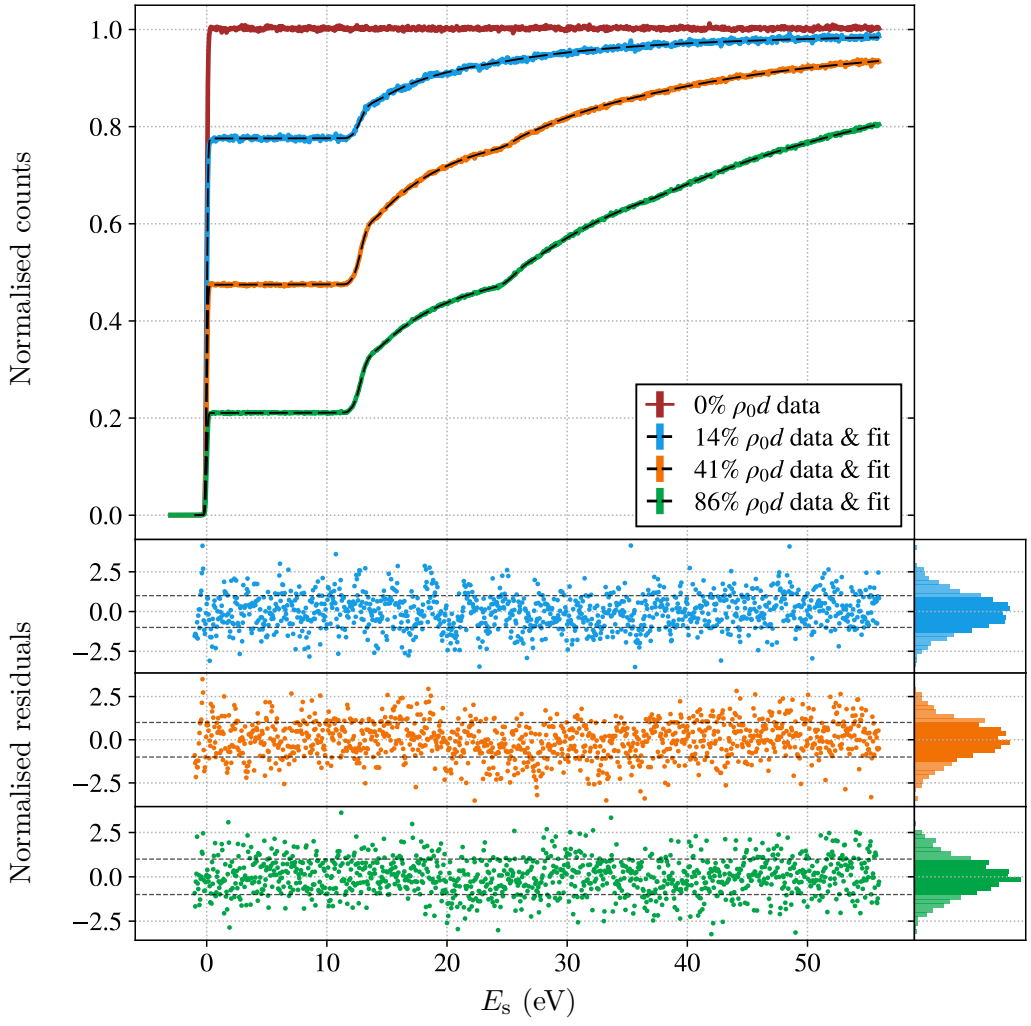


Figure A.1: Combined fit to the integral response functions for $T_2$ together with the normalised residuals $(y_{\text{data}} - y_{\text{fit}}) \cdot \sigma^{-1}$. The histograms on the right show the distribution of the residuals, with the shaded area indicating the $1\sigma$ range.

Table A.1: Parameters for the energy-loss function (see Eq. (7.15)) of molecular tritium and the nuisance parameters as obtained from a combined $\chi^2$ fit to the integral response functions. The best-fit result is obtained at a value of $\chi^2/N_{\mathrm{dof}} = 1.173$. The covariance and correlation matrices for the subset of the nine energy-loss function parameters are provided in Fig. A.2.

| Parameter | Unit | Value | $\sigma_{\mathrm{fit}}$ |
|---|---|---|---|
| $a_1$ | $\mathrm{eV}^{-1}$ | 0.056 39 | 0.002 97 |
| $m_1$ | eV | 11.8441 | 0.0337 |
| $\sigma_1$ | eV | 0.067 65 | 0.003 59 |
| $a_2$ | $\mathrm{eV}^{-1}$ | 0.282 772 | 0.000 433 |
| $m_2$ | eV | 12.780 30 | 0.002 91 |
| $\sigma_2$ | eV | 0.459 703 | 0.000 731 |
| $a_3$ | $\mathrm{eV}^{-1}$ | 0.070 071 5 | 0.000 068 3 |
| $m_3$ | eV | 14.966 83 | 0.003 99 |
| $\sigma_3$ | eV | 1.282 00 | 0.003 87 |
| | | Nuisance parameters: integral | |
| $A_{14}$ | | 1.019 587 | 0.000 157 |
| $\mu_{14}$ | | 0.253 927 | 0.000 288 |
| $A_{14}^{\mathrm{bg}}$ | | 0.000 288 6 | 0.000 034 3 |
| $A_{41}$ | | 1.065 644 | 0.000 188 |
| $\mu_{41}$ | | 0.745 407 | 0.000 276 |
| $A_{41}^{\mathrm{bg}}$ | | 0.000 626 4 | 0.000 039 7 |
| $A_{86}$ | | 1.236 233 | 0.000 372 |
| $\mu_{86}$ | | 1.557 929 | 0.000 381 |
| $A_{86}^{\mathrm{bg}}$ | | 0.003 033 1 | 0.000 095 3 |


Figure A.2: Correlation matrix (top) and covariance matrix (bottom) for the energy-loss function parameters in Tab. A.1 as obtained from the combined $\chi^2$ fit using only integral response functions for molecular tritium.

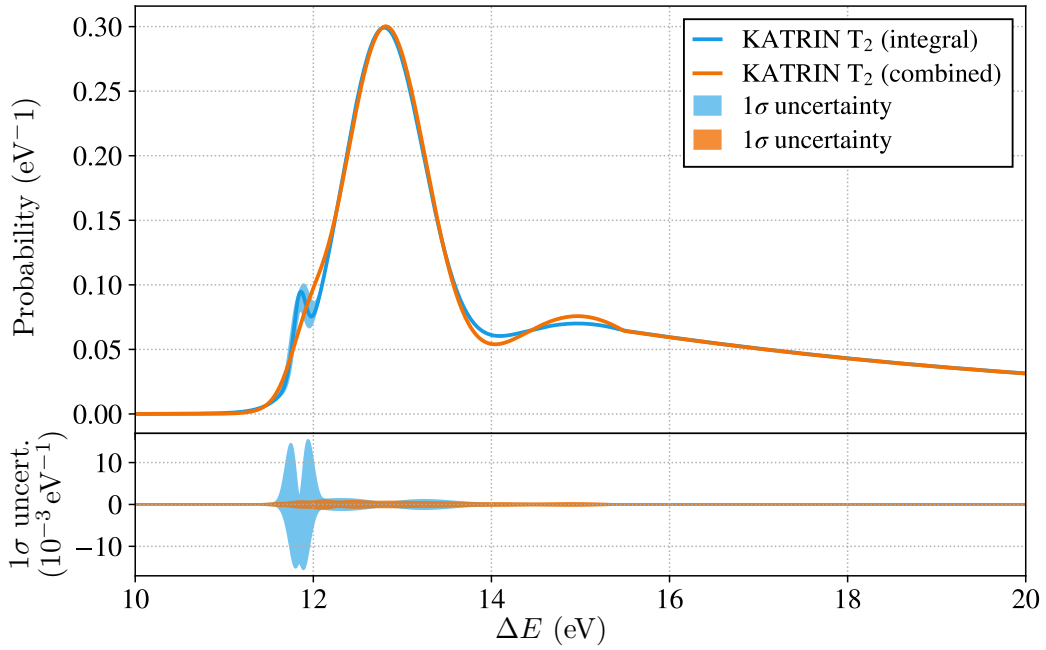


Figure A.3: Shape of the energy-loss function as obtained from the combined fit to integral response function measurements for molecular tritium. The $1\sigma$ uncertainty band is additionally drawn in the bottom panel, as most parts are too small to be visible in the top panel. For comparison, the results from the combined fit to both the integral and the differential response functions is included. As it can be seen, the position of the first Gaussian cannot be determined with as high precision as for the combined fit. This was already observed in the analysis of the deuterium data (see Fig. 7.17).

## A.4 The response function generator module

The `responseGenerator` module is included in the `elossPackage` and allows one to generate response functions and to modify them in a modular way.

The `responseGenerator` needs to be initialized by providing the mean number of scatterings `mu` and a list of equidistant surplus energy values `E` at which the shape of the response function should be evaluated

```
import responseGenerator
response=responseGenerator.responseGenerator(E, mu)
```

The properties of the transmission function, i.e. the width and the position, need to be set by calling the command

```
response=setTransmissionFunctionProperties(position, width)
```

Depending on the type of the response function, i.e. integral or differential, the raw response function has to be constructed by calling one of the following functions

```
response.makeIntegralResponseFunction(nUnscatteredPerBin)
response.makeTofResponseFunction(countsOfPeak1a=heightOf1aPeak)
```

The response function is then generated according to Eq. (7.4) by using the best-fit parameters of the energy-loss function as provided in Tab. 8.4. As transmission function model, an error function (see Eq. (5.10)) is used in the case of the integral response function and a Gaussian kernel in the case of the differential response function. The contributions of $n$-fold scattered electrons is calculated depending on the provided energy interval, i.e. up to the four-fold scattering function for a maximal surplus energy of 60 eV will be taken into account.

At this point it is required to define the number of unscattered electrons `nUnscatteredPerBin` for an integral response function or the height of the first scattering peak `heightOfPeak1a`, when generating a differential response. For the generation of the differential response, a second option `areaOfPeak1a` exist, which allows one to define the scale of the response by providing the integral of the first scattering peak in the range of $E = [11, 14]$ eV. Especially when mimicking the measurement data, the latter option is more convenient, as the height of the peak has a larger statistical uncertainty, than the integrated amount of counts.

In order to manipulate the plain response functions, the option of adding scaling functions by providing a list of scaling values `scaling` (as a function of the list of surplus energies `E`)

```
response.addScalingFunction(scaling)
```

or by adding contributions from measurement backgrounds given by a list of values `bg`

```
response.addBackground(bg)
```

Any amount of scaling functions and backgrounds can be added in this manner.

By calling

```
y,yErr=response.buildResponse(addStatNoise=True)
```

the final response function is constructed by multiplying the plain response function with all defined scaling functions and by adding the backgrounds. The optional parameter `addStatNoise` allows one to add a Poisson sampling to the returned list of `y` values mimicking statistical fluctuations of the count rate. The returned list `yErr` is the corresponding Poisson uncertainty, i.e. $\sqrt{y}$. Since the background events originate from a different source than the signal electrons, the added backgrounds are randomised individually, if the option `addStatNoise` is selected.

More specific options exist, such as the simulation of column density drifts, which are not explained in detail here.

## A.5 Additional figures and tables

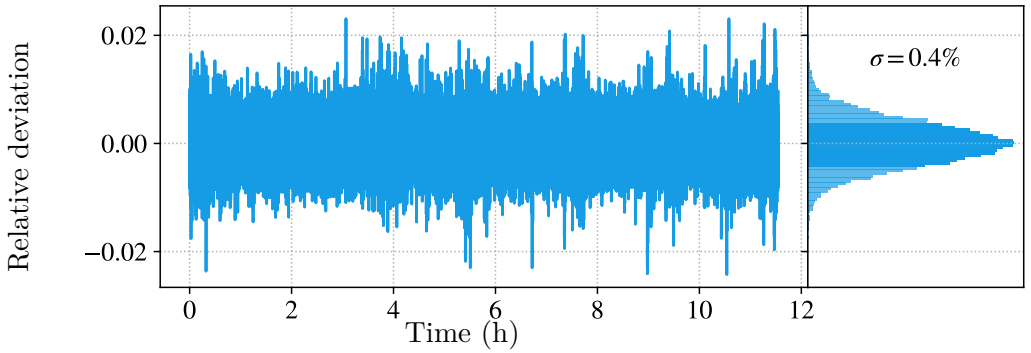


Figure A.4: Relative deviation of the diode signal of the light intensity monitoring system of the rear section. The deviation is obtained from the difference of the diode output to the smoothed signal using a floating average including eight data points. The distribution of residuals is shown on the right, with the shaded area indicating the $1\sigma$ range. A standard deviation of 0.4 % is obtained.

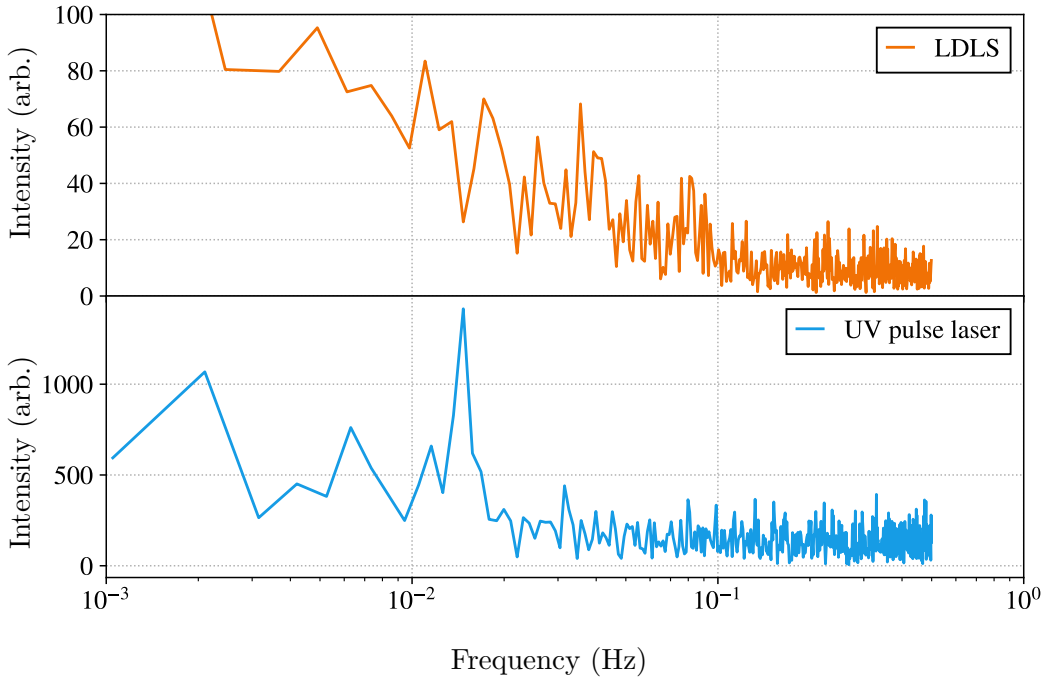


Figure A.5: Fourier spectrum of the light intensity of the LDLS and the UV laser. In the case of the UV laser, a peak is visible at 13.7 mHz, i.e. 73 s.

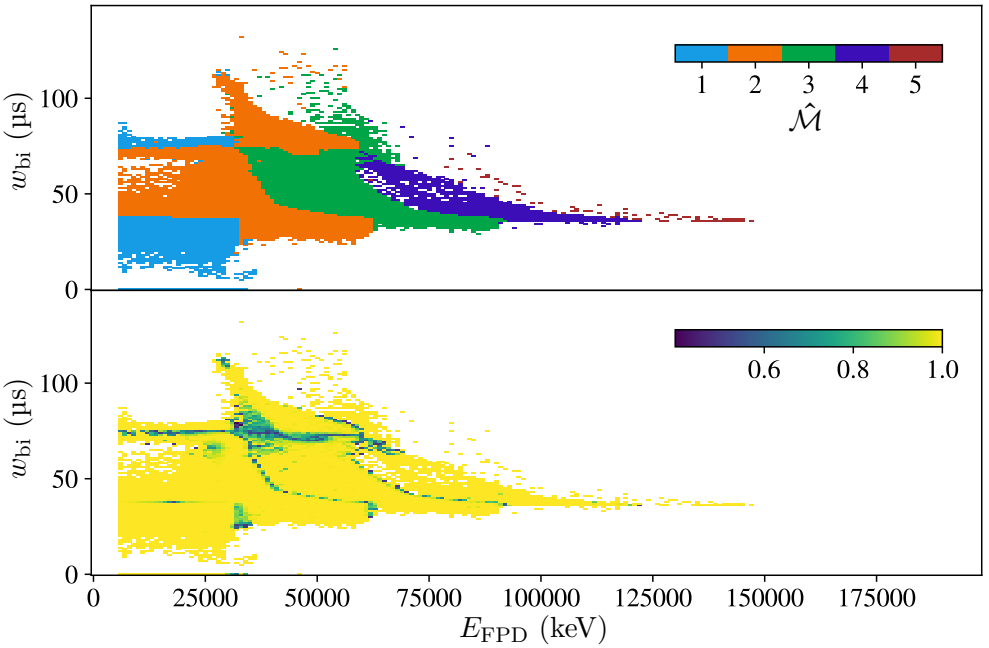


Figure A.6: The remaining ambiguous regions of the multiplicity look-up table $\hat{\mathcal{M}}(E_{\mathrm{FPD}}, w_{\mathrm{bi}})$ (top panel, settings: $\mu = 1.65$, $f_{\mathrm{P}} = 120\,\mathrm{kHz}$) are visualised in the bottom panel. The colours in the bottom panel indicate the maximum probability of the multiplicity distribution. A value of 1 indicates no ambiguity, smaller values indicate an overlap with at least one other multiplicity region. The ambiguities are taken into account by sampling from the probability distribution of the overlapping multiplicities.

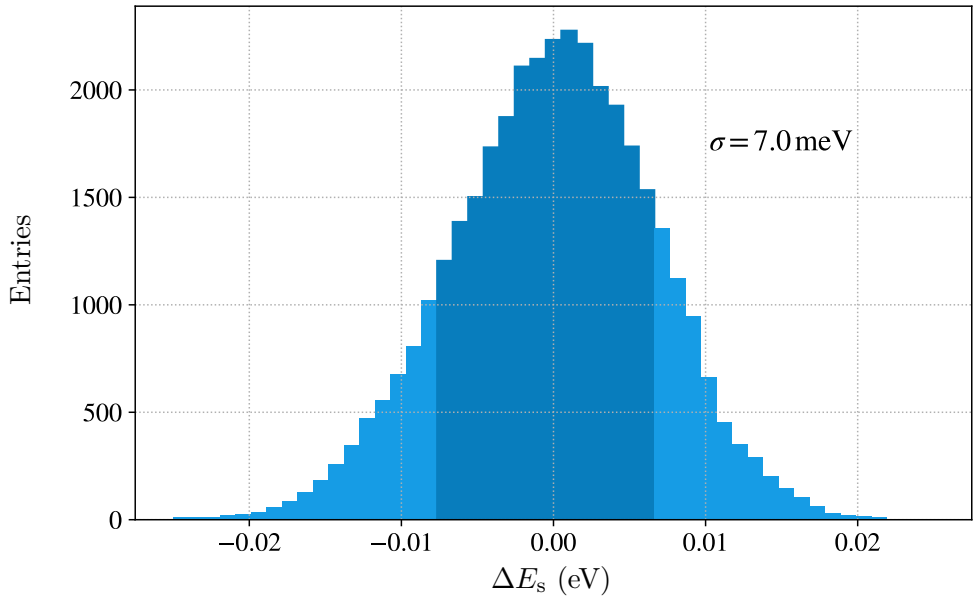


Figure A.7: Distribution of the residuals $\Delta E_{\mathrm{s}}$ of a linear fit to the continuously ramped surplus energy $E_{\mathrm{s}} = q \cdot (U_{\mathrm{em}} - U_{\mathrm{ie}})$ (comp. Fig. 7.2). The analysis uses the runs 52084 to 52106. A standard deviation of $\sigma(E_{\mathrm{s}}) = 7.0\,\mathrm{meV}$ is obtained.

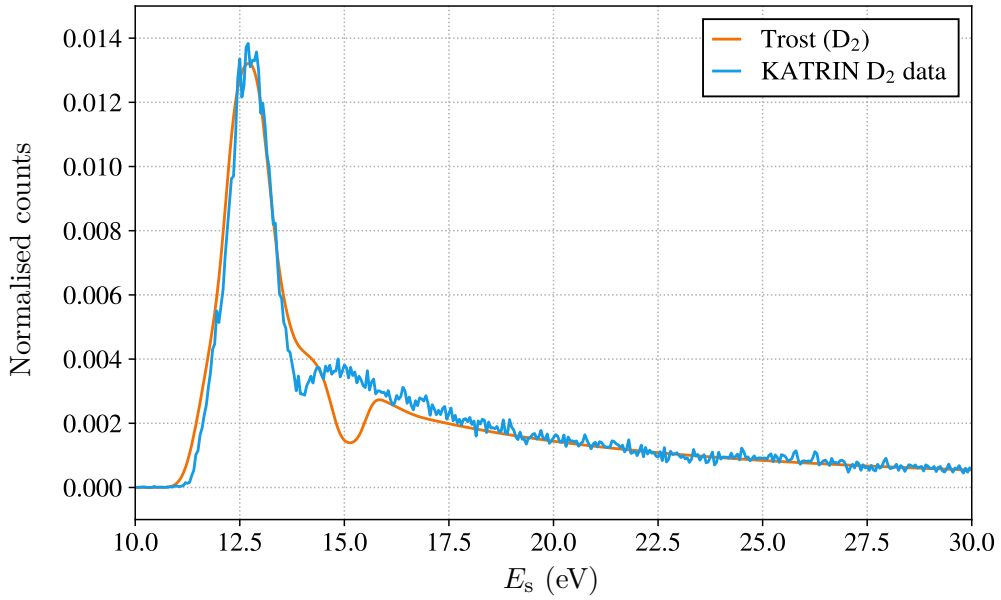


Figure A.8: Comparison of the literature-based energy-loss function model of N. Trost [Tro19] (broadened by 0.2 eV) and the differential response function data for $D_2$. A significant deviation of the model is visible in the range of $E_s = [13.5, 16]$ eV, which was already seen in the comparison with the other models in Fig. 4.4. This discrepancy cannot be improved by adjusting only the cross sections of the individual excitation states. The Trost model is thus not suitable to describe the shape of the measurement data and cannot be used as fit model.

Table A.2: Normalisation constants of the data sets as applied during the fit for the determination of the energy-loss function in Chaps. 7 and 8.

$D_2$: integral

| Column density ($\rho_0 d$) | 0 % | 5 % | 35 % | 88 % |
|---|---|---|---|---|
| Normalisation | 477125 | 789975 | 1175595 | 1204355 |

$D_2$: differential

| Column density ($\rho_0 d$) | 5 % |
|---|---|
| Normalisation | 4613 |

$T_2$: integral

| Column density ($\rho_0 d$) | 0 % | 14 % | 41 % | 86 % |
|---|---|---|---|---|
| Normalisation | 204861 | 111279 | 223006 | 238940 |

$T_2$: differential

| Column density ($\rho_0 d$) | 15 % | 22 % | 39 % | 84 % |
|---|---|---|---|---|
| Normalisation | 8024 | 8861 | 12533 | 22070 |

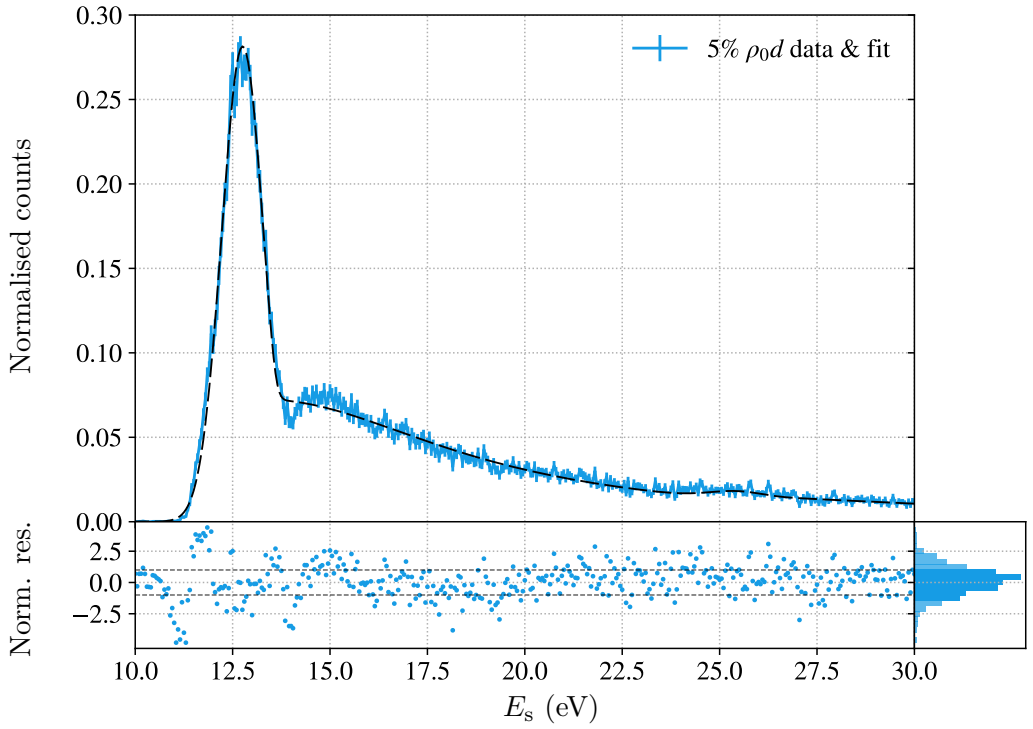


Figure A.9: Fit to the differential response function ($D_2$) using the parametrisation of Aseev et al. (see Eq. (4.32)). The model does not describe the measurement data with sufficient precision, especially on the interval $E_s = [12.5, 16]$ eV, where the Lorentz curve deviates significantly from the data. Furthermore, the approximation of the electronic excitation states using only one Gaussian kernel causes visible structures in the residuals below $E_s < 12.5$ eV.

Table A.3: Preliminary energy-loss function parameter used to construct the fit function of the combined fit to the background measurements (see Sec. 8.2.1).

| Parameter | Unit | Value |
|---|---|---|
| $a_1$ | $\mathrm{eV}^{-1}$ | $3.139\,120\,34 \times 10^{-2}$ |
| $m_1$ | eV | $1.193\,594\,93 \times 10^{1}$ |
| $\sigma_1$ | eV | $1.797\,123\,52 \times 10^{-1}$ |
| $a_2$ | $\mathrm{eV}^{-1}$ | $2.981\,920\,64 \times 10^{-1}$ |
| $m_2$ | eV | $1.282\,672\,38 \times 10^{1}$ |
| $\sigma_2$ | eV | $4.707\,867\,32 \times 10^{-1}$ |
| $a_3$ | $\mathrm{eV}^{-1}$ | $7.648\,877\,21 \times 10^{-2}$ |
| $m_3$ | eV | $1.497\,259\,35 \times 10^{1}$ |
| $\sigma_3$ | eV | $8.699\,995\,41 \times 10^{-1}$ |

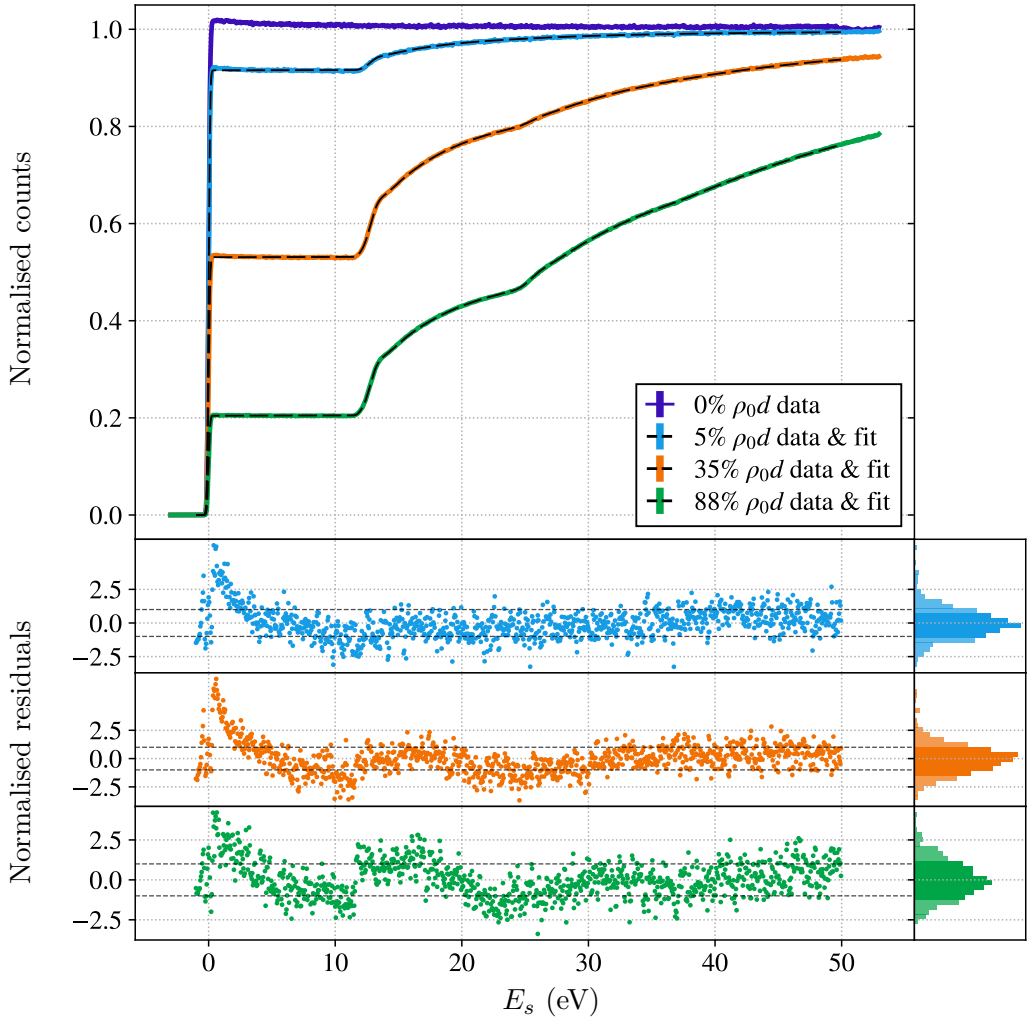


Figure A.10: Combined fit to the integral response functions for $D_2$ with the fit model constructed from an analytical transmission function instead of using the 0 % $\rho_0 d$ measurement data. Thus, the slope in the measurement data close to the transmission edge is not included in the fit model. In this case, the normalised residuals show a significant deviation of more than $2.5\sigma$ close to the transmission edge.

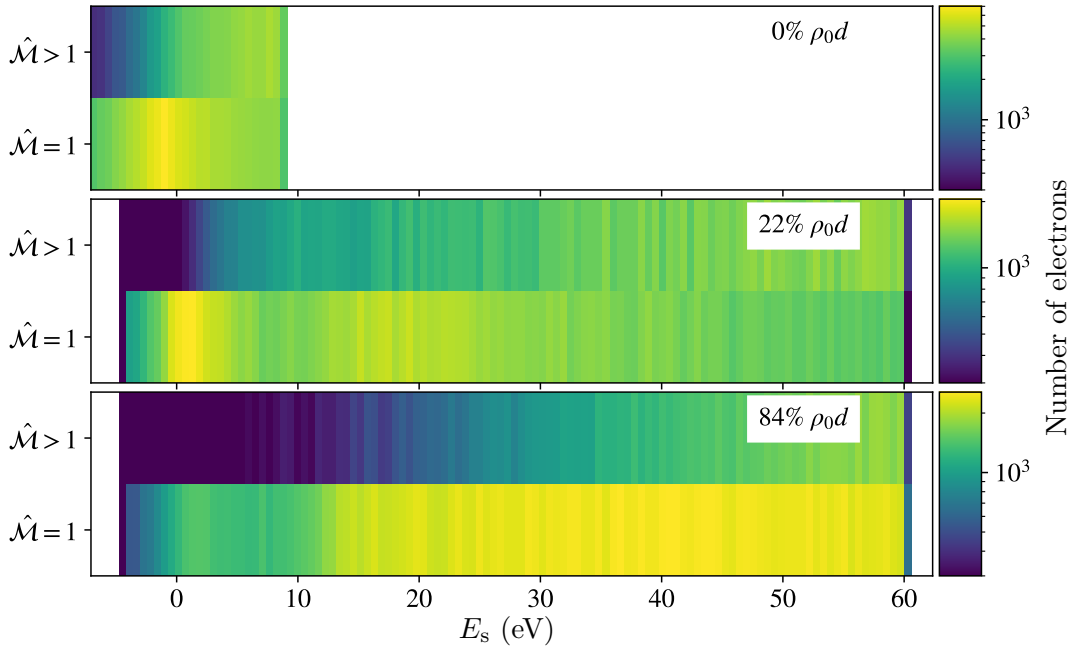


Figure A.11: Multiplicity distribution of the background measurements (see Sec. 8.2) as a function of the surplus energy. The amount of electrons with $\hat{\mathcal{M}} = 1$ changes as a function of the surplus energy. A strong increase of the number of electrons with $\hat{\mathcal{M}} = 1$ is visible especially at the transmission edge. The amount of electrons with $\hat{\mathcal{M}} = 1$ decreases again until the threshold energy of elastic scattering is reached. The opposite behaviour is visible for the number of electrons with $\hat{\mathcal{M}} > 1$.

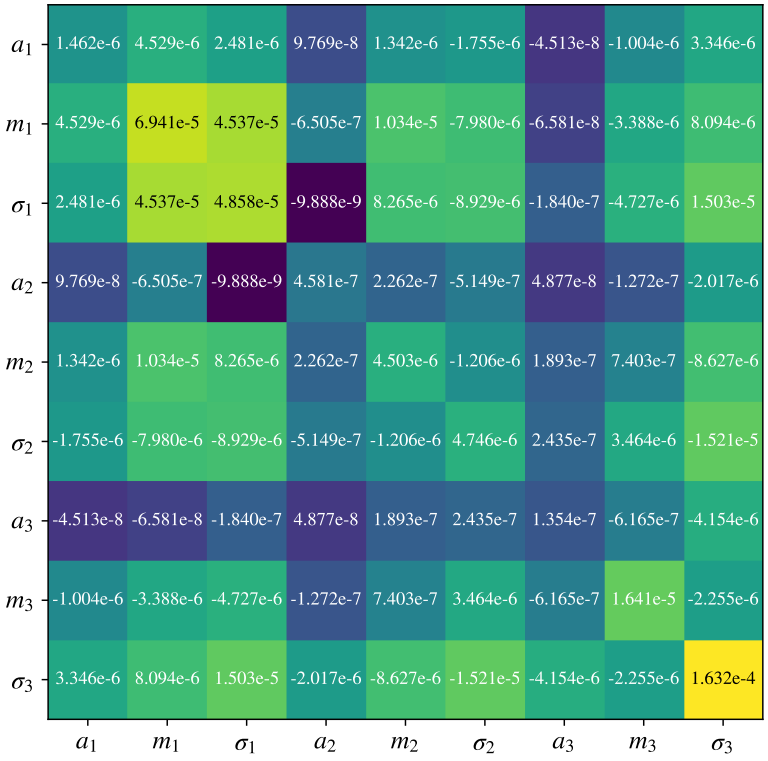


Figure A.12: Covariance matrix for the energy-loss function parameters in Tab. 8.4 as obtained from the combined $\chi^2$ fit to integral and differential response functions for molecular tritium. The covariances are obtained after rescaling the $\chi^2$ function so that a value of $\chi^2/N_{\mathrm{dof}} = 1$ is obtained for the best-fit result.

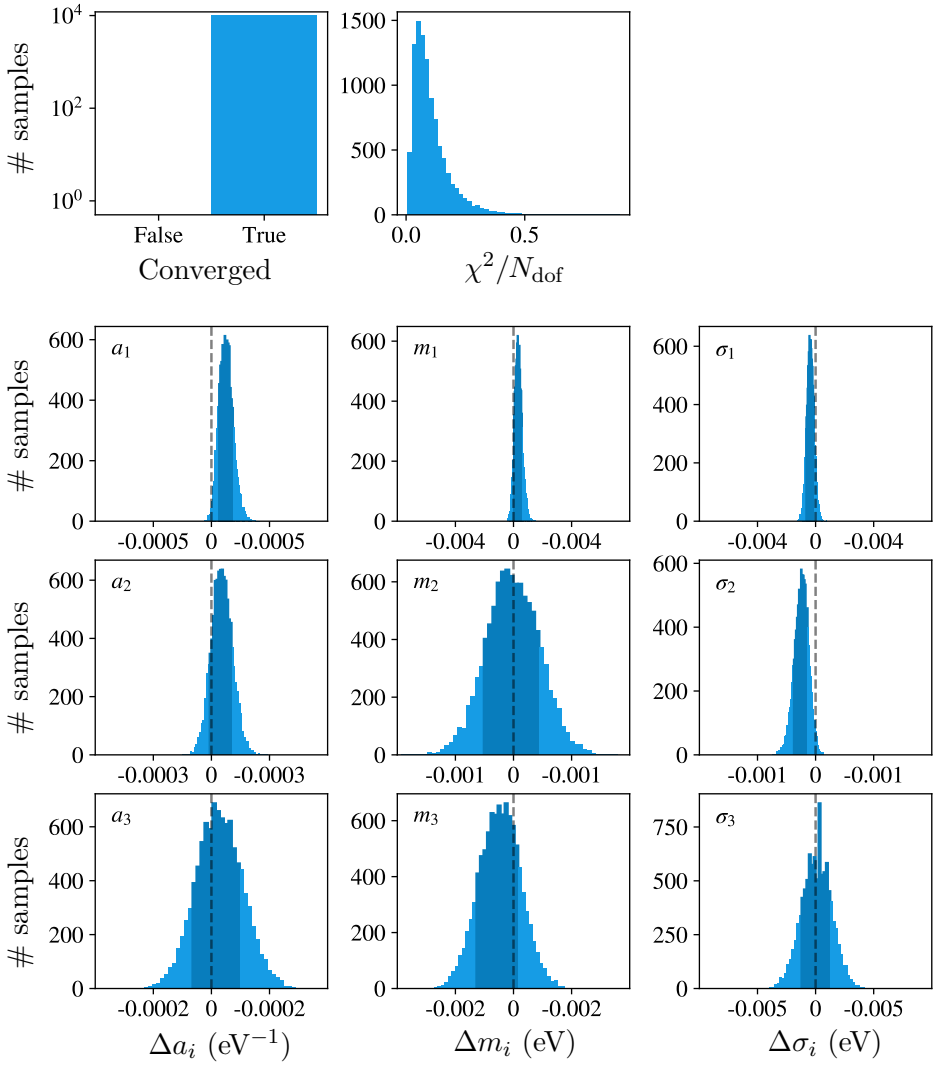


Figure A.13: Parameter distributions of the ensemble test including only systematic uncertainties. The histograms show the parameter deviations of the best-fit results of the individual fits to the Monte Carlo data sets and the initial value, i.e. $\mathcal{P}_{i,\mathrm{MC}} - \mathcal{P}_{i,\mathrm{data}}$. The shaded area indicates the $1\sigma$ interval of the distributions. The range of the x-axis is a factor of four smaller than in Fig. 8.20.

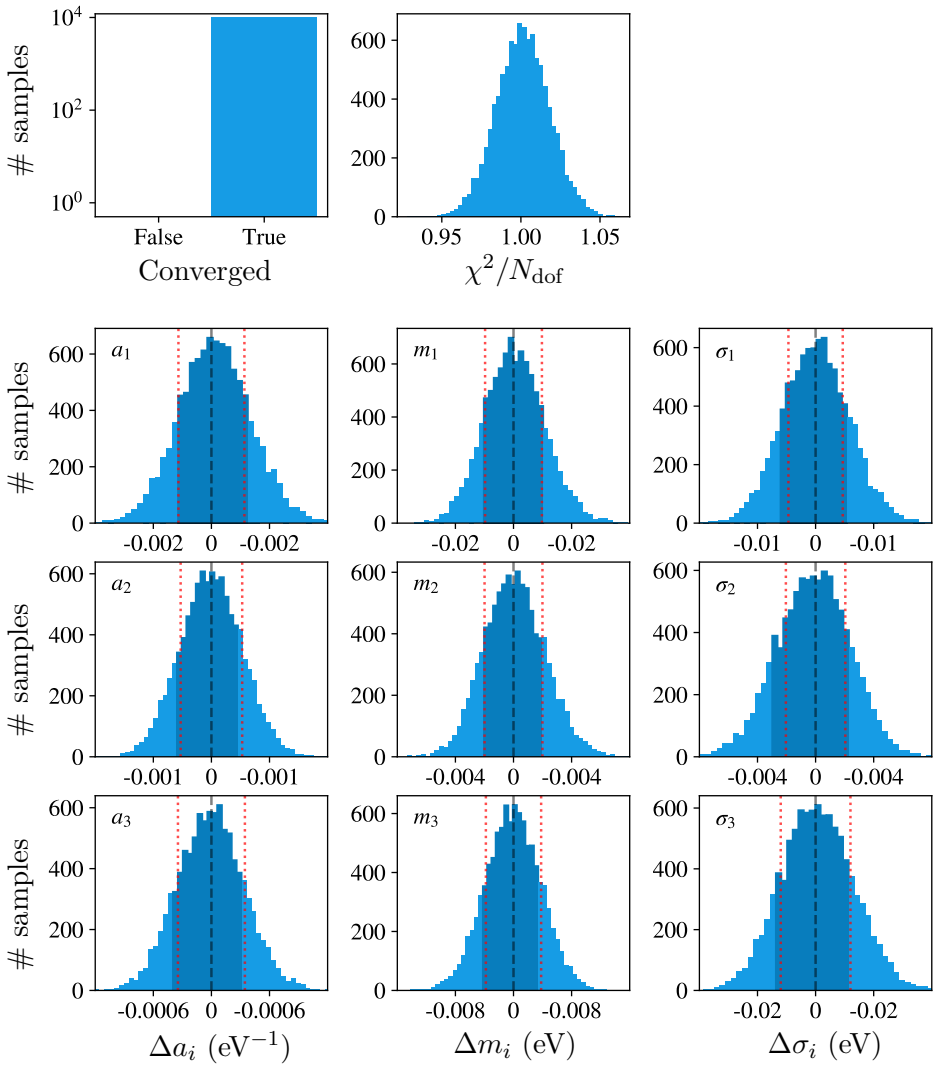


Figure A.14: Parameter distributions of the ensemble test including only statistical uncertainties. The histograms show the relative deviations of the best-fit results of the individual fits to the Monte Carlo data sets and the initial value, i.e. $\mathcal{P}_{i,\mathrm{MC}} - \mathcal{P}_{i,\mathrm{data}}$. The shaded area indicates the $1\sigma$ interval of the distributions. For a comparison, the parameter uncertainty of the best-fit result using the measurement data (comp. Tab. 8.4) is indicated by the red dotted lines.

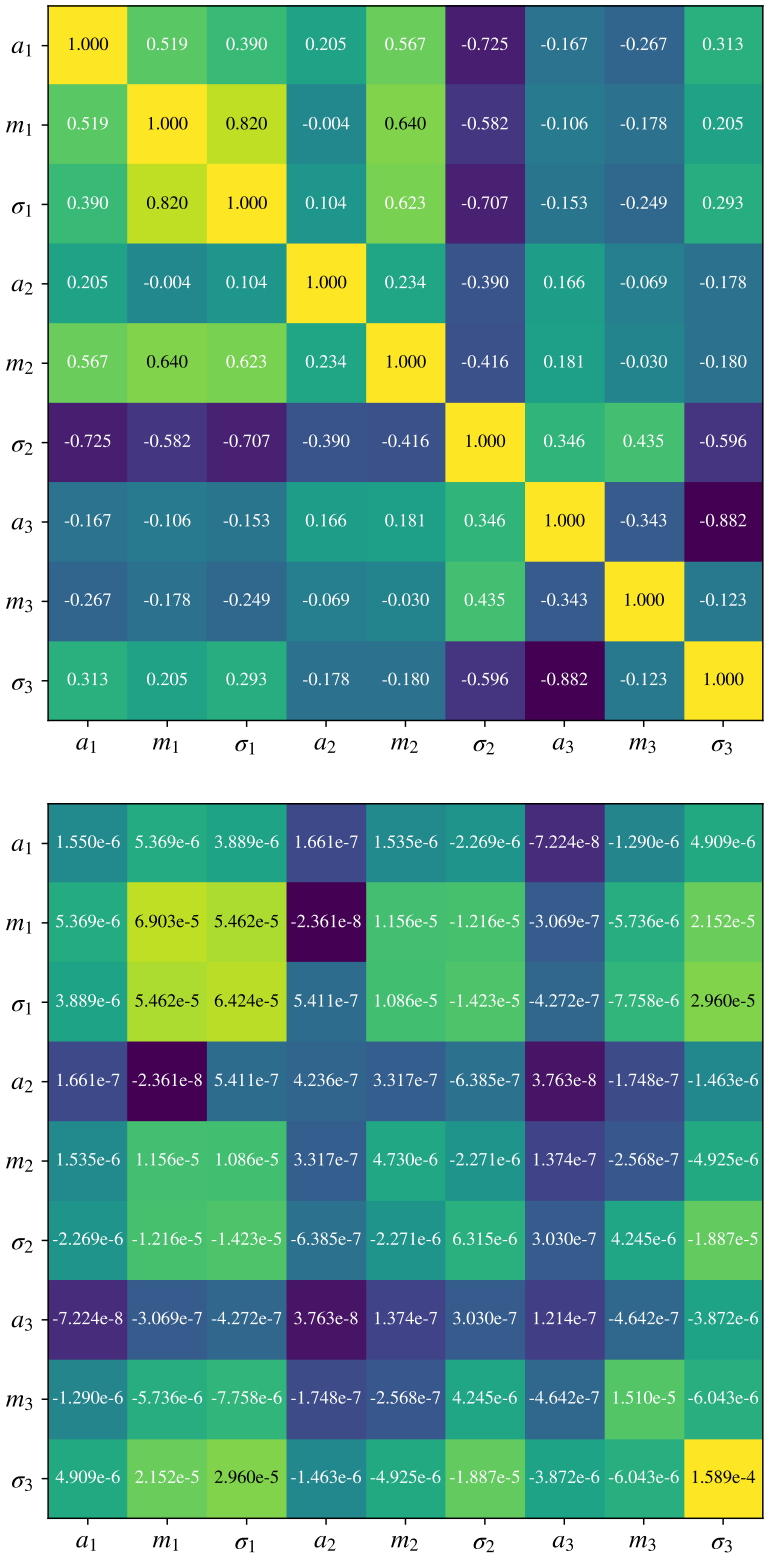


Figure A.15: Correlation matrix (top) and covariance matrix (bottom) for the energy-loss function parameters as obtained from the ensemble test using the Monte Carlo data with both statistical and systematic uncertainties included.

# List of Figures

# List of Tables

# Acronyms

**ADC** Analog-to-digital converter 66
**AGS** Alternating gradient synchrotron 7

**BED** Binary encounter dipole model 52, 100, 115, 118, 128
**Bi-CGSTAB** Stabilized biconjugate gradient method 97
**BIXS** Beta induced X-ray spectroscopy 43
**BOSS** Baryon oscillation spectroscopic survey 19

**CAD** Computer-aided design 32, 34, 35, 40, 41
**CMB** Cosmic microwave background 19
**CPS** Cryogenic pumping section 31, 34, 35

**DAQ** Data acquisition 40, 70, 81, 83, 124, 169
**DPS** Differential pumping section 31, 33, 34
**DPSS** Diode pumped solid state laser 70
**DRIPS** Detector readout simulator 87, 88, 90, 149, 150, 151, 152, 166, 169

**e-gun** Electron gun 43, 61, 63, 66
**EMCS** Earth magnetic field compensation system 37

**FBM** Forward beam monitor 35
**FPD** Focal plane detector 31, 40, 43, 66, 70, 81, 82, 83, 88, 90, 102, 105, 124, 143, 150, 164

**HV** High voltage 63, 65

**KNM1** KATRIN neutrino mass measurement campaign 1 139, 160
**KNM2** KATRIN neutrino mass measurement campaign 2 134, 177

**LDLS** Laser-driven light source 66, 68, 70, 71, 75, 76, 77, 81, 101, 102
**LED** Light emitting diode 70
**LFCS** Low field correction system 37, 104
**LHe** Liquid helium 35
**LN** Liquid nitrogen 39

**MAC-E** Magnetic adiabatic collimation with an electrostatic filter 1, 25, 26, 27, 28, 35, 37, 39, 55, 73, 75
**MC** Monte Carlo 110, 112, 133, 134
**MSW** Mikheyew-Smirnov-Wolfenstein 14, 15

**NEG** Non-evaporable getter 37

**PI** Proportional integral controller 66, 68
**PS** Pre-spectrometer 35
**PS1** Pre-spectrometer magnet 1 37
**PS2** Pre-spectrometer magnet 2 37

**PULCINELLA** Precision ultra-low current integrating normalization electrometer for low-level analysis 41

**RS** Rear section 41
**RSCM** Rear section superconducting magnet 41
**RW** Rear wall 41

**SDD** Silicon drift detector 35, 43
**SVD** Singular value decomposition 3, 95, 97, 98, 99, 108, 110, 112, 128, 134, 137, 139, 186

**UHV** Ultra high vacuum 37, 39

**vev** Vacuum expectation value 16, 17

**WGTS** Windowless gaseous tritium source 31, 32, 31, 33, 35, 39, 41, 43, 58, 59, 61, 63, 66, 95, 96, 101, 141, 160, 182

# Bibliography


[A+17] D. N. Abdurashitov et al. Electron scattering on hydrogen and deuterium molecules at 14–25 keV by the "Troitsk nu-mass" experiment. *Phys. Part. Nuclei Lett.*, 14(6):892–899, 2017. DOI: 10.1134/S1547477117060024.

[A+18] M. Arenz et al. The KATRIN superconducting magnets: Overview and first performance results. *JINST*, 13(08):T08005, 2018. DOI: 10.1088/1748-0221/13/08/T08005.

[A+20] M. Agostini et al. First Direct Experimental Evidence of CNO neutrinos. 6 2020. arXiv: 2006.15115.

[AA08] E. N. Alexeyev and L. N. Alexeyeva. Detection of a neutrino signal from SN 1987a on february 23, 1987 at 7:35 UT: Data from the baksan underground scintillation telescope. *Astron. Lett.*, 34(11):745–752, November 2008. DOI: 10.1134/s1063773708110030.

[AAA+02] Q. R. Ahmad, R. C. Allen, T. C. Andersen, et al. Direct evidence for neutrino flavor transformation from neutral-current interactions in the sudbury neutrino observatory. *Phys. Rev. Lett.*, 89:011301, June 2002. DOI: 10.1103/PhysRevLett.89.011301.

[AAA+14] P. Adamson, I. Anghel, A. Aurisano, et al. Combined analysis of $\nu_\mu$ disappearance and $\nu_\mu \rightarrow \nu_e$ appearance in MINOS using accelerator and atmospheric neutrinos. *Phys. Rev. Lett.*, 112(19), May 2014. DOI: 10.1103/physrevlett.112.191801.

[AAA+16a] Y. Abe, S. Appel, T. Abrahão, et al. Measurement of $\theta$ 13 in double chooz using neutron captures on hydrogen with novel background rejection techniques. *J. High Energ. Phys.*, 2016(1), January 2016. DOI: 10.1007/jhep01(2016)163.

[AAA+16b] R. Adam, P. A. R. Ade, N. Aghanim, et al. Planck 2015 results. *A&A*, 594:A1, September 2016. DOI: 10.1051/0004-6361/201527101.

[AAA+16c] F. An, G. An, Q. An, et al. Neutrino physics with JUNO. *J. Phys. G: Nucl. Part. Phys.*, 43(3):030401, February 2016. DOI: 10.1088/0954-3899/43/3/030401.

[AAA+18a] M. Aartsen, M. Ackermann, J. Adams, et al. Multimessenger observations of a flaring blazar coincident with high-energy neutrino IceCube-170922a. *Science*, 361(6398):eaat1378, July 2018. DOI: 10.1126/science.aat1378.

[AAA+18b] K. Abe, R. Akutsu, A. Ali, et al. Search for *cp* violation in neutrino and antineutrino oscillations by the T2K experiment with $2.2 \times 10^{21}$ protons on target. *Phys. Rev. Lett.*, 121:171802, October 2018. DOI: 10.1103/PhysRevLett.121.171802.

[AAA+19a] M. A. Acero, P. Adamson, L. Aliaga, et al. First measurement of neutrino oscillation parameters using neutrinos and antineutrinos by NOvA. *Phys. Rev. Lett.*, 123:151803, October 2019. DOI: 10.1103/PhysRevLett.123.151803.

[AAA+19b] M. Aker, K. Altenmüller, M. Arenz, et al. Improved upper limit on the neutrino mass from a direct kinematic method by KATRIN. *Phys. Rev. Lett.*, 123(22), November 2019. DOI: 10.1103/physrevlett.123.221802.

[AAA+19c] S. I. Alvis, I. J. Arnquist, F. T. Avignone, et al. Search for neutrinoless double-$\beta$ decay in $^{76}$Ge with 26 kg yr of exposure from the majorana demonstrator. *Phys. Rev. C*, 100:025501, August 2019. DOI: 10.1103/PhysRevC.100.025501.

[AAB+18] D. Adey, F. P. An, A. B. Balantekin, et al. Measurement of the electron antineutrino oscillation with 1958 days of operation at Daya Bay. *Phys. Rev. Lett.*, 121:241805, December 2018. DOI: 10.1103/PhysRevLett.121.241805.

[AAB+19] K. Altenmüller, M. Arenz, W.-J. Baek, et al. Muon-induced background in the KATRIN main spectrometer. *Astropart. Phys.*, 108:40 – 49, 2019. DOI: 10.1016/j.astropartphys.2019.01.003.

[ABB+00] V. N. Aseev, A. I. Belesev, A. I. Berlev, et al. Energy loss of 18 keV electrons in gaseous $T_2$ and quench condensed $D_2$ films. *Eur. Phys. J. D*, 10:39–52, 2000. DOI: 10.1007/s100530050525.

[ABB+11] V. N. Aseev, A. I. Belesev, A. I. Berlev, et al. Upper limit on the electron antineutrino mass from the Troitsk experiment. *Phys. Rev. D*, 84:112003, 2011. DOI: 10.1103/PhysRevD.84.112003.

[ABB+15] J. F. Amsbaugh, J. Barrett, A. Beglarian, et al. Focal-plane detector system for the KATRIN experiment. *Nucl .Instrum. Meth. A*, 778:40–60, 2015. DOI: 10.1016/j.nima.2014.12.116.

[ABB+16] M. Arenz, M. Babutzka, M. Bahr, et al. Commissioning of the vacuum system of the KATRIN main spectrometer. *JINST*, 11:P04011, 2016. DOI: 10.1088/1748-0221/11/04/P04011.

[ABB+19a] M. Agostini, A. M. Bakalyarov, M. Balata, et al. Probing majorana neutrinos with double-β decay. *Science*, 365(6460):1445–1448, September 2019. DOI: 10.1126/science.aav8613.

[ABB+19b] G. Anton, I. Badhrees, P. S. Barbeau, et al. Search for neutrinoless double-$\beta$ decay with the complete EXO-200 dataset. *Phys. Rev. Lett.*, 123:161802, October 2019. DOI: 10.1103/PhysRevLett.123.161802.

[ABG80] G.P. Arrighini, F. Biondi, and C. Guidotti. A study of the inelastic scattering of fast electrons from molecular hydrogen. *Mol. Phys.*, 41(6):1501–1514, December 1980. DOI: 10.1080/00268978000103701.

[Ada01] J. B. Adams. Bonding energy models. In *Encyclopedia of Materials: Science and Technology*, pages 763–767. Elsevier, 2001. DOI: 10.1016/b0-08-043152-6/00146-7.

[AGG+09] J. N. Abdurashitov, V. N. Gavrin, V. V. Gorbachev, et al. Measurement of the solar neutrino capture rate with gallium metal. III. results for the 2002–2007 data-taking period. *Phys. Rev. C*, 80:015807, July 2009. DOI: 10.1103/PhysRevC.80.015807.

[AHH+16] K. Abe, Y. Haga, Y. Hayato, et al. Solar neutrino measurements in Super-Kamiokande-IV. *Phys. Rev. D*, 94:052010, September 2016. DOI: 10.1103/PhysRevD.94.052010.

[Bab14] M. Babutzka. *Design and development for the Rearsection of the KATRIN experiment*. PhD thesis, Karlsruher Institut für Technologie, 2014. DOI: 10.5445/IR/1000045598.

[BAF79] R. A. Baragiola, E. V. Alonso, and A. Oliva Florio. Electron emission from clean metal surfaces induced by low-energy light ions. *Phys. Rev. B*, 19(1):121–129, January 1979. DOI: 10.1103/physrevb.19.121.

[Bah] J. N. Bahcall. Solar neutrinos: An overview. In *Confluence of Cosmology, Massive Neutrinos, Elementary Particles, and Gravitation*, pages 37–52. Kluwer Academic Publishers. DOI: 10.1007/0-306-47094-2_4.

[Bah64] J. N. Bahcall. Solar Neutrinos. I. Theoretical. *Phys. Rev. Lett.*, 12:300–302, March 1964. DOI: 10.1103/PhysRevLett.12.300.

[BBB+87] R. M. Bionta, G. Blewitt, C. B. Bratton, et al. Observation of a neutrino burst in coincidence with supernova 1987a in the large magellanic cloud. *Phys. Rev. Lett.*, 58:1494–1496, April 1987. DOI: 10.1103/PhysRevLett.58.1494.

[BBS+17] B. Bornschein, U. Besserer, M. Steidl, et al. The five phases to standard tritium operation of KATRIN. *Fusion Science and Technology*, 71(3):231–235, 2017. DOI: 10.1080/15361055.2016.1273703.

[BC84] S. Baker and R. D. Cousins. Clarification of the use of CHI-square and likelihood functions in fits to histograms. *Nucl. Instrum. Meth.*, 221(2):437–442, April 1984. DOI: 10.1016/0167-5087(84)90016-4.

[Beh17] J. D. Behrens. *Design and commissioning of a mono-energetic photoelectron source and active background reduction by magnetic pulse at the KATRIN spectrometers*. PhD thesis, Westfälische Wilhelms-Universität Münster, 2017. http://www.katrin.kit.edu/publikationen/phd_behrens.pdf.

[BFIS63] J. N. Bahcall, William A. Fowler, Jr. Iben I., and R. L. Sears. Solar neutrino flux. *Astrophys. J.*, 137:344, January 1963. DOI: 10.1086/147513.

[Blo] F. Block. *Statistical Data Analysis Tools and Magnetic Field Systematics for Neutrino Mass Analysis with KATRIN (in preparation)*. PhD thesis, Karlsruher Institut für Technologie (KIT).

[BLW+13] C. L. Bennett, D. Larson, J. L. Weiland, et al. Nine-year wilkinson microwave anisotropy probe (WMAP) observations: Final maps and results. *ApJS*, 208(2):20, September 2013. DOI: 10.1088/0067-0049/208/2/20.

[BMW85] R. A. Burger, H. Moraal, and G. M. Webb. Drift theory of charged particles in electric and magnetic fields. *Astrophys Space Sci*, 116(1):107–129, 1985. DOI: 10.1007/bf00649278.

[Boe56] J. H. De Boer. Adsorption phenomena. volume 8 of *Advances in Catalysis*, pages 17 – 161. Academic Press, 1956. DOI: 10.1016/S0360-0564(08)60538-6.

[Bok13] K. Bokeloh. *Calibration of hot and cold dark matter experiments: An angular selective photoelectron source for the KATRIN experiment and an apparatus to determine the reflection properties of PTFE for vacuum UV light*. PhD thesis, Westfälische Wilhelms-Universität Münster, 2013. http://nbn-resolving.de/urn:nbn:de:hbz:6-34329395924.

[BP34] H. Bethe and R. Peierls. The "neutrino". *Nature*, 133(3362):532–532, April 1934. DOI: 10.1038/133532a0.

[BPB01] J. N. Bahcall, M. H. Pinsonneault, and S. Basu. Solar models: Current epoch and time dependences, neutrinos, and helioseismological properties. *Astrophys. J.*, 555(2):990–1012, July 2001. DOI: 10.1086/321493.

[BPT80] G. Beamson, H. Q. Porter, and D. W. Turner. The collimating and magnifying properties of a superconducting field photoelectron spectrometer. *J. Phys. E: Sci. Instrum.*, 13(1):64, 1980. DOI: 10.1088/0022-3735/13/1/018.

[BR97] R. Brun and F. Rademakers. ROOT - an object oriented data analysis framework. *Nucl .Instrum. Meth. A*, 389(1–2):81–86, 1997. DOI: 10.1016/S0168-9002(97)00048-X.

[BRB+17] J. Behrens, P. C.-O. Ranitzsch, M. Beck, et al. A pulsed, monoenergetic and angular-selective UV photo-electron source for the commissioning of the KATRIN experiment. *Eur. Phys. J. C*, 77(6):410, 2017. DOI: 10.1140/epjc/s10052-017-4972-9.

[BSS+14] F. Beutler, S. Saito, H.-J. Seo, et al. The clustering of galaxies in the SDSS-III baryon oscillation spectroscopic survey: testing gravity with redshift space distortions using the power spectrum multipoles. *Mon. Not. Roy. Astron. Soc.*, 443(2):1065–1089, July 2014. DOI: 10.1093/mnras/stu1051.

[CAA+20] DUNE Collaboration, B. Abi, R. Acciarri, et al. Long-baseline neutrino oscillation physics potential of the DUNE experiment. 2020. arXiv: 2006.16043.

[CCGV11] G. Cowan, K. Cranmer, E. Gross, and Ofer Vitells. Asymptotic formulae for likelihood-based tests of new physics. *Eur. Phys. J. C*, 71(2), February 2011. DOI: 10.1140/epjc/s10052-011-1554-0.

[CDRD+98] B. T. Cleveland, T. Daily, Jr. R. Davis, et al. Measurement of the solar electron neutrino flux with the homestake chlorine detector. *Astrophys. J.*, 496(1):505–526, March 1998. DOI: 10.1086/305343.

[CEN17] CENPA. *Annual Report 2017*. 2017. ISBN: 978-1-119-41016-4.

[Cha14] J. Chadwick. Intensitätsverteilung im magnetischen Spectrum der β-Strahlen von radium B + C. *Verhandl. Dtsc. Phys. Ges.*, 16:383, 1914.

[Cha32] J. Chadwick. The existence of a neutron. *Proc. R. Soc. Lond. A*, 136(830):692–708, June 1932. DOI: 10.1098/rspa.1932.0112.

[CK03] D. Cahen and A. Kahn. Electron energetics at surfaces and interfaces: Concepts and experiments. *Adv. Mater.*, 15(4):271–277, February 2003. DOI: 10.1002/adma.200390065.

[CM95] Z. Chen and A. Z. Msezane. Calculation of the excitation cross sections for the $^1\sigma_u^+$ and c $^1\pi_u^+$ states in e-$H_2$ scattering at 60 eV. *Phys. Rev. A*, 51(5):3745–3750, May 1995. DOI: 10.1103/physreva.51.3745.

[CT91] C. Cohen-Tannoudji. *Quantum Mechanics, Vol. 1*. Wiley, jan 1991. ISBN: 047116433X.

[Deb19] K. Debowski. Optimization of the Integral Measurement of the Electron Energy Loss Function at KATRIN. Master's thesis, Karlsruher Institut für Technologie (KIT), April 2019. https://www.katrin.kit.edu/publikationen/mth-debowski.pdf.

[Dem18] W. Demtröder. *Atoms, Molecules and Photons.* Springer Berlin Heidelberg, 2018. DOI: 10.1007/978-3-662-55523-1.

[DGG+62] G. Danby, J.-M. Gaillard, K. Goulianos, et al. Observation of high-energy neutrino reactions and the existence of two kinds of neutrinos. *Phys. Rev. Lett.*, 9(1):36–44, July 1962. DOI: 10.1103/physrevlett.9.36.

[DMv+11] R. Dvornický, K. Muto, F. Šimkovic, et al. Absolute mass of neutrinos and the first unique forbidden $\beta$ decay of $^{187}$Re. *Phys. Rev. C*, 83:045502, April 2011. DOI: 10.1103/PhysRevC.83.045502.

[DPD+20] H. Dembinski, P. Ongmongkolkul, Ch. Deil, et al. scikit-hep/iminuit: v1.4.9, 2020.

[Dre03] G. Drexlin. Final neutrino oscillation results from LSND and KARMEN. *Nucl. Phys. B Proc. Suppl.*, 118:146–153, April 2003. DOI: 10.1016/s0920-5632(03)01312-4.

[EAB+17] A. Ashtari Esfahani, D. M. Asner, S. Böser, et al. Determining the neutrino mass with cyclotron radiation emission spectroscopy—project 8. *J. Phys. G: Nucl. Part. Phys.*, 44(5):054004, March 2017. DOI: 10.1088/1361-6471/aa5b4f.

[EBB+14] M. Erhard, S. Bauer, A. Beglarian, et al. High-voltage monitoring with a solenoid retarding spectrometer at the KATRIN experiment. *JINST*, 9(6):P06022, 2014. DOI: 10.1088/1748-0221/9/06/P06022.

[EBB+15] S. Eliseev, K. Blaum, M. Block, et al. Direct measurement of the mass difference ofHo163anddy163solves theQ-value puzzle for the neutrino mass determination. *Phys. Rev. Lett.*, 115(6), August 2015. DOI: 10.1103/physrevlett.115.062501.

[EHM87] S. R. Elliott, A. A. Hahn, and M. K. Moe. Direct evidence for two-neutrino double-beta decay in Se82. *Phys. Rev. Lett.*, 59(18):2020–2023, November 1987. DOI: 10.1103/physrevlett.59.2020.

[Erh16] M. G. Erhard. *Influence of the magnetic field on the transmission characteristics and neutrino mass systematic of the KATRIN experiment.* PhD thesis, Karlsruher Institut für Technologie, 2016. DOI: 10.5445/IR/1000065003.

[FBD+11] F. M. Fränkle, L. Bornschein, G. Drexlin, et al. Radon induced background processes in the KATRIN pre-spectrometer. *Astropart. Phys.*, 35(3):128–134, 2011. DOI: 10.1016/j.astropartphys.2011.06.009.

[Fer34] E. Fermi. Versuch einer theorie der $\beta$-Strahlen. *Zeitschrift für Physik*, 88(3–4):161–177, 1934. DOI: 10.1007/BF01351864.

[FGT+17] D. Furse, S. Groh, N. Trost, et al. Kassiopeia: a modern, extensible C++ particle tracking package. *New J. Phys.*, 19(5):053012, 2017. DOI: 10.1088/1367-2630/aa6950.

[FHI+98] Y. Fukuda, T. Hayakawa, E. Ichihara, et al. Evidence for oscillation of atmospheric neutrinos. *Phys. Rev. Lett.*, 81:1562–1567, August 1998. DOI: 10.1103/PhysRevLett.81.1562.

[FHK+86] M. Fritschi, E. Holzschuh, W. Kündig, et al. An upper limit for the mass of $\overline{\nu}_e$ from tritium β-decay. *Phys. Lett. B*, 173(4):485–489, June 1986. DOI: 10.1016/0370-2693(86)90420-x.

[Fra17] F. M. Fraenkle. Background processes in the KATRIN main spectrometer. *J. Phys.: Conf. Ser.*, 888(1):012070, 2017. DOI: 10.1088/1742-6596/888/1/012070.

[FRS+19] F. Friedel, C. Röttele, L. Schimpf, et al. Time-dependent simulation of the flow reduction of $D_2$ and $T_2$ in the KATRIN experiment. *Vacuum*, 159:161 – 172, 2019. DOI: 10.1016/j.vacuum.2018.10.002.

[GBB+18] S. Görhardt, J. Bonn, L. Bornschein, et al. Impact of a cryogenic baffle system on the suppression of radon-induced background in the KATRIN pre-spectrometer. *JINST*, 13(10):T10004, 2018. DOI: 10.1088/1748-0221/13/10/T10004.

[GBC+17] L. Gastaldo, K. Blaum, K. Chrysalidis, et al. The electron capture in 163Ho experiment – ECHo. *Eur. Phys. J. Spec. Top.*, 226(8):1623–1694, June 2017. DOI: 10.1140/epjst/e2017-70071-y.

[Gei64] J. Geiger. Streuung von 25 keV-elektronen an gasen. *Z. Physik*, 181(4):413–425, August 1964. DOI: 10.1007/bf01380873.

[GFGV00] M. Galeazzi, F. Fontanelli, F. Gatti, and S. Vitale. End-point energy and half-life of the187reβdecay. *Phys. Rev. C*, 63(1), December 2000. DOI: 10.1103/physrevc.63.014302.

[GK07] C. Giunti and C. W. Kim. Atmospheric neutrinos. In *Fundamentals of Neutrino Physics and Astrophysics*, pages 390–427. Oxford University Press, March 2007. DOI: 10.1093/acprof:oso/9780198508717.003.0011.

[GMP55] M. Gell-Mann and A. Pais. Behavior of neutral particles under charge conjugation. *Phys. Rev.*, 97:1387–1389, Mar 1955. DOI: 10.1103/PhysRev.97.1387.

[Gro15] S. Groh. *Modeling of the response function and measurement of transmission properties of the KATRIN experiment.* PhD thesis, Karlsruher Institut für Technologie (KIT), 2015. DOI: 10.5445/IR/1000046546.

[HAA+20] T. Houdy, A. Alborini, K. Altenmüller, et al. Hunting keV sterile neutrinos with KATRIN: Building the first TRISTAN module. *J. Phys.: Conf. Ser.*, 1468:Article No.012177, 2020. DOI: 10.1088/1742-6596/1468/1/012177. 51.03.01; LK 01.

[Hei27] W. Heisenberg. Über den anschaulichen inhalt der quantentheoretischen kinematik und mechanik. *Z. Physik*, 43(3-4):172–198, March 1927. DOI: 10.1007/bf01397280.

[HHW+17] V. Hannen, I. Heese, C. Weinheimer, A. Sejersen Riis, and K. Valerius. Deconvolution of the energy loss function of the KATRIN experiment. *Astropart. Phys.*, 89:30 – 38, 2017. DOI: 10.1016/j.astropartphys.2017.01.010.

[HIK+06] J. Hosaka, K. Ishihara, J. Kameda, et al. Solar neutrino measurements in Super-Kamiokande-I. *Phys. Rev. D*, 73(11), June 2006. DOI: 10.1103/physrevd.73.112001.

[HKK+87] K. Hirata, T. Kajita, M. Koshiba, et al. Observation of a neutrino burst from the supernova SN1987A. *Phys. Rev. Lett.*, 58:1490–1493, April 1987. DOI: 10.1103/PhysRevLett.58.1490.

[HW04] H. Haken and H. Ch. Wolf. *Molecular Physics and Elements of Quantum Chemistry.* Springer Berlin Heidelberg, 2004. DOI: 10.1007/978-3-662-08820-3.

[Ino71] M. Inokuti. Inelastic collisions of fast charged particles with atoms and molecules—the bethe theory revisited. *Rev. Mod. Phys.*, 43(3):297–347, July 1971. DOI: 10.1103/revmodphys.43.297.

[JAK+00] C. Jensen, F. Aaserud, H. Kragh, Erik Rüdinger, and Roger H. Stuewer. *Controversy and Consensus: Nuclear Beta Decay 1911-1934*. Birkhäuser Basel, 2000. DOI: 10.1007/978-3-0348-8444-0.

[Jan17] H.-T. Janka. Neutrino emission from supernovae. In *Handbook of Supernovae*, pages 1575–1604. Springer International Publishing, 2017. DOI: 10.1007/978-3-319-21846-5_4.

[Jou16] K. Jousten. *Handbook of Vacuum Technology*. John Wiley & Sons, New York, 2016. ISBN: 978-3-527-41338-6.

[JR75] F. James and M. Roos. Minuit - a system for function minimization and analysis of the parameter errors and correlations. *Comput. Phys. Commun.*, 10(6):343–367, December 1975. DOI: 10.1016/0010-4655(75)90039-9.

[KAT05] KATRIN collaboration. KATRIN design report. FZKA scientific report 7090, 2005. DOI: 10.5445/IR/270060419.

[KBB+05] C. Kraus, B. Bornschein, L. Bornschein, et al. Final results from phase II of the mainz neutrino mass search in tritium $\beta$ decay. *Eur. Phys. J. C*, 40(4):447–468, 2005. DOI: 10.1140/epjc/s2005-02139-7.

[KBD+19] M. Kleesiek, J. Behrens, G. Drexlin, et al. β-decay spectrum, response function and statistical model for neutrino mass measurements with the KATRIN experiment. *Eur. Phys. J. C*, 79(3), March 2019. DOI: 10.1140/epjc/s10052-019-6686-7.

[Kir98] T. A. Kirsten. GALLEX solar neutrino results. *Prog. Part. Nucl. Phys*, 40:85–99, January 1998. DOI: 10.1016/s0146-6410(98)00013-1.

[Kit05] Ch. Kittel. *Introduction to solid state physics*. Wiley, Hoboken, NJ, 8 edition, 2005. ISBN: 9780471680574.

[Kle18] M. Klein. *Tritium ions in KATRIN: blocking, removal and detection*. PhD thesis, Karlsruher Institut für Technologie (KIT), 2018. DOI: 10.5445/IR/1000093526.

[Kon47] E. J. Konopinski. $H^3$ and the Mass of the Neutrino. *Phys. Rev.*, 72(6):518–519, September 1947. DOI: 10.1103/physrev.72.518.2.

[Kor20] M. Korzeczek. *Sterile neutrino search with KATRIN - modeling and design-criteria of a novel detector system*. PhD thesis, Karlsruher Institut für Technologie (KIT), 2020. 51.03.02; LK 01. DOI: 10.5445/IR/1000120634.

[KR94] Y.-K. Kim and M. E. Rudd. Binary-encounter-dipole model for electron-impact ionization. *Phys. Rev. A*, 50(5):3954–3967, November 1994. DOI: 10.1103/physreva.50.3954.

[KSP00] Y.-K. Kim, J. P. Santos, and F. Parente. Extension of the binary-encounter-dipole model to relativistic incident electrons. *Phys. Rev. A*, 62(5), October 2000. DOI: 10.1103/physreva.62.052710.

[KUA+01] K. Kodama, N. Ushida, C. Andreopoulos, et al. Observation of tau neutrino interactions. *Phys. Lett. B*, 504(3):218–224, April 2001. DOI: 10.1016/s0370-2693(01)00307-0.

[Kuc16] L. Kuckert. *The Windowless Gaseous Tritium Source of the KATRIN Experiment – Characterisation of Gas Dynamical and Plasma Properties.* PhD thesis, Karlsruher Institut für Technologie (KIT), 2016. DOI: 10.5445/IR/1000065077.

[Lan80] N. F. Lane. The theory of electron-molecule collisions. *Rev. Mod. Phys.*, 52(1):29–119, January 1980. DOI: 10.1103/revmodphys.52.29.

[Lis17] L. Lista. *Statistical Methods for Data Analysis in Particle Physics.* Springer International Publishing, 2017. DOI: 10.1007/978-3-319-62840-0.

[Liu73] J. W. Liu. Total inelastic cross section for collisions of $H_2$ with fast charged particles. *Phys. Rev. A*, 7(1):103–109, January 1973. DOI: 10.1103/physreva.7.103.

[Liu87] J. W. Liu. Total cross sections for high-energy electron scattering by $H_2(1\sigma_g^+)$, $N_2(1\sigma_g^+)$, and $O_2(3\sigma_g^-)$. *Phys. Rev. A*, 35(2):591–597, January 1987. DOI: 10.1103/physreva.35.591.

[LL02] T. J. Loredo and D. Q. Lamb. Bayesian analysis of neutrinos observed from supernova SN 1987A. *Phys. Rev. D*, 65:063002, February 2002. DOI: 10.1103/PhysRevD.65.063002.

[LM52] L. M. Langer and R. J. D. Moffat. The beta-spectrum of tritium and the mass of the neutrino. *Phys. Rev.*, 88(4):689–694, November 1952. DOI: 10.1103/physrev.88.689.

[LP12] J. Lesgourgues and S. Pastor. Neutrino mass from cosmology. *Adv. High Energy Phys.*, 2012:1–34, 2012. DOI: 10.1155/2012/608515.

[Maj15] B. Majorovits. Phase II upgrade of the GERDA experiment for the search of neutrinoless double beta decay. *Phys. Procedia*, 61:254–259, 2015. DOI: 10.1016/j.phpro.2014.12.041.

[Mar20] A. C. Marsteller. *Characterization and Optimization of the KATRIN Tritium Source.* PhD thesis, Karlsruher Institut für Technologie (KIT), 2020. DOI: 10.5445/IR/1000127553.

[MBB+21] A. Marsteller, B. Bornschein, L. Bornschein, et al. Neutral tritium gas reduction in the KATRIN differential pumping sections. *Vacuum*, 184:109979, February 2021. DOI: 10.1016/j.vacuum.2020.109979.

[MHFT12] J. J. Munro, S. Harrison, M. M. Fujimoto, and J. Tennyson. A dissociative electron attachment cross-section estimator. *J. Phys.: Conf. Ser.*, 388(1):012013, November 2012. DOI: 10.1088/1742-6596/388/1/012013.

[MNS62] Z. Maki, M. Nakagawa, and S. Sakata. Remarks on the unified model of elementary particles. *Prog. Theor. Phys.*, 28(5):870–880, November 1962. DOI: 10.1143/ptp.28.870.

[Mor29] P. M. Morse. Diatomic molecules according to the wave mechanics. II. vibrational levels. *Phys. Rev.*, 34(1):57–64, July 1929. DOI: 10.1103/physrev.34.57.

[MS86] S. P. Mikheyev and A. Yu. Smirnov. Resonant amplification of $\nu$ oscillations in matter and solar-neutrino spectroscopy. *Il Nuovo Cimento C*, 9(1):17–26, January 1986. DOI: 10.1007/bf02508049.

[NA37] S. H. Neddermeyer and C. D. Anderson. Note on the nature of cosmic-ray particles. *Phys. Rev.*, 51(10):884–886, May 1937. DOI: 10.1103/physrev.51.884.

[NAB+18] A. Nucciotti, B. Alpert, M. Balata, et al. Status of the HOLMES experiment to directly measure the neutrino mass. *J. Low Temp. Phys.*, 193(5-6):1137–1145, July 2018. DOI: 10.1007/s10909-018-2025-x.

[P+07] W. Press et al. *Numerical recipes : the art of scientific computing.* Cambridge University Press, Cambridge, UK New York, 2007. ISBN: 978-0-521-88068-8.

[PAB+75] M. L. Perl, G. S. Abrams, A. M. Boyarski, et al. Evidence for anomalous lepton production in $e^+ - e^-$ annihilation. *Phys. Rev. Lett.*, 35:1489–1492, 12 1975. DOI: 10.1103/PhysRevLett.35.1489.

[Pat01] T. Patzak. First direct observation of the tau neutrino. *Europhys. News*, 32(2):56–57, March 2001. DOI: 10.1051/epn:2001205.

[PB02] Z. Pei and C. N. Berglund. Angular distribution of photoemission from gold thin films. *Jpn. J. Appl. Phys.*, 41(Part 2, No. 1A/B):L52–L54, January 2002. DOI: 10.1143/jjap.41.l52.

[PBB+92] A. Picard, H. Backe, H. Barth, et al. A solenoid retarding spectrometer with high resolution and transmission for keV electrons. *Nucl. Instrum. Meth. B*, 63(3):345–358, 1992. DOI: 10.1016/0168-583X(92)95119-C.

[Piq06] F. Piquemal. The SuperNEMO project. *Phys. Atom. Nuclei*, 69(12):2096–2100, December 2006. DOI: 10.1134/s1063778806120131.

[PKW64] W. E. F. Pauli, R. Kronig, and V. F. Weisskopf. *Collected scientific papers.* Interscience, New York, NY, 1964. Offener Brief an die Gruppe der Radioaktiven bei der Gauvereinstagung zu Tübingen (datiert 4. Dez. 1930).

[Pon58] B. Pontecorvo. Inverse beta processes and nonconservation of lepton charge. *Sov. Phys. JETP*, 7:172–173, 1958.

[PP55] A. Pais and O. Piccioni. Note on the decay and absorption of the $\theta^0$. *Phys. Rev.*, 100:1487–1489, December 1955. DOI: 10.1103/PhysRev.100.1487.

[PVCI09] G. Pagliaroli, F. Vissani, M.L. Costantini, and A. Ianni. Improved analysis of SN1987a antineutrino events. *Astropart. Phys.*, 31(3):163–176, April 2009. DOI: 10.1016/j.astropartphys.2008.12.010.

[RBS+91] R. G. H. Robertson, T. J. Bowles, G. J. Stephenson, et al. Limit on $\overline{\nu}_e$ mass from observation of the $\beta$ decay of molecular tritium. *Phys. Rev. Lett.*, 67:957–960, 1991. DOI: 10.1103/PhysRevLett.67.957.

[RC53] F. Reines and C. L. Cowan. Detection of the free neutrino. *Phys. Rev.*, 92:830–831, 1953. DOI: 10.1103/PhysRev.92.830.

[RC56] F. Reines and C. L. Cowan. The neutrino. *Nature*, 178(4531):446–449, September 1956. DOI: 10.1038/178446a0.

[RK88] R. G. H. Robertson and D. A. Knapp. Direct measurements of neutrino mass. *Ann. Rev. Nucl. Part. Sci.*, 38(1):185–215, 1988. DOI: 10.1146/annurev.ns.38.120188.001153.

[Rod] C. Rodenbeck. *Investigation of inelastic scattering of beta electrons in KATRIN's gaseous tritium source using time of flight methods to determine the neutrino mass (in preparation).* PhD thesis, Westfälische Wilhelms-Universität Münster.

[Röl15] M. Röllig. *Tritium analytics by beta induced X-ray spectrometry.* PhD thesis, Karlsruher Institut für Technologie (KIT), 2015. DOI: 10.5445/IR/1000054050.

[Röt19] C. Röttele. *Tritium suppression factor of the KATRIN transport section.* PhD thesis, Karlsruher Institut für Technologie (KIT), 2019. DOI: 10.5445/IR/1000096733.

[Rud91] M. E. Rudd. Differential and total cross sections for ionization of helium and hydrogen by electrons. *Phys. Rev. A*, 44(3):1644–1652, August 1991. DOI: 10.1103/physreva.44.1644.

[Rut99] E. Rutherford. VIII. uranium radiation and the electrical conduction produced by it. *The London, Edinburgh, and Dublin Philosophical Magazine and Journal of Science*, 47(284):109–163, January 1899. DOI: 10.1080/14786449908621245.

[RV17] P. Radvanyi and J. Villain. The discovery of radioactivity. *Comptes Rendus Physique*, 18(9-10):544–550, November 2017. DOI: 10.1016/j.crhy.2017.10.008.

[RWB+19] O. Rest, D. Winzen, S. Bauer, et al. A novel ppm-precise absolute calibration method for precision high-voltage dividers. *Metrologia*, 56(4):045007, July 2019. DOI: 10.1088/1681-7575/ab2997.

[S+17] J. Shirai et al. Results and future plans for the KamLAND-zen experiment. *J. Phys.: Conf. Ser.*, 888:012031, September 2017. DOI: 10.1088/1742-6596/888/1/012031.

[SA+20] C. D. Shin, , Z. Atif, et al. Observation of reactor antineutrino disappearance using delayed neutron capture on hydrogen at RENO. *J. High Energ. Phys.*, 2020(4), April 2020. DOI: 10.1007/jhep04(2020)029.

[SAB+04] M. Sisti, C. Arnaboldi, C. Brofferio, et al. New limits from the milano neutrino mass experiment with thermal microcalorimeters. *Nucl. Instrum. Methods Phys. Res. A*, 520(1-3):125–131, March 2004. DOI: 10.1016/j.nima.2003.11.273.

[Sac20] R. Sack. *Measurement of the energy loss of 18.6 keV electrons on deuterium gas and determination of the tritium Q-value at the KATRIN experiment.* PhD thesis, Westfälische Wilhelms-Universität Münster, 2020. http://nbn-resolving.de/urn:nbn:de:hbz:6-59069498754.

[Sch16] K. Schönung. *Development of a Rear Wall for the KATRIN Rear Section and investigation of tritium compatibility of Rear Section components.* PhD thesis, Karlsruher Institut für Technologie, 2016. DOI: 10.5445/IR/1000056077.

[Sch20] Ch. F. R. Schwachtgen. Characterisation of Systematics of the Energy Loss Measurement of $e^-$-$T_2$ Scattering inside the Source of KATRIN. Master's thesis, Karlsruher Institut für Technologie (KIT), December 2020.

[SD95] W. Stoeffl and D. J. Decman. Anomalous structure in the beta decay of gaseous molecular tritium. *Phys. Rev. Lett.*, 75(18):3237–3240, October 1995. DOI: 10.1103/physrevlett.75.3237.

[Smo99] G. F. Smoot. COBE observations and results. In *AIP Conf. Proc.* ASCE, 1999. DOI: 10.1063/1.59326.

[TMW09] T. Thümmler, R. Marx, and C. Weinheimer. Precision high voltage divider for the KATRIN experiment. *New J. Phys.*, 11(10):103007, 2009. DOI: 10.1088/1367-2630/11/10/103007.

[Tro19] N. R.-M. Trost. *Modeling and measurement of Rydberg-State mediated Background at the KATRIN Main Spectrometer*. PhD thesis, Karlsruher Institut für Technologie (KIT), 2019. DOI: 10.5445/IR/1000090450.

[UL00] M. P. Unterweger and L. L. Lucas. Calibration of the national institute of standards and technology tritiated-water standards. *Appl. Radiat. Isot.*, 52(3):527–531, March 2000. DOI: 10.1016/S0969-8043(99)00205-5.

[Upa19] A. Upadhye. Neutrino mass and dark energy constraints from redshift-space distortions. *JCAP*, 2019(05):041–041, May 2019. DOI: 10.1088/1475-7516/2019/05/041.

[Val09] K. Valerius. *Spectrometer-related background processes and their suppression in the KATRIN experiment*. PhD thesis, Westfälische Wilhelms-Universität Münster, 2009. http://nbn-resolving.de/urn:nbn:de:hbz:6-28479494638.

[Vej82] E. Veje. Secondary electron emission from gold bombarded with $H^+$, $H_2^+$, $H_3^+$, $He^+$, and $HeH^+$. *Nucl. Instrum. Meth.*, 194(1-3):433–436, March 1982. DOI: 10.1016/0029-554x(82)90559-6.

[WDF+13] N. Wandkowsky, G. Drexlin, F. M. Fränkle, et al. Validation of a model for radon-induced background processes in electrostatic spectrometers. *J. Phys. G: Nucl. Part. Phys.*, 40(8):085102, 2013. DOI: 10.1088/0954-3899/40/8/085102.

[Weh66] G. Wehner. Energieverteilung der von 2, 5, 10 und 15 keV He- und Ar-Ionen an Molybdän ausgelösten Elektronen. *Z. Physik*, 193(3):439–442, October 1966. DOI: 10.1007/bf01326441.

[WJH99] P. Weck, B. Joulakian, and P. A. Hervieux. Fivefold differential cross section of fast $(e, 2e)$ ionization of $H_2$, $D_2$, and $T_2$ by a Franck-Condon approach. *Phys. Rev. A*, 60:3013–3019, October 1999. DOI: 10.1103/PhysRevA.60.3013.

[Wol78] L. Wolfenstein. Neutrino oscillations in matter. *Phys. Rev. D*, 17:2369–2374, May 1978. DOI: 10.1103/PhysRevD.17.2369.

[YMYH+08] J.-S. Yoon, M.-Y.Song, J.-M. Han, et al. Cross sections for electron collisions with hydrogen molecules. *J. Phys. Chem. Ref. Data*, 37(2):913–931, June 2008. DOI: 10.1063/1.2838023.

[Zac15] M. Zacher. *High-field electrodes design and an angular-selective photoelectron source for the KATRIN spectrometers*. PhD thesis, Westfälische Wilhelms-Universität Münster, 2015.

[ZB+20] P. A. Zyla, , R. M. Barnett, et al. Review of particle physics. *PTEP*, 2020(8), August 2020. DOI: 10.1093/ptep/ptaa104.

[ZBB+13] M. Zbořil, S. Bauer, M. Beck, et al. Ultra-stable implanted $^{83}Rb/^{83m}Kr$ electron sources for the energy scale monitoring in the KATRIN experiment. *JINST*, 8(03):P03009, 2013. DOI: 10.1088/1748-0221/8/03/P03009.

[Zub12] K. Zuber. *Neutrino physics*. Series in high energy physics, cosmology, and gravitation. CRC Press / Taylor & Francis, 2nd edition, 2012. ISBN: 9781420064711.

# Acknowledgments

Als Abschluss dieser Arbeit möchte ich mich bei den vielen Personen bedanken, die zum Gelingen der Arbeit wichtige Beiträge geleistet haben. Ein sehr großer Dank gilt Prof. Dr. Kathrin Valerius für die Möglichkeit, dass ich diese Doktorarbeit unter ihrer persönlichen Betreuung anfertigen konnte. Genauso möchte ich mich bei Prof. Dr. Bernhard Holzapfel bedanken, dass er die Aufgabe des Korreferats dieser Arbeit übernommen hat.

Ein wichtiger Beitrag zum Gelingen dieser Arbeit war die guten Zusammenarbeit mit dem sogenannten *e-Gauner* Team um Dr. Jan Behrens, Dr. Rudolf Sack und Caroline Rodenbeck. Mit euch haben sich die zahlreichen Wochenendschichten während der Inbetriebnahme und den darauffolgenden Messungen gut aushalten lassen. Genauso wichtig war die Zusammenarbeit im Eloss-Team, zu dem neben den bereits genannten *e-Gaunern* auch Dr. Volker Hannen und Dr. Björn Lehnert zählen. Durch ihr Fachwissen im Bereich der Datenanalyse habe ich viel gelernt.

Jetzt folgt vermutlich der schwierigste Teil: sich bei all denjenigen zu bedanken, die mich während meiner Zeit bei KATRIN und zum Teil auch schon während des Studiums begleitet und unterstützt haben, ohne jemanden dabei zu vergessen.

Hier möchte ich mich selbstverständlich bei Dr. Fabian Friedel bedanken, mit dem ich seit Tag eins des Studiums eine Freundschaft geschlossen habe und mit dem ich gemeinsam die Hürden des Studiums und der darauffolgenden Promotion gemeistert habe. Mit dir hat man selbst beim Lernen auf Prüfungen viele sehr lustige Momente erlebt, konnte aber auch jederzeit ernste physikalische Probleme mit dir diskutieren.

Ähnliches gilt für Dr. Carsten Röttele, mit dem ich mehrere Jahre das Büro geteilt habe, was einer der Gründe war, weshalb ich immer gerne morgens zur Arbeit gekommen bin. Auf dich konnte man sich in den unterschiedlichsten Situationen verlassen, was ich sehr an dir schätze.

Ich möchte mich auch bei Klaus Mehret bedanken, der mich besonders beim Bau der e-gun Mk II und Mk III durch die schnelle, präzise und unkomplizierte Fertigung von Bauteilen unterstützt hat. Vor allem hat es mich gefreut, dass ich dir jederzeit über die Schulter schauen konnte und dabei viel über Metallverarbeitung lernen konnte.

Ein großer Dank gilt auch den Personen, die Zeit damit verbracht haben meine Arbeit Korrektur zu lesen.

Persönlich möchte ich mich bei meinen Freunden Woo-Jeong Baek und Andreas Schulik bedanken. Besonders während stressigen Zeiten der Promotion tat es gut, sich mit euch zu verabreden oder zu telefonieren.

Zum guten Schluss möchte ich mich natürlich bei meiner Familie bedanken. Hier benötigt es keine großen Worte, denn ihr wisst weshalb :).

Lutz Schimpf acknowledges the support by the Doctoral School „Karlsruhe School of Elementary and Astroparticle Physics: Science and Technology“